A Mimetic Spectral Element Implementation

of the Maxwell Eigenvalue Problem

Gerardo Ureña Baltierra

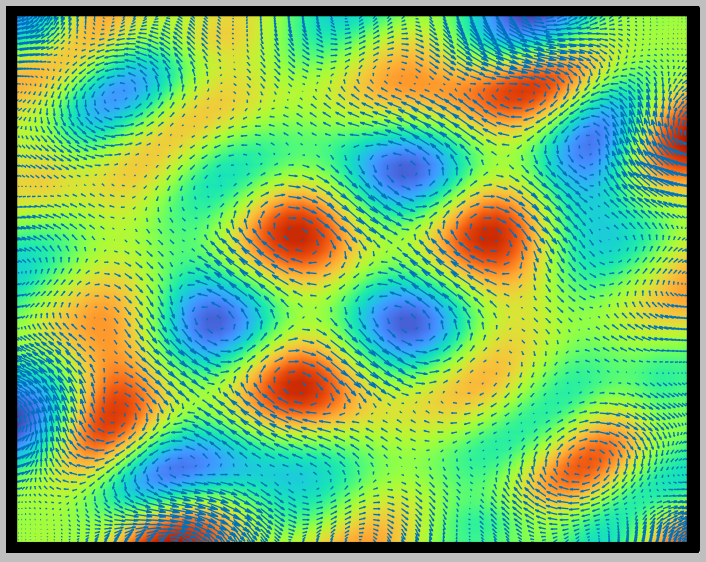

Aerodynamics

Faculty of Aerospace Engineering

TU Delft

Delft University of Technology

A Mimetic Spectral Element Implementation

of the Maxwell Eigenvalue Problem

by

Gerardo Ureña Baltierra

to obtain the degree of Master of Science in Aerospace Engineering at
the Delft University of Technology, to be defended on
Thursday, October 13, 2022 at 2:00 PM.

Student Number : 4736966

Thesis Supervisor :	Dr. ir. M. I. Gerritsma,	TU Delft
Thesis Committee :	Dr. S. J. Hulshoff,	TU Delft
	Dr. D. Toshniwal,	TU Delft
	Dr. ir. R. F. Remis,	TU Delft

An electronic version of this thesis is available at
http://repository.tudelft.nl/.

Science is a wonderful thing
if one does not have to earn one's living at it.

Albert Einstein

Abstract

Mimetic formulations, also known as structure-preserving methods, are numerical schemes that preserve fundamental properties of the continuous differential operators at a discrete level. Additionally, they are well-known for satisfying constraints such as conservation of mass or momentum.

In the present work, a Mimetic Spectral Element Method based on quadrilaterals is explored. As an introduction, the framework is first implemented and tested on the classical Poisson equation, the Hartmann Flow system and several eigenvalue problems for the Laplacian operator. Solutions are attained by direct/mixed formulations and the extension to multi-element approaches is dealt with using either gathering or connectivity matrices. Different boundary conditions and various geometries are utilized.

Afterwards, the Maxwell Eigenvalue problem for the electric field $\mathbf{E}$ with general material properties is tackled in an attempt to generate spurious-free solutions by incorporating the condition $\nabla \cdot \mathbf{D} = 0$ into the discrete system. The formulation is further scrutinized on geometries with Betti number $b_1 > 0$ as to verify if the proposed scheme captures the physical zero eigenvalues.

In the end, a mixed formulation for the eigenproblem is proposed in which the curl-curl operator is separated. The approximation of the electrostatic field energy is then computed with this formulation and compared to the solution obtained with a direct method allowing to create an upper and a lower bound for this variable.

Contents

1

Introduction

1.1 Relation Between Geometry and Physics

There are plenty of different physical quantities spread along the many areas of science and, as weird as it may sound, *all* of them have an association to a specific geometric object. Consider, for instance, the density which is computed as $\rho = {}^{m}/_{V}$. Mathematically, however, the *exact* value would be given by the expression:

$$\rho = \lim_{V \to 0} \frac{m}{V}$$

Once the *mathematically correct* concept of limit has been applied, the notion of the density being associated to a volume has disappeared and the new variable is now associated to a point. Such result might be irrelevant if equations are considered only as mathematical entities. Nevertheless, if equations are regarded as instruments that model reality, it is odd to give up such association. It would make sense to nurture equations with as much *reality* as possible in hopes of better results.

Unfortunately, removing the association of variables to their geometric objects is quite common in many numerical methods where variables end up being linked to points even though such association is false. Ideally, numerical methods would translate all physical notions into an appropriate mathematical language. This change of paradigm would start by, firstly, not emptying physical quantities from their properties and, secondly, by not thinking of differential equations but rather of physical problems [66].

The idea of relating geometry and physics was explored, at least, about a hundred of years ago. In [25], James Clerk Maxwell points out the analogy between certain kind of problems such as equations in electromagnetism resembling problems from heat conduction and vice versa. Thus, the results from Fourier regarding heat could explain situations in electrical problems while the knowledge for the Poisson equation in electricity could be applied to heat conduction.

From Maxwell's perspective, there must be principles that are of a more *fundamental* nature for such analogies to exist. The latter had remained well hidden since all physical quantities are treated the same way once a problem has been reduced to a mathematical form. Hence, maintaining the physical ideas of nature itself within the equations might be a step in the right direction to unveil such principles.

Developing the aforementioned concept would commence with a classification of physical quantities. By categorizing variables, it would be readily known how to treat them within the mathematical framework. Additionally, it would allow to detect similarities between areas of science so that, according to Maxwell [25, p. 225], "we should lose no time in availing ourselves of the mathematical labours of those who had already solved problems essentially the same".

The notion of a more fundamental concept within nature was mentioned also by the physicist Richard Feynman. Such idea arose by wondering about how so different phenomena could be described by so similar-looking equations. In Feynman's terms, the answer would be the *underlying unity of nature* [35, Section 12-7]. In fact, the physicist would also argue that the common ground between problems is that they all involve *space* which all differential equations attempt to imitate.

Around the mid-1970s, Enzo Tonti [88] came up with a whole mathematical structure that was common to all physical theories and which took into consideration the geometric features of variables. This study relied not only on a thorough analysis of variables (as previously suggested by Maxwell) but also on an examination of the equations within each area of science. This framework became a numerical technique on itself called *Cell Method*[1] but the general ideas permeated into the scientific community and spread to other methods as well.

The aforementioned concepts are predominant in the development of numerical methods in electromagnetism by Bossavit who utilized differential forms to mimic the topological structures of the Tonti diagrams. Furthermore, he successfully discretized such diagrams with the so-called *Whitney Forms*. This pioneering work is presented and summarized in the *Japanese papers*[2] where it is further elucidated

[1] Additional information on the method can be found in references [230-232, 234] from [89].
[2] The whole documentation can be easily read from a website hosted by the University of Washington: https://faculty.washington.edu/seattle/physics544/2011-lectures/bossavit.pdf

how the geometric content can be captured by means of differential forms and its applications in solving PDEs.

Plenty of other authors from a variety of disciplines have adopted such framework by taking into consideration geometry. Some of them have been named above but others worth reading are Brezzi [23], Hiptmair [42, 46], Bochev [7, 8], Perot [74], Flanders [36] and Teixeira. Additionally, for time-dependent problems, the discretization for the temporal variable is treated by Mattiusi [66] following a framework compatible with these principles.

Nowadays, the literature related to numerical schemes based on this school of thought is still ongoing. The latter is only a testament of the benefits of considering the geometry embedded in the differential equations is a characteristic worth being exploited to create physically accurate numerical schemes.

1.2 What are mimetic methods?

Mimetic methods (also known as *structure-preserving methods*) are numerical methods that aim to preserve fundamental properties of the continuous problems. For these techniques, the main premise is to capture the physics that are intrinsic to a PDE rather than solely focusing on the mathematical properties. In fact, experience has confirmed that the best results are usually obtained when the discrete model preserves the underlying properties of the physical system [64].

One of the main characteristics of these types of discretizations is their robustness and accuracy. Additionally, they are well-known for conserving mass, momentum or kinetic energy [70] which is one of the main reasons their popularity has been increasing throughout the years[3]. As a consequence of satisfying properties at a discrete level, these methods are quite convenient since they **cannot** produce solutions that violate physical constraints. Typical examples of such constraints include the continuity equation for incompressible flows or, in electromagnetism, the condition $\nabla \cdot \underline{\mathrm{B}} = 0$ stating the nonexistence of magnetic monopoles.

Creating these kind of schemes, however, is not entirely trivial and some principles should be satisfied. According to Robidoux [79], there are five conditions that must be met to attain a complete mimetic discretization of vector calculus:

1. Discretization of the differential operators gradient, divergence and curl.
2. Discretization of integrals over curves, surfaces and volumes.
3. Discrete analogs of the fundamental theorems of vector calculus.

[3] A short historic perspective detailing the evolution of mimetic methods is shown in [64].

4. A discrete analog of the exact *commuting diagram*.

5. Discrete analogs of the product rules.

The first condition is obvious since any differential equation possesses at least one of those operators and, as a result, a proper discretization for each must be available. By *proper* it is meant, as explained in [64], that a correct characterization of the null spaces must be obtained. The popular examples are the known facts that the divergence of the curl must vanish as well as the curl of a gradient. Failure to achieve the latter will inevitably lead to non-physical parasitic solutions.

The second point stems from the fact that degrees of freedom may be associated not only to nodes but also to lines, surfaces or volumes, hence, a proper representation for those cases is needed. In [8], this condition is denoted as the *reduction* operation $\mathcal{R}$ or **De Rham map** that establishes a discrete representation of the continuous variables. This step is further supplemented with a *reconstruction* operation $\mathcal{I}$ or **Whitney map** in which the continuous variables are retrieved from the discrete values via interpolation.

The third condition requires the potential theorem, Stokes' theorem and the divergence theorem (differential geometry condenses all three in the so-called *Generalized Stokes Theorem*) to hold at a discrete level.

The fourth condition is related to mimic the diagram shown in Figure 1.1 where H_P and H_V are scalar fields related to points and volumes, respectively, while H_C and H_S denote vector fields where the subscript C means curves and S means surfaces. Copying such structure on the discrete level requires the introduction of an analog of the Hodge star from differential geometry as to create a bijection identifying point scalars with volume scalar fields and curve vector fields with surface vector fields [79]. If differential forms are preferred, then the Hodge star identifies k-forms with $(n-k)$-forms with n being the dimension of the embedding space.

$$\begin{array}{ccccccccccc}
\mathbb{R} & \longrightarrow & H_P & \xrightarrow{\vec{\nabla}} & H_C & \xrightarrow{\vec{\nabla}\times} & H_S & \xrightarrow{\vec{\nabla}\cdot} & H_V & \longrightarrow & 0 \\
 & & \star\downarrow & & \star\downarrow & & \star\downarrow & & \star\downarrow & & \\
0 & \longleftarrow & H_V & \xleftarrow{\vec{\nabla}\cdot} & H_S & \xleftarrow{\vec{\nabla}\times} & H_C & \xleftarrow{\vec{\nabla}} & H_P & \longleftarrow & \mathbb{R}
\end{array}$$

Figure 1.1: Dual De Rham sequence as shown in [79].

The fifth point requires equations such as $\nabla\cdot(f\underline{v}) = \nabla f\cdot\underline{v} + f\nabla\cdot\underline{v}$ to have a proper analog in the discrete setting. This is related to the products between quantities belonging to different spaces. For example, by following the exact sequence shown in

Figure 1.1, the previous equation only makes sense if $f \in H_P$ and $\underline{v} \in H_S$ such that $\nabla \cdot (f\underline{v}) \in H_V$. In the language of differential forms, this point means that a proper *wedge product* between forms must be recreated. A mimetic scheme must find a way to make sure that using differential operators on products between different spaces lead to the correct spots from the diagram described in the fourth condition.

It could be thought that since all mimetic methods must satisfy the same requirements then they are all essentially the same. It is true, however, that the underlying structure is identical but the main differences (at least from a pragmatic point of view) arise on the choice of the *Whitney Map*. The latter has an effect on the domain discretization too since some maps are created to handle triangular meshes while others are suited for quadrilateral grids. A clear example of the former are the classical *Whitney forms* [11] while for the latter the literature presented in the next section is a good example.

1.3 Where has it been used?

The literature presented in this section utilizes a reconstruction operator $\mathcal{I}$ on quadrilaterals on a variety of problems from different areas of science. The present work attempts to, hopefully, use the same methodology and achieve the same quality of results on the area of electromagnetism.

The following list is meant to provide a swift look into the problems the mimetic spectral element method (MSEM) methodology has handled when the basis functions from [51] were utilized as the *Whitney Map*. Such list is comprised by the following:

- The scalar Poisson Equation is solved in [72] using differential forms in single and dual grids. The analysis is extended to anisotropic tensors $\mathbb{K}$ in the constitutive equation leading to equations of the type $\underline{u} = -\mathbb{K}\nabla\phi$ coupled with $\nabla \cdot \underline{u} = f$.
- In [39], the Darcy problem is further analyzed in 2 examples. Firstly, a sand-shale system of 400 blocks is solved for $\mathbb{K} = k\,\mathbb{I}$. Secondly, an impermeable streak system with 3 regions is solved in which one subdomain has an anisotropic permeability tensor. Both cases are solved in $\Omega = [0, \pi]^2$.
- The mimetic discretization method was applied to the mixed formulation of the Stokes problem which had vorticity, velocity and pressure as variables. More importantly, pointwise divergence-free solutions for the velocity were computed for a number of benchmark problems [58].
- Regarding non-linear elliptic PDEs, an Eulerian Grad–Shafranov solver based

on the mimetic spectral element framework was developed in [71] where the computed equilibrium solutions were accurate up to machine precision.

- In [62], a mixed mimetic spectral element method was utilized to solve the rotating shallow water equations where mass conservation was satisified pointwise and the vorticity was globally conserved.
- Concerning linear Elasticity, hybrid approaches were used in [93] for 3D problems were sparse algebraic systems were obtained by using dual basis functions. The method proved to satisfy equilibrium forces point wise and was free of spurious kinematic modes in both orthogonal and curvilinear meshes.

1.4 Research Questions

As stated before, the present work develops upon the concepts of mimetic discretization and follows the approach presented in the literature shown in Section 1.3 by incorporating a very specific set of basis functions as *Whitney Map*. Even when the problems being discussed are not exaggeratedly complicated, they should serve as an introduction of the methodology to electromagnetism.

A priori, the method should work efficiently since the geometric structure inherent to electromagnetism is perfectly suited for such mimetic framework. Thus, a positive outcome of this thesis should rely on the correct implementation of the methodology. Particularly, work will be done to respond to the following questions:

- Is it possible to produce a mimetic spectral element method formulation to Maxwell's Eigenvalue Problem that avoids spurious solutions and provides faster rates of convergence than traditional FEM?
  - If so, is the proposed formulation able to detect zero eigenvalues for geometries with arbitrary Betti numbers b_1 in 2D geometries?
- What effect does anisotropy and geometry have on the eigenvalue convergence?

Finally, an additional question will be answered which is not totally related to the previous ones but arose from a genuine curiosity on how to adapt the MSEM machinery from the literature in Section 1.3 to problems in 1D that involve the first derivative. Thus, the following question should be considered a minor deviation from the previously stated ones.

- Can the mimetic framework described in literature like [72] be modified to tackle 1D differential equations such as $\frac{\mathrm{d}^2 y}{\mathrm{d}x^2} + \alpha \frac{\mathrm{d}y}{\mathrm{d}x} + \beta y = -f(x)$ for $x \in [a, b]$?

2

Theoretical Background

Along this chapter most of the theory required for the thesis will be explored. The mathematical side of the story, however, will be described in Chapter 3. This chapter contains information on a variety of topics as detailed in the following list:

- Some of the methods used in Computational Electromagnetics (CEM) will be explored along with a swift history of the method.
- The framework created by Enzo Tonti is introduced and will conclude with the *classification diagram* for electromagnetism.
- The importance of differential forms will be described along with other topics such as the De Rham complex and the Hodge Operators. The section will conclude on how differential forms shaped their way into CEM.
- The Maxwell equations are introduced along with the respective constitutive relations and boundary conditions. The equations for time harmonic fields are also obtained for the electric and magnetic fields.
- The cavity eigenvalue problem is explored and the topic of spurious solutions is addressed. Additionally, variational formulations for the problem are shown.

2.1 Computational Methods in Electromagnetics

In this section, some of the commonly used methods in Computational Electromagnetics (CEM) are detailed. Moreover, their history and characteristics are quickly

reviewed. The list is by no means exhaustive since covering every single available method is out of the scope of the present work but references to specialized literature are mentioned.

2.1.1 Finite-Difference Time-Domain Method

The finite-difference time-domain (FDTD) scheme was originally introduced by Yee [92] in 1966 and it has remained relevant along the years due to its simplicity, efficiency and ease of adaptation to a variety of problems.

This scheme is built on a structured cartesian mesh where the space and time derivatives are approximated by finite differences. Both of the field variables **E** and **H** are staggered in space with a very peculiar arrangement as depicted in Figure 2.1.

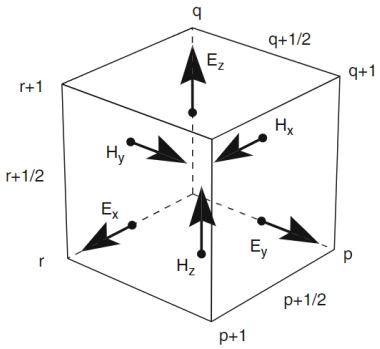

Figure 2.1: Unit Yee cell in $\mathbb{R}^3$ used in the FDTD algorithm from [80, p. 72].

A weakness of the method in its basic form, however, is related to how it deals with boundaries that cannot be aligned with its grid. This issue leads to the use of *staircase approximations* that harm its accuracy. Additionally, for a given cell size h, the scheme has a time-step limit $t < \sqrt{3}h/c$ in $\mathbb{R}^3$ [80, p. 66] with c denoting the speed of light. The latter imposes limitations for applications such as eddy current problems. On the other hand, for cavity problems requiring resonant frequencies the method can be used by computing the Fourier transform of selected signals.

Extensions and *tweaks* to the method are countless. In [50], for example, a *mimetic finite difference method* was constructed to approximate Maxwell's equations with approximations that actually satisfied discrete versions of vector and tensor calculus identities. Trying to list all the relevant literature would be extremely challenging. Instead, the books of Taflove, such as [85], should give a great overview of FDTD and its implementation/application as well as extension to general meshes.

2.1.2 Finite Element Method

This method is widely known for being extensively utilized to solve problems of structural analysis. However, its usage has extended to a wide variety of other engineering and mathematical problems. Unlike Finite Difference Methods where the differential operators on the governing equations are directly discretized, the Finite Element Method (FEM) discretizes the space of solutions.

In electromagnetics, the first application of FEM can be traced back to 1969 [55, p. 510] when Peter P. Silvester utilized the method for wave propagation problems on hollow waveguides and, since then, its use spread throughout the community.

Without a doubt, a quite important breakthrough in the finite element analysis for vector problems came with the introduction of the edge-based vector elements [68] by Nédélec which allowed tangential continuity between elements. Such characteristics allowed to accurately model the physical nature of the fields in electromagnetism and got rid of many of the issues that traditional node-based elements had such as spectral pollution for eigenvalue problems.

More generally, finite elements related to geometric objects gained popularity due to the pioneering work of Bossavit who, in 1988, introduced the so-called *Whitney forms* [11]. Under such theoretical framework, the lowest order Nédélec elements fell under the category of edge w_{ij} Whitney elements while the notation w_{ijk} was reserved for facet elements as the ones described by Raviart & Thomas [78].

2.1.3 Method of Moments

The method was first utilized for CEM on scattering problems around 1960s by Mei & Van Bladel, Andreasen and Richmond [54, Chapter 10, Ref. 1, 2, 4] but the unified formulation is attributed to Harrington who presented the scheme in [44].

The Method of Moments (MoM) is closely related to FEM. Consider, for example, the equation $\mathcal{L}\phi = f$ where $\mathcal{L}$ is a linear operator, ϕ is the unknown and f is the forcing function. A system of the type $\sum_{m=1}^{M}\sum_{n=1}^{N} c_n\,(w_m,\,\mathcal{L}v_n) = \sum_{m=1}^{M}(w_m, f)$ is obtained by expanding the solution as $\sum_{n=1}^{N} c_n v_n$ and using test functions w_m to perform the inner product. The expansion coefficients are then retrieved by solving the matrix system $[S]\{c\} = \{b\}$ with $S_{mn} = (w_m,\,\mathcal{L}v_n)$ and $b_m = (w_m,\,f)$.

Such procedure is valid for both differential and integral operators. In fact, it is widely used to formulate the finite element method when $\mathcal{L}$ is a differential operator. In CEM, however, the term *moment method* is reserved for the case when $\mathcal{L}$ is an integral operator involving a Green's function [55, p. 561] whereas, in mathematics, the same scheme is known as the *Boundary Element Method* (BEM) [80, p. 185].

Due to the difference in the nature of the operator $\mathcal{L}$, the choice of the basis and the test functions changes dramatically. For instance, in FEM, due to differentiation, the basis needs to be at least linear while the test functions tend to be chosen the same as the basis. In MoM the basis could be a constant while the test functions could be chosen as delta peaks as to simplify integration [55, Chapter 10.1].

Another drastic difference with respect to FEM is that formulations using MoM end up with integrals over surfaces which means that for problems in $\mathbb{R}^3$ a surface has to be discretized while for FEM the discretization of a volume is needed. Thus, MoM effectively reduces the problem dimension.

A basic introduction about MoM can be found in [55, Chapter 10] while the references therein serve as examples of applications of the method. For a more specific compilation about the topic, [40] might be a good starting point.

2.1.4 Other Methods

The very swift introduction to some of the methods commonly used in CEM should have made it clear that each scheme possesses advantages and disadvantages. Combining the previously discussed methods can improve their respective strengths and eliminate some of their weaknesses. This idea gives rise to the so-called *Hybrid Techniques*.

A scheme combining FEM in time domain (FETD) with the classic FDTD could, for example, overcome the need for staircase approximations to curved boundaries and take advantage of all the algorithms that have been used throughout the years in FDTD (quite useful for treating boundary conditions for instance). In Figure 2.2, the transition between the meshes of the FDTD and FETD is shown where the interface region is utilized to exchange information between both schemes.

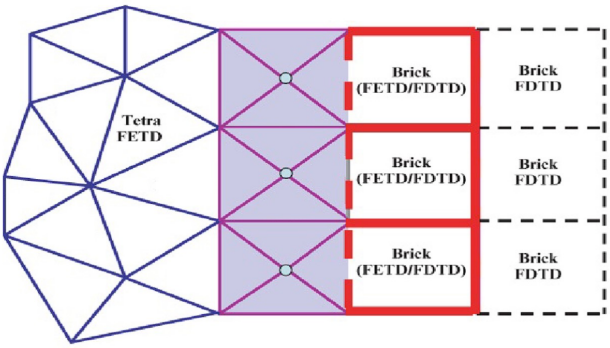

Figure 2.2: Meshing regions with a hybrid FETD-FDTD approach from [55, p. 737].

Another possible hybrid method could be obtained by putting together FEM and MoM. The former is known for its capability to adapt to complex geometries, however, it requires special treatments when dealing with unbounded problems such as the ones arising from scattering. The latter, on the other hand, is very well suited for open region problems while it struggles handling complex geometries/materials.

The result of merging those schemes is the Finite Element - Boundary Integral method (FE-BI) which uses a surface to delimit the computational domain. Outside such surface, MoM is used while FEM is applied at the interior. The coupling between both computations is done at the surface via continuity conditions. Examples of formulations of the FE-BI method are shown at [55, Chapter 11.8]. Its use for eddy current problems using Nédélec elements can be found in [20] while approximations utilizing Whitney forms and *boundary-stiffness* operators can be found in [13], both by Bossavit.

The area of mimetic discretizations is also active in CEM and mostly focused on Mimetic Finite Differences (MFD). In [23], for example, a structure is presented for electromagnetic problems at high and low frequencies in the time-harmonic regime which shown to be adaptable to *basically* any polyhedral decomposition. The extension of MFD to 3D and its application to engineering problems can be found in [63]. For very recent literature of MFD on triangular meshes the work by Adler et al. found in [1, 2] is relevant, however, for general knowledge and up-to-date information on this method [91] is certainly the place to start.

Regarding mimetic implementations of the Finite Element Method, it should be noted that any framework in FEM utilizing *Whitney Forms*[4] should be considered as a mimetic method. This is because this specific choice of *Whitney map* is an example of a regular mimetic reconstruction operator [8].

2.2 Tonti's diagrams

The notion of geometry playing a fundamental role in the mathematical description of physics can, at least, be traced back to James Clerk Maxwell [25]. During the 1970s, however, Enzo Tonti, in [88], described how physical quantities of ***any*** theory could be associated to geometrical and chrono-metrical objects. This idea gave rise to the so-called *Tonti diagrams* which, essentially, classify variables and equations from many physical theories using the notion of geometry as a cornerstone.

[4] Bossavit was among the many authors who extended *Whitney Forms* to various supporting shapes [19] and higher order forms [18, 77]. A summary of this evolution, up to 2020, is found in [65].

2.2.1 Space and Time Elements

In the framework described by Tonti, *orientation* is key and such topic is described in the following sections for space and time elements. The latter is described briefly for completeness since this thesis will not analyze time-dependent problems.

2.2.1.1 Space Elements and Their Orientation

In Tonti's notation, space elements are denoted by the boldface letters **P**, **L**, **S** and **V** which refer to *points*, *lines*, *surfaces* and *volumes*[5].

The idea of orientation is, essentially, a notion of order [89, p. 40] and a set of elements is said to be oriented whenever a decision has been made specifying which is the preceding element and which is the next. This concept is important because the sign of a variable (with its previous association to a space element) is inverted whenever the orientation is reversed. A classic example would be the mass balance within a volume where the outward normal is usually chosen as positive.

An additional distinction should be made when referring to orientation: *inner* and *outer* orientation. The idea of *inner orientation* is based on the fact that imposing a notion of *order* requires only elements from the given set. For instance, consider a set of points on a surface forming a curvilinear triangle, setting an order for the vertices will fix its orientation [89, p. 44]. On the other hand, an *outer orientation* is determined when the notion of *order* is established by elements outside the given set. The outer orientation for the previous example would require crossing the surface which cannot be imposed by the elements of the set. An example for the different orientations is shown in Figure 2.3.

Discerning between orientations is done by its notation. A bar is placed above space elements with inner orientation as $\bar{P}$, $\bar{L}$, $\bar{S}$, $\bar{V}$ while a tilde is used for outer orientation as $\tilde{P}$, $\tilde{L}$, $\tilde{S}$, $\tilde{V}$. For additional remarks on this topic, reading [89, pp. 39-57] is recommended.

2.2.1.2 Time Elements and Their Orientation

Time elements refer to *instants* and *intervals* and are denoted as **I** and **T**, respectively, and their analysis requires a geometric representation of time. If an analogue clock were to be used as an example, its hands would indicate *instants* in time while its angle of rotation would be associated to an *interval*. Since such a construction is impractical, time is set on a straight line referred to as *time axis* where instants are matched to points and intervals are matched to segments.

[5] Refers to a region in space not the scalar denoting the amount of 3D space enclosed by a surface.

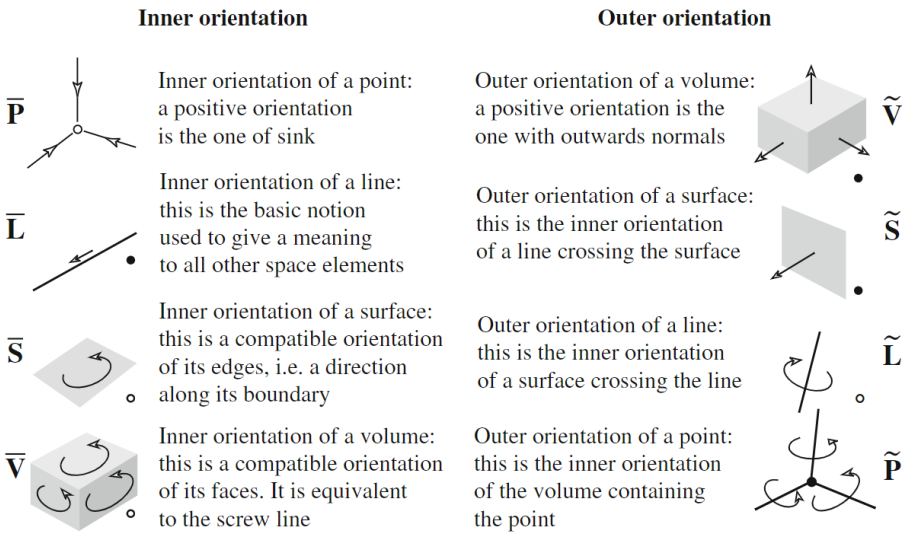

Figure 2.3: Inner and Outer orientations for **P**, **L**, **S** and **V** from [90].

By dividing the *time axis*, a cell complex in time is obtained in which the segments correspond to time intervals while its boundaries correspond to instants. Such complex is known as *primal* and denoted with the time elements $\bar{\mathbf{I}}$ and $\bar{\mathbf{T}}$. Intervals $\bar{\mathbf{T}}$ are oriented from preceding time instant to the following one while instants $\bar{\mathbf{I}}$ are given an inner orientation as sinks.

A dual complex is used with *dual instants*, $\tilde{\mathbf{I}}$, and *dual intervals*, $\tilde{\mathbf{T}}$. The former are defined as time instants between primal intervals while the latter are the intervals between dual instants. Both complexes are shown in Figure 2.4. For the interested reader, further information about the relevance of such complexes can be found in [89, Chapter 3.8].

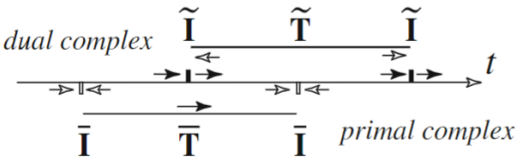

Figure 2.4: Primal and Dual Complex for Time Elements from [90].

2.2.2 CELL COMPLEXES

Translating any physical notion into an appropriate mathematical language requires the use of geometry as an intermediary via coordinate systems. Such systems must

not contain only *sets of points* since physical variables are not always associated to nodes but also to lines, surfaces and volumes. Thus, the appropriate coordinate system to utilize is the so-called *cell complex* which offer all the required space elements, namely, vertices, edges, faces and volumes.

Cell complexes are a subdivision of a space region in $\mathbb{R}^n$ into smaller sections named *cells*. The latter receive their name from algebraic topology. In numerical analysis, for example, cells are usually known as *elements* while the collection of elements is usually denoted as a mesh/grid. The simplest elements to create such subdivisions are triangles ($\mathbb{R}^2$) and tetrahedra ($\mathbb{R}^3$), hence, cell complexes discretized with such elements are creatively named as *simplicial complexes* [89]. However, any kind of shape can be utilized.

At this point, it should be recalled that all space elements can be endowed with two types of orientation, hence, cell complexes inherit such characteristic. Some physical variables might be better suited for an inner orientation while for others an outer one would be preferred. In order to accommodate for both cases, two complexes are built, one for each orientation leading to a staggered scheme[6] and shown for the 2D case in Figure 2.5. It is customary to distinguish both complexes by the name *primal* and *dual* having inner and outer orientations, respectively.

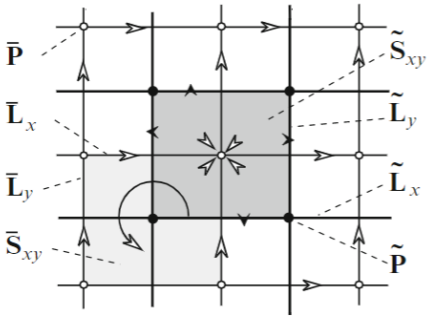

Figure 2.5: Oriented Cartesian complex and its dual (thick lines) from [89, p. 77].

In the figure above, the following can be noticed: (1) Primal vertices lie in the center of dual 2D volumes, (2) primal edges cross dual edges and (3) dual nodes are located at the center of each primal 2D volume. Such connections between the elements of each complex are known as a *duality* relation. In fact, for the presented 2D complex, the number of interior elements in $\bar{\mathbf{P}}$ and $\bar{\mathbf{L}}$ equal the number of elements in $\tilde{\mathbf{S}}$ and $\tilde{\mathbf{L}}$, respectively, where the term *interior* refers to elements not at the boundary. Similarly, $\dim\left(\bar{\mathbf{V}}\right) = \dim\left(\tilde{\mathbf{P}}\right)$.

[6] A typical scheme using staggered grids in electromagnetics is the one from Yee [92].

Consider the primal space elements in $\mathbb{R}^2$ given by $\bar{\mathbf{P}}$, $\bar{\mathbf{L}}$, $\bar{\mathbf{S}}$ and their duals $\tilde{\mathbf{P}}$, $\tilde{\mathbf{L}}$, $\tilde{\mathbf{V}}$. The duality relation is further emphasized by inverting the dual space elements and relating them to the primal elements as shown in Figure 2.6. In each row, the sum of dimensions equals the dimension of the embedding space which, in this case, is 2. Hence, primal points are related to dual surfaces, primal edges to dual edges and primal surfaces to dual vertices.

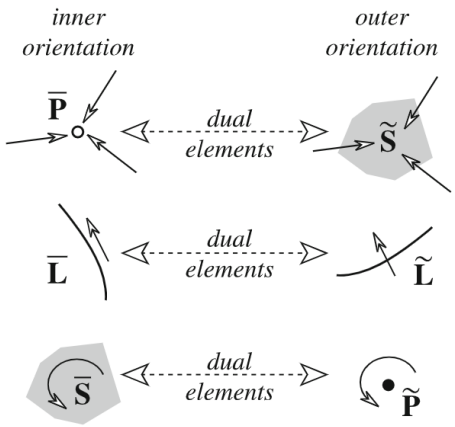

Figure 2.6: Duality Relation in $\mathbb{R}^2$ from [89, p. 85].

The dimension of the dual element associated to the primal space element is obtained by the formula $\tilde{d} = n - d$ where n is the dimension of the embedding space and d the dimension of the space element. Due to the latter, it is obvious that the dimension of the dual elements depend on the embedding space. Thus, in $\mathbb{R}^3$, primal points ($d = 0$) are related to dual volumes ($\tilde{d} = 3$) such that adding up the dimensions of both space elements, a value of $n = 3$ is obtained. The duality relations for $\mathbb{R}^3$ and $\mathbb{R}^1$ can be found in [89, Figure 4.28 & Figure 4.29], respectively.

2.2.3 Global Variables & Field Variables

In Tonti's view, a distinction should be made between variables. Firstly, there are *global variables* which are not line/surface/volume densities of another variable. On the other hand, there are *field variables* which are, indeed, a density of a global variable [90].

Forming field variables in the traditional manner deletes any of the geometric association to a space element. This is because computing a density requires performing a limiting process and all field functions end up referring to points. In this sense, the use of field variables leads to the classical differential formulations.

According to Tonti, by the so-called *Association Principle*, global physical variables have a natural association with the space-time elements from Section 2.2.1. Similarly, field variables can also be associated to a space element (instead of being typically associated to nodes). This is due to the notion of *inherit association* by which the field variables share the space-time elements of its parent global variable [89, Chapter 5.13]. For instance, the electric field strength **E** is associated to inner oriented lines and dual time instants just as the voltage or the mass density inherits an association with volumes just as mass content.

2.2.4 Classification Diagrams

Due to the *duality relation*, classification diagrams of physical variables contain two columns. One of those columns has space elements with inner orientation while the other one is exclusive to outer oriented variables and each row satisfies $\tilde{d} = n - d$ as described in Section 2.2.2.

Each diagram compiles the physical variables relevant to a specific theory and assigns them to oriented space-time elements. In doing the latter, each diagram suggests how each variable is related to a cell complex (or its dual). Additionally, basic equations from each theory are included. Topological relations are written out on vertical links while constitutive equations are contained in horizontal links.

For electromagnetism, the Tonti diagram is shown in Figure 2.7. This *Maxwell House*[7] is contained within four pillars where each row contains the same dimensional value (time instants correspond to zero while intervals correspond to a value of one). The variables on the primal cell complex are linked to those on the dual complex via constitutive equations where the material parameters are included. Finally, from top to bottom, each of the vertical links on the left side of the diagram is related to the vector operators **grad**, **curl** and **div**, respectively. For the right side, the relation is reversed such that **div**, **curl** and **grad** is utilized.

Using Tonti diagrams for computational simulations is greatly beneficial since it immediately gives an idea of where to place the degrees of freedom in a cell complex. Additionally, depending on the variables being analyzed, relying on the diagrams helps in realizing if both primal and dual complexes need to be constructed.

A closer look at Figure 2.7 reveals that **E** and **H** belong to primal and dual edges, respectively. The former belongs to inner oriented complexes while the latter has to be connected to a complex with outer orientation. In fact, looking back at Figure 2.1, it is evident that degrees of freedom for both the electric and magnetic field are, indeed, arranged according to what the presented Tonti Diagram describes.

[7] As named by Bossavit [14].

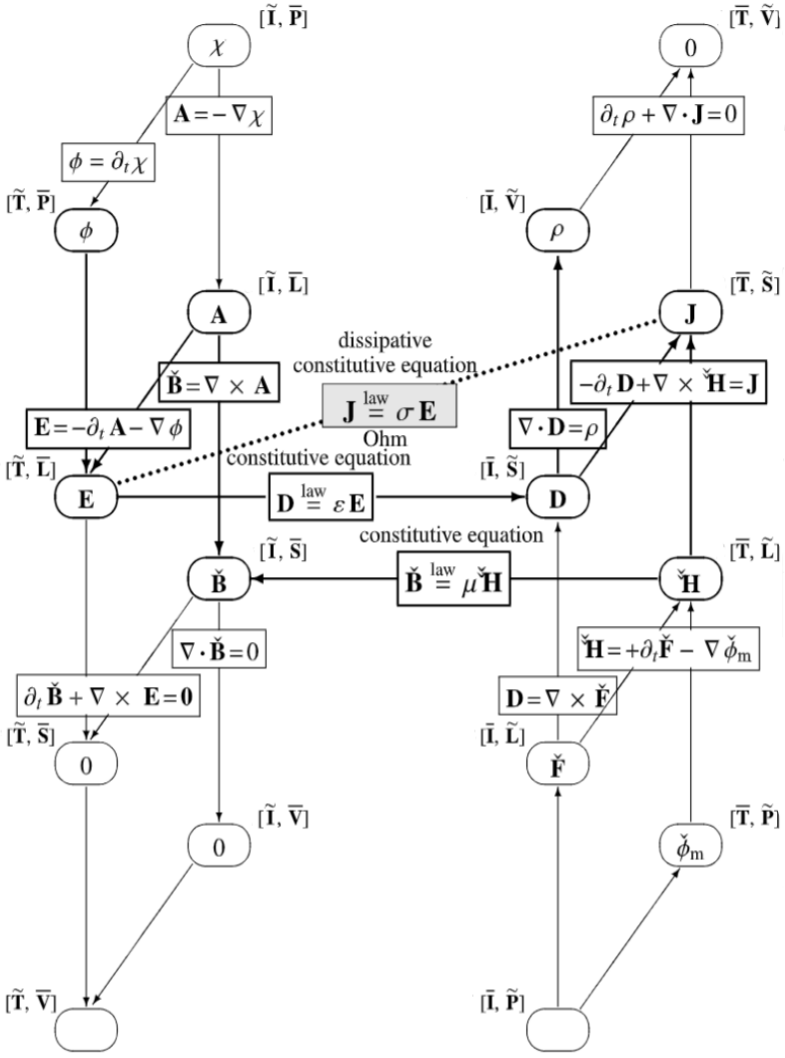

Figure 2.7: Tonti Diagram for Electromagnetism with vector notation from [90].

2.3 Differential Forms

Differential forms are, as absurdly or simplistic as it may sound, the objects that are found under the integral sign [36] and, as a result, are perfect candidates to be integrated over oriented k-dimensional manifolds.

Even though the current work will not use the language of differential forms, it is important to delineate some of the aspects related to this area since they will provide useful intuition into the framework to be used.

In this section, some of the concepts surrounding the so-called De Rham complex will be discussed. The main ideas to be described are the Hodge operator and the exterior derivative as to make the connection on how they will be discretized when the MSEM formulation is utilized in the upcoming chapters.

2.3.1 The De Rham Complex

An important notion in the calculus of differential forms is the *De Rham complex* which establishes a relation between spaces of *oriented* differential forms of different degrees. This complex is, essentially, a sequence of spaces and mappings [3] which, for $\mathbb{R}^3$, is given by,

$$\mathbb{R} \longrightarrow \Lambda^0(\Omega) \xrightarrow{\mathrm{d}} \Lambda^1(\Omega) \xrightarrow{\mathrm{d}} \Lambda^2(\Omega) \xrightarrow{\mathrm{d}} \Lambda^3(\Omega) \longrightarrow 0 \tag{2.1}$$

with d denoting the so-called *exterior derivative* that allows the differentiation of forms and is a generalization of the operators **grad**, **curl** and **div** from vector calculus. The notation $\Lambda^k(\Omega)$ indicates the space of k-forms in Ω with $k = \{0, 1, \cdots, n\}$ and n being the dimension of the embedding space. Additionally, the sequence is *exact* on contractible domains meaning that the range of one space equals the kernel of the next space.

Even though this diagram originates from the language of differential forms, an equivalent can be created using vector operators instead of the more general exterior derivative while the space of forms is modified to represent scalar fields associated to points/volumes and vector fields related to curves/surfaces as shown in [79].

$$\mathbb{R} \longrightarrow H_P \xrightarrow{\nabla} H_C \xrightarrow{\nabla\times} H_S \xrightarrow{\nabla\cdot} H_V \longrightarrow 0 \tag{2.2}$$

Regardless of the notation, the sequences created by the space of differential forms in (2.1) or the scalar/vector spaces in (2.2) do not have an inner or outer orientation specified yet. The only requirement is that the whole sequence from start to finish possesses the same orientation. The latter immediately suggests that

a second sequence can be constructed with the remaining choice of orientation. In doing so, the so-called double De Rham complex is obtained.

This complex will now be written in terms of the Hilbert space of functions (L^2 De Rham complex) such that diagram is now composed as:

$$\begin{array}{ccccccccccc}
\mathbb{R} & \longrightarrow & H^1(\Omega) & \xrightarrow{\nabla} & H(\mathrm{curl};\Omega) & \xrightarrow{\nabla\times} & H(\mathrm{div};\Omega) & \xrightarrow{\nabla\cdot} & L^2(\Omega) & \longrightarrow & 0 \\
 & & \star\updownarrow & & \star\updownarrow & & \star\updownarrow & & \star\updownarrow & & \\
0 & \longleftarrow & \widetilde{L}^2(\Omega) & \xleftarrow{\nabla\cdot} & \widetilde{H}(\mathrm{div};\Omega) & \xleftarrow{\nabla\times} & \widetilde{H}(\mathrm{curl};\Omega) & \xleftarrow{\nabla} & \widetilde{H}^1(\Omega) & \longleftarrow & \mathbb{R}
\end{array} \tag{2.3}$$

where the tilde is meant to denote that the lower row of the complex has a different orientation that the upper row.

Comparing (2.3) with the Tonti diagram from Figure 2.7 makes it quite evident that both are closely related. In fact, the complex seems to be a purely mathematical description while the diagram focuses on the geometric description of the theory. Consider, for instance, the following examples detailing the synergy between both descriptions.

- The electric potential ϕ, according to the Tonti diagram, is associated to nodes. Comparing this to the De Rham complex leads to the fact that $\phi \in H^1(\Omega)$.
- The magnetic potential $\check{\phi}_m$ belonging to nodes on the dual mesh. From the De Rham complex then $\check{\phi}_m \in \widetilde{H}^1(\Omega)$.
- Computing $\mathbf{E}$ from the electric potential requires the gradient operator. Hence, according to the flow of the complex, the electric field belongs to $H(\mathrm{curl};\Omega)$. Thus, the operator **grad** is effectively mapping from $H^1(\Omega)$ to the new space.
- Consider the constitutive law $\mathbf{D} = \underline{\underline{\epsilon}}\,\mathbf{E}$ where no differential operators are involved. From the diagram, both variables belong to different grids. However, thanks to the complex, it can be quickly realized that communication between both is achieved due to the *Hodge star*. Thence, a map from $H(\mathrm{curl};\Omega)$ to $\widetilde{H}(\mathrm{div};\Omega)$ is obtained.

If the function spaces shown in (2.3) can be discretized and then appropriate descriptions for the differential operators are found, then a scheme will truly mimic such sequences. Since the physically reliable Tonti diagrams are quite entangled to the De Rham complex, a proper discretization of the latter will inevitably lead to physically sound results.

In the present work, the vector operators will be obtained by means of *incidence matrices* which are quite sparse constructions containing only -1, 0 and 1. Finding discrete descriptions for operator $\star$ allows for much freedom since they are not

uniquely defined and many approaches are possible. The approach to be followed will be the next topic of discussion.

2.3.2 Hodge Operator

In the language of differential forms, the operator $\star : \Lambda^k(\Omega) \to \Lambda^{(n-k)}(\Omega)$ which means that it acts as a link between forms associated to different geometric objects. In this case, such forms have different orientation.

For the current framework, the Hodge matrices will appear as a consequence of using the basis functions and will be associated to the so-called *mass matrices*. In [87], Bossavit establishes the relation between the Hodge and the mass matrices in the context of FEM when tackling a curl-curl problem for the potential $\check{\phi}_m$.

Additionally, Hiptmair, in [45], establishes how mass matrices are, indeed, linear mappings between spaces of discrete differential forms based on a primary mesh $\mathcal{T}_h$ and a secondary mesh $\widetilde{\mathcal{T}}_h$ which is exactly the behavior to be expected the Hodge to simulate according to the Tonti diagrams.

2.3.3 Differential Forms in Electromagnetics

The discussion of differential forms can be traced back to many years ago. For instance, the book by Flanders [36] in 1964 was born as an attempt to introduce the topic to a wider audience.

In electromagnetics, however, the first appearance of exterior differential forms can be tracked back to George A. Deschamps [31] in 1970. Nearly a decade later, the topic arose again in a conference paper named *Applications of Exterior Differential Forms to Electromagnetics* where it is discussed how differential forms are the most natural and convenient representation of electromagnetic quantities. Shortly after, in [30], the topic is once again reviewed and the so-called *Deschamps graphs* make their first appearance which were constructions as the ones from Tonti but only relating k-forms by means of the exterior derivative.

These publications were amongst the first that attempted to introduce the language of differential forms in electromagnetism. Probably hoping that the prediction of Flanders about exterior calculus became true: "*Physicists are beginning to realize its usefulness. Perhaps it will soon make its way into engineering.*"

The latter, up to some extent, started to become true. The biggest breakthrough of differential forms in electromagnetism occurred thanks to Alain Bossavit. Back in 1988, in [11], he addressed a problem that had been hindering numerical approximations in electromagnetism. It was known that magnetic fields required elements

whose degrees of freedom were not values at mesh nodes which was the common procedure in classic Finite Element Method. His *cure* relied on expressing the equations in terms of differential forms instead of the regular vector notation.

The work from Bossavit resounded orders of magnitude above any other work on the topic at that time and, up to the present day, is still a predominant figure. Such impact was, probably, not related to the idea of utilizing differential forms but rather related to the fact that he offered a concrete way to *apply* such framework. By introducing *Whitney Forms*[8], differential forms stopped being entirely theoretical and became an effective tool for problem solving in engineering. Additionally, it was soon realized that the lowest order Nédélec edge elements [68] created in previous years to deal with electromagnetic problems were, in fact, the Whitney edge elements. The latter gave further credibility to the whole *machinery* and catapulted the use of edge elements to new heights.

The complete set of ideas from Bossavit appeared years later in what today is known as the *Japanese Papers* [16]. Even though this series of papers focuses on electromagnetism, the ideas are general enough as to be applied to any other field of science. The latter is probably the reason why it is one of his most well-known works.

The consequences of associating Whitney forms to the discretization of differential forms ended up having a huge impact outside electromagnetism. If Whitney forms are considered to be a natural tool to discretize the De Rham complex, then any theory that could be fitted into such complex would be a candidate for the novel framework. Luckily, there was not a lack of prospects since plenty of theories met the requirement. This was particularly possible due to the work from Tonti [88] since his *classification diagrams* had a very close connection to the de Rham theory as shown in [89, p. 416] and, in this way, the geometric concepts brought by the use of differential forms quickly migrated to several other areas of science. Testament of the latter is the literature presented in Section 1.3.

There is plenty of up-to-date literature using differential forms as a cornerstone but, perhaps, one of the most relevant is the one from Hiptmair [46] who was strongly influenced by the ideas of Bossavit. Even though Whitney forms are used throughout the whole text, the theory applies to any other basis forming part of a De Rham sequence.

[8] Funnily enough, the original purpose of Whitney forms was far from the Finite Element Theory. The first documented connection between both was given by G. Strang at the end of [32] who informed Dodziuk that the techniques used in his paper were very closely related to FEM.

2.4 Maxwell Equations

Electromagnetic analysis has been quite a fundamental part of many engineering and scientific analyses/studies since the electromagnetic theory was completed back in the 1870s. Its importance has been predominant through the years due to its predictive power that extends from static to optical regimes and from subatomic to intergalactic length scales [54].

Throughout the years, the equations have undergone a series of changes in their notation. This topic is lightly touched upon by Bossavit [17, p. 1] for the original formulation, the contemporary vector notation and the modern differential geometric formalism by stating that despite describing the same phenomena, 'they are as different as 3 sentences with the same meaning can be in three different languages'.

2.4.1 Differential Equations

$$\nabla \times \mathbf{H} = \mathbf{J} + \frac{\partial \mathbf{D}}{\partial t} \quad \text{Maxwell - Ampère's Law} \tag{2.4a}$$

$$\nabla \times \mathbf{E} = -\frac{\partial \mathbf{B}}{\partial t} \quad \text{Faraday's Law} \tag{2.4b}$$

$$\nabla \cdot \mathbf{D} = \rho \quad \text{Gauss's Law} \tag{2.4c}$$

$$\nabla \cdot \mathbf{B} = 0 \quad \text{Gauss's Law: Magnetic} \tag{2.4d}$$

where the vectors used are $\mathbf{E}$, electric field intensity ($^{\mathrm{V}}/_{\mathrm{m}}$); $\mathbf{D}$, electric flux density ($^{\mathrm{C}}/_{\mathrm{m}^2}$); $\mathbf{H}$, magnetic field intensity ($^{\mathrm{A}}/_{\mathrm{m}}$); $\mathbf{B}$, magnetic flux density ($^{\mathrm{Wb}}/_{\mathrm{m}^2}$); $\mathbf{J}$, electric current density ($^{\mathrm{A}}/_{\mathrm{m}^2}$) and ρ, electric charge density ($^{\mathrm{C}}/_{\mathrm{m}^3}$).

When charge is conserved, both of Gauss's equations are a direct consequence of (2.4a) and (2.4b). Such result is obtained by taking the divergence of the latter equations and switching the time and space derivatives for $\mathbf{B}$ and $\mathbf{D}$. Thus,

$$\nabla \cdot \frac{\partial \mathbf{B}}{\partial t} = \frac{\partial}{\partial t}(\nabla \cdot \mathbf{B}) = 0 \quad \text{and} \quad \nabla \cdot \frac{\partial \mathbf{D}}{\partial t} = \frac{\partial}{\partial t}(\nabla \cdot \mathbf{D}) = -\nabla \cdot \mathbf{J}$$

and by supplementing the above with the *equation of continuity* $\nabla \cdot \mathbf{J} + \frac{\partial \rho}{\partial t} = 0$ (due to charge conservation), the second equation is rewritten as:

$$\frac{\partial}{\partial t}(\nabla \cdot \mathbf{D}) = \frac{\partial \rho}{\partial t} \quad \rightarrow \quad \frac{\partial}{\partial t}(\nabla \cdot \mathbf{D} - \rho) = 0 \quad \therefore \quad \nabla \cdot \mathbf{D} = \rho$$

Therefore, if (2.4c) and (2.4d) hold at one instant in time, they will automatically

hold for all $t \in \mathbb{R}$. This argument might propose the fact that the divergence equations are, indeed, useless and can be discarded. However, any *sensible* numerical approximation of the Maxwell equations must satisfy at some degree the discrete analogues of both Gauss's Laws [67, Chapter 1]. Failing to do so will give rise to *spurious solutions*.

As an aside note, in [15], Bossavit considers computational electromagnetism to be concerned with a different system of equations which include both (2.4a) and (2.4b) supplemented by two *constitutive laws* accounting for the *presence of matter* and its *interaction with the fields*. The reasoning for this is based on the fact that the solenoidal condition for $\mathbf{B}$ stems from Faraday's Law and enforcing it only requires to satisfy it at the initial time. Gauss's Law, however, is considered as a mere definition. Hence, in his eyes, both equations are demoted to a lower tier of importance.

2.4.2 Integral Equations

The differential formulation (2.4a)-(2.4d) hides quite well the geometric objects the variables are acting onto. A formulation based on integral equations would, on the other hand, give more insight about this topic since the variables would have to be integrated on appropriate manifolds. For the general time-varying fields, Maxwell's equations are given by [54, Chapter 1.2]:

$$\oint_C \mathbf{H} \cdot \mathrm{d}\mathbf{l} = \frac{\mathrm{d}}{\mathrm{d}t} \iint_S \mathbf{D} \cdot \mathrm{d}\mathbf{s} + \iint_S \mathbf{J} \cdot \mathrm{d}\mathbf{s} \quad \text{Maxwell - Ampère's Law} \tag{2.5a}$$

$$\oint_C \mathbf{E} \cdot \mathrm{d}\mathbf{l} = -\frac{\mathrm{d}}{\mathrm{d}t} \iint_S \mathbf{B} \cdot \mathrm{d}\mathbf{s} \quad \text{Faraday's Law} \tag{2.5b}$$

$$\oiint_S \mathbf{D} \cdot \mathrm{d}\mathbf{s} = \iiint_V \rho \, \mathrm{d}V \quad \text{Gauss's Law} \tag{2.5c}$$

$$\oiint_S \mathbf{B} \cdot \mathrm{d}\mathbf{s} = 0 \quad \text{Gauss's Law: Magnetic} \tag{2.5d}$$

$$\oiint_S \mathbf{J} \cdot \mathrm{d}\mathbf{s} = -\frac{\mathrm{d}}{\mathrm{d}t} \iiint_V \rho \, \mathrm{d}V \quad \text{Equation of Continuity} \tag{2.5e}$$

where (2.5a) & (2.5b) are integrated over an open surface S bounded by a contour C while for (2.5c) & (2.5e) S denotes a closed surface delimiting a volume V [54].

The integral formulation is valid regardless of the medium or shape of the integration manifold and might be considered as the fundamental equations governing the behavior of EM fields [54]. Historically, such integral formulations came first and, up to some extent, are more germane to physics [15].

2.4.3 Differential Forms

By using differential forms, the Maxwell's equations are written as follows [46]:

$$\mathrm{d}\mathbf{h} = \partial_t \mathbf{d} + \mathbf{j} \quad \text{Maxwell - Ampère's Law} \tag{2.6a}$$

$$\mathrm{d}\mathbf{e} = -\partial_t \mathbf{b} \quad \text{Faraday's Law} \tag{2.6b}$$

$$\mathrm{d}\mathbf{d} = \boldsymbol{\rho} \quad \text{Gauss's Law} \tag{2.6c}$$

$$\mathrm{d}\mathbf{b} = 0 \quad \text{Gauss's Law: Magnetic} \tag{2.6d}$$

where $\mathbf{e}$ and $\mathbf{h}$ denote the electric and magnetic field intensities which are 1-forms. There is a triplet of 2-forms: $\mathbf{d}$, $\mathbf{b}$ and $\mathbf{j}$ with the first two being the electric and magnetic flux density, respectively, while the last is the electric current density. The only 3-form in the system is the electric charge density $\boldsymbol{\rho}$. Finally, the operator d denotes the *exterior derivative* which is the generalization of the vector operators **grad**, **curl** and **div** and maps k-forms to $(k+1)$-forms.

2.4.4 Constitutive Relations

Maxwell's equations must be augmented to have equal number of equations and variables. This is done by supplementing the system with a set of constitutive laws relating $\mathbf{E}$ and $\mathbf{H}$ to $\mathbf{D}$ and $\mathbf{B}$, respectively. Under the framework established by Tonti, the equations explored in this section are the *horizontal links* from Figure 2.7. Constitutive relations describe the macroscopic properties of the medium [54] and how it affects the surrounding field. Specifically, a medium can affect electromagnetic fields through three phenomena, namely, *electric polarization*, *magnetization* and *electric conduction* [55, Chapter 1.3].

2.4.4.1 Electric Polarization

The first constitutive law considered reads,

$$\mathbf{D} = \varepsilon_0 \mathbf{E} + \mathbf{P}$$

where $\mathbf{P}$ is the so-called *polarization intensity* or *polarization vector* $\mathbf{P}$ which accounts for the effects of tiny dipoles on the material [55] and ε_0 is the permittivity of free space which is $8.854 \times 10^{-12}\,\mathrm{F/m}$ in the MKS unit system. In most dielectric materials this quantity is proportional to $\mathbf{E}$ such that $\mathbf{P} = \varepsilon_0 \chi_c \mathbf{E}$ with χ_c being the *electric susceptibility*. As a result, the electric flux density can be rewritten as:

$$\mathbf{D} = \varepsilon_0 \left(1 + \chi_c\right) \mathbf{E} = \varepsilon\, \mathbf{E} \tag{2.7}$$

and the new variable is denoted as permittivity of the dielectric. For engineering purposes, however, the *relative permittivity* is often used $\varepsilon_r = {}^{\varepsilon}/_{\varepsilon_0} = 1 + \chi_e$. In vacuum, the vector $\mathbf{P}$ vanishes while in air it is often negligible which reduces the constitutive relation to simply $\mathbf{D} = \varepsilon_0 \mathbf{E}$.

2.4.4.2 Magnetization

The constitutive law relating $\mathbf{H}$ and $\mathbf{B}$ reads,

$$\mathbf{B} = \mu_0 (\mathbf{H} + \mathbf{M})$$

where $\mathbf{M}$ denotes a *magnetization intensity* which is defined as the sum of the magnetic dipole moments per unit volume [55] and μ_0 is the permeability of free space with a value of $4\pi \times 10^{-7}\,{}^{\mathrm{H}}/_{\mathrm{m}}$ in the MKS unit system. Similarly to the electric polarization case, in most materials the vector $\mathbf{M}$ is proportional to $\mathbf{H}$ using the so-called *magnetic susceptibility* χ_m. Thus, the magnetic flux can be rewritten as:

$$\mathbf{B} = \mu_0 \, (1 + \chi_m) \, \mathbf{H} = \mu \mathbf{H} \tag{2.8}$$

and the new variable is simply and originally called *permeability of the material*. The use of the relative permeability $\mu_r = {}^{\mu}/_{\mu_0} = 1 + \chi_m$ is common in engineering practice. In vacuum, $\mathbf{M}$ vanishes while in air (and any other non-magnetic medium) its value is negligible such that the constitutive equation reduces to $\mathbf{B} = \mu_0 \mathbf{H}$.

2.4.4.3 Electric Conduction

This phenomenon happens in a medium containing free charges such that when an electric field is applied, those charges tend to flow forming *conduction currents* [55]. In most materials, the current density is proportional to the electric field such that $\mathbf{J} = \sigma \mathbf{E}$ where σ is called *conductivity*.

2.4.4.4 Classification of Media

The parameters ε, μ and σ allow to characterize the electromagnetic properties of the medium under consideration. For example, if any of the variables is a function of space, the medium is called *heterogeneous*; otherwise, it is an *homogeneous* medium [81]. If the parameters show time dependence, they are named *non-stationary*; otherwise, they are called *stationary*.

More importantly, perhaps, is the classification concerning the direction of $\mathbf{D}$ and $\mathbf{B}$ relative to $\mathbf{E}$ and $\mathbf{H}$. When, for instance, the electric flux density is parallel to its intensity, the medium is called *isotropic*; otherwise, is called *anisotropic*. The same logic applies for the relation between the $\mathbf{B}$ and $\mathbf{H}$. For anisotropy to be accounted

for, some modifications have to be made to both (2.7) and (2.8) as follows:

$$\underbrace{\begin{bmatrix} \mathrm{D}_x \\ \mathrm{D}_y \\ \mathrm{D}_z \end{bmatrix}}_{\mathbf{D}} = \underbrace{\begin{bmatrix} \varepsilon_{xx} & \varepsilon_{xy} & \varepsilon_{xz} \\ \varepsilon_{yx} & \varepsilon_{yy} & \varepsilon_{yz} \\ \varepsilon_{zx} & \varepsilon_{zy} & \varepsilon_{zz} \end{bmatrix}}_{\underline{\underline{\varepsilon}}} \underbrace{\begin{bmatrix} \mathrm{E}_x \\ \mathrm{E}_y \\ \mathrm{E}_z \end{bmatrix}}_{\mathbf{E}}, \quad \underbrace{\begin{bmatrix} \mathrm{B}_x \\ \mathrm{B}_y \\ \mathrm{B}_z \end{bmatrix}}_{\mathbf{B}} = \underbrace{\begin{bmatrix} \mu_{xx} & \mu_{xy} & \mu_{xz} \\ \mu_{yx} & \mu_{yy} & \mu_{yz} \\ \mu_{zx} & \mu_{zy} & \mu_{zz} \end{bmatrix}}_{\underline{\underline{\mu}}} \underbrace{\begin{bmatrix} \mathrm{H}_x \\ \mathrm{H}_y \\ \mathrm{H}_z \end{bmatrix}}_{\mathbf{H}} \tag{2.9}$$

where $\underline{\underline{\varepsilon}}$ and $\underline{\underline{\mu}}$ are the permittivity and permeability tensors, respectively. In case the former is purely diagonal, the medium is denoted as *biaxial* if all three entries are different and *uniaxial* if any two of the three are equal.

Unsurprisingly, categories also exist based on conductivity and permeability. For the former, if $\sigma = 0$, the medium is a *perfect dielectric* (insulator) whereas if $\sigma \to \infty$ then the medium is catalogued as a *perfect electric conductor*.

If permeability is to be used as a classification criterion, *diamagnetic* and *paramagnetic* media are two well known categories. The first one refers to media where χ_m is a very small negative number while for the second category $0 < \chi_m << 1$. In any case, both categories can be approximated by $\mu_r = 1$ since the difference between value of χ_m for those classifications is rarely higher than 10^{-4}. Additional categories include *ferromagnetics* ($\mu_r >> 1$, $\sigma >> 1$) and *ferrites* ($\mu_r >> 1$, $\sigma > 1$).

More complex classifications can be found in literature which are associated to equally intricate constitutive laws. Notorious examples include the so-called *bi-isotropic* laws [69, Chapter 2.2.2] in which $\mathbf{D} = \underline{\underline{\varepsilon}}\,\mathbf{E} + \underline{\underline{\xi}}\,\mathbf{H}$ and $\mathbf{B} = \underline{\underline{\mu}}\,\mathbf{H} + \underline{\underline{\zeta}}\,\mathbf{E}$ (ξ and ζ measure magneto-electric effects). Classifications based on frequency also exist in which $\varepsilon = \varepsilon(f)$ or $\mu = \mu(f)$ leading to *dispersive* media. Finally, perhaps one of the most well-recognized categories is the *non-linear* media in which $\varepsilon = \varepsilon(E)$ and/or $\mu = \mu(H)$.

2.4.4.5 Constitutive Relations for Differential Forms

In the language of differential forms, the material parameters relate the 1-forms $\mathbf{e}$, $\mathbf{h}$ to the 2-forms $\mathbf{d}$, $\mathbf{b}$, $\mathbf{j}$ by means of the *Hodge operator* $\star$ which induces the isomorphisms $\Lambda^1(\mathbb{R}^n) \cong \Lambda^{n-1}(\mathbb{R}^n)$ [46]. The constitutive relations are written as:

$$\mathbf{d} = \star_\epsilon \mathbf{e} \qquad \mathbf{b} = \star_\mu \mathbf{h} \qquad \mathbf{j} = \star_\sigma \mathbf{e}$$

where the subscripts are used as to remind that either the parameter $\underline{\underline{\epsilon}}$, $\underline{\underline{\mu}}$ or $\underline{\underline{\sigma}}$ has to be included. A similar notation is followed, for instance, by Bossavit [15] who also extrapolates the notation of subscripts to mass matrices depending on material parameters.

2.4.5 Time-Harmonic Fields

The four dimensional system of the Maxwell's equations can be reduced by using the so-called *time-Harmonic* Maxwell system which might be desirable whenever the source currents vary in a sinusoidally in time [67]. Firstly, it is assumed that the variables behave as follows:

$$\begin{aligned} \boldsymbol{\mathcal{E}}(t,\underline{x}) &= \Re\left(e^{-i\omega t}\ \mathbf{E}\,(\underline{x})\right), \quad \boldsymbol{\mathcal{D}}(t,\underline{x}) = \Re\left(e^{-i\omega t}\ \mathbf{D}\,(\underline{x})\right) \\ \boldsymbol{\mathcal{H}}(t,\underline{x}) &= \Re\left(e^{-i\omega t}\ \mathbf{H}\,(\underline{x})\right), \quad \boldsymbol{\mathcal{B}}(t,\underline{x}) = \Re\left(e^{-i\omega t}\ \mathbf{B}\,(\underline{x})\right) \\ \boldsymbol{\mathcal{J}}(t,\underline{x}) &= \Re\left(e^{-i\omega t}\ \mathbf{J}\,(\underline{x})\right), \quad \hat{\boldsymbol{\rho}}(t,\underline{x}) = \Re\left(e^{-i\omega t}\ \ \boldsymbol{\rho}(\underline{x})\right) \end{aligned}$$

where $\Re$ denotes the *real part* of the function. The time-harmonic equations are obtained by inserting the above relations in the system (2.4a) - (2.4d). The most notable changes appear in the *Maxwell - Ampère Law* and *Faraday's Law* since those equations contain the time derivatives and, hence, are the ones shown below:

$$\nabla \times \mathbf{H} + i\,\omega\,\underline{\underline{\varepsilon}}\,\mathbf{E} = \mathbf{J} \tag{2.10a}$$

$$\nabla \times \mathbf{E} - i\,\omega\,\underline{\underline{\mu}}\,\mathbf{H} = 0 \tag{2.10b}$$

where the constitutive relations have been introduced to replace $\mathbf{D}$ and $\mathbf{B}$.

It is a usual practice to eliminate either $\mathbf{E}$ or $\mathbf{H}$ from the equations above to work with a second order system rather than doing it with two first order equations. Eliminating, for example, $\mathbf{H}$ is done by isolating the magnetic intensity from the time-harmonic Faraday's equation and substituting it into the remaining equation as follows:

$$\mathbf{H} = \frac{1}{i\,\omega}\,\underline{\underline{\mu}}^{-1}\,\nabla \times \mathbf{E} \xrightarrow[\text{into (2.10a)}]{\text{substituting}} \nabla \times \left(\frac{1}{i\,\omega}\,\underline{\underline{\mu}}^{-1}\,\nabla \times \mathbf{E}\right) + i\,\omega\,\underline{\underline{\varepsilon}}\,\mathbf{E} = \mathbf{J}$$

which after reshuffling the terms leads to the final second-order equation for $\mathbf{E}$:

$$\nabla \times \left(\underline{\underline{\mu}}^{-1} \times \mathbf{E}\right) = i\,\omega\,\mathbf{J} + \omega^2\,\underline{\underline{\varepsilon}}\,\mathbf{E} \tag{2.11}$$

The choice of setting up an equation for the electric field intensity rather than for the magnetic field intensity was, of course, arbitrary. Obtaining the system for $\mathbf{H}$ is done by solving for $\mathbf{E}$ in (2.10a) and then substituting the result back into (2.10b) which leads to the following equation:

$$\nabla \times \left(\underline{\underline{\varepsilon}}^{-1}\,\nabla \times \mathbf{H}\right) = \nabla \times \left(\underline{\underline{\varepsilon}}^{-1}\,\mathbf{J}\right) + \omega^2\,\underline{\underline{\mu}}\,\mathbf{H} \tag{2.12}$$

2.4.6 Boundary Conditions

No problem is complete without boundary conditions and the Maxwell system is no exception to the rule. Consider, for example, the interface S between two media with different electric and magnetic properties. The behavior of the fields is then governed by boundary relations which can be formulated using the integral form as a starting point [80]. At the interface, the equations to be satisfied are:

$$\mathbf{n} \times \left(\mathbf{E}_1 - \mathbf{E}_2\right) = 0 \tag{2.13a}$$

$$\mathbf{n} \times \left(\mathbf{H}_1 - \mathbf{H}_2\right) = \mathbf{J}_s \tag{2.13b}$$

$$\mathbf{n} \cdot \left(\mathbf{D}_1 - \mathbf{D}_2\right) = \rho_s \tag{2.13c}$$

$$\mathbf{n} \cdot \left(\mathbf{B}_1 - \mathbf{B}_2\right) = 0 \tag{2.13d}$$

where $\mathbf{n}$ is the unit normal vector pointing from region 2 to 1 while $\mathbf{J}_s$ and ρ_s are the surface current and surface charge density on the interface, respectively [54].

Both (2.13c) and (2.13d), even if ρ_s and $\mathbf{J}_s$ are negligible, will lead to non-continuous fields if $\underline{\underline{\varepsilon}}$ and $\underline{\underline{\mu}}$ are discontinuous across the interface. Hence, any numerical scheme that attempts to approximate the Maxwell system with discontinuous material properties must take into account that tangential components are continuous while normal ones are allowed to jump across boundaries [67, p. 8].

Whenever the media at one side of the interface is a *perfect conductor*, $\sigma \to \infty$ and, from Ohm's Law, if $\mathbf{J}$ is to remain bounded then $\mathbf{E} \to 0$ which immediately suggests that for such conditions, the electric field vanishes. So, if the media with label 2 is a PEC (perfect electric conductor), then the fields with such label disappear from the boundary relations. Even when this might not be feasible in reality, it really simplifies engineering calculations and, for the present work, it will be the mainly utilized boundary condition.

A more realistic situation might be one where the neither side is a PEC but one of them allows the field to slightly penetrate. This leads to the so-called *imperfectly conducting boundary condition* described as $\mathbf{n}\times\mathbf{H}-\lambda(\mathbf{n}\times\mathbf{E})\times\mathbf{n} = 0$ where the index "1" denotes the region with the good conducting properties and λ is the impedance [67, Section 1.2.2].

A more complete summary of boundary conditions for several cases can be found in [5, Table 1-3] with the relations to be followed for all the fields across the interfaces between media. Some other conditions, such as radiation ones, are discussed in several literature such as [54, Chapter 1.6] while an overview of conditions for open regions can be found in [80, Chapter 5.3].

2.5 The Cavity Eigenvalue Problem

In eigenvalue problems, differential equations and boundary conditions are homogeneous which means that there is no source or excitation at all. Upon discretization, these type of problems lead to the so-called generalized eigenvalue equation such that its representation in algebraic form is given by [54, Chapter 7]:

$$[A]\{\phi\} - \lambda[B]\{\phi\} = \{0\} \tag{2.14}$$

where both A and B are matrices related to the discretization while $\{\phi\}$ denotes the unknowns. The objective of the problem is to determine λ such that the system becomes singular which means finding an eigenvalue for which $\det|A-\lambda B|$ vanishes. The non-trivial solution associated to the eigenvalue is then called eigenvector.

In electromagnetics, eigenvalue problems are often encountered in the form of cavity resonance and wave propagation problems in closed/open structures. The objective of such problems is determining the resonant frequencies corresponding to eigenvalues and its associated resonant modes related to the eigenvectors.

For closed waveguides, two approaches are usually considered: scalar and vector formulations. For the former, a behavior $\boldsymbol{u}(x,y,z) = \boldsymbol{u}(x,y)\exp[j(\omega t - k_z z)]$ is assumed for both $\mathbf{E}$ and $\mathbf{H}$ where the z-axis is taken as aligned to the infinite axis of the waveguide. In doing so, both E_z and H_z determine all the other components. Hence the reason why this approach is known as E_z-H_z formulation. As a downside, this approach has the inability to treat general anisotropic materials for which the permittivity/permeability tensors cannot be diagonalized [54].

For vector formulations, the eigenvalue problem can be cast for either $\mathbf{E}$ or $\mathbf{H}$. The equations are quite similar to (2.11) and (2.12), the only difference being that $\mathbf{J} = 0$. Thus, the problem reads,

$$\nabla \times \left(\underline{\underline{\mu}}^{-1} \nabla \times \mathbf{E} \right) = \omega^2 \underline{\underline{\varepsilon}}\, \mathbf{E} \quad \begin{cases} n \times \mathbf{E} = 0, & \text{electric walls} \\ n \cdot \mathbf{E} = 0, & \text{magnetic walls} \end{cases} \tag{2.15a}$$

$$\nabla \times \left(\underline{\underline{\varepsilon}}^{-1} \nabla \times \mathbf{H} \right) = \omega^2 \underline{\underline{\mu}}\, \mathbf{H} \quad \begin{cases} n \times \mathbf{H} = 0, & \text{magnetic conducting surface} \\ n \cdot \mathbf{H} = 0, & \text{electric conducting surface} \end{cases} \tag{2.15b}$$

As any eigenvalue problem, the solution is sought for scalars ω^2 and *non-trivial* eigenfunctions $\mathbf{E}$ or $\mathbf{H}$ and, depending of the chosen formulation, the appropriate divergence relation should be included to discard non-physical solutions.

2.5.1 Variational Formulation

Using the Galerkin method, the variational formulation for the cavity problem can be found by multiplying either (2.15a) or (2.15b) with a test function and integrating. As usual, the highest order term (in this case the curl-curl term) is split by standard integration by parts formulas [61]. The eigenvalue problem for the field $\mathbf{E}$ reads,

$$\int_\Omega \left(\nabla \times \widetilde{\mathbf{E}}\right) \cdot \left(\underline{\underline{\mu}}^{-1} \nabla \times \mathbf{E}\right) \mathrm{d}\Omega - \int_{\partial\Omega} \left(\mathbf{n} \times \widetilde{\mathbf{E}}\right) \cdot \left(\underline{\underline{\mu}}^{-1} \nabla \times \mathbf{E}\right) \mathrm{d}\Gamma = \omega^2 \int_\Omega \widetilde{\mathbf{E}}\, \underline{\underline{\varepsilon}}\, \mathbf{E}\, \mathrm{d}\Omega$$

while for the field $\mathbf{H}$ the formulation reads,

$$\int_\Omega \left(\nabla \times \widetilde{\mathbf{H}}\right) \cdot \left(\underline{\underline{\varepsilon}}^{-1} \nabla \times \mathbf{H}\right) \mathrm{d}\Omega - \int_{\partial\Omega} \left(\mathbf{n} \times \widetilde{\mathbf{H}}\right) \cdot \left(\underline{\underline{\varepsilon}}^{-1} \nabla \times \mathbf{H}\right) \mathrm{d}\Gamma = \omega^2 \int_\Omega \widetilde{\mathbf{H}}\, \underline{\underline{\mu}}\, \mathbf{H}\, \mathrm{d}\Omega$$

After imposing boundary conditions, appropriate function spaces can be defined for the solution. For instance, in the $\mathbf{E}$ formulation, considering a PEC would require to satisfy the relation $\mathbf{n} \times \mathbf{E} = 0$ at $\partial\Omega$. Thus, the problem reduces to finding *non-trivial* eigenfunctions $\mathbf{E} \in H_0(\mathrm{curl}; \Omega)$ and eigenvalues $\omega^2 \in \mathbb{R}$. The formulation for this configuration would then read,

$$\int_\Omega \left(\nabla \times \widetilde{\mathbf{E}}\right) \cdot \left(\underline{\underline{\mu}}^{-1} \nabla \times \mathbf{E}\right) \mathrm{d}\Omega = \omega^2 \int_\Omega \widetilde{\mathbf{E}}\, \underline{\underline{\varepsilon}}\, \mathbf{E}\, \mathrm{d}\Omega, \quad \forall\, \widetilde{\mathbf{E}} \in H_0(\mathrm{curl}; \Omega) \tag{2.16}$$

where the function space for $\widetilde{\mathbf{E}}$ is chosen as to eliminate the boundary term.

The same result can be obtained by using the functional $J(\mathbf{E})$ [54] given by:

$$J(\mathbf{E}) = \frac{1}{2} \int_\Omega \underline{\underline{\mu}}^{-1} (\nabla \times \mathbf{E}) \cdot (\nabla \times \mathbf{E})\, \mathrm{d}\Omega - \omega^2 \int_\Omega \frac{1}{2}\, \underline{\underline{\varepsilon}}\, \mathbf{E} \cdot \mathbf{E}\, \mathrm{d}\Omega \tag{2.17}$$

and perform a process known as *taking variations*. The latter consists in evaluating the modified functional $V = J\left(E + \alpha\widetilde{E}\right)$ with $\alpha << 1$ and then computing $\frac{\mathrm{d}V}{\mathrm{d}\alpha} = 0$. In case the magnetic field is preferred, the positions of the tensors $\underline{\underline{\mu}}$ and $\underline{\underline{\varepsilon}}$ are switched and $\mathbf{H}$ replaces $\mathbf{E}$ in the functional.

2.5.2 Spurious Solutions

The term *spurious solutions* refers to numerical solutions that converge to a *wrong solution* of a PDE (or system of PDEs). If not possible to recognize them and tell them apart from the true solutions, they are quite dangerous for applications [49].

In [84], these unphysical solutions are named *vector parasites* while Bossavit, in [12], refers to these solutions as a *curse* and even a *plague*. A general concensus is,

however, that the reason these unwanted solutions arise is mainly due to violating the divergence-free conditions of any of the fields [49].

In several publications, such as [84], it is pointed out that the root of the problem is not failing to satisfy the solenoidal conditions at the discrete level, but, instead, a poor discretization of the kernel and range of the operators. In simpler terms, it means that the Lagrange finite elements fail to accommodate within a De Rham complex. However, in [33], Lagrange vector elements were used that avoided spurious solutions. These elements were part of a smoother version of the de Rham complex (a Stokes complex) and the solution obtained on Powell-Sabin triangulations with a modified variational formulation. Thus, nodal elements seem to be usable on specific situations under severe modifications.

Careless use of nodal approximations, however, will lead to spurious solutions also in source problems as shown in [3] where the vector Laplacian problem led to wrong solutions on L-shape domains and annuli.

In words of Bossavit, the *plague* of spurious solutions must be eliminated or, at least, frightened away. Such solutions can be sorted out by monitoring the divergence of the fields or kept at bay by penalizing the divergence.

2.5.3 Untreated Disease

If (2.15a) or (2.15b) are not coupled with their correspondent divergence-free conditions, the obtained eigenvalues can potentially be *polluted* by unwanted solutions.

Even when edge elements are utilized, the presence of spurious zero eigenvalues is observed. This is, technically speaking, not a huge problem since they are easily identifiable. In fact, the number of zero eigenvalues is known *a priori* to be equal to the number of internal nodes in the mesh when the boundary is simply connected [80, p. 127]. The appearance of these spurious zeros is due to the fact that the formulations do not enforce the zero divergence conditions at such nodes [54] which allows for the non-physical solutions $\mathbf{E} = \operatorname{grad}\Psi$ and $\mathbf{H} = \operatorname{grad}\Phi$ to pollute the computations [15, Chapter 9.3.3].

2.5.4 Kikuchi Formulation

Around 1987, a mixed method was proposed by Kikuchi [56] which attempted to solve a problem of the type $\operatorname{rot}(\operatorname{rot}\underline{u}) = \lambda\underline{u}$ with boundary conditions $\underline{u}\times\underline{n} = 0$ subject to the constraint $\operatorname{div}\underline{u} = 0$ for domains with continuous boundaries $\partial\Omega$. This proposed mixed method was supported by the work of Brezzi [22] on the approximation of saddle-point problems using Lagrangian Multipliers and resembled the

so-called *displacement method* used in structural mechanics. The mixed formulation from [56] requires finding $(\lambda, u, p) \in \mathbb{R}^1 \times U(\Omega) \times H_0^1(\Omega)$:

$$\Big(\operatorname{rot} u, \operatorname{rot} v\Big) + \Big(\operatorname{grad} p, v\Big) = \lambda\Big(u, v\Big) \quad \forall v \in U(\Omega) \tag{2.18a}$$

$$\Big(u, \operatorname{grad} q\Big) = 0 \quad \forall q \in H_0^1(\Omega) \tag{2.18b}$$

where $U(\Omega) = \Big\{ v \in L_2(\Omega) \mid \operatorname{rot}(v) \in L_2(\Omega),\ \mathbf{n} \times v = 0 \Big\}$, p is the Lagrange multiplier and $(\cdot\,,\cdot)$ indicates the standard inner product where integration is performed on Ω.

Consider, for instance, that the material parameters in (2.16) are set to the identity tensor and the problem is rewritten in terms of u, p, v. It can be stated that both (2.16) and the system (2.18) solve the same problem and are, indeed, equivalent. Such claim is proved in two steps. Firstly, it is clear that any pair (λ, u) satisfying (2.16) satisfies (2.18a) by setting $p = 0$. Secondly, if $v = \operatorname{grad} p$ in (2.18a), then $(\operatorname{grad} p, \operatorname{grad} p) = \lambda(u, \operatorname{grad} p)$ and using the fact that the sought solution was forced to be orthogonal to all gradients in (2.18b) only $(\operatorname{grad} p, \operatorname{grad} p) = 0$ remains which implies $\operatorname{grad} p = 0$. Since the multiplier is sought in $H_0^1(\Omega)$, then $p = 0$ [9] and any eigenpair from (2.18) satisfies (2.16) and the divergence-free condition.

In the original article by Kikuchi, Nédéelec elements were utilized such that the mixed formulation removed the large null space of the curl operator and, as a result, all the *spurious* zero eigenvalues were eliminated in a domain with a continuous boundary $\partial\Omega$.

2.5.5 Penalty Methods

At the beginning of the 1980s, the so-called *penalty methods* starting to be used for the Maxwell Equations. This is the case of [48] where an interior boundary value problem was analyzed with a penalty parameter γ used on the boundary terms.

In 1983, a penalty method was discussed for the eigenvalue problem of the second order curl-curl problem of the electric field $\mathbf{E}$ [43]. If the penalty parameter is not chosen appropriately, eigenvalues of physical and non-physical solutions may be similar and the whole spectra becomes unreliable. Unfortunately, an appropriate value selection for the penalty parameter is an *ad hoc* (problem-dependent) treatment. Assuring that the solutions extracted with this type of formulations are, indeed, physical has to be done by examining either $\nabla \cdot \mathbf{D} = 0$ or $\nabla \cdot \mathbf{B} = 0$.

Adding penalty terms to the variational formulations to *eliminate* the spurious solutions is, in the words of Konrad [57], unacceptable since no reduction occurs

[9] Had a general tensor $\underline{\underline{\epsilon}}$ been considered, the fact that it is positive definite has to be used.

in the size of the matrix eigenvalue problem. In fact, what really happens with this type of *solution* is that the non-physical modes are not eliminated but rather ***pushed*** towards higher frequencies and therefore do not show up among the first few physically meaningful modes.

Examples for penalty methods for the eigenvalue problem (2.16) for $\underline{\underline{\epsilon}} = \underline{\underline{\mu}} = \mathbb{I}$ are shown also in [56] apart from the mixed problem shown in the previous section. Such formulations require finding $s > 0$ [10] and an eigenpair $(\lambda, u) \in \mathbb{R}^1 \times V(\Omega)$ with $u \neq 0$:

$$\Big(\operatorname{rot} u, \operatorname{rot} v\Big) + s^{-1}\Big(\operatorname{div} u, \operatorname{div} v\Big) = \lambda\Big(u, v\Big) \quad \forall\, v \in V(\Omega) \tag{2.19}$$

with $V(\Omega) = \Big\{v \in U(\Omega) \mid \operatorname{div}(v) \in L_2(\Omega)\Big\}$. Any (λ, u) from (2.19) is also an eigenpair of (2.18) but some solutions from the penalty equation might not be the ones from the original problem [56]. The latter just supports the fact that spurious solutions are not eliminated but rather moved around within the spectra.

A combination of a perturbation problem and a penalty method can also be utilized which requires finding $(\lambda, u, p) \in \mathbb{R}^1 \times U(\Omega) \times H_0^1(\Omega)$ with $s > 0$ and $u \neq 0$:

$$\Big(\operatorname{rot} u, \operatorname{rot} v\Big) + \Big(\operatorname{grad} p, v\Big) = \lambda\Big(u, v\Big) \quad \forall\, v \in U(\Omega) \tag{2.20a}$$

$$\Big(u, \operatorname{grad} q\Big) = s\Big(p, q\Big) \quad \forall\, q \in H_0^1(\Omega) \tag{2.20b}$$

which is the same size as the formulation shown in Section 2.5.4 but requires solving the additional eigenvalue problem given by $(\operatorname{grad} r, \operatorname{grad} q) = \beta(r, q)$ for all $q \in H_0^1(\Omega)$ which helps determining the penalty parameter s since the relation $0 < s < {}^{\beta}/_{\lambda_0}$ has to be satisfied with λ_0 being an arbitrary fixed positive number.

[10] In [56] ε denotes the penalty parameter but s is used as to not confuse it with the permittivity.

3

Mathematical Background

In this segment of the thesis, the mathematical background required to implement the mimetic spectral formulation is explored. The first half of the chapter deals with the grid construction, the *De Rham Maps* and the interpolation functions, *Whitney Maps*, to be utilized. Additionally, mass matrices and incidence matrices are discussed. The second half of the chapter considers topics such as domain partitioning, weak forms and error computation.

3.1 Construction of Finite Elements

The construction of the finite elements used within this thesis is shown in [51] by defining the triplet $(K, \mathcal{P}, \mathcal{N})$ as described by Brenner & Scott [6] following classical definitions by Ciarlet.

Such triplet consists of the following elements:

- K: bounded closed set with non-empty interior and smooth boundary.
- $\mathcal{P}$: a finite dimensional space of functions on K with dimension $d_{\mathcal{P}}$.
- $\mathcal{N}$: linear functionals representing the degrees of freedom. In [6], this is defined as ***the set of nodal variables*** but such delineation is not strictly followed as some functionals $\mathcal{N}_i$ will not be attached to nodes. Furthermore, the set $\mathcal{N}$ (with dimension $\mathbb{R}^{d_{\mathcal{P}}}$) acts on elements of $\mathcal{P}$ such that the linear map

$$p^h \in \mathcal{P} \mapsto \left(\mathcal{N}_1\left(p^h\right), \cdots, \mathcal{N}_{d_{\mathcal{P}}}\left(p^h\right)\right) \text{ is bijective.}$$

To create a basis in $\mathcal{P}$, the **Kronecker-delta** condition must be satisfied [51]:

A basis $\{\Psi_1, ..., \Psi_{d_\mathcal{P}}\}$ exists in $\mathcal{P}$ such that $\mathcal{N}_i(\Psi_j) = \delta_{ij},\ 1 \leq i,\ j \leq d_\mathcal{P}$

The next sections detail the mesh construction and the basis utilized in the remainder of the thesis.

3.2 Grid Construction

A domain $K = [-1,\ 1]$ is considered and a *Gauss-Lobatto-Legendre* (GLL) grid is constructed. The mesh points are determined by finding the roots of the equation

$$\left(1 - \xi^2\right) \frac{\mathrm{d}L_\mathrm{N}}{\mathrm{d}\xi} = 0 \tag{3.1}$$

where L_N represents the Legendre's polynomial of degree N which arises as one of the possible eigenfunctions of the singular Sturm-Liouville problem given by

$$\frac{\mathrm{d}}{\mathrm{d}\xi}\left((1-\xi)^{1+\alpha}(1+\xi)^{1+\beta}\frac{\mathrm{d}u}{\mathrm{d}\xi}\right) + \lambda(1-\xi)^\alpha(1+\xi)^\beta u = 0, \quad \xi \in [-1,\ 1] \tag{3.2}$$

For $\alpha = \beta = 0$, the eigenvalue becomes $\lambda = N(N+1)$ and the eigenfunction $u(\xi)$ becomes the sought Legendre polynomial $L_\mathrm{N}(\xi)$ [24, p. 75]. The derivative of a Legendre polynomial of degree N has $N-1$ roots within $[-1,\ 1]$ which means that (3.1) produces $N+1$ solutions due to the added roots from the polynomial $\left(1-\xi^2\right)$.

Direct solution of (3.2) is not the only available method to compute the Legendre polynomials for arbitrary values of N. The use of Rodrigues' Formula [86] allows to compute directly a polynomial of order N by means of the equation,

$$L_\mathrm{N}(\xi) = \frac{1}{2^N\ N!}\frac{\mathrm{d}^N}{\mathrm{d}\xi^N}\left[(x^2-1)^N\right]$$

however, other methods rely on recurrence relations such as Bonnet's formula [24],

$$L_{\mathrm{N}+1}(\xi) = \frac{(2N+1)\,\xi\,L_\mathrm{N}(\xi) - N\,L_{\mathrm{N}-1}(\xi)}{N+1} \quad \text{where} \quad L_0(\xi) = 1,\ L_1(\xi) = \xi \tag{3.3}$$

The last approach was used to compute the polynomials up to degree N using as a first guess for ξ_j the Chebyshev-Gauss-Lobatto nodes $x_j = \cos\left(\frac{j\pi}{N}\right),\ 0 \leq j \leq N$, and then (3.3) was solved using a Newton-Raphson method. The distribution of the GLL nodes on $[-1,\ 1]^2$ is shown in Figure 3.1 where it is observed that the mesh allocates more points towards the boundaries. In this case, the nodes ξ_j were distributed for both axis and then spread within the domain.

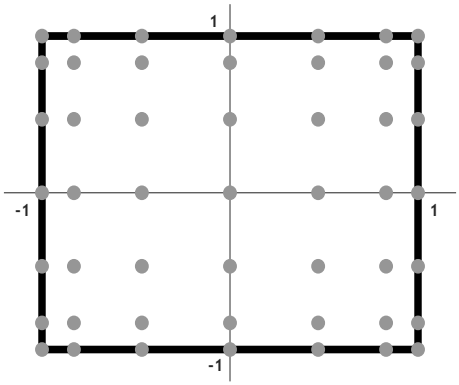

Figure 3.1: Node distribution for a Gauss-Lobatto-Legendre grid on $\Omega = [\text{-}1, 1]^2$ with $N = 6$

3.3 Basis and Degrees of Freedom

This section is devoted to define both degrees of freedom and basis functions (the *Whitney Map*) for 1D and 2D cases. These two components are essential to represent a function at every single point within a given mesh.

3.3.1 Primal Basis

Firstly, the nodal basis functions are introduced followed by the edge functions. Following the notation from [51], a canonical domain $K = [\text{-}1, 1]$ with polynomial spaces $\mathcal{P}$ and $\mathcal{Q}$ are defined such that they represent the space of polynomials of degree N and $(N-1)$, respectively. This notation is kept throughout this chapter.

For any $\alpha^h \in \mathcal{P}$ and for any $\beta^h \in \mathcal{Q}$, the degrees of freedom for the nodal and the edge functions are defined, respectively, by the following terms:

$$\mathcal{N}_i^0(\alpha^h) := \alpha^h(\xi_i), \qquad i = 0, 1, ..., N \tag{3.4a}$$

$$\mathcal{N}_i^1(\beta^h) := \int_{\xi_{j-1}}^{\xi_j} \beta^h(\xi_i)\, \mathrm{d}\xi, \quad i = 1, 2, ..., N \tag{3.4b}$$

In the equations above, ξ_i denotes the GLL nodes obtained in Section 3.2 and the superscripts d in $\mathcal{N}^d(\cdot)$ indicate the geometrical dimension onto which the degrees of freedom are attached to. For instance, $\mathcal{N}^0(\cdot)$ indicates sampling on points while $\mathcal{N}^1(\cdot)$ specifies association to line segments [51].

Once the degrees of freedom for both $\mathcal{P}$ and $\mathcal{Q}$ have been defined, the basis functions are constructed such that the condition $\mathcal{N}_i(\Psi_j) = \delta_{ij}$ described in Section 3.1 is fulfilled. For the functionals $\mathcal{N}_i^0(\cdot)$, the Lagrange polynomials $h(\xi)$ are the correct

set of functions while the functionals $\mathcal{N}_i^1(\cdot)$ require the edge functions $e(\xi)$:

$$h_i(\xi) = \frac{\left(\xi^2 - 1\right) L'_{\mathrm{N}}}{N(N+1)L_{\mathrm{N}}(\xi_i)(\xi - \xi_i)}, \quad i \in \mathbb{Z}^{N*} \tag{3.5a}$$

$$e_i(\xi) = -\sum_{k=0}^{i-1} \frac{\mathrm{d}h_k}{\mathrm{d}\xi}(\xi), \quad i \in \mathbb{Z}^{N+} \tag{3.5b}$$

The values for the index i are defined by using the set of integers $\mathbb{Z}$ such that $\mathbb{Z}^{\mu*} = \{m \in \mathbb{Z} \mid 0 \leq m \leq \mu\}$ and $\mathbb{Z}^{\mu+} = \{m \in \mathbb{Z} \mid 0 < m \leq \mu\}$ with $\mu = N$. A more detailed study and analysis of the edge functions is presented in [38] which also includes the rationale behind the need for such formulation.

Both sets of basis functions are shown in Figure 3.2. The **Kronecker-delta condition** for nodal basis functions is clearly satisfied by observing that at $\xi = \xi_i$ only one function peaks at an amplitude of unity while the rest of the set goes to zero. For edge functions, however, the integral between consecutive GLL nodes equals unity for only one function while the integral for the other ones vanishes.

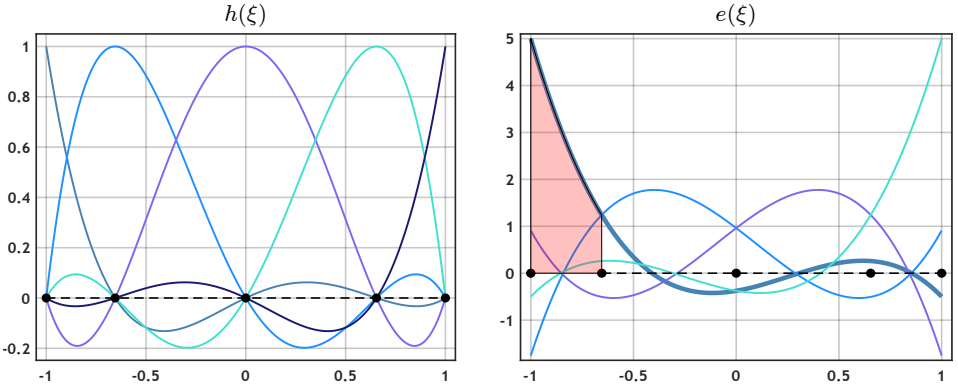

Figure 3.2: Primal Basis functions. Nodal (*left*) and edge (*right*) functions for $N = 4$. The shaded area shows the region where $\int_{\xi_0}^{\xi_1} e_1(\xi)\,\mathrm{d}\xi = 1$ while for the rest the integral equals zero.

With the basis defined, then it becomes possible to represent functions belonging to the function spaces $\mathcal{P}$ and $\mathcal{Q}$. If, for example, the functions α^h and β^h are sought to be represented by nodal basis functions and edge functions, respectively, then:

$$\alpha^h = \sum_{i=0}^{N} \mathcal{N}_i^0(\alpha^h)\, h_i(\xi) \quad \text{and} \quad \beta^h = \sum_{i=1}^{N} \mathcal{N}_i^1(\beta^h)\, e_i(\xi) \tag{3.6}$$

In order to minimize notation, and following the one in [51], the collection of degrees of freedom is gathered into column vectors $\mathcal{N}^d(\cdot)$ while basis functions are

grouped in row vectors $\Psi^d(\xi)$. The superscript d describes the dimension of the geometric object the basis/functional is attached to. Thus, with this new notation, the functions α^h and β^h are succinctly expressed as:

$$\alpha^h = \Psi^0(\xi)\,\mathcal{N}^0(\alpha^h) \quad \text{and} \quad \beta^h = \Psi^1(\xi)\,\mathcal{N}^1(\beta^h) \tag{3.7}$$

3.3.2 Mass Matrices for Primal Basis

Mass matrices are an important part of the methodology since they act as Hodge matrices which means that they communicate the primal and the dual complexes. Even if the latter concept is not familiar, it will be observed in Chapter 4 that these matrices arise naturally from the formulation itself.

The mass matrix $\mathbb{M}^{(0)}$ is defined by considering products between nodal basis functions while the matrix $\mathbb{M}^{(1)}$ is constructed by utilizing edge basis functions.

$$\mathbb{M}^{(0)} = \int_K \Psi^0(\xi)^{\mathrm{T}}\,\Psi^0(\xi)\,\mathrm{d}K \quad \text{and} \quad \mathbb{M}^{(1)} = \int_K \Psi^1(\xi)^{\mathrm{T}}\,\Psi^1(\xi)\,\mathrm{d}K \tag{3.8}$$

If the components of the basis functions belong to different polynomial spaces, the matrices to be obtained would be rectangular. This would be the case for integrals of the form $\int_K \Psi^1(\xi)^{\mathrm{T}}\Psi^0(\xi)\,\mathrm{d}K$ or $\int_K \Psi^0(\xi)^{\mathrm{T}}\Psi^1(\xi)\,\mathrm{d}K$ and, as for now, there is not a notation for such cases[11]. In Chapter 4, this issue will be addressed and further discussed when solving ordinary differential equations in which the first derivative is present.

3.3.3 Dual Basis

A thorough overview of what is shown in the forthcoming paragraphs can be found in [51]. Defining an algebraic dual basis is quite useful to increase the sparsity pattern of problems that would usually involve full matrices. Additionally, in more complicated problems arising in 2D and 3D cases, it is likely that not all variables are represented on the *primal mesh* but also on a *dual mesh* as depicted in Figure 2.5 on page 14. The latter requires its own type of degrees of freedom and basis functions for interpolation. Thus, a section is devoted to describe both.

Dual operators are denoted by placing a tilde above the primal notation and, similarly to the latter, are attached to a geometric object which is calculated as $\tilde{d} = n - d$. The parameter n indicates the dimension of the embedding space while the parameter d satisfies $0 \leq d \leq n$.

[11] In terms of differential forms, this can be interpreted as the wedge product.

The case $n = 1$ is now described. A function α^h expanded in nodal basis functions with degrees of freedom $\mathcal{N}^0(\alpha^h)$ and a function β^h expanded in edge basis functions with degrees of freedom $\mathcal{N}^1(\beta^h)$ are considered. For $\alpha^h \rightarrow d = 0$ and $\tilde{d} = 1$ while for $\beta^h \rightarrow d = 1$ and $\tilde{d} = 0$ and the associated dual degrees of freedom become:

$$\widetilde{\mathcal{N}}^1(\alpha^h) := \mathbb{M}^{(0)}\,\mathcal{N}^0(\alpha^h) \quad \text{and} \quad \widetilde{\mathcal{N}}^0(\beta^h) := \mathbb{M}^{(1)}\,\mathcal{N}^1(\beta^h)$$

The basis functions are determined using the **Kronecker-delta** condition. By letting $\mathrm{R}(j)$ and $\mathrm{C}(j)$ denote the matrix column and row number, respectively, the following is obtained for $\widetilde{\mathcal{N}}^1$:

$$\widetilde{\mathcal{N}}_i^1\left(\widetilde{\Psi}_j^1\right) = \mathbb{M}^{(0)}_{\mathrm{R}(j)}\,\widetilde{\Psi}_j^1(\xi_i) = \delta_{ij}$$

The choice that resolves the problem is $\widetilde{\Psi}_j^1(\xi_i) = h_j(\xi_i)\left(\mathbb{M}^{(0)}\right)^{-1}_{\mathrm{C}(j)}$ which allows to use the fact that $h_j(\xi_i) = \delta_{ij}$ leading to the final result:

$$\widetilde{\mathcal{N}}_i^1(\widetilde{\Psi}_j^1) = \mathbb{M}^{(0)}_{\mathrm{R}(j)}\,\delta_{ij}\left(\mathbb{M}^{(0)}\right)^{-1}_{\mathrm{C}(j)} = \begin{cases} 1, & \text{if } i = j \\ 0, & \text{if } i \neq j \end{cases}$$

Doing the latter for all columns in $\mathbb{M}^{(0)}$ produces $\widetilde{\Psi}^1(\xi)$. In order to obtain $\widetilde{\Psi}^0(\xi)$ an an identical analysis has to be done using $\widetilde{\mathcal{N}}^0$. In doing so, the dual functions end up being represented by (3.9) and are shown in Figure 3.3.

$$\widetilde{\Psi}^1(\xi) := \Psi^0(\xi)\left(\mathbb{M}^{(0)}\right)^{-1} \quad \text{and} \quad \widetilde{\Psi}^0(\xi) := \Psi^1(\xi)\left(\mathbb{M}^{(1)}\right)^{-1} \tag{3.9}$$

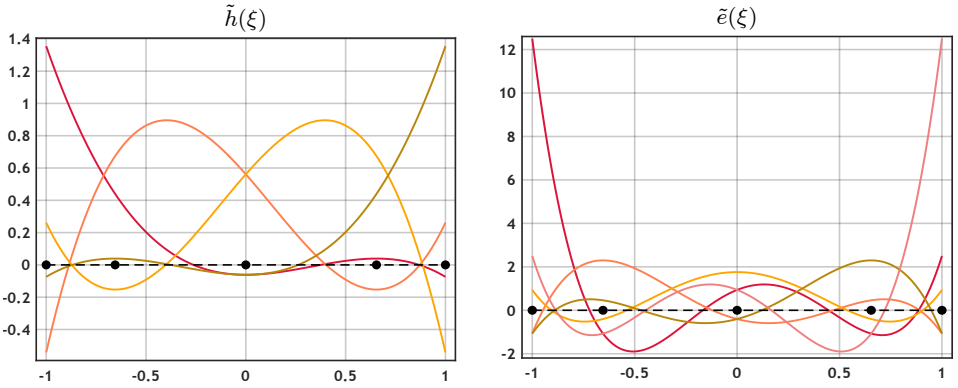

Figure 3.3: Dual Basis functions. Dual nodal (*left*) and dual edge (*right*) functions for $N = 4$.

At the end of Section 3.3.1, it was shown that any $\alpha^h \in \mathcal{P}$ could be expanded using $\Psi^0(\xi)$ while any $\beta^h \in \mathcal{Q}$ could be rewritten using $\Psi^1(\xi)$. Due to the inclusion

of the dual space, a new representation using the dual basis functions in $\mathcal{P}'$ and $\mathcal{Q}'$ is possible. The functions α^h and β^h can be written as [51]:

$$\alpha^h = \Psi^{(0)}(\xi)\,\mathcal{N}^0(\alpha^h) = \Psi^{(0)}\left(\mathbb{M}^{(0)}\right)^{-1}\mathbb{M}^{(0)}\,\mathcal{N}^0(\alpha^h) = \widetilde{\Psi}^1(\xi)\,\widetilde{\mathcal{N}}^1(\alpha^h)$$
$$\beta^h = \Psi^{(1)}(\xi)\,\mathcal{N}^1(\alpha^h) = \Psi^{(1)}\left(\mathbb{M}^{(1)}\right)^{-1}\mathbb{M}^{(1)}\,\mathcal{N}^1(\alpha^h) = \widetilde{\Psi}^0(\xi)\,\widetilde{\mathcal{N}}^0(\alpha^h)$$

The fact that β^h can be rewritten in two formats is relevant for problems solved with *Mixed Formulations*. In primal-primal methods, the solutions are sought in $\mathcal{P}-\mathcal{Q}$ while in primal-dual formulations $\mathcal{P}-\mathcal{Q}'$ is utilized. For the former, the reconstruction of $\beta^h \in \mathcal{Q}$ is done with $\Psi^1(\xi)$ whereas the latter requires $\widetilde{\Psi}^0(\xi)$.

3.3.4 Mass Matrices for Dual Basis

In Section 3.3.2, the primal mass matrices were introduced by using the L^2-inner product between functions in the same polynomial space. For the dual mass matrices, this would be the *appropriate* manner to define them. However, such matrices were already utilized and *disguised* in (3.9). Thus, notation is now formalized as:

$$\widetilde{\mathbb{M}}^{(1)} := \left(\mathbb{M}^{(0)}\right)^{-1} \quad \text{and} \quad \widetilde{\mathbb{M}}^{(0)} := \left(\mathbb{M}^{(1)}\right)^{-1} \tag{3.10}$$

where it is clear that $\widetilde{\mathbb{M}}^{(1)}\mathbb{M}^{(0)}$ and $\widetilde{\mathbb{M}}^{(0)}\mathbb{M}^{(1)}$ lead to identity matrices. Writing the dual mass matrices with L^2-inner products leads to the following definitions:

$$\widetilde{\mathbb{M}}^{(0)} = \int_K \widetilde{\Psi}^0(\xi)^{\mathrm{T}}\,\widetilde{\Psi}^0(\xi)\,\mathrm{d}K \quad \text{and} \quad \widetilde{\mathbb{M}}^{(1)} = \int_K \widetilde{\Psi}^1(\xi)^{\mathrm{T}}\,\widetilde{\Psi}^1(\xi)\,\mathrm{d}K \tag{3.11}$$

There might be an inclination to favour (3.11) over the first definition since it does not require the computation of an inverse matrix. This, however, would be far from true since the mere definition of $\widetilde{\Psi}^{\tilde{d}}(\xi)$ requires the explicit computation of such inverse as shown in (3.9).

For the work presented in this thesis, the dual basis will be utilized to increase the sparsity of the algebraic systems as to alleviate the computational effort when seeking a solution. This point will be further elaborated in future chapters when primal-dual formulations are explored.

3.3.5 Two-Dimensional Basis Functions and Mass Matrices

More challenging problems/applications rely on 2D geometries and, as a result, finite element basis for such cases must be constructed as described in [51].

For the two-dimensional case, the canonical domain is given by $K = [\text{-}1, 1]^2$ and its mesh is constructed by GLL points $\xi_i, \eta_i \in [\text{-}1, 1]$. Three sets of degrees of freedom and three sets of basis functions have to be specified to represent functions represented on points, lines and surfaces on the primal space. Similarly, the dual space would require the same number of degrees of freedom/basis functions.

The degrees of freedom for functions represented on nodes are given by nodal sampling and its basis is built as a tensor product of the 1D basis presented in (3.5a) such that a polynomial space $C(K) := \mathcal{P} \otimes \mathcal{P}$ is established. Thus, for any $\alpha^h \in C(K)$ the correspondent degrees of freedom and basis are given by:

$$\mathcal{N}^0_{i(N+1)+j}\left(\alpha^h\right) := \alpha^h(\xi_i, \eta_j) \qquad \text{and} \quad i, j \in \mathbb{Z}^{N*} \tag{3.12}$$

$$\Psi^0(\xi, \eta) = \Psi^0(\xi) \otimes \Psi^0(\eta) \quad \text{and} \quad \dim\Big(\Psi^0(\xi, \eta)\Big) = (N+1)^2 \tag{3.13}$$

where $\Psi^0(\xi, \eta)$ is arranged such that $\Psi^0_{i(N+1)+j}(\xi, \eta) = \Psi^0_i(\xi)\Psi^0_j(\eta)$. For functions represented on lines, the spaces $D_\xi := \mathcal{P} \otimes \mathcal{Q}$ and $D_\eta := \mathcal{Q} \otimes \mathcal{P}$ are combined to construct $D(K) = D_\xi \times D_\eta$ such that the basis becomes

$$\Psi^1(\xi, \eta) = \begin{cases} \Psi^1_\xi(\xi, \eta) = \Psi^0(\xi) \otimes \Psi^1(\eta), & \dim\Big(\Psi^1_\xi(\xi, \eta)\Big) = N\,(N+1) \\ \Psi^1_\eta(\xi, \eta) = \Psi^1(\xi) \otimes \Psi^0(\eta), & \dim\Big(\Psi^1_\eta(\xi, \eta)\Big) = N\,(N+1) \end{cases} \tag{3.14}$$

with $\Psi^0(\cdot)$ and $\Psi^1(\cdot)$ being described in Section 3.3.1. In this case, the k-th component of $\Psi^1(\xi, \eta) = \begin{bmatrix} \Psi^1_\xi(\xi, \eta) & \Psi^1_\eta(\xi, \eta) \end{bmatrix}^{\mathrm{T}}$ is given by:

$$\Psi^1_{k_1}(\xi, \eta) = h_i(\xi) e_j(\eta) \boldsymbol{e}_\xi \qquad \begin{cases} i \in \mathbb{Z}^{N*} \text{ and } j \in \mathbb{Z}^{N+} \\ k_1 = iN + j \end{cases} \tag{3.15a}$$

$$\Psi^1_{k_2}(\xi, \eta) = e_i(\xi) h_j(\eta) \boldsymbol{e}_\eta \qquad \begin{cases} i \in \mathbb{Z}^{N+} \text{ and } j \in \mathbb{Z}^{N*} \\ k_2 = (i-1)(N+1) + j + 1 + N(N+1) \end{cases} \tag{3.15b}$$

where $\boldsymbol{e}_\xi$ and $\boldsymbol{e}_\eta$ denote the unit vectors in the ξ and η directions [51]. By following the same numbering as for $\Psi^1(\xi, \eta)$, the degrees of freedom for any $\boldsymbol{\alpha}^h \in D(K)$ are:

$$\mathcal{N}^1_{k_1} := \int_{\eta_{j-1}}^{\eta_j} \boldsymbol{\alpha}^h(\xi_i, \eta) \cdot \boldsymbol{e}_\xi \, \mathrm{d}\eta \tag{3.16a}$$

$$\mathcal{N}^1_{k_2} := \int_{\xi_{j-1}}^{\xi_j} \boldsymbol{\alpha}^h(\xi, \eta_j) \cdot \boldsymbol{e}_\eta \, \mathrm{d}\xi \tag{3.16b}$$

Finally, the space $S(K) := \mathcal{Q} \otimes \mathcal{Q}$. The latter requires edge functions while the degrees of freedom are defined as integrals over surfaces. Thus, for any $\alpha^h \in S(K)$:

$$\mathcal{N}^2_{(i-1)N+j}\left(\alpha^h\right) := \int_{\eta_{j-1}}^{\eta_j} \int_{\xi_{i-1}}^{\xi_i} \alpha^h(\xi,\eta)\,\mathrm{d}\xi\,\mathrm{d}\eta \quad \text{and} \quad i,j \in \mathbb{Z}^{N+} \tag{3.17}$$

$$\Psi^2(\xi,\eta) = \Psi^1(\xi) \otimes \Psi^1(\eta) \quad \text{and} \quad \dim\Big(\Psi^2(\xi,\eta)\Big) = N^2 \tag{3.18}$$

The primal mass matrices are defined via an L^2-inner product. In this case, however, there are three different definitions since 3 function spaces have been considered. Nevertheless, the notation can be combined in a single expression as,

$$\mathbb{M}^{(d)} = \iint_K \Psi^d(\xi,\eta)^{\mathrm{T}}\,\Psi^d(\xi,\eta)\,\mathrm{d}K \tag{3.19}$$

For $d = \{0, 2\}$, the components $\mathbb{M}^{(d)}_{i,j}$ are given by the scalar multiplication of $\Psi^d_m(\boldsymbol{\xi})\Psi^d_n(\boldsymbol{\xi})$ while for $\mathbb{M}^{(1)}_{i,j}$ the dot product is required. Once $\mathbb{M}^{(d)}$ is defined, the dual basis is constructed. For simplicity, its definition follows the notation from (3.11) instead of an L^2-inner product. The dual basis functions are given as:

$$\widetilde{\Psi}^{\tilde{d}}(\xi,\eta) = \Psi^d(\xi,\eta)\,\left(\mathbb{M}^{(d)}\right)^{-1} = \Psi^d(\xi,\eta)\,\widetilde{\mathbb{M}}^{(\tilde{d})} \tag{3.20}$$

where $\tilde{d} = n - d$. Hence, $\widetilde{S}(K)$, $\widetilde{D}(K)$ and $\widetilde{C}(K)$ are represented by $\tilde{d} = \{0, 1, 2\}$, respectively. Additionally, the same convention used in (3.10) has been applied to the dual mass matrices by defining them as the inverse of a primal mass matrix.

Finally, all the different basis functions presented in this section can be visualized in Figure 3.4, Figure 3.5, Figure 3.6 and Figure 3.7.

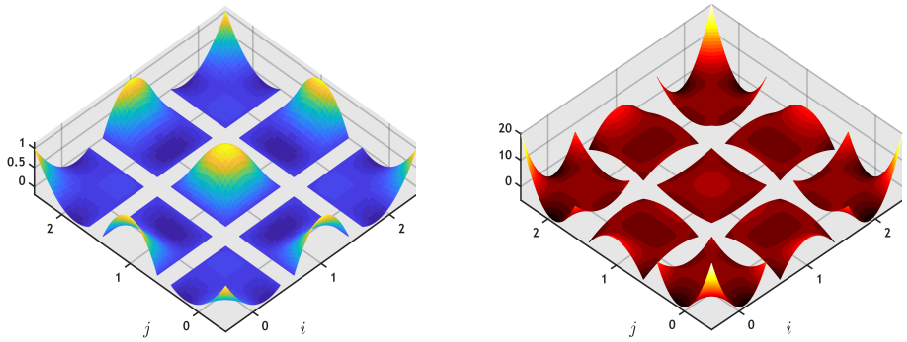

(a) Primal basis $\Psi^0(\xi,\eta)$ (b) Dual basis $\widetilde{\Psi}^2(\xi,\eta)$

Figure 3.4: To the left, basis functions on $C(K)$ and its dual $\widetilde{C}(K)$ to the right. $N = 2$.

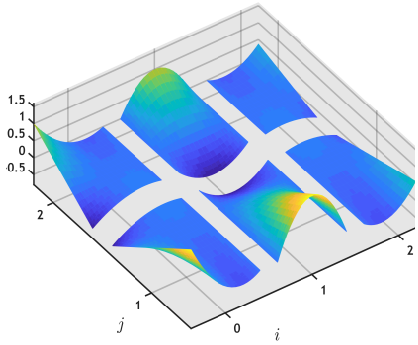

(a) Primal Basis Ψ^1_ξ

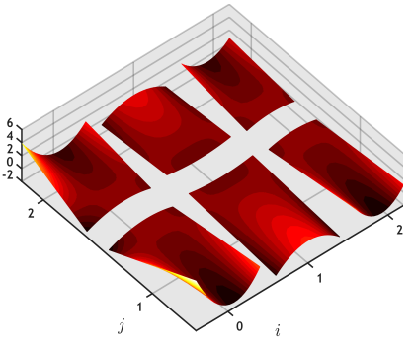

(b) Dual Basis $\widetilde{\Psi}^1_\xi$

Figure 3.5: To the left, basis functions on $D_\xi(K)$ and its dual $\widetilde{D}_\xi(K)$ to the right. $N = 2$.

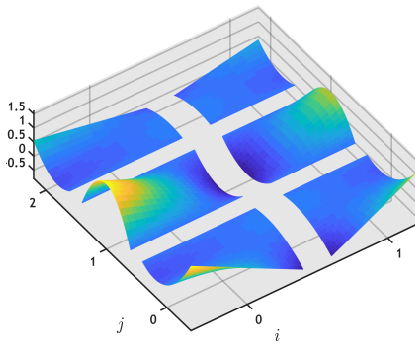

(a) Primal Basis Ψ^1_η

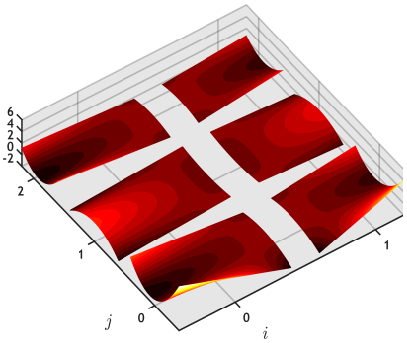

(b) Dual Basis $\widetilde{\Psi}^1_\eta$

Figure 3.6: To the left, basis functions on $D_\eta(K)$ and its dual on $\widetilde{D}_\eta(K)$ to the right. $N = 2$.

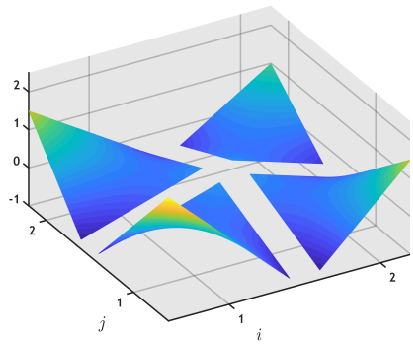

(a) Primal Basis Ψ^2

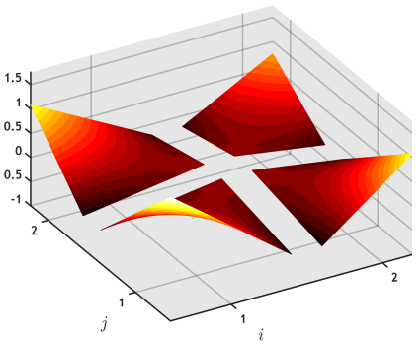

(b) Dual Basis $\widetilde{\Psi}^0$

Figure 3.7: To the left, basis $\Psi^2(\xi, \eta)$ and its dual $\widetilde{\Psi}^0(\xi, \eta)$ to the right. $N = 2$.

3.4 Non-Canonical Domains in $\mathbb{R}^1$ and $\mathbb{R}^2$

The framework presented up to this point has been specified in the canonical domain $K = [\text{-}1, 1]$. However, situations may arise in which such domain is not suitable and the basis functions need to be *modified* to accommodate for the new domain.

Such inconvenience may arise from two circumstances. Firstly, the problem is defined on an interval $I \neq K$ or, secondly, a multi-element approach is sought such that the sub-domains I_k do not coincide with K. Whatever the case may be, using

$$x = \Phi(\xi) = \frac{a}{2}(1-\xi) + \frac{b}{2}(1+\xi) \tag{3.21}$$

allows to change from $\xi \in K$ to $x \in I$ or I_k and vice-versa. If only one element is used within the domain, then a refers to the left boundary of I while b denotes its right boundary. If a multi-element approach is utilized, then a and b are the left and right boundary of I_k, respectively. Thus, the basis $h(x)$ and $e(x)$ become [51]:

$$\Psi_i^0(x) = h_i \circ \Phi^{-1}(x) \quad \text{and} \quad \Psi_i^1(x) = e_i \circ \frac{\Phi^{-1}(x)}{\mathbf{J}} \tag{3.22}$$

where $\mathbf{J} = \frac{b-a}{2}$ denotes the Jacobian. In order to perform interpolation on the new elements, the equations above are required to reconstruct the solution. The mass matrices, however, do not require explicit construction of the *new basis* since they can be computed using information from the canonical domain as:

$$\mathbb{M}^{(0)} = \int_\Omega \Psi^0(x)^{\mathrm{T}}\, \Psi^0(x)\, \mathrm{d}\Omega = \mathbf{J} \int_K \Psi^0(\xi)^{\mathrm{T}}\, \Psi^0(\xi)\, \mathrm{d}K, \tag{3.23}$$

$$\mathbb{M}^{(1)} = \int_\Omega \Psi^1(x)^{\mathrm{T}}\, \Psi^1(x)\, \mathrm{d}\Omega = \frac{1}{\mathbf{J}} \int_K \Psi^1(\xi)^{\mathrm{T}}\, \Psi^1(\xi)\, \mathrm{d}K \tag{3.24}$$

Similarly to the one-dimensional case, in 2D it is essential to define the mathematical framework on more general domains since most applications would seldom coincide with the canonical domain $K = [\text{-}1, 1]^2$ from Figure 3.1 and, as a result, the basis functions need to be extended to arbitrary 2D domains.

A mapping function $\boldsymbol{\Phi}(\boldsymbol{\xi}) = [\Phi_1(\boldsymbol{\xi}) \;\; \Phi_2(\boldsymbol{\xi})]^{\mathrm{T}}$ cannot be determined *a priori* as was done for the 1D case. Its construction can be done, for example, by using the Gordon-Hall transform [28]. This procedure creates an **invertible** map from a reference square domain onto a closed and bounded region which is very well suited to approximate curved boundaries. The expressions for the latter method as well as its methodology can be found in [41] while examples of different mappings from the canonical domain to the physical domain are shown in Figure 3.8.

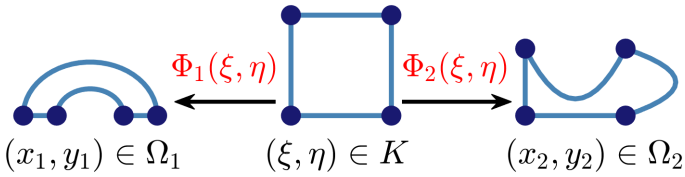

Figure 3.8: Mapping Functions $\Phi : \boldsymbol{\xi} \in K \mapsto \boldsymbol{x} \in \Omega$ from the canonical to the physical domain.

The transfinite mapping method, unlike isoparametric element formulations, decouples the mapping of the independent variables and the interpolation of the dependent variables [41]. Therefore, it is possible to use $\Psi^d(\boldsymbol{\xi})$ only to *build* the independent variable of the problem.

Regardless of the method, the mapping $\boldsymbol{\Phi}(\boldsymbol{\xi})$ allows to compute the Jacobian as:

$$\mathbf{J} = \begin{bmatrix} \frac{\partial \Phi_1}{\partial \xi} & \frac{\partial \Phi_1}{\partial \eta} \\ \frac{\partial \Phi_2}{\partial \xi} & \frac{\partial \Phi_2}{\partial \eta} \end{bmatrix}$$

which is required for the transformation of functions to and from the canonical domain. For functions $\overline{f} \in C(K)$, $\overline{\boldsymbol{u}} \in D(K)$ and $\overline{g} \in S(K)$ the transformations to the physical domain Ω are given by [51]:

$$f = \overline{f} \circ \Phi^{-1} \quad \Big| \quad \boldsymbol{u} = \frac{\mathbf{J} \circ \Phi^{-1}}{\det\left(\mathbf{J} \circ \Phi^{-1}\right)} \left(\overline{\boldsymbol{u}} \circ \Phi^{-1}\right) \quad \Big| \quad g = \frac{\overline{g} \circ \Phi^{-1}}{\det\left(\mathbf{J} \circ \Phi^{-1}\right)}$$

A relevant application of the transformations above is their use in integration as

$$\iint_\Omega f_1 \; f_2 \, \mathrm{d}\Omega = \iint_K \overline{f}_1 \; \overline{f}_2 \det(\mathbf{J}) \, \mathrm{d}K, \quad f_1, f_2 \in C(K) \tag{3.25}$$

$$\iint_\Omega \boldsymbol{u}_1^{\mathrm{T}} \; \boldsymbol{u}_2 \, \mathrm{d}\Omega = \iint_K \frac{\overline{\boldsymbol{u}}_1^{\mathrm{T}} \; \mathbf{J}^{\mathrm{T}} \; \mathbf{J} \; \overline{\boldsymbol{u}}_2}{\det(\mathbf{J})} \, \mathrm{d}K, \quad \boldsymbol{u}_1, \boldsymbol{u}_2 \in D(K) \tag{3.26}$$

$$\iint_\Omega g_1 \; g_2 \, \mathrm{d}\Omega = \iint_K \frac{\overline{g}_1 \; \overline{g}_2}{\det(\mathbf{J})} \, \mathrm{d}K, \quad g_1, g_2 \in S(K) \tag{3.27}$$

which, among other things, allows the calculation of mass matrices for any domain.

3.5 Incidence Matrices

The sections above have dealt with the interpolation of functions. This next segment, however, focuses on the discretization of differential operators such that problems in the continuous setting can be fully converted to discrete algebraic problems.

3.5.1 Incidence Matrix in $\mathbb{R}^1$

The 1D case is certainly not a very interesting one, however, it constitutes the base to understand the fundamentals on how the differential operators in higher dimensions will be discretized. As a result, this case will be reviewed first.

An important analytical tool to generate such matrices with relative ease comes from a property that connects the nodal and the edge basis functions via the derivative. The latter is further explained and proved in [38, 51]. Consider a function $\alpha^h \in \mathcal{P}$ which is expanded using nodal basis functions. If its derivative $\frac{\mathrm{d}\alpha^h}{\mathrm{d}\xi}$ is sought, then it can be computed as:

$$\frac{\mathrm{d}\alpha^h}{\mathrm{d}\xi} = \frac{\mathrm{d}}{\mathrm{d}\xi}\left[\sum_{i=0}^{N} \alpha_i^h h_i(\xi)\right] = \sum_{i=1}^{N} \left[\alpha_i^h - \alpha_{i-1}^h\right] e_i(\xi) \tag{3.28}$$

Thus, the nodal degrees of freedom are modified by the differential operator such that they become suitable degrees of freedom for the edge functions. With this property defined, the incidence matrix $\mathbb{E}^{1,0}$ is introduced. Its notation indicates that the matrix requires nodal degrees of freedom (dimension $d = 0$) as input and the output is a set of degrees of freedom based on lines (dimension $d = 1$). When this matrix is introduced into (3.28), it will collect all the signs from the nodal degrees of freedom and, as a result, its construction only requires the entries -1, 0 and 1.

To settle the idea, suppose $\alpha^h = \sum_{i=0}^{3} \alpha_i^h \, h_i(\xi)$. Using (3.28) leads to:

$$\frac{\mathrm{d}\alpha^h}{\mathrm{d}\xi} = \left[\alpha_1^h - \alpha_0^h\right] e_1(\xi) + \left[\alpha_2^h - \alpha_1^h\right] e_2(\xi) + \left[\alpha_3^h - \alpha_2^h\right] e_3(\xi) =$$

$$= \Psi^1(\xi) \underbrace{\begin{bmatrix} -1 & 1 & 0 & 0 \\ 0 & -1 & 1 & 0 \\ 0 & 0 & -1 & 1 \end{bmatrix}}_{\mathbb{E}^{1,0}} \mathcal{N}^0(\alpha^h) \tag{3.29}$$

where $\Psi^1(\xi) = [\, e_1(\xi) \; e_2(\xi) \; e_3(\xi) \,]$ and $\mathcal{N}^0(\alpha^h) = [\, \alpha_0^h \;\; \alpha_1^h \;\; \alpha_2^h \;\; \alpha_3^h \,]^{\mathrm{T}}$. The size of $\mathbb{E}^{1,0}$ is given by $N \times (N+1)$ and its sparsity keeps increasing as N increases. For this matrix, unlike the mass matrices, the shape of the mesh is irrelevant since only the connectivity between the degrees of freedom matters. Thus, if the degrees of freedom are labeled in a different way, the placement of the entries will change. For the $\mathbb{R}^1$ problems presented in this thesis, the degrees of freedom, either $\mathcal{N}^0(\cdot)$ or $\mathcal{N}^1(\cdot)$, are always labeled from left to right as it is customary.

3.5.2 Incidence Matrices in $\mathbb{R}^2$

In this section, the differential operators ∇, $\nabla\cdot$ and $\nabla\times$ are constructed. However, similarly to the $\mathbb{R}^1$ case, the distribution of the entries -1, 0, 1 within the incidence matrices depends on the labeling of the degrees of freedom. Therefore, such issue will be addressed first in a canonical element in $\mathbb{R}^2$ by using the labeling of outer and inner oriented variables presented in Figure 3.9.

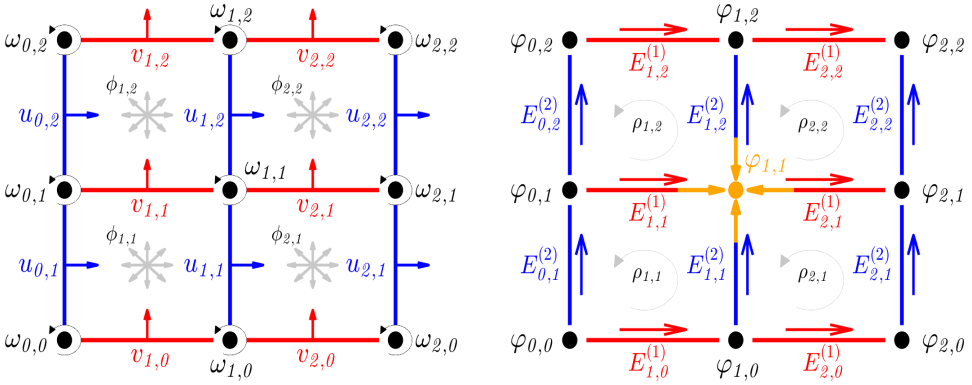

(a) Outer-oriented variables

(b) Inner-oriented variables

Figure 3.9: Outer and inner oriented nodal, edge and surface degrees of freedom.

The arrangement of the nodal degrees of freedom $\mathcal{N}^0(\cdot)$ is:

$$\begin{aligned}\mathcal{N}^0(\omega) &= \begin{bmatrix}\omega_{0,0} & \omega_{0,1} & \omega_{0,2} & \omega_{1,0} & \omega_{1,1} & \omega_{1,2} & \omega_{2,0} & \omega_{2,1} & \omega_{2,2}\end{bmatrix}^{\mathrm{T}} \\ \mathcal{N}^0(\varphi) &= \begin{bmatrix}\varphi_{0,0} & \varphi_{0,1} & \varphi_{0,2} & \varphi_{1,0} & \varphi_{1,1} & \varphi_{1,2} & \varphi_{2,0} & \varphi_{2,1} & \varphi_{2,2}\end{bmatrix}^{\mathrm{T}}\end{aligned} \tag{3.30}$$

Edge degrees of freedom $\mathcal{N}^1(\cdot)$ are written as:

$$\begin{aligned}\mathcal{N}^1(\boldsymbol{u}) &= \begin{bmatrix}u_{0,1} & u_{0,2} & u_{1,1} & u_{1,2} & u_{2,1} & u_{2,2} & v_{1,0} & v_{1,1} & v_{1,2} & v_{2,0} & v_{2,1} & v_{2,2}\end{bmatrix}^{\mathrm{T}} \\ \mathcal{N}^1(\mathbf{E}) &= \begin{bmatrix}\mathrm{E}^{(2)}_{0,1} & \mathrm{E}^{(2)}_{0,2} & \mathrm{E}^{(2)}_{1,1} & \mathrm{E}^{(2)}_{1,2} & \mathrm{E}^{(2)}_{2,1} & \mathrm{E}^{(2)}_{2,2} & \mathrm{E}^{(1)}_{1,0} & \mathrm{E}^{(1)}_{1,1} & \mathrm{E}^{(1)}_{1,2} & \mathrm{E}^{(1)}_{2,0} & \mathrm{E}^{(1)}_{2,1} & \mathrm{E}^{(1)}_{2,2}\end{bmatrix}^{\mathrm{T}}\end{aligned} \tag{3.31}$$

The degrees of freedom $\mathcal{N}^2(\cdot)$ are arranged as:

$$\begin{aligned}\mathcal{N}^2(\phi) &= \begin{bmatrix}\phi_{1,1} & \phi_{1,2} & \phi_{2,1} & \phi_{2,2}\end{bmatrix}^{\mathrm{T}} \\ \mathcal{N}^2(\rho) &= \begin{bmatrix}\rho_{1,1} & \rho_{1,2} & \rho_{2,1} & \rho_{2,2}\end{bmatrix}^{\mathrm{T}}\end{aligned} \tag{3.32}$$

3.5.2.1 Incidence Matrix for Gradient

The gradient acts on scalar functions and results in vector-valued functions. Consider a scalar function $\varphi \in K$ such that $\nabla\varphi = (\frac{\partial\varphi}{\partial\xi},\ \frac{\partial\varphi}{\partial\eta})^{\mathrm{T}}$. Using the expansion $\varphi = \sum_{i=0}^{N}\sum_{j=0}^{N}\varphi_{i,j}\,h_i(\xi)\,h_j(\eta)$ and applying (3.28) leads to the required incidence matrix. In order to visualize it, suppose $N = 2$ such that the individual components of the gradient are defined by,

$$\begin{aligned}
\frac{\partial\varphi}{\partial\eta} &= \sum_{i=0}^{2}\sum_{j=1}^{2}(\varphi_{i,j}-\varphi_{i,j-1})\ h_i(\xi)\,e_j(\eta) = (\varphi_{0,1}-\varphi_{0,0})\,\Psi_1^1(\boldsymbol{\xi}) + (\varphi_{0,2}-\varphi_{0,1})\,\Psi_2^1(\boldsymbol{\xi}) + \\
&+ (\varphi_{1,1}-\varphi_{1,0})\,\Psi_3^1(\boldsymbol{\xi}) + (\varphi_{1,2}-\varphi_{1,1})\,\Psi_4^1(\boldsymbol{\xi}) + (\varphi_{2,1}-\varphi_{2,0})\,\Psi_5^1(\boldsymbol{\xi}) + (\varphi_{2,2}-\varphi_{2,1})\,\Psi_6^1(\boldsymbol{\xi}) \\
\frac{\partial\varphi}{\partial\xi} &= \sum_{i=1}^{2}\sum_{j=0}^{2}(\varphi_{i,j}-\varphi_{i-1,j})\ e_i(\xi)\,h_j(\eta) = (\varphi_{1,0}-\varphi_{0,0})\,\Psi_7^1(\boldsymbol{\xi}) + (\varphi_{1,1}-\varphi_{0,1})\,\Psi_8^1(\boldsymbol{\xi}) + \\
&+ (\varphi_{1,2}-\varphi_{0,2})\,\Psi_9^1(\boldsymbol{\xi}) + (\varphi_{2,0}-\varphi_{1,0})\,\Psi_{10}^1(\boldsymbol{\xi}) + (\varphi_{2,1}-\varphi_{1,1})\,\Psi_{11}^1(\boldsymbol{\xi}) + (\varphi_{2,2}-\varphi_{1,2})\,\Psi_{12}^1(\boldsymbol{\xi})
\end{aligned}$$

From here onwards, the second component of the gradient is written out first as to follow the numbering of $\Psi^1(\boldsymbol{\xi})$ described in Section 3.3.5. By using Figure 3.9 to allocate the degrees of freedom in the correct order, the gradient can be written as,

$$\nabla\varphi = \begin{pmatrix} \frac{\partial\varphi}{\partial\eta} \\ \frac{\partial\varphi}{\partial\xi} \end{pmatrix} = \Psi^1(\boldsymbol{\xi})\ \underbrace{\left[\begin{array}{ccccccccc}
-1 & 1 & 0 & 0 & 0 & 0 & 0 & 0 & 0 \\
0 & -1 & 1 & 0 & 0 & 0 & 0 & 0 & 0 \\
0 & 0 & 0 & -1 & 1 & 0 & 0 & 0 & 0 \\
0 & 0 & 0 & 0 & -1 & 1 & 0 & 0 & 0 \\
0 & 0 & 0 & 0 & 0 & 0 & -1 & 1 & 0 \\
0 & 0 & 0 & 0 & 0 & 0 & 0 & -1 & 1 \\
\hline
-1 & 0 & 0 & 1 & 0 & 0 & 0 & 0 & 0 \\
0 & -1 & 0 & 0 & 1 & 0 & 0 & 0 & 0 \\
0 & 0 & -1 & 0 & 0 & 1 & 0 & 0 & 0 \\
0 & 0 & 0 & -1 & 0 & 0 & 1 & 0 & 0 \\
0 & 0 & 0 & 0 & -1 & 0 & 0 & 1 & 0 \\
0 & 0 & 0 & 0 & 0 & -1 & 0 & 0 & 1
\end{array}\right]}_{\mathbb{E}^{1,0}_{\mathrm{grad}} = \begin{bmatrix} \mathbb{E}^{1,0}_{\eta} \\ \mathbb{E}^{1,0}_{\xi} \end{bmatrix}} \mathcal{N}^0(\varphi) \tag{3.33}$$

Subscripts η and ξ denote that the former is related to $\frac{\partial}{\partial\eta}$, upper half of $\mathbb{E}^{1,0}_{\mathrm{grad}}$, while the latter is associated to $\frac{\partial}{\partial\xi}$, lower half of $\mathbb{E}^{1,0}_{\mathrm{grad}}$. Even when (3.33) leads to a *flipped* gradient $\nabla\varphi = (\varphi_\eta,\ \varphi_\xi)^{\mathrm{T}}$ which should not be an issue as long as the correct basis functions are utilized.

3.5.2.2 Incidence Matrix for Divergence

The divergence acts on vector-valued functions and results in a scalar one. Consider a function $\boldsymbol{u} = (u(\boldsymbol{\xi})\ v(\boldsymbol{\xi}))^{\mathrm{T}} \in K$ such that $\nabla\cdot\boldsymbol{u} = \frac{\partial u}{\partial\xi} + \frac{\partial v}{\partial\eta}$. The ex-

pansions for the individual components are $u = \sum_{i=0}^{N}\sum_{j=1}^{N} u_{i,j}\, h_i(\xi)\, e_j(\eta)$ and $v = \sum_{i=1}^{N}\sum_{j=0}^{N} v_{i,j}\, e_i(\xi)\, h_j(\eta)$. Once again, by implementing (3.28), the individual derivatives are obtained. To fix ideas, the polynomial degree is set to $N = 2$ which leads to the following:

$$\begin{aligned}
\frac{\partial u}{\partial \xi} = \sum_{i=1}^{2}\sum_{j=1}^{2} (u_{i,j} - u_{i-1,j})\; e_i(\xi)\, e_j(\eta) \;&=\; (u_{1,1} - u_{0,1})\, \Psi_1^2(\boldsymbol{\xi}) + (u_{1,2} - u_{0,2})\, \Psi_2^2(\boldsymbol{\xi}) + \\
&\quad + (u_{2,1} - u_{1,1})\, \Psi_3^2(\boldsymbol{\xi}) + (u_{2,2} - u_{1,2})\, \Psi_4^2(\boldsymbol{\xi}) \\
\frac{\partial v}{\partial \eta} = \sum_{i=1}^{2}\sum_{j=1}^{2} (v_{i,j} - v_{i,j-1})\; e_i(\xi)\, e_j(\eta) \;&=\; (v_{1,1} - v_{1,0})\, \Psi_1^2(\boldsymbol{\xi}) + (v_{1,2} - v_{1,1})\, \Psi_2^2(\boldsymbol{\xi}) + \\
&\quad + (v_{2,1} - v_{2,0})\, \Psi_3^2(\boldsymbol{\xi}) + (v_{2,2} - v_{2,1})\, \Psi_4^2(\boldsymbol{\xi})
\end{aligned}$$

The incidence matrix for the divergence is then given by:

$$\nabla \cdot \boldsymbol{u} = \frac{\partial u}{\partial \xi} + \frac{\partial v}{\partial \eta} = \Psi^2(\boldsymbol{\xi}) \underbrace{\left[\begin{array}{cccccc|cccccc} -1 & 0 & 1 & 0 & 0 & 0 & -1 & 1 & 0 & 0 & 0 & 0 \\ 0 & -1 & 0 & 1 & 0 & 0 & 0 & -1 & 1 & 0 & 0 & 0 \\ 0 & 0 & -1 & 0 & 1 & 0 & 0 & 0 & 0 & -1 & 1 & 0 \\ 0 & 0 & 0 & -1 & 0 & 1 & 0 & 0 & 0 & 0 & -1 & 1 \end{array}\right]}_{\mathbb{E}^{2,1}_{\mathrm{div}} = \left[\, \mathbb{E}^{2,1}_{\xi} \;\; \mathbb{E}^{2,1}_{\eta} \,\right]} \mathcal{N}^1(\boldsymbol{u}) \tag{3.34}$$

Similarly to the gradient case, subscripts η and ξ are denote that the former is related to $\frac{\partial}{\partial \eta}$, right half of $\mathbb{E}^{2,1}_{\mathrm{div}}$, while the latter is associated to $\frac{\partial}{\partial \xi}$, left half of $\mathbb{E}^{2,1}_{\mathrm{div}}$.

3.5.2.3 Incidence Matrix for Curl

In this section, the curl applied to scalar and vector fields is examined.

Firstly, a scalar field ω is considered such that $\nabla \times \omega = \left(\frac{\partial \omega}{\partial \eta},\, -\frac{\partial \omega}{\partial \xi}\right)^{\mathrm{T}}$. It is clear the similitude with the discretization of the gradient operator, hence, the incidence matrix for the curl applied to scalars can be immediately written as:

$$\mathbb{E}^{1,0}_{\mathrm{curl}} = \begin{bmatrix} \mathbb{E}^{1,0}_{\eta} \\ -\mathbb{E}^{1,0}_{\xi} \end{bmatrix} \tag{3.35}$$

Secondly, the curl applied to vector fields $\mathbf{E} = \left(\mathrm{E}^{(1)},\, \mathrm{E}^{(2)}\right)^{\mathrm{T}}$ is considered such that the following operation holds $\nabla \times \mathbf{E} = \frac{\partial \mathrm{E}^{(2)}}{\partial \xi} - \frac{\partial \mathrm{E}^{(1)}}{\partial \eta}$. The components, unlike the divergence case, are chosen to be expanded as $\mathrm{E}^{(1)} = \sum_{i=1}^{N}\sum_{j=0}^{N} \mathrm{E}^{(1)}_{i,j}\, e_i(\xi)\, h_j(\eta)$ and $\mathrm{E}^{(2)} = \sum_{i=0}^{N}\sum_{j=1}^{N} \mathrm{E}^{(2)}_{i,j}\, h_i(\xi)\, e_j(\eta)$. For $N = 2$, the following is obtained:

$$\frac{\partial \mathrm{E}^{(2)}}{\partial \xi} = \sum_{i=1}^{2}\sum_{j=1}^{2}\left(\mathrm{E}^{(2)}_{i,j} - \mathrm{E}^{(2)}_{i-1,j}\right) e_i(\xi)\, e_j(\eta) = \left(\mathrm{E}^{(2)}_{1,1} - \mathrm{E}^{(2)}_{0,1}\right)\Psi^2_1(\boldsymbol{\xi}) + \left(\mathrm{E}^{(2)}_{1,2} - \mathrm{E}^{(2)}_{0,2}\right)\Psi^2_2(\boldsymbol{\xi}) + \\ + \left(\mathrm{E}^{(2)}_{2,1} - \mathrm{E}^{(2)}_{1,1}\right)\Psi^2_3(\boldsymbol{\xi}) + \left(\mathrm{E}^{(2)}_{2,2} - \mathrm{E}^{(2)}_{1,2}\right)\Psi^2_4(\boldsymbol{\xi})$$

$$\frac{\partial \mathrm{E}^{(1)}}{\partial \eta} = \sum_{i=1}^{2}\sum_{j=1}^{2}\left(\mathrm{E}^{(1)}_{i,j} - \mathrm{E}^{(1)}_{i,j-1}\right) e_i(\xi)\, e_j(\eta) = \left(\mathrm{E}^{(1)}_{1,1} - \mathrm{E}^{(1)}_{1,0}\right)\Psi^2_1(\boldsymbol{\xi}) + \left(\mathrm{E}^{(1)}_{1,2} - \mathrm{E}^{(1)}_{1,1}\right)\Psi^2_2(\boldsymbol{\xi}) + \\ + \left(\mathrm{E}^{(1)}_{2,1} - \mathrm{E}^{(1)}_{2,0}\right)\Psi^2_3(\boldsymbol{\xi}) + \left(\mathrm{E}^{(1)}_{2,2} - \mathrm{E}^{(1)}_{2,1}\right)\Psi^2_4(\boldsymbol{\xi})$$

The incidence matrix for the curl applied to vectors is given by:

$$\nabla \times \mathbf{E} = \frac{\partial \mathrm{E}^{(2)}}{\partial \xi} + \frac{\partial \mathrm{E}^{(1)}}{\partial \eta} = \Psi^2(\boldsymbol{\xi}) \underbrace{\left[\begin{array}{cccccc|cccccc} -1 & 0 & 1 & 0 & 0 & 0 & 1 & -1 & 0 & 0 & 0 & 0 \\ 0 & -1 & 0 & 1 & 0 & 0 & 0 & 1 & -1 & 0 & 0 & 0 \\ 0 & 0 & -1 & 0 & 1 & 0 & 0 & 0 & 0 & 1 & -1 & 0 \\ 0 & 0 & 0 & -1 & 0 & 1 & 0 & 0 & 0 & 0 & 1 & -1 \end{array}\right]}_{\mathbb{E}^{2,1}_{\mathrm{curl}}} \mathcal{N}^1(\mathbf{E})$$

Comparing the matrix above with the one obtained in (3.34) for the divergence makes it clear that both are quite similar. In fact, the matrix $\mathbb{E}^{2,1}_{\mathrm{curl}}$ can be assembled with the block matrices from the discrete divergence operator as:

$$\mathbb{E}^{2,1}_{\mathrm{curl}} = \left[\begin{array}{cc} \mathbb{E}^{2,1}_{\xi} & -\mathbb{E}^{2,1}_{\eta} \end{array}\right] \tag{3.36}$$

3.5.3 A Geometric Approach Towards Incidence Matrices

So far all the incidence matrices were put together by using (3.28) and then the assembly relied on the signs of the degrees of freedom. However, as specified before, these matrices depend on the connectivity of the variables and, as a result, are independent of the basis functions used. The latter just means that the procedure used in the previous sections is not the only course of action.

An approach relying on the orientations of the degrees of freedom is discussed:

- Consider the gradient which links $\mathcal{N}^0(\cdot)$ to $\mathcal{N}^1(\cdot)$. In Figure 3.9b, nodes are given a default orientation as sinks as illustrated by the central orange node. On the other hand, $\mathrm{E}^{(1)}$ and $\mathrm{E}^{(2)}$ have default orientations from west-to-east and south-to-north, respectively.

  Building $\mathbb{E}^{1,0}_{\mathrm{grad}}$ is done by examining the orientation of each line and of those nodes corresponding to its boundary. For example, for $\mathrm{E}^{(2)}_{0,1}$, the boundary

nodes are $\varphi_{0,0}$ and $\varphi_{0,1}$. The *sink-type* orientation of the former does not agree with the *south-to-north* orientation of $\mathrm{E}^{(2)}_{0,1}$ while the *sink-type* orientation of $\varphi_{0,1}$ does. If the orientations *match*, then a value 1 is assigned, otherwise, -1 is used. Thus, this first equation would simply read:

$$\mathrm{E}^{(2)}_{0,1} = \begin{bmatrix} \text{-1} & 1 & 0 & 0 & 0 & 0 & 0 & 0 & 0 \end{bmatrix} \mathcal{N}^0(\varphi)$$

Doing the same for all the other lines on the mesh following the numbering of $\mathcal{N}^1(\mathbf{E})$ retrieves $\mathbb{E}^{1,0}_{\text{grad}}$ exactly as shown in (3.33).

- Consider the divergence which links $\mathcal{N}^1(\cdot)$ to $\mathcal{N}^2(\cdot)$. In Figure 3.9a, surface degrees of freedom $\mathcal{N}^2(\phi)$ are given default orientations as sources. For $\mathcal{N}^1(\boldsymbol{u})$, $u_{i,j}$ has a default orientation *west-to-east* while for $v_{i,j}$ it is *south-to-north*.

  Building $\mathbb{E}^{2,1}_{\text{div}}$ is done by examining the orientation of each surface and the 4 lines from its boundary. For $\phi_{1,1}$, the boundary lines are $u_{0,1}$, $u_{1,1}$, $v_{1,0}$ and $v_{1,1}$. The *source-type* orientation of $\phi_{1,1}$ agrees with the orientation of both $u_{1,1}$ and $v_{1,1}$ but not with $u_{0,1}$ and $v_{1,0}$. Thus, this relation is written out as:

$$\phi_{1,1} = \begin{bmatrix} \text{-1} & 0 & 1 & 0 & 0 & 0 \end{bmatrix} \begin{bmatrix} \text{-1} & 1 & 0 & 0 & 0 & 0 \end{bmatrix} \mathcal{N}^1(\boldsymbol{u})$$

  Doing the same for all the other surfaces following the numbering of $\mathcal{N}^2(\phi)$ retrieves $\mathbb{E}^{2,1}_{\text{div}}$ exactly as shown in (3.34).

- The curl applied to scalar quantities links $\mathcal{N}^0(\cdot)$ to $\mathcal{N}^1(\cdot)$. In Figure 3.9a, nodes are given a default orientation anti-clockwise while the orientation of lines is the same as the one discussed previously for the divergence operator.

  Building $\mathbb{E}^{1,0}_{\text{curl}}$ is done by examining the orientation of each line and of those nodes corresponding to its boundary. The boundary nodes of $u_{0,1}$ are $\omega_{0,0}$ & $\omega_{0,1}$. The anti-clockwise rotation of the former agrees with the orientation of $u_{0,1}$ while the orientation of the later does not. This first relation reads:

$$u_{0,1} = \begin{bmatrix} \text{-1} & 1 & 0 & 0 & 0 & 0 & 0 & 0 & 0 \end{bmatrix} \mathcal{N}^0(\omega)$$

  Doing the same for all the other lines on the mesh following the numbering of $\mathcal{N}^1(\boldsymbol{u})$ retrieves $\mathbb{E}^{1,0}_{\text{curl}}$ exactly as shown in Equation 3.35.

- The curl applied to vectors links $\mathcal{N}^1(\cdot)$ to $\mathcal{N}^2(\cdot)$. In Figure 3.9b, surfaces are given a default orientation anti-clockwise while lines have the orientation discussed for the gradient operator.

  Building $\mathbb{E}^{2,1}_{\text{curl}}$ is done by examining the orientation of each surface and the 4

lines from its boundary. The boundary lines of $\rho_{1,1}$ are $\mathrm{E}^{(1)}_{1,0}$, $\mathrm{E}^{(1)}_{1,1}$, $\mathrm{E}^{(2)}_{0,1}$ and $\mathrm{E}^{(2)}_{1,1}$. The orientation of the surface agrees with $\mathrm{E}^{(1)}_{1,0}$ and $\mathrm{E}^{(2)}_{1,1}$ but not with $\mathrm{E}^{(1)}_{1,1}$ and $\mathrm{E}^{(2)}_{0,1}$. Thus, the following is obtained:

$$\rho_{1,1} = \left[\begin{array}{cccccc|cccccc} -1 & 0 & 1 & 0 & 0 & 0 & 1 & -1 & 0 & 0 & 0 & 0 \end{array}\right] \mathcal{N}^1(\mathbf{E})$$

Doing the same for all the other surfaces on the mesh following the numbering of $\mathcal{N}^2(\rho)$ retrieves $\mathbb{E}^{2,1}_{\mathrm{curl}}$ exactly as shown in (3.36).

3.6 Domain Partitioning

Back in Section 3.4 it was mentioned that there are instances in which a single spectral element cannot be used. For such cases, a mesh covering the computational domain Ω is split into non-overlapping M subdomains:

$$\Omega = \bigcup_{k=1}^{M} \Omega_k, \quad \Omega_n \cap \Omega_l = \emptyset \quad \text{for} \quad n \neq l$$

where each Ω_k is discretized using a Gauss-Lobatto-Legendre mesh such as the one shown in Figure 3.1 for the 2D case. Even though there is no overlap between elements, such the case is not true for their boundaries $\partial\Omega_k$.

The latter will pose a problem for any degrees of freedom are located at the boundaries since these will be shared between two or, possibly, more elements. To settle the idea, consider a domain $\Omega = [-1,\ 1]^2$ which is split into four subdomains using a GLL-mesh with $N = 1$ as shown in Figure 3.10 where the indices for the degrees of freedom have been reduced to a single index to minimize notation.

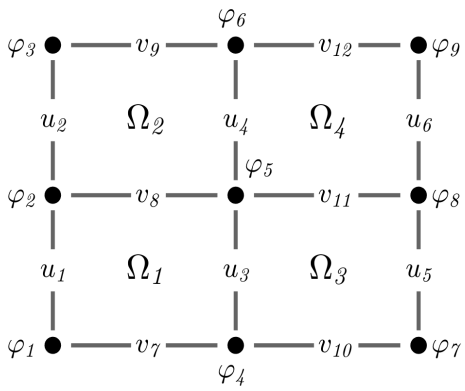

Figure 3.10: Domain $\Omega = [-1,\ 1]^2$, subdomains Ω_k and degrees of freedom $\mathcal{N}^0(\varphi)$ & $\mathcal{N}^1(\boldsymbol{u})$

By following the numbering of the nodal and edge degrees of freedom shown in (3.30) and (3.31), respectively, the degrees of freedom for Ω_k are:

$$\begin{aligned}
\Omega_1 \;&\rightarrow\; \mathcal{N}^0_{\Omega_1}(\varphi) = \begin{pmatrix} \varphi_1 & \varphi_2 & \varphi_4 & \varphi_5 \end{pmatrix}^{\mathrm{T}},\; \mathcal{N}^1_{\Omega_1}(\boldsymbol{u}) = \begin{pmatrix} u_1 & u_3 & v_1 & v_2 \end{pmatrix}^{\mathrm{T}} \\
\Omega_2 \;&\rightarrow\; \mathcal{N}^0_{\Omega_2}(\varphi) = \begin{pmatrix} \varphi_2 & \varphi_3 & \varphi_5 & \varphi_6 \end{pmatrix}^{\mathrm{T}},\; \mathcal{N}^1_{\Omega_2}(\boldsymbol{u}) = \begin{pmatrix} u_2 & u_4 & v_2 & v_3 \end{pmatrix}^{\mathrm{T}} \\
\Omega_3 \;&\rightarrow\; \mathcal{N}^0_{\Omega_3}(\varphi) = \begin{pmatrix} \varphi_4 & \varphi_5 & \varphi_7 & \varphi_8 \end{pmatrix}^{\mathrm{T}},\; \mathcal{N}^1_{\Omega_3}(\boldsymbol{u}) = \begin{pmatrix} u_3 & u_5 & v_4 & v_5 \end{pmatrix}^{\mathrm{T}} \\
\Omega_4 \;&\rightarrow\; \mathcal{N}^0_{\Omega_4}(\varphi) = \begin{pmatrix} \varphi_1 & \varphi_2 & \varphi_4 & \varphi_5 \end{pmatrix}^{\mathrm{T}},\; \mathcal{N}^1_{\Omega_4}(\boldsymbol{u}) = \begin{pmatrix} u_4 & u_6 & v_5 & v_6 \end{pmatrix}^{\mathrm{T}}
\end{aligned}$$

Assume that the equation being solved in Ω_k is discretized such that an algebraic system of the form $A_k\,\underline{x}_k = \underline{\mathrm{F}}_k$ is obtained, then the discretized system for the entirety of Ω would be given by the following matrix structure,

$$\begin{bmatrix} A_1 & 0 & 0 & 0 \\ 0 & A_2 & 0 & 0 \\ 0 & 0 & A_3 & 0 \\ 0 & 0 & 0 & A_4 \end{bmatrix} \begin{bmatrix} \underline{x}_1 \\ \underline{x}_2 \\ \underline{x}_3 \\ \underline{x}_4 \end{bmatrix} = \begin{bmatrix} \underline{\mathrm{F}}_1 \\ \underline{\mathrm{F}}_2 \\ \underline{\mathrm{F}}_3 \\ \underline{\mathrm{F}}_4 \end{bmatrix} \quad \rightarrow \quad A\,\underline{x} = \underline{\mathrm{F}} \tag{3.37}$$

where $\underline{x}_k$ could correspond to any of $\mathcal{N}^d(\cdot)$, $d = \{0, 1, 2\}$. Since all surfaces are non-overlapping, $\mathcal{N}^2_{\Omega_n}(\cdot) \cap \mathcal{N}^2_{\Omega_l}(\cdot) = \emptyset$. However, for $d = \{0, 1\}$, $\mathcal{N}^d_{\Omega_n}(\cdot) \cap \mathcal{N}^d_{\Omega_l}(\cdot) \neq \emptyset$ and some degrees of freedom in $\underline{x}$ are repeated. For a solution to be obtained, the degrees of freedom belonging to $d = \{0, 1\}$ have to somehow get *glued together* which will inevitably have an impact on the shape of matrix A and the vector $\underline{\mathrm{F}}$. This topic is treated in Section 3.6.1 and Section 3.6.2.

3.6.1 Gathering Matrix

This approach reorganizes the structure of the matrices A_k and the vectors F_k using a *map* relating the degrees of freedom in Ω_k to global degrees of freedom in Ω. Such map is called Gathering Matrix (GM) which has the following form:

$$\mathrm{GM}\Big(\#\text{ Element},\ \#\text{ Local Degree of Freedom}\Big) = \text{Global Degree of Freedom}$$

If the definition above is applied to the geometry presented in Figure 3.10, the gathering matrices GM for $\mathcal{N}^0(\varphi)$ and $\mathcal{N}^1(\boldsymbol{u})$ would read,

$$\mathrm{GM}_{\varphi} = \begin{bmatrix} 1 & 2 & 4 & 5 \\ 2 & 3 & 5 & 6 \\ 4 & 5 & 7 & 8 \\ 5 & 6 & 8 & 9 \end{bmatrix} \qquad \mathrm{GM}_{\boldsymbol{u}} = \begin{bmatrix} 1 & 3 & 7 & 8 \\ 2 & 4 & 8 & 9 \\ 3 & 5 & 10 & 11 \\ 4 & 6 & 11 & 12 \end{bmatrix} \tag{3.38}$$

By utilizing this map, A_k and $\underline{\mathrm{F}}_k$ are reshuffled and merged accounting for the connectivity of the degrees of freedom in a process called *assembly*. Such process results in the global matrix and vector A_{GM} and $\underline{\mathrm{F}}_{\mathrm{GM}}$, respectively. A method to derive such matrices is via a sequence of nested *for-loops* as follows,

$A_{\mathrm{GM}} = [\,]$; $\underline{\mathrm{F}}_{\mathrm{GM}} = [\,]$;
for $k = 1$ to Number of Elements
for $i = 1$ to $\dim\left(\mathcal{N}^d_{\Omega_k}(\cdot)\right)$
for $j = 1$ to $\dim\left(\mathcal{N}^d_{\Omega_k}(\cdot)\right)$

$$A_{\mathrm{GM}}\Big(\mathrm{GM}(k,i),\mathrm{GM}(k,j)\Big) = A_{\mathrm{GM}}\Big(\mathrm{GM}(k,i),\mathrm{GM}(k,j)\Big) + A_k\,(i,j)$$

end

$$\underline{\mathrm{F}}_{\mathrm{GM}}\Big(\mathrm{GM}(k,i)\Big) = \underline{\mathrm{F}}_{\mathrm{GM}}\Big(\mathrm{GM}(k,i)\Big) + \underline{\mathrm{F}}_k(i)$$

end
end

where $\dim\left(\mathcal{N}^d_{\Omega_k}(\cdot)\right)$ is the number of degrees of freedom $\mathcal{N}^d(\cdot)$ in each subdomain which remains unchanged since the same degree N is used for all Ω_k. By performing the aforementioned steps, the system from (3.37) becomes $A_{\mathrm{GM}}\,\mathcal{N}^d_{\Omega}(\cdot) = \underline{\mathrm{F}}_{\mathrm{GM}}$ where all the *shared* degrees of freedom have been merged and a solution can now be sought.

3.6.2 Connectivity Matrix

Contrary to the previous section which focused on reorganizing A_k and $\underline{\mathrm{F}}_k$, this approach uses the non-connected matrix A and vector $\underline{\mathrm{F}}$ from (3.37) and enforces continuity between the shared degrees of freedom via a *connectivity matrix*.

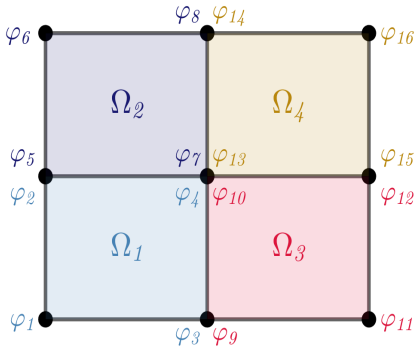

Figure 3.11: Domain $\Omega = [-1,\,1]^2$ from Figure 3.10 with non-connected degrees of freedom $\mathcal{N}^0(\varphi)$.

To illustrate the idea behind this approach, consider the disjointed discretization of the domain from Figure 3.11 where each degree of freedom in all subdomains is accounted for even if it is shared with another element. The degrees of freedom are arranged according to the numbering described in (3.30) such that,

$$\begin{gathered}
\mathcal{N}^0_{\Omega_1}(\varphi) = \begin{pmatrix} \varphi_1 & \varphi_2 & \varphi_3 & \varphi_4 \end{pmatrix}^{\mathrm{T}}, \quad \mathcal{N}^0_{\Omega_3}(\varphi) = \begin{pmatrix} \varphi_9 & \varphi_{10} & \varphi_{11} & \varphi_{12} \end{pmatrix}^{\mathrm{T}} \\
\mathcal{N}^0_{\Omega_2}(\varphi) = \begin{pmatrix} \varphi_5 & \varphi_6 & \varphi_7 & \varphi_8 \end{pmatrix}^{\mathrm{T}}, \quad \mathcal{N}^0_{\Omega_4}(\varphi) = \begin{pmatrix} \varphi_{13} & \varphi_{14} & \varphi_{15} & \varphi_{16} \end{pmatrix}^{\mathrm{T}} \\
\downarrow \\
\mathcal{N}^0(\varphi) = \Big(\mathcal{N}^0_{\Omega_1}(\varphi) \;\; \mathcal{N}^0_{\Omega_2}(\varphi) \;\; \mathcal{N}^0_{\Omega_3}(\varphi) \;\; \mathcal{N}^0_{\Omega_4}(\varphi) \Big)^{\mathrm{T}} \\
\dim\Big(\mathcal{N}^0(\varphi)\Big) = \Big(\#\,\text{Elements}\Big)\Big(N+1\Big)^2
\end{gathered}$$

At this point, a connectivity matrix, $\mathbb{N}$, is utilized to couple the shared degrees of freedom by equating them. This is shown below for the geometry of Figure 3.11:

$$\underbrace{\begin{bmatrix}
0 & -1 & 0 & 0 & 1 & 0 & 0 & 0 & 0 & 0 & 0 & 0 & 0 & 0 & 0 & 0 \\
0 & 0 & 0 & -1 & 0 & 0 & 1 & 0 & 0 & 0 & 0 & 0 & 0 & 0 & 0 & 0 \\
0 & 0 & 0 & 0 & 0 & 0 & 0 & 0 & 0 & -1 & 0 & 0 & 1 & 0 & 0 & 0 \\
0 & 0 & 0 & 0 & 0 & 0 & 0 & 0 & 0 & 0 & 0 & -1 & 0 & 0 & 1 & 0 \\
0 & 0 & -1 & 0 & 0 & 0 & 0 & 0 & 1 & 0 & 0 & 0 & 0 & 0 & 0 & 0 \\
0 & 0 & 0 & -1 & 0 & 0 & 0 & 0 & 0 & 1 & 0 & 0 & 0 & 0 & 0 & 0 \\
0 & 0 & 0 & 0 & 0 & 0 & 0 & -1 & 0 & 0 & 0 & 0 & 0 & 1 & 0 & 0
\end{bmatrix}}_{\mathbb{N}} \mathcal{N}^0(\varphi) = \begin{pmatrix} 0 \\ 0 \\ 0 \\ 0 \\ 0 \\ 0 \\ 0 \end{pmatrix} \tag{3.39}$$

A column of zeros is added to the right-hand side such that the shared degrees of freedom in Ω are forced to be equal. Thus, either $\mathbb{N}$ or -$\mathbb{N}$ could be used as a connectivity matrix and the decision to use either could be deemed as *personal preference*. Geometrically speaking, however, the *correct* matrix to use should obey the orientation being utilized within the grid. In this case, the matrix $\mathbb{N}$ from (3.39) follows the sign convention from Section 3.5 which considers nodes as sources.

Denoting by S the number of degrees of freedom $\mathcal{N}^0(\varphi)$ that must be equated, the size of the connectivity matrix should be given by $S \times \dim(\mathcal{N}^0(\varphi))$. For the present example, $S = 8$, such that the equivalences to enforce are $\varphi_2 = \varphi_5$, $\varphi_3 = \varphi_9$, $\varphi_8 = \varphi_{14}$, $\varphi_{12} = \varphi_{15}$, $\varphi_4 = \varphi_{10}$, $\varphi_7 = \varphi_{13}$, $\varphi_4 = \varphi_7$ and $\varphi_{10} = \varphi_{13}$ where the last four equations belong to the central node in Figure 3.11.

Nonetheless, the size of $\mathbb{N}$ is $7 \times \dim\big(\mathcal{N}^0(\varphi)\big)$. The discrepancy arises from the fact that only 3 out of the 4 equations from the central node can be enforced otherwise erroneous results are obtained. In this case, $\varphi_7 = \varphi_{13}$ is omitted. As an aside note, this issue is present in $\mathbb{R}^2$ only for $\mathcal{N}^0(\varphi)$. In $\mathbb{R}^3$, however, this would occur for $\mathcal{N}^0(\cdot)$ and $\mathcal{N}^1(\cdot)$.

Once the matrix $\mathbb{N}$ is obtained, it can be used to solve the problem as follows:

$$\begin{bmatrix} A & \mathbb{N}^{\mathrm{T}} \\ \mathbb{N} & 0 \end{bmatrix} \begin{pmatrix} \mathcal{N}^0(\varphi) \\ \underline{\lambda} \end{pmatrix} = \begin{pmatrix} \underline{\mathrm{F}} \\ \underline{0} \end{pmatrix} \tag{3.40}$$

where A and $\underline{\mathrm{F}}$ are those in (3.37). It can be noted that by including $\mathbb{N}$, extra equations are added to the global matrix such that the latter is no longer square. This issue is solved by adding $\mathbb{N}^{\mathrm{T}}$ and a set of variables $\underline{\lambda}$ which are called *Lagrange Multipliers*. Using this type of formulations gives rise to the so-called *Hybrid Formulations* which will be explored in Chapter 4.

Even though the matrix $\mathbb{N}$ for $\mathcal{N}^1(\boldsymbol{u})$ is not discussed, its construction follows the same logic as for $\mathcal{N}^0(\varphi)$. The main difference, however, is that the size of $\mathbb{N}$ will indeed coincide with $S \times \dim(\mathcal{N}^1(\boldsymbol{u}))$ where $\dim(\mathcal{N}^1(\boldsymbol{u})) = 2N(\#\,\text{Elements})(N+1)$.

3.7 Weak Forms

The starting point of any *Finite Element* methodology begins by defining the so-called *weak form* from which an algebraic system of equations can then be obtained.

There are 2 main ways to obtain the weak formulation, via a minimisation problem or by using test functions and performing integration by parts. Both of the approaches are described below.

3.7.1 Minimization Problem

To exemplify this approach, consider the following functional [10]:

$$J(q; f) = \frac{1}{2} \int_\Omega |\operatorname{grad} q|^2 \, \mathrm{d}\Omega - \int_\Omega f\, q \, \mathrm{d}\Omega - \int_{\partial\Omega} g\, q \, \mathrm{d}\Gamma$$

where $|\operatorname{grad} q|^2 = \operatorname{grad} q \cdot \operatorname{grad} q$ and $g = \frac{\partial q}{\partial n}$ on $\partial\Omega$. The next step consists on taking small variations on the functional which means evaluating the functional at $J(q + \varepsilon\tilde{q}; f)$ with $\varepsilon << 1$:

$$V = J(q + \varepsilon\tilde{q}; f) = \frac{1}{2} \int_\Omega |\operatorname{grad}(q + \varepsilon\tilde{q})|^2 \, \mathrm{d}\Omega - \int_\Omega f\,(q + \varepsilon\tilde{q}) \, \mathrm{d}\Omega - \int_{\partial\Omega} g\,(q + \varepsilon\tilde{q}) \, \mathrm{d}\Gamma$$

Then, the derivative of the functional is taken with respect to the *small parameter* and set equal to zero so that the weak form is obtained:

$$\left.\frac{\mathrm{d}V}{\mathrm{d}\varepsilon}\right|_{\varepsilon=0} = 0 \rightarrow \boxed{\int_\Omega \operatorname{grad} q \cdot \operatorname{grad} \tilde{q} \, \mathrm{d}\Omega = \int_\Omega f\, \tilde{q} \, \mathrm{d}\Omega + \int_{\partial\Omega} g\, \tilde{q} \, \mathrm{d}\Gamma} \tag{3.41}$$

A natural question would be what kind of equation is associated to the weak form described above. Consider the following:

$$\int_\Omega \nabla\cdot(\tilde{q}\,\nabla q)\,\mathrm{d}\Omega = \int_\Omega \nabla\tilde{q}\cdot\nabla q\,\mathrm{d}\Omega + \int_\Omega \tilde{q}\,\nabla^2 q\,\mathrm{d}\Omega$$

$$\downarrow$$

$$\int_{\partial\Omega} \tilde{q}\,\underbrace{(\nabla q\cdot\boldsymbol{n})}_{g}\,\mathrm{d}\Gamma - \int_\Omega \nabla\tilde{q}\cdot\nabla q\,\mathrm{d}\Omega = \int_\Omega \tilde{q}\,\nabla^2 q\,\mathrm{d}\Omega$$

Inserting the equations above into (3.41) leads to,

$$\int_\Omega f\,\tilde{q}\,\mathrm{d}\Omega + \int_\Omega \tilde{q}\,\nabla^2 q\,\mathrm{d}\Omega = 0 \;\rightarrow\; \int_\Omega \tilde{q}\,\left(f+\nabla^2 q\right)\mathrm{d}\Omega = 0 \;\therefore\; \nabla^2 q = -f$$

and the functional from above satisfies a Poisson equation with Neumann boundary conditions. There are many situations, however, in which the problem has no relation whatsoever to optimization [7]. A typical example is the convection-diffusion-reaction problem given by,

$$-\varepsilon\nabla^2\phi + \mathbf{b}\cdot\nabla\phi + c\phi = f \quad \text{in} \quad \Omega \quad \text{and} \quad \phi = 0 \quad \text{on} \quad \partial\Omega$$

for which Galerkin principles should be used as described in the next section.

3.7.2 Test Functions

For this approach, the *strong form* of the equation is required. The same problem from the previous section is used as an example, that is, the Poisson problem with $\frac{\partial q}{\partial n} = g$ at $\partial\Omega$. The first step consists on multiplying the *strong form* by a test function and performing integration by parts on the term with the highest derivative:

$$\int_\Omega \tilde{q}\,\nabla^2 q\,\mathrm{d}\Omega = -\int_\Omega \tilde{q}\,f\,\mathrm{d}\Omega \;\rightarrow\; \int_{\partial\Omega}\tilde{q}\,(\nabla q\cdot\boldsymbol{n})\,\mathrm{d}\Gamma - \int_\Omega \nabla\tilde{q}\cdot\nabla q\,\mathrm{d}\Omega = -\int_\Omega \tilde{q}\,f\,\mathrm{d}\Omega$$

By reorganizing the terms becomes, the final result is obtained,

$$\boxed{\int_\Omega \nabla\tilde{q}\cdot\nabla q\,\mathrm{d}\Omega = \int_\Omega \tilde{q}\,f\,\mathrm{d}\Omega + \int_{\partial\Omega}\tilde{q}\,\underbrace{(\nabla q\cdot\boldsymbol{n})}_{g}\,\mathrm{d}\Gamma} \tag{3.42}$$

and it can be noticed that both 3.41 and 3.42 are identical. Even if the minimization problem arising from the functional J is unknown, it is clear now that Galerkin principles retrieve the *optimality* system [7].

Even though this methodology might look simpler than working with the functional J, there is some arbitrariness to it as shown in [34, p. 4-7] where the Dirichlet problem is given 3 different formulations. The first formulation is related to the one already shown, while the second and third are obtained by splitting the problem into two first order systems leading to *mixed formulations*. The key difference in the last two resides, however, on whether or not integration by parts is used.

For the problems described in the remainder of this thesis, this last approach will be utilized and, when possible, the associated functional will be annexed.

3.8 Error Computation

Numerical solutions can be compared qualitatively to the analytical results by creating, for example, contour plots. Nevertheless, a quantitative approach based on measuring the error with a set of specified *norms* allows to verify the effect of mesh or polynomial refinement such that the convergence of the method can be determined. The required tools to measure the error are explored in the succeeding sections.

3.8.1 Function Spaces

Function spaces dictate the properties a function possesses and also determine the norm to utilize when *measuring* the error of the numerical solution relative to the exact solution (or a highly precise approximation to the real solution). As a common practice, when considering any problem, the function space onto which the solution belongs is specified prior to solving the problem.

A function space is accompanied by the domain on which it is acting. Thus, the notation Ω is used to refer to the computational domain while $\partial\Omega$ refers to its boundary which will be assumed to be Lipschitz continuous. Firstly, the most general function space is considered, the space of *square integrable functions* [10],

$$L^2(\Omega) := \left\{ v \;\middle|\; \int_\Omega |\, v \,|^2 \, \mathrm{d}\Omega \;=\; ||\, v \,||^2_{L^2(\Omega)} \;<\; \infty \right\}, \tag{3.43}$$

which makes it possible to define to the following spaces:

$$H^1(\Omega) := \left\{ v \in L^2(\Omega) \;\middle|\; \nabla v \in L^2(\Omega)^n \right\}, \tag{3.44a}$$

$$H(\mathrm{div};\Omega) := \left\{ \boldsymbol{v} \in L^2(\Omega)^n \;\middle|\; \nabla \cdot \boldsymbol{v} \in L^2(\Omega)^n \right\}, \tag{3.44b}$$

$$H(\mathrm{curl};\Omega) := \left\{ \boldsymbol{v} \in L^2(\Omega)^n \;\middle|\; \nabla \times \boldsymbol{v} \in L^2(\Omega)^d \right\}. \tag{3.44c}$$

where, for the curl space, $d = 1$ in $\mathbb{R}^2$ and $d = 3$ in $\mathbb{R}^2$ [10]. Functions in $H(\mathrm{div};\Omega)$ and $H(\mathrm{curl};\Omega)$ admit traces of the normal and tangential component, respectively, on $\partial\Omega$ which allows to define the following subspaces:

$$H_0^1(\Omega) := \left\{ v \;\middle|\; v \in H^1(\Omega),\ v|_{\partial\Omega} = 0 \right\}, \tag{3.45a}$$

$$H_0(\mathrm{div};\Omega) := \left\{ \boldsymbol{v} \;\middle|\; \boldsymbol{v} \in H(\mathrm{div};\Omega),\ \boldsymbol{v}\cdot\mathbf{n} = 0 \text{ on } \partial\Omega \right\}, \tag{3.45b}$$

$$H_0(\mathrm{curl};\Omega) := \left\{ \boldsymbol{v} \;\middle|\; \boldsymbol{v} \in H(\mathrm{div};\Omega),\ \boldsymbol{v}\times\mathbf{n} = 0 \text{ on } \partial\Omega \right\}. \tag{3.45c}$$

3.8.2 Norms

Firstly, the $L^2(\Omega)$ norm for scalar functions $\phi(\boldsymbol{x})$ is defined and then used as a starting point for vector-valued functions $\boldsymbol{u}(\boldsymbol{x}) = [u(\boldsymbol{x})\ v(\boldsymbol{x})]^{\mathrm{T}}$ as follows,

$$||\,\boldsymbol{\epsilon}_\phi\,||^2_{L^2(\Omega)} = \int_\Omega \left(\phi^{ex}(\boldsymbol{x}) - \phi^h(\boldsymbol{x})\right)^2 \mathrm{d}\Omega \tag{3.46a}$$

$$||\,\boldsymbol{\epsilon}_{\boldsymbol{u}}\,||^2_{L^2(\Omega)} = ||\,\boldsymbol{\epsilon}_u\,||^2_{L^2(\Omega)} + ||\,\boldsymbol{\epsilon}_v\,||^2_{L^2(\Omega)} \tag{3.46b}$$

where the $L^2(\Omega)$ norm form a vector-valued function in $\mathbb{R}^3$ would simply include the additional component. Finally, the norms for the spaces $H_0^1(\Omega)$, $H_0(\mathrm{div};\Omega)$ and $H_0(\mathrm{curl};\Omega)$ are given by,

$$||\,\boldsymbol{\epsilon}_\phi\,||^2_{H^1(\Omega)} = ||\,\boldsymbol{\epsilon}_\phi\,||^2_{L^2(\Omega)} + ||\,\boldsymbol{\epsilon}\,\nabla\phi\,||^2_{L^2(\Omega)} \tag{3.47a}$$

$$||\,\boldsymbol{\epsilon}_{\boldsymbol{u}}\,||^2_{H(\mathrm{div};\Omega)} = ||\,\boldsymbol{\epsilon}_{\boldsymbol{u}}\,||^2_{L^2(\Omega)} + \ell^2\,||\,\boldsymbol{\epsilon}_{\mathrm{div}\,\boldsymbol{u}}\,||^2_{L^2(\Omega)} \tag{3.47b}$$

$$||\,\boldsymbol{\epsilon}_{\boldsymbol{u}}\,||^2_{H(\mathrm{curl};\Omega)} = ||\,\boldsymbol{\epsilon}_{\boldsymbol{u}}\,||^2_{L^2(\Omega)} + \ell^2\,||\,\boldsymbol{\epsilon}_{\mathrm{curl}\,\boldsymbol{u}}\,||^2_{L^2(\Omega)} \tag{3.47c}$$

where the term ℓ^2 denotes a characteristic length which could be, for example, the diameter of Ω and its purpose is to avoid adding up objects of different physical dimensions [10]. In this thesis, $\ell^2 = 1$ will be used as to follow what is popularly utilized in most literature even if physical dimensions are still present in the problem.

Finally, it is worth mentioning that in two dimensions, the space $H(\mathrm{curl};\Omega)$ is isomorphic to $H(\mathrm{div};\Omega)$, [10], such that the following statements

$$\mathrm{curl}\,\boldsymbol{u} = -\mathrm{div}\left(\boldsymbol{u}^\perp\right) \quad \text{and} \quad \mathrm{curl}\,\phi = -\left(\mathrm{grad}\,\phi\right)^\perp$$

are true. The latter supports the fact that $\mathbb{E}^{2,1}_{\mathrm{curl}}$ and $\mathbb{E}^{1,0}_{\mathrm{curl}}$ can be constructed using the block matrices from the divergence and the gradient, respectively.

3.8.3 Convergence

Once the function space and its associated norm are specified, the influence of either the mesh or the polynomial refinement can be determined quantitatively by considering that the error behaves as

$$\boldsymbol{\epsilon} = Ch^k$$

where C is a positive constant, h is a measure of the mesh spacing and k is the so-called *order of convergence* which may be affected by a number of factors such as boundary conditions, mesh quality or singularities.

When using multi-element approaches, the measure of h when computing the error will be given by the average of all the lengths of the elements which will be useful if, for any reason, non-uniform meshes are used.

For refinements of the polynomial order, plots with a linear scale for N and a logarithmic scale for $\boldsymbol{\epsilon}$ will be used where a straight line is expected showing exponential convergence. Showcasing mesh refinements requires logarithmic scales for the error and the mesh spacing will be used and optimal convergence will be achieved whenever the slope of the plot matches the value of the polynomial degree.

4

Introductory Application of Mimetic Discretization

In the following sections, the concepts described throughout Chapter 3 are applied to a series of problems to showcase how the mimetic spectral element method works and the results it produces. In Section 4.1 & Section 4.2, problems in $\mathbb{R}^1$ are examined while in Section 4.3 equations in $\mathbb{R}^2$ are considered for simple geometries.

4.1 The Poisson Problem in $\mathbb{R}^1$

The problem discussed in this section is given by:

$$\frac{\mathrm{d}^2\phi}{\mathrm{d}x^2} = -f(x) \quad \text{in } I \tag{4.1}$$

where either Dirichlet or Neumann boundary conditions are imposed at ∂I. Depending on the choice, either a *Direct Method* or a *Mixed Formulation* will be more suitable for solving the problem.

4.1.1 Direct Method

This approach is showcased by solving the Poisson problem supplemented with $\frac{\mathrm{d}\phi}{\mathrm{d}x} = g$ at ∂I. The weak formulation for the $\mathbb{R}^1$ case is quite similar as the one shown

in Section 3.7 where the gradient operators are switched to the regular derivative,

$$\begin{aligned} \tilde{\phi}\, g|_{\partial I} - \int_I \tilde{\phi}'\phi' \,\mathrm{d}I &= -\int_I \tilde{\phi}\, f \,\mathrm{d}I \\ &\downarrow \\ \left(\tilde{\phi}', \phi'\right)_I &= \left(\tilde{\phi}, f\right)_I + \mathbb{B}, \quad \forall\, \tilde{\phi} \in H^1(I) \end{aligned} \tag{4.2}$$

where the notation $(\cdot\,,\cdot)_\Omega$ denotes a regular integral over the domain Ω and $\mathbb{B}$ represents the boundary contribution. Due to the boundary conditions, the solution is defined up to a constant. Additionally, the forcing function needs to meet the *compatibility condition* $\int_I f \,\mathrm{d}I = -(g_R - g_L)$ which can be concluded by setting $\tilde{\phi} = 1$ in the formulation above.

For simplicity, the contribution $\mathbb{B}$ is dropped. Both ϕ and $\tilde{\phi}$ are expanded using the basis $\Psi^0(x)$ and, by property (3.28), their derivatives can be written using the basis $\Psi^1(x)$ and the incidence matrix $\mathbb{E}^{1,0}$ from (3.29) leading to the following:

$$\begin{aligned} \left(\frac{\mathrm{d}\tilde{\phi}}{\mathrm{d}x}, \frac{\mathrm{d}\phi}{\mathrm{d}x}\right)_I \quad \rightarrow \quad & \int_I \Psi^1(x)\, \mathbb{E}^{1,0}\, \mathcal{N}^0\left(\tilde{\phi}^h\right)\, \Psi^1(x)\, \mathbb{E}^{1,0}\, \mathcal{N}^0(\phi^h)\,\mathrm{d}I = \\ & = \mathcal{N}^0\left(\tilde{\phi}^h\right)^{\mathrm{T}} \left(\mathbb{E}^{1,0}\right)^{\mathrm{T}} \Bigg[\underbrace{\int_I \Psi^1(x)^{\mathrm{T}}\, \Psi^1(x)\,\mathrm{d}I}_{\mathbb{M}^{(1)}}\Bigg] \mathbb{E}^{1,0} \mathcal{N}\left(\phi^h\right) \\ & = \mathcal{N}^0\left(\tilde{\phi}^h\right)^{\mathrm{T}} \left(\mathbb{E}^{1,0}\right)^{\mathrm{T}}\, \mathbb{M}^{(1)}\, \mathbb{E}^{1,0} \mathcal{N}\left(\phi^h\right) \\ \left(\tilde{\phi}^h, f\right)_I \quad \rightarrow \quad & \int_I \Psi^0(x) \mathcal{N}^0\left(\tilde{\phi}^h\right)\, f \,\mathrm{d}I = \mathcal{N}^0\left(\tilde{\phi}^h\right)^{\mathrm{T}} \int_I \Psi^0(x)^{\mathrm{T}}\, f \,\mathrm{d}I \end{aligned}$$

The degrees of freedom $\mathcal{N}^0\left(\tilde{\phi}^h\right)$ are eliminated by realizing that the system should hold for all $\tilde{\phi}$ which leads to the algebraic system to solve:

$$\left(\mathbb{E}^{1,0}\right)^{\mathrm{T}}\, \mathbb{M}^{(1)}\, \mathbb{E}^{1,0} \mathcal{N}\left(\phi^h\right) = \underline{\mathrm{F}} \quad \text{with} \quad \mathrm{F}_i = \int_I \Psi_i^0(x)\, f \,\mathrm{d}I \tag{4.3}$$

which allows to solve for $\mathcal{N}\left(\phi^h\right)$. At this point, however, the solution is still defined up to a constant and, hence, not unique. This can be solved easily by imposing an extra condition such as $\int_I \phi^h \,\mathrm{d}I = 0$ or by imposing a *pseudo Dirichlet condition* $\phi(x_0) = a$ with $x_0 \in I$. Along this thesis, the latter approach will be used since it will be slightly easier to compare the numerical solutions to the analytical ones.

If a multi-element approach were to be used such that K elements span the

domain I, then the system would be written as:

$$\begin{bmatrix} A_{I_1} & 0 & 0 & 0 \\ 0 & A_{I_2} & 0 & 0 \\ 0 & 0 & \ddots & 0 \\ 0 & 0 & 0 & A_{I_K} \end{bmatrix} \begin{pmatrix} \mathcal{N}_{I_1}\left(\phi^h\right) \\ \mathcal{N}_{I_2}\left(\phi^h\right) \\ \vdots \\ \mathcal{N}_{I_K}\left(\phi^h\right) \end{pmatrix} = \begin{pmatrix} \underline{\mathrm{F}}_{I_1} \\ \underline{\mathrm{F}}_{I_2} \\ \vdots \\ \underline{\mathrm{F}}_{I_K} \end{pmatrix}$$

where $A_{I_k} = \left(\mathbb{E}^{1,0}\right)^{\mathrm{T}} \mathbb{M}^{(1)}_{I_k} \mathbb{E}^{1,0}$ and $\mathrm{F}_{I_k} = \int_{I_k} \Psi^0_{I_k}(x)^{\mathrm{T}} f \, \mathrm{d}I_k$. The subindices I_k indicate that they must be computed according to the new domain following what was explained in Section 3.4. Additionally, the system would have to be *glued* by either using a *Gathering Matrix* or a *Connectivity Matrix* as depicted in Section 3.6.

Regardless of the choice, once the degrees of freedom are known, the continuous solution is reconstructed by $\phi^h = \Psi^0(x)\mathcal{N}\left(\phi^h\right)$ and, if for some reason its derivative is required, then it can be computed as $\frac{\mathrm{d}\phi^h}{\mathrm{d}x} = \Psi^1(x)\mathbb{E}^{1,0}\mathcal{N}\left(\phi^h\right)$.

4.1.2 Mixed Formulation

This formulation can easily incorporate Dirichlet conditions since they appear naturally through the process of obtaining the weak form. The process starts by splitting the original *strong form* equation into a system of coupled first order equations as:

$$u = \frac{\mathrm{d}\phi}{\mathrm{d}x} \quad \& \quad \frac{\mathrm{d}u}{\mathrm{d}x} = \text{-}f$$

After multiplying each equation in the system with an appropriate test function and integrating by parts the term containing $\frac{\mathrm{d}\phi}{\mathrm{d}x}$ on the first equation, the formulation becomes,

$$(p,u)_I = (p,\phi')_I \;\rightarrow\; (p,u)_I = \langle p,\, \phi\rangle_{\partial I} - (p',\phi)_I \qquad \forall\, p \in H^1_0(I) \tag{4.4a}$$

$$(q,u')_I = (q,\text{-}f)_I \qquad \forall\, q \in L^2(I) \tag{4.4b}$$

where the boundary term will be replaced by $\mathbb{B}$. The weak form for the case $\phi\,|_{\partial\Omega} = 0$ can be also obtained by using the functional,

$$J(v,q;f) = \frac{1}{2}\int_I v^2 \, \mathrm{d}I + \int_I f\, q \, \mathrm{d}I - \int_I q\, \frac{\mathrm{d}v}{\mathrm{d}x} \, \mathrm{d}I,$$

and taking variations with respect to both v and q to obtain $V_1 = J(v+\varepsilon_1\tilde{v},q;f)$ and $V_2 = J(v,q+\varepsilon_2\tilde{q};f)$. The last step would correspond to compute $\frac{\mathrm{d}V_1}{\mathrm{d}\varepsilon_1} = 0$ and $\frac{\mathrm{d}V_2}{\mathrm{d}\varepsilon_2} = 0$ which will retrieve the optimality system as discussed in Section 3.7.

At this point, it is clear that this approach is based on two main unknowns. Mixed formulations might be preferred in cases in which the dual variable is of as much interest as the primary variable. Consider, for example, the stress in elasticity or a flux in thermo-diffusion problems [4] where the heat flux is often more important than the temperature [10]. If a direct approach were to be utilized, the secondary variable would have to be computed by subsequent differentiation leading to a possible loss of accuracy.

4.1.2.1 Primal - Primal Formulation

The primal-primal algebraic system is obtained by expanding u and p with nodal basis functions while for ϕ and q edge basis functions are used. The remaining terms from the weak formulation (4.4b) become:

$$
\begin{aligned}
(p,u)_\Omega \quad &\rightarrow \quad \mathcal{N}^0\left(p^h\right)^{\mathrm{T}}\left[\int_I \Psi^0(x)^{\mathrm{T}}\,\Psi^0(x)\,\mathrm{d}I\right]\mathcal{N}\left(\phi^h\right) = \\
&\qquad = \mathcal{N}^0\left(p^h\right)^{\mathrm{T}}\,\mathbb{M}^{(0)}\,\mathcal{N}\left(\phi^h\right) \\
(p',\phi)_\Omega \quad &\rightarrow \quad \mathcal{N}^0\left(p^h\right)^{\mathrm{T}}\left(\mathbb{E}^{1,0}\right)^{\mathrm{T}}\left[\int_I \Psi^1(x)^{\mathrm{T}}\,\Psi^1(x)\,\mathrm{d}I\right]\mathcal{N}^0\left(\phi^h\right) = \\
&\qquad = \mathcal{N}^0\left(p^h\right)^{\mathrm{T}}\left(\mathbb{E}^{1,0}\right)^{\mathrm{T}}\,\mathbb{M}^{(1)}\,\mathcal{N}\left(\phi^h\right) \\
(q,u')_\Omega \quad &\rightarrow \quad \mathcal{N}^0\left(q^h\right)^{\mathrm{T}}\left[\int_I \Psi^1(x)^{\mathrm{T}}\,\Psi^1(x)\,\mathrm{d}I\right]\mathbb{E}^{1,0}\,\mathcal{N}^0\left(\phi^h\right) = \\
&\qquad = \mathcal{N}^0\left(q^h\right)^{\mathrm{T}}\,\mathbb{M}^{(1)}\,\mathbb{E}^{1,0}\,\mathcal{N}^0\left(u^h\right) \\
(q,\text{-}f)_\Omega \quad &\rightarrow \quad \text{-}\mathcal{N}^0\left(q^h\right)^{\mathrm{T}}\int_I \Psi^0(x)^{\mathrm{T}}\,f\,\mathrm{d}I
\end{aligned}
$$

A system for the unknowns can be assembled as:

$$
\begin{bmatrix} \mathbb{M}^{(0)} & \left(\mathbb{E}^{1,0}\right)^{\mathrm{T}}\,\mathbb{M}^{(1)} \\ \mathbb{M}^{(1)}\,\mathbb{E}^{1,0} & 0 \end{bmatrix}\begin{pmatrix} \mathcal{N}^0(u^h) \\ \mathcal{N}^1(\phi^h) \end{pmatrix} = \begin{pmatrix} 0 \\ \underline{\mathrm{F}} \end{pmatrix} \tag{4.6}
$$

with $\mathrm{F}_i = \text{-}\int_I \Psi^1_i(x)\,f\,\mathrm{d}I$. If K elements span the mesh, consider the system:

$$
\begin{bmatrix} \tilde{A} & \tilde{B}^T \\ \tilde{B} & 0 \end{bmatrix}\begin{pmatrix} \mathcal{N}^0(u^h) \\ \mathcal{N}^1(\phi^h) \end{pmatrix} = \begin{pmatrix} \mathbb{B} \\ \underline{\mathrm{F}} \end{pmatrix}
$$

where $\tilde{A} = \mathrm{diag}\left(\mathbb{M}^{(0)}_1, \cdots, \mathbb{M}^{(0)}_K\right)$, $\tilde{B} = \mathrm{diag}\left(\mathbb{M}^{(1)}_1\,\mathbb{E}^{1,0}, \cdots \mathbb{M}^{(1)}_K\,\mathbb{E}^{1,0}\right)$ while the last term is $\tilde{B}^{\mathrm{T}} = \mathrm{diag}\left(\left(\tilde{B}_1\right)^{\mathrm{T}}, \cdots, \left(\tilde{B}_K\right)^{\mathrm{T}}\right)$. If the system is *glued* using a *Gath-*

ering Matrix, the process follows the algorithm shown in Section 3.6.1. However, if a *Connectivity Matrix* is utilized, then the so-called *Lagrange Multipliers*, λ, are incorporated into the system as,

$$\begin{bmatrix} \tilde{A} & \tilde{B}^T & \mathbb{N}^{\mathrm{T}} \\ \tilde{B} & 0 & 0 \\ \mathbb{N} & 0 & 0 \end{bmatrix} \begin{pmatrix} \mathcal{N}^0(u^h) \\ \mathcal{N}^1(\phi^h) \\ \lambda \end{pmatrix} = \begin{pmatrix} \mathbb{B} \\ \underline{\mathrm{F}} \\ 0 \end{pmatrix}$$

and the opportunity to use the so-called *static condensation* arises such that the system decouples. The technicalities of this procedure are shown in Appendix A.

4.1.2.2 Primal - Dual Formulation

The primal-dual formulation can be deduced from the primal-primal system from (4.6) by following 3 main steps:

- Firstly, the forcing function $f(x)$ is interpolated using edge functions such that $f(x) = \Psi^1(x)\mathcal{N}^1(f^h)$ where the degrees of freedom are calculated according to (3.4b). Hence, the term $\underline{\mathrm{F}}$ becomes: $-\mathbb{M}^{(1)}\mathcal{N}^{(1)}(f^h)$.
- Next, the second row is multiplied by $\widetilde{\mathbb{M}}^{(0)} = \left(\mathbb{M}^{(1)}\right)^{-1}$.
- Finally, following the theory from Section 3.3.3, the dual degrees of freedom $\widetilde{\mathcal{N}}^0(\phi^h) = \mathbb{M}^{(1)}\,\mathcal{N}^1(\phi^h)$ are used instead of $\mathcal{N}^1(\phi^h)$.

This 3-step process exploits the fact that $\widetilde{\mathbb{M}}^{(0)}\,\mathbb{M}^{(1)} = \mathbb{I}$ leading to the system,

$$\begin{bmatrix} \mathbb{M}^{(0)} & \left(\mathbb{E}^{1,0}\right)^{\mathrm{T}} \\ \mathbb{E}^{1,0} & 0 \end{bmatrix} \begin{pmatrix} \mathcal{N}^0(u^h) \\ \widetilde{\mathcal{N}}^0(\phi^h) \end{pmatrix} = \begin{pmatrix} \mathbb{B} \\ -\mathcal{N}^1(f^h) \end{pmatrix} \tag{4.7}$$

which is much sparser than the one shown in (4.6). Additionally, the use of dual polynomials can also be thought as a type of inverse type mixed preconditioning [51] which alleviates the increment of the condition number of the left-hand side matrix caused by increasing the polynomial degree N.

Once the system is solved, the functions are reconstructed as $u^h = \Psi^0(x)\,\mathcal{N}^0(u^h)$ and $\phi^h = \widetilde{\Psi}^0(x)\widetilde{\mathcal{N}}^0(\phi^h)$. If, as stated before, the secondary variable u is of more importance than the primary variable, then the inverse mass matrices required for the basis will not have to be computed, otherwise, they are mandatory.

As a final note, the multi-element approach follows the same logic as shown for the Primal-Primal formulation. The *Gathering Matrix* and *Connectivity Matrix* used for element *gluing* are the same as before. Special care must be taken when reconstructing ϕ^h when the mesh has non-uniform elements since the basis $\widetilde{\Psi}^{(0)}(x)$ will vary from element to element.

4.1.3 Dirichlet Problem

This approach is tested with a forcing function $f(x) = \pi^2 \sin(\pi x)$ on $I = [-2, 1]$ such that $\phi^{ex} = \sin(\pi x)$ and the convergence of the method is investigated. By using a mixed formulation with 2 spectral elements and a polynomial degree $N = 6$ in each of them, the solution for $\phi(x)$, Figure 4.1, and $u(x)$, Figure 4.2, are obtained.

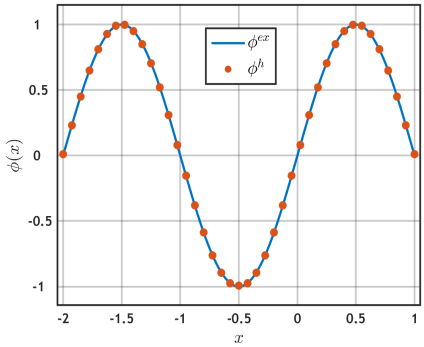

Figure 4.1: Primary Variable $\phi^{ex}(x)$ and its approximation $\phi^h = \Psi^1(x)\mathcal{N}^1(\phi^h)$ for the Homogeneous Dirichlet Poisson problem. Obtained using $N = 6$ and $K = 2$.

The functions ϕ^h, u^h and $\frac{\mathrm{d}u^h}{\mathrm{d}x}$ are interpolated with their correspondent basis. To keep a clean layout, the numerical solutions are plotted by a collection of points instead of lines to avoid an overlap with the exact solutions.

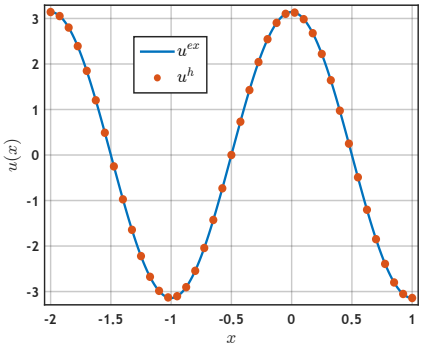

(a) $u^h = \Psi^0(x)\mathcal{N}^0(\phi^h)$

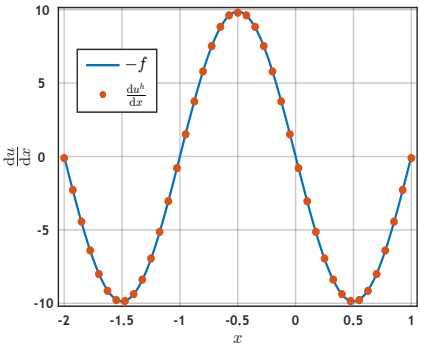

(b) $\frac{\mathrm{d}u^h}{\mathrm{d}x} = \Psi^1(x)\,\mathbb{E}^{1,0}\mathcal{N}^0(u^h)$

Figure 4.2: Secondary variable $u(x)$ from the Poisson problem using $\phi|_{\partial I} = 0$, $N = 6$ and $K = 2$.

A variety of multi-element approaches can be utilized and, when implemented, they lead to the same values for the degrees of freedom. The sparsity patterns for the primal-primal formulations are shown in Figure 4.3 where the ◤ blocks for the connectivity matrix approach are the blocks for a one element formulation as shown in (4.6). For primal-dual formulations, the patterns are shown in Figure 4.4.

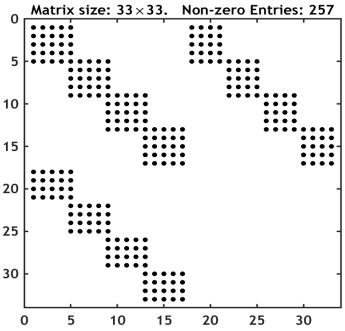

(a) Gathering Matrix

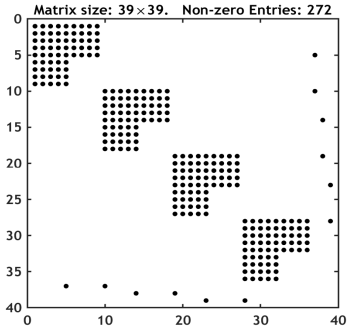

(b) Connectivity Matrix $\mathbb{N}$

Figure 4.3: Sparsity patterns for Primal-Primal Formulation. $N = 4$ and $K = 4$.

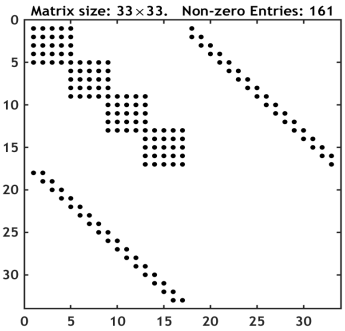

(a) Gathering Matrix

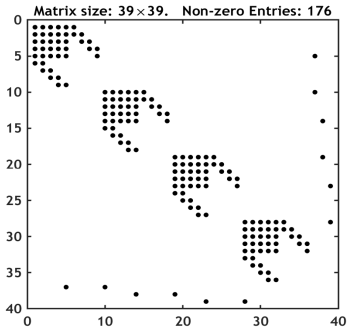

(b) Connectivity Matrix $\mathbb{N}$

Figure 4.4: Sparsity patterns for Primal-Dual Formulation. $N = 4$ and $K = 4$.

Since $\phi \in L^2(I)$ and $u \in H^1(I)$, the norms to use are $||\epsilon_\phi||_{L^2(I)}$ and $||\epsilon_u||_{H^1(I)}$, respectively. The convergence trends for both are shown in Figure 4.5 and Figure 4.6.

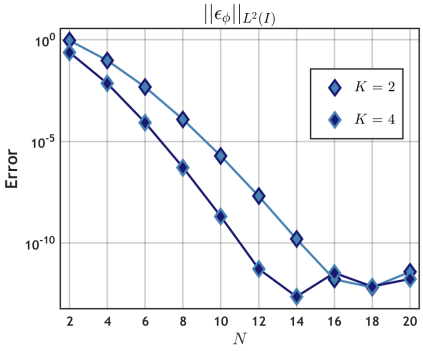

(a) p-convergence

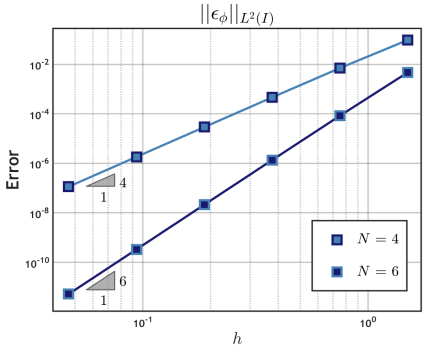

(b) h-convergence

Figure 4.5: Convergence trends for ϕ^h in the Homogeneous Dirichlet Poisson Problem.

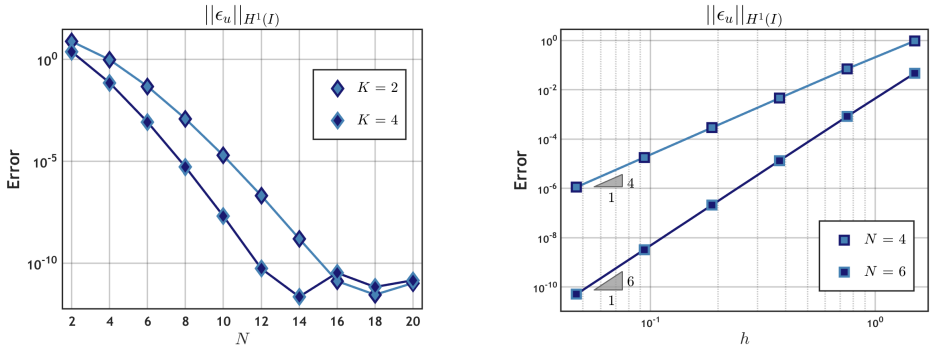

(a) p-convergence (b) h-convergence

Figure 4.6: Convergence trends for u^h in the Homogeneous Dirichlet Poisson Problem.

In the error trends above, for p-convergence, a logarithmic scale for the error is utilized and the variation of N depicts exponential convergence. For mesh refinement, however, log-log plots are implemented where $h = \frac{1}{K}$ (uniform mesh). In this case, the slopes of the lines coincide with the degree N utilized.

4.1.4 Neumann Problem

This approach is tested with a forcing function $f(x) = \pi^2 \cos(\pi x)$ on $I = [-1, 2]$ such that $\phi^{ex} = \cos(\pi x)$ and the convergence of the method is investigated. By using a direct method and 2 spectral elements with a polynomial degree $N = 6$ in each of them, the results of Figure 4.7 are obtained.

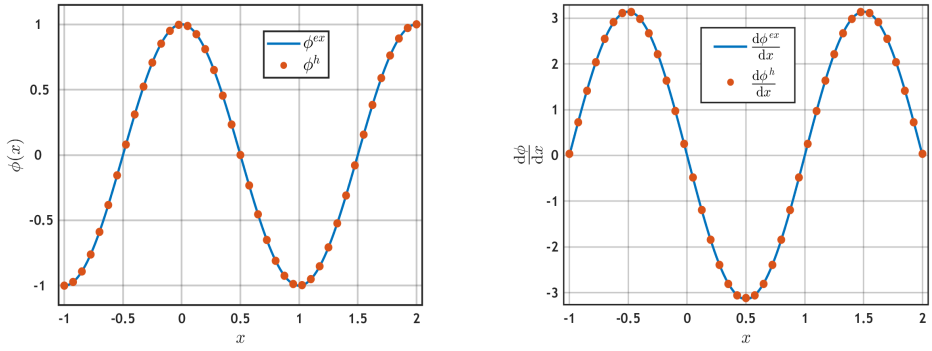

(a) $\phi^h = \Psi^0(x)\mathcal{N}^0(\phi^h)$ (b) $\frac{d\phi^h}{dx} = \Psi^1(x)\mathbb{E}^{1,0}\mathcal{N}^0(\phi^h)$

Figure 4.7: Solution to the Poisson problem using $\phi'|_{\partial I} = 0$, $N = 6$ & $K = 2$.

Even though the approximations are shown as dots, they were interpolated and only some points were used to shape the numerical solution. Had a continuous approximation been plotted, it would have overlapped completely the exact solutions.

The multi-element approach using the *Gathering Matrix* or the *Connectivity Matrix* procedure leads to the exact same results. The only difference, however, is the size of the system to solve. In Figure 4.8, this is observed for a discretization using a polynomial degree $N = 6$ and $K = 5$ spectral elements.

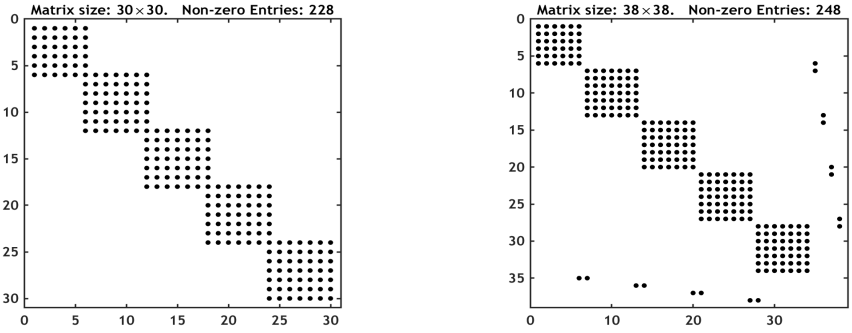

(a) Gathering Matrix (b) Connectivity Matrix $\mathbb{N}$

Figure 4.8: Sparsity patterns after imposing $\phi(a) = \cos(a\pi)$

In reality, the size of the system should be increased by one. Since there is not a unique solution, an extra condition has to be enforced (for instance $\int_I \phi \, \mathrm{d}I = 0$). In this case, $\phi(a) = \cos(a\pi)$ was opted for and the first row in (4.3) was replaced by $\mathcal{N}_{I_1}^0(\phi_1^h) = \cos(a\pi)$. Before solving, the known values are sent to the right-hand side and the first row is excluded from the computations to obtain a square system.

Since $\phi \in H^1(I)$, the *correct* norm for the error is $||\epsilon_\phi||_{H^1(I)}$. In Figure 4.9a, p-convergence is shown where a logarithmic scale is used to depict exponential convergence for varying N. In Figure 4.9b, refinement of the element size is shown where $h = \frac{1}{K}$ and the slopes of the lines coincide with the degree N utilized.

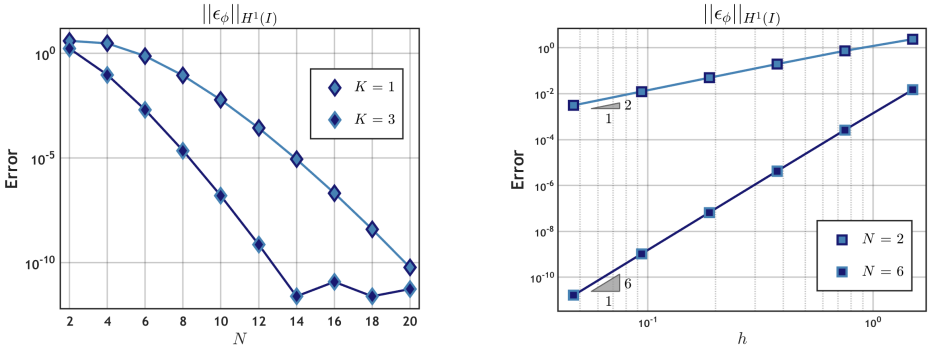

(a) p-convergence (b) h-convergence

Figure 4.9: Convergence trends for the Homogeneous Neumann Poisson problem in $I = [-1, 2]$.

4.2 Full Second Order ODE

The next subsections showcase the discretization of differential equations of the type

$$\frac{\mathrm{d}^2\phi}{\mathrm{d}x^2} + \alpha\frac{\mathrm{d}\phi}{\mathrm{d}x} + \beta\phi = -f(x) \quad \text{and} \quad I = [-1,\, 1]$$

where α and β are constants. The process starts by multiplying the equation by a test function $\tilde{\phi}$ and then integrating the second order derivative as follows:

$$\langle \tilde{\phi},\, \phi' \rangle_{\partial I} - \left(\tilde{\phi}',\, \phi'\right)_I + \alpha\, \left(\tilde{\phi},\, \phi'\right)_I + \beta\, \left(\tilde{\phi},\, \phi\right)_I = -\left(\tilde{\phi},\, f\right)_I$$

where $\langle \cdot\,,\, \cdot \rangle_{\partial I}$ indicates a boundary term. If in the next step, we were to expand both $\tilde{\phi}$ and ϕ with nodal basis functions, then the term $\left(\tilde{\phi},\, \phi'\right)_I$ would pose a problem since the test function is a polynomial of degree N while ϕ' is a polynomial of degree $N-1$ and the resulting mass matrix would be rectangular of size $N+1 \times N$.

Rewriting the problem in terms of the known mass matrices, a variable $Q = \phi'$ expanded using $\Psi^0(x)$ is introduced. In doing so, the spaces of all inner products are compatible to the current notation. The following is obtained:

$$\begin{gathered}
\langle \tilde{\phi},\, \phi' \rangle_{\partial I} - \left(\tilde{\phi}',\, \phi'\right)_I + \alpha\, \left(\tilde{\phi},\, Q\right)_I + \beta\, \left(\tilde{\phi},\, \phi\right)_I = -\left(\tilde{\phi},\, f\right)_I \\
\downarrow \\
\mathbb{B} - \left(\mathbb{E}^{1,0}\right)^{\mathrm{T}}\, \mathbb{M}^{(1)}\, \mathbb{E}^{1,0} \mathcal{N}^0(\phi^h) + \alpha\, \mathbb{M}^{(0)} \mathcal{N}^0(Q^h) + \beta\, \mathbb{M}^{(0)} \mathcal{N}^0(\phi^h) = -\underline{\mathrm{F}}
\end{gathered}$$

To find the discrete relation between Q and ϕ, both are expanded with their correspondent basis functions. To fix ideas, assume $N = 3$:

$$\begin{aligned}
&\mathcal{N}^0\left(Q_0^h\right) h_0(\xi) + \mathcal{N}^0\left(Q_1^h\right) h_1(\xi) + \mathcal{N}^0\left(Q_2^h\right) h_2(\xi) + \mathcal{N}^0\left(Q_3^h\right) h_3(\xi) + \mathcal{N}^0\left(Q_4^h\right) h_4(\xi) = \\
&= \left[\mathcal{N}^0\left(\phi_1^h\right) - \mathcal{N}^0\left(\phi_0^h\right)\right] e_1(\xi) + \left[\mathcal{N}^0\left(\phi_2^h\right) - \mathcal{N}^0\left(\phi_1^h\right)\right] e_2(\xi) + \left[\mathcal{N}^0\left(\phi_3^h\right) - \mathcal{N}^0\left(\phi_2^h\right)\right] e_3(\xi)
\end{aligned}$$

To find a relation between $\mathcal{N}^0(Q^h)$ and $\mathcal{N}^0(\phi^h)$, the equation above is evaluated at the *Gauss-Lobatto-Legendre* nodes. Since the nodal basis functions satisfy the **Kronecker-delta** condition, the following relation is obtained:

$$\begin{aligned}
\mathcal{N}^0\left(Q_0^h\right) &= \left(\phi_1^h - \phi_0^h\right) e_1(\xi_0) + \left(\phi_2^h - \phi_1^h\right) e_2(\xi_0) + \left(\phi_3^h - \phi_2^h\right) e_3(\xi_0) \\
\mathcal{N}^0\left(Q_1^h\right) &= \left(\phi_1^h - \phi_0^h\right) e_1(\xi_1) + \left(\phi_2^h - \phi_1^h\right) e_2(\xi_1) + \left(\phi_3^h - \phi_2^h\right) e_3(\xi_1) \\
\mathcal{N}^0\left(Q_2^h\right) &= \left(\phi_1^h - \phi_0^h\right) e_1(\xi_2) + \left(\phi_2^h - \phi_1^h\right) e_2(\xi_2) + \left(\phi_3^h - \phi_2^h\right) e_3(\xi_2) \\
\mathcal{N}^0\left(Q_3^h\right) &= \left(\phi_1^h - \phi_0^h\right) e_1(\xi_3) + \left(\phi_2^h - \phi_1^h\right) e_2(\xi_3) + \left(\phi_3^h - \phi_2^h\right) e_3(\xi_3)
\end{aligned}$$

In matrix notation, a more succinct relation is obtained:

$$\mathcal{N}^0(Q^h) = \begin{bmatrix} e_1(\xi_0) & e_2(\xi_0) & e_3(\xi_0) \\ e_1(\xi_1) & e_2(\xi_1) & e_3(\xi_1) \\ e_1(\xi_2) & e_2(\xi_2) & e_3(\xi_2) \\ e_1(\xi_3) & e_2(\xi_3) & e_3(\xi_3) \end{bmatrix} \mathbb{E}^{1,0}\mathcal{N}^0(\phi^h) = \underbrace{\begin{bmatrix} \Psi^1(\xi_0) \\ \Psi^1(\xi_1) \\ \Psi^1(\xi_2) \\ \Psi^1(\xi_3) \end{bmatrix}}_{\mathbb{C}^{0,1}} \mathbb{E}^{1,0}\mathcal{N}^0(\phi^h) \tag{4.8}$$

where in lack of a better notation $\mathbb{C}^{0,1}$ is used as the matrix *changes*/maps the degrees of freedom of geometric dimension one (lines) to degrees of freedom of geometric dimension zero (nodes). As a result, the algebraic system to solve is:

$$\left[\left(\mathbb{E}^{1,0}\right)^{\mathrm{T}} \mathbb{M}^{(1)} \mathbb{E}^{1,0} - \alpha \mathbb{M}^{(0)} \mathbb{C}^{0,1} \mathbb{E}^{1,0} - \beta \mathbb{M}^{(0)}\right] \mathcal{N}^0(\phi) = \underline{\mathrm{F}} - \mathbb{B} \tag{4.9}$$

where it is clear that $\alpha = \beta = 0$ supplemented with $\phi'|_{\partial I} = 0$ retrieves the formulation from the Direct Method shown previously in (4.3).

4.2.1 Manufactured Solution

The following sample equation is tested:

$$\frac{\mathrm{d}^2\phi}{\mathrm{d}x^2} + \frac{\mathrm{d}\phi}{\mathrm{d}x} + \phi = -f, \quad x \in [0,\, 3] \tag{4.10}$$

where $f(x)$ is computed such that $\phi^{ex}(x) = -\cos(\pi x)$. Additionally, $\phi'|_{\partial I} = 0$ is imposed. By using 3 spectral elements and $N = 6$, Figure 4.10 is obtained:

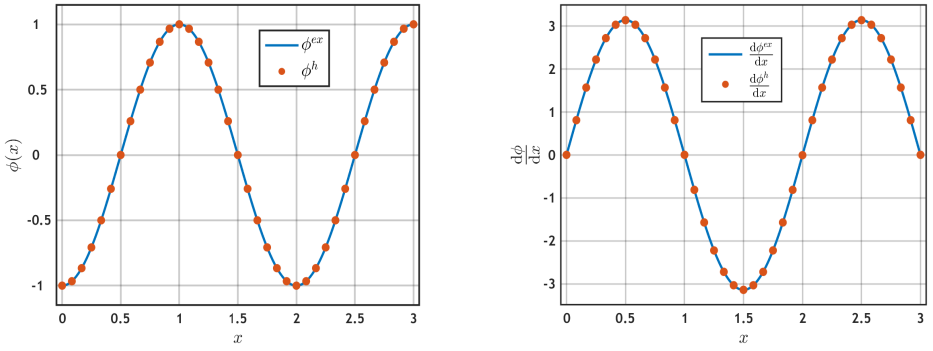

(a) $\phi^h = \Psi^0(x)\mathcal{N}^0(\phi^h)$ (b) $\frac{\mathrm{d}\phi^h}{\mathrm{d}x} = \Psi^1(x)\,\mathbb{E}^{1,0}\mathcal{N}^0(\phi^h)$

Figure 4.10: Solution to $\phi'' + \phi' + \phi = -f$ using $\phi'|_{\partial I} = 0$, $N = 6$ & $K = 2$.

The derivative was computed using $\mathcal{N}^0(\phi^h)$ but it can also be computed using $\mathcal{N}^0(Q^h)$ which will lead to the same result. If the latter is used, then even the

term ϕ'' could be computed as $\Psi^1(x)\mathbb{E}^{1,0}\mathcal{N}^0(Q^h)$. This approach was not followed because, even if the second derivative is required, it can be obtained directly from the differential equation since ϕ^h, $\frac{\mathrm{d}\phi^h}{\mathrm{d}x}$ and f are known.

The sparsity patterns for this formulation for either a *Gathering Matrix* or a *Connectivity Matrix* approach is the same as the one from the Dirichlet problem shown in Section 4.1 and, hence, not shown here. The error norm for ϕ is taken to be $||\epsilon_\phi||_{H^1(I)}$ such that the trends from Figure 4.11 are obtained.

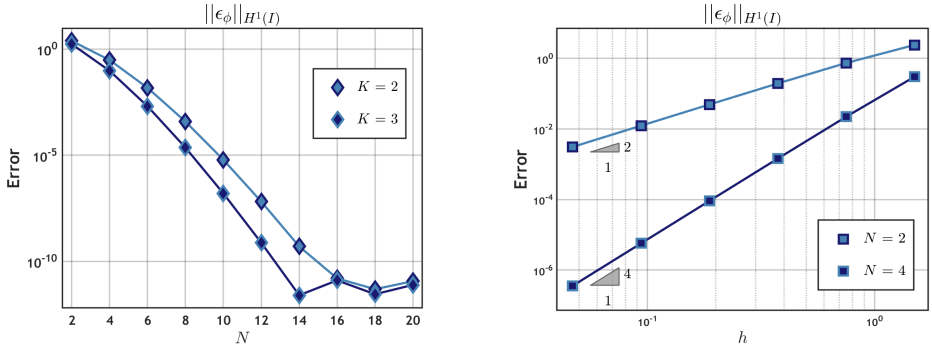

(a) p-convergence (b) h-convergence

Figure 4.11: Convergence trends for ϕ^h.

4.2.2 Hartmann Flow

This section analyzes a typical flow studied in Magnetohydrodynamics (MHD). Hartmann flows are the MHD analogous of Poiseuille flows and consist of an incompressible fluid traveling in the presence of a transverse magnetic field $\mathbf{B}$.

Hartmann flows are often utilized to validate MHD solvers and, as a result, are covered in plenty of literature. For the interested reader, an excellent introduction to the topic is given by Shercliff [83] who focuses mainly on physical understanding of the MHD phenomena rather than utilizing complex mathematical refinement.

The derivation from the 3D-MHD problem to the system examined in this section can be found in [52, p. 132-133]. The latter showcases a coupled system of differential equations for the velocity u and the first component of the magnetic field $\mathbf{B}$ plus their boundary conditions as shown below:

$$\left.\begin{aligned} \frac{\mathrm{d}^2 u}{\mathrm{d}y^2} + S\,\mathrm{Re}\,\frac{\mathrm{d}b}{\mathrm{d}y} &= -G\,\mathrm{Re} \\ \frac{\mathrm{d}^2 b}{\mathrm{d}y^2} + \mathrm{Rm}\,\frac{\mathrm{d}u}{\mathrm{d}y} &= 0 \end{aligned}\right\} \quad \begin{aligned} u(-1) = 0, \quad u(1) = 0 \\ b(-1) = 0, \quad b(1) = 0 \end{aligned} \tag{4.11}$$

where Rm is the *Magnetic Reynolds Number*, Re is the *Reynolds Number*, G is a given constant, S is a coupling parameter equal to $\frac{\mathrm{Ha}^2}{\mathrm{Re}\,\mathrm{Rm}}$ and Ha is the *Hartmann Number* equal to $B\,L(\sigma/\eta)^{1/2}$ with B being a reference magnetic field intensity, L being a characteristic length scale while σ and η are the electrical conductivity and dynamic viscosity, respectively.

The discretization of the system follows the same logic as the one presented for the manufactured solution. The terms $\frac{\mathrm{d}}{\mathrm{d}y}$ are replaced by the product $\mathbb{M}^{(0)}\,\mathbb{C}^{0,1}\,\mathbb{E}^{1,0}$ while the other terms follow the conventional procedure. Since the system is coupled, the discrete system will have a *mixed formulation* type structure. The degrees of freedom for the system are set as $\mathcal{N}^0 = [\mathcal{N}^0(u^h)\;\mathcal{N}^0(b^h)]^{\mathrm{T}}$ and, as done throughout the thesis, labeled from left to right. In doing so, the following system is obtained,

$$\begin{bmatrix} \left(\mathbb{E}^{1,0}\right)^{\mathrm{T}}\,\mathbb{M}^{(1)}\,\mathbb{E}^{1,0} & -S\,\mathrm{Re}\,\mathbb{M}^{(0)}\,\mathbb{C}^{0,1}\,\mathbb{E}^{1,0} \\ -\mathrm{Rm}\,\mathbb{M}^{(0)}\,\mathbb{C}^{0,1}\,\mathbb{E}^{1,0} & \left(\mathbb{E}^{1,0}\right)^{\mathrm{T}}\,\mathbb{M}^{(1)}\,\mathbb{E}^{1,0} \end{bmatrix} \begin{pmatrix} \mathcal{N}^0(u^h) \\ \mathcal{N}^0(b^h) \end{pmatrix} = \begin{pmatrix} \mathrm{F} \\ 0 \end{pmatrix} \tag{4.12}$$

where the boundary term has disappeared since the test functions are chosen to be zero at the boundary. The boundary conditions are applied by deleting the correspondent rows and columns from the system. Once the latter is done, the numerical approximations can be compared to the analytical solutions [52, p. 133],

$$u(y) = \frac{G\,\mathrm{Re}}{\mathrm{Ha}\,\tanh(\mathrm{Ha})}\left(1 - \frac{\cosh(\mathrm{Ha}\,y)}{\cosh(\mathrm{Ha})}\right) \quad \text{and} \quad b(y) = \frac{G}{S}\left(\frac{\sinh(\mathrm{Ha}\,y)}{\sinh(\mathrm{Ha})} - y\right).$$

In Figure 4.12, the approximation for the horizontal velocity and the magnetic field is found to match very well the exact solutions. The system was solved using a *Gathering Matrix* and the sparsity pattern after incorporating the boundary information can be observed in Figure 4.13 for the left-hand side matrix.

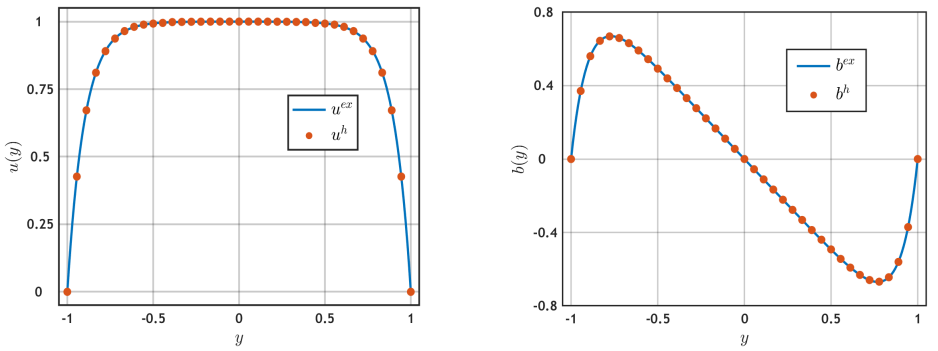

(a) $u^h = \Psi^0(x)\,\mathcal{N}^0(u^h)$ (b) $b^h = \Psi^0(x)\,\mathcal{N}^0(b^h)$

Figure 4.12: Solution to the Hartmann Flow system. $N = 6$ and $K = 3$.

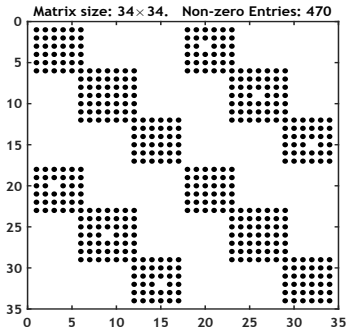

Figure 4.13: Sparsity pattern with $N = 6$ & $K = 2$ after imposing $u|_{\partial I} = 0$ & $b|_{\partial I} = 0$.

The convergence trends for $u(y)$ and $b(y)$ are shown in Figure 4.14 and Figure 4.15, respectively. For the h-convergence, the slopes are basically equal to the polynomial degree N which matches the observed trends of the previous cases.

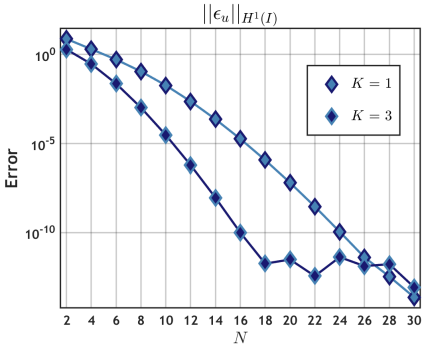

(a) p-convergence

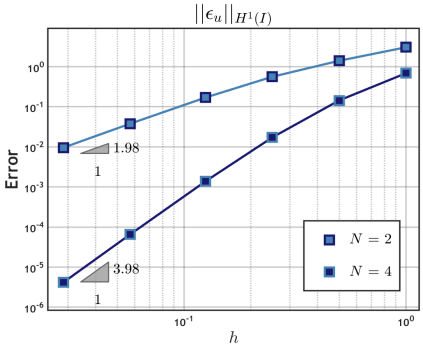

(b) h-convergence

Figure 4.14: Convergence trends for u^h.

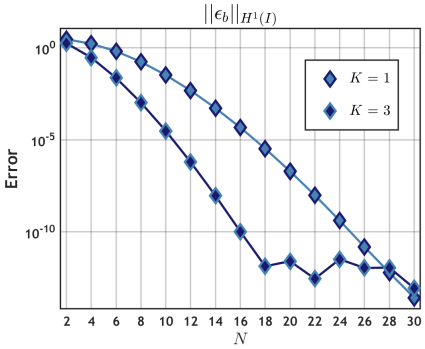

(a) p-convergence

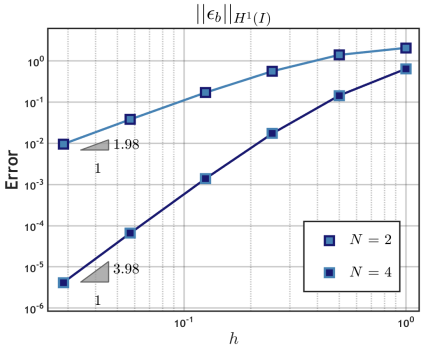

(b) h-convergence

Figure 4.15: Convergence trends for b^h.

4.3 The Poisson Problem in $\mathbb{R}^2$

The problem considered in this section is:

$$\nabla^2 \phi = -f \quad \text{in } \Omega$$

where the explored domains will be rectangles $\Omega = [a,\, b] \times [c,\, d]$ and $(a, b, c, d) \in \mathbb{Z}$.

4.3.1 Direct Method

The direct method for the $\mathbb{R}^2$ problem follows the same procedure as the one for the one-dimensional problem. Once again, the weak form can be obtained performing variations on the functional shown in Section 3.7 or by Galerkin principles.

If the information at boundary is given by $\frac{\partial \phi}{\partial n}|_{\partial\Omega} = g(\boldsymbol{x})$ and the functions ϕ and $\tilde{\phi}$ are expanded using the nodal basis $\Psi^0(\boldsymbol{x})$, then the formulation becomes,

$$\begin{gathered} \left(\nabla\tilde{\phi},\, \nabla\phi\right)_\Omega = \left(\tilde{\phi},\, f\right)_\Omega + \left\langle \tilde{\phi},\, g \right\rangle_{\partial\Omega}, \quad \forall\, \tilde{\phi} \in H^1(\Omega) \\ \downarrow \\ \left(\mathbb{E}^{1,0}\right)^{\mathrm{T}}\, \mathbb{M}^{(1)}\, \mathbb{E}^{1,0}\, \mathcal{N}^0(\phi^h) = \underline{\mathrm{F}} + \mathbb{B} \end{gathered} \tag{4.13}$$

with $\mathrm{F}_i = \int_\Omega \Psi_i^1(\boldsymbol{x})\, f(\boldsymbol{x})\, \mathrm{d}\Omega$ and $\mathbb{B}$ represents the contribution from the boundary $\partial\Omega$. Even though the notation is the same, the matrix $\mathbb{E}^{1,0}$ is the one from (3.33) instead of the matrix used for the previous $\mathbb{R}^1$ cases.

4.3.2 Mixed Formulation

Deriving the weak form, follows the same logic as for the one-dimensional case. The main difference relies on the test functions to use and their respective function spaces. A combination of both scalar and vector-valued functions are utilized.

Such as before, the weak form for this problem can be obtained by *taking variations* of a given functional. For the case with homogeneous Dirichlet conditions, the functional $J(v, q; f)$ below leads to the weak form:

$$J(\boldsymbol{v}, q; f) = \frac{1}{2}\int_\Omega |\boldsymbol{v}^2|\, \mathrm{d}\Omega - \int_\Omega f\, q\, \mathrm{d}\Omega + \int_\Omega \boldsymbol{v} \cdot \nabla\, q\, \mathrm{d}\Omega$$

where variations with respect to $\boldsymbol{v}$ and q need to be computed. If Galerkin principles are favored, the process starts by splitting the system into two first order equations and multiplying by test functions. Then, integration by parts on the term containing

$\nabla\phi$ is performed which easily allows to introduce Dirichlet boundary conditions:

$$\begin{aligned}(\boldsymbol{p},\boldsymbol{u})_\Omega = (\boldsymbol{p},\nabla\,\phi)_\Omega \;\rightarrow\; (\boldsymbol{p},\boldsymbol{u})_\Omega &= \langle \boldsymbol{p}\cdot n\,,\,\phi\rangle_{\partial\Omega} - (\nabla\cdot\boldsymbol{p},\phi)_\Omega\,, \quad \forall\, p\in H_0(\mathrm{div},\Omega)\\ (q,\nabla\cdot\boldsymbol{u})_\Omega &= (q,\text{-}f)_\Omega\,, \qquad\qquad\qquad\qquad \forall\, q\in L^2(\Omega)\end{aligned}$$

The functions $\boldsymbol{u}$ and $\boldsymbol{p}$ are expanded with the basis $\Psi^1(\boldsymbol{x})$ while ϕ and q are expanded with $\Psi^2(\boldsymbol{x})$. In doing so, the primal-primal formulation system is obtained:

$$\begin{bmatrix} \mathbb{M}^{(1)} & \left(\mathbb{E}^{2,1}\right)^{\mathrm{T}}\,\mathbb{M}^{(2)} \\ \mathbb{M}^{(2)}\,\mathbb{E}^{2,1} & 0 \end{bmatrix} \begin{pmatrix} \mathcal{N}^1(u^h) \\ \mathcal{N}^2(\phi^h) \end{pmatrix} = \begin{pmatrix} \mathbb{B} \\ \underline{\mathrm{F}} \end{pmatrix} \tag{4.14}$$

where $\mathrm{F}_i = \text{-}\int_\Omega \Psi_i^2(\boldsymbol{x}) f(\boldsymbol{x})\,\mathrm{d}\Omega$ and the boundary term is squeezed into $\mathbb{B}$. For the primal-dual formulation, the same logic as for the $\mathbb{R}^1$ case is followed:

- Interpolate the forcing function as $f(x) = \Psi^2(\boldsymbol{x})\mathcal{N}^2(f^h)$ where $\mathcal{N}^2(f^h)$ is calculated according to (3.17) such that $\underline{\mathrm{F}}$ becomes $\text{-}\,\mathbb{M}^{(2)}\mathcal{N}^{(2)}(f^h)$.
- The second row is multiplied by $\widetilde{\mathbb{M}}^{(0)} = \left(\mathbb{M}^{(2)}\right)^{\text{-}1}$.
- Use the dual degrees of freedom $\widetilde{\mathcal{N}}^0(\phi^h) = \mathbb{M}^{(2)}\mathcal{N}^2(\phi^h)$ instead of $\mathcal{N}^2(\phi^h)$.

The primal-dual formulation in $\mathbb{R}^2$ reads:

$$\begin{bmatrix} \mathbb{M}^{(1)} & \left(\mathbb{E}^{2,1}\right)^{\mathrm{T}} \\ \mathbb{E}^{2,1} & 0 \end{bmatrix} \begin{pmatrix} \mathcal{N}^1(u^h) \\ \mathcal{N}^2(\phi^h) \end{pmatrix} = \begin{pmatrix} \mathbb{B} \\ \text{-}\mathcal{N}^2(f^h) \end{pmatrix} \tag{4.15}$$

4.3.3 Dirichlet Problem: Square Domain

In this section, a Mixed Formulation for the Dirichlet problem of the Poisson equation is set up for the variables ϕ and $\boldsymbol{u} = [u\,,\,v]^{\mathrm{T}}$. The manufactured solutions $\phi^{ex}(\boldsymbol{x}) = \sin(\pi x)\sin(\pi y)$, $u^{ex} = \pi\cos(\pi x)\sin(\pi y)$ and $v^{ex} = \pi\sin(\pi x)\cos(\pi y)$ are used which fixes the forcing term as $f(\boldsymbol{x}) = \text{-}2\pi^2\sin(\pi x)\sin(\pi y)$.

The rectangular domain $\Omega = [\text{-}1,\,1]\times[0,\,2]$ is used and, due to the nature of the manufactured solution, $\phi|_\Omega = 0$ is imposed. In this formulation the primary variable is sought in $\phi\in L^2(\Omega)$ and, for this problem, the secondary variable is sought in $\boldsymbol{u}\in H_0(\mathrm{div},\Omega)$ which defines the error norms to compute.

The domain is covered by a mesh of $K = 4$ elements with $K_x = 2$ elements in the x-direction and $K_y = 2$ elements in the y-direction. A polynomial degree $N = 6$ is utilized. The subdomains Ω_k used for this problem are reminiscent to the mesh shown in Figure 3.10 or Figure 3.11. The approximations for the primary and secondary variables are found in Figure 4.16 and Figure 4.17, respectively.

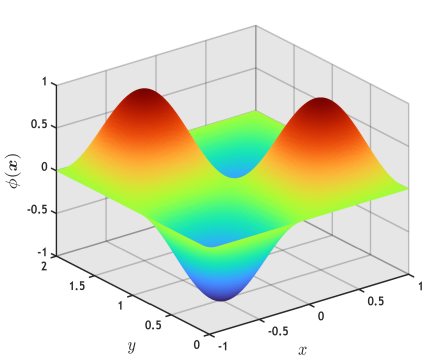

(a) $\phi^h = \Psi^2(\boldsymbol{x})\mathcal{N}^2(\phi^h)$

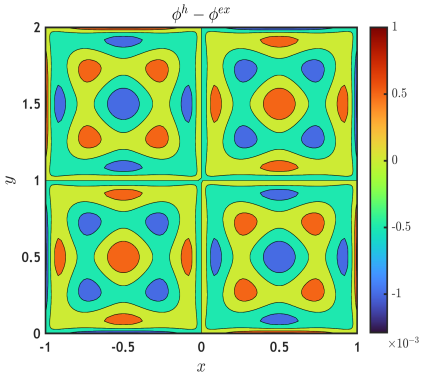

(b) Comparison between ϕ^h and ϕ^{ex}

Figure 4.16: Primary variable ϕ^h. Obtained using $N = 6$, $K_x = 2$, $K_y = 2$.

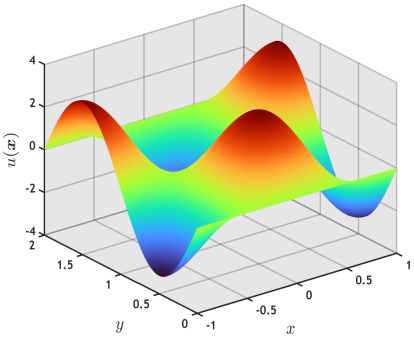

(a) $u^h = \Psi^1_x(\boldsymbol{x})\mathcal{N}^1(u^h)$

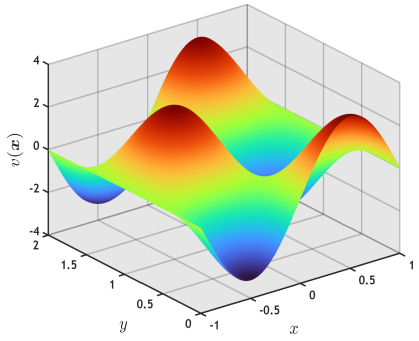

(b) $v^h = \Psi^1_y(\boldsymbol{x})\mathcal{N}^1(v^h)$

Figure 4.17: Secondary variable $\underline{u}^h = \Psi^1(\boldsymbol{x})\mathcal{N}^1(\underline{u}^h)$. Obtained using $N = 6$, $K_x = 2$, $K_y = 2$.

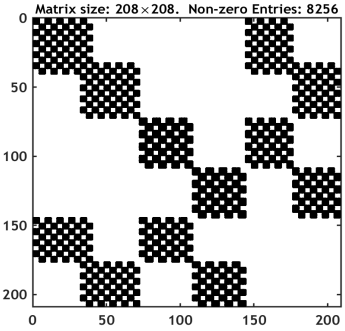

(a) Gathering Matrix

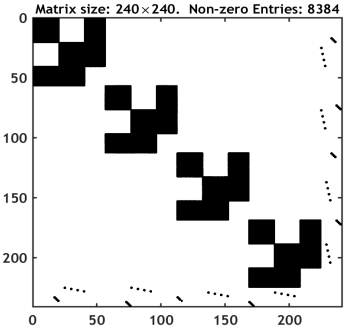

(b) Connectivity Matrix $\mathbb{N}$

Figure 4.18: Sparsity patterns for Primal-Primal Formulation. $N = 4$, $K_x = 2$, $K_y = 2$.

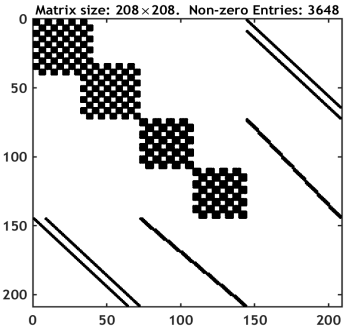

(a) Gathering Matrix

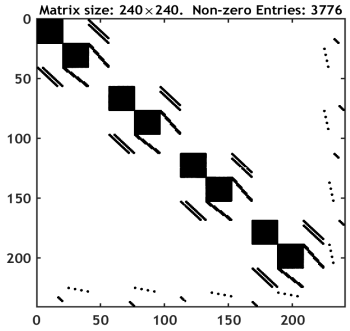

(b) Connectivity Matrix $\mathbb{N}$

Figure 4.19: Sparsity patterns for Primal-Dual Formulation. $N = 4$, $K_x = 2$, $K_y = 2$.

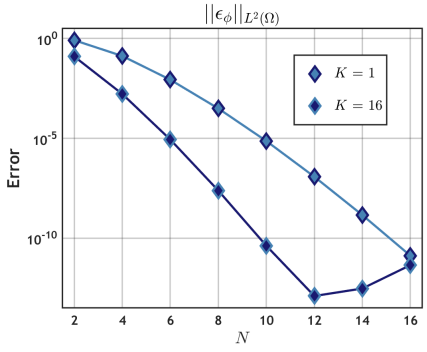

(a) p-convergence

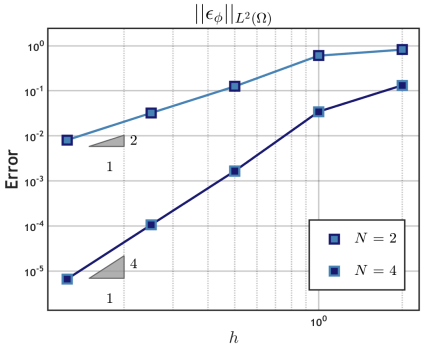

(b) h-convergence

Figure 4.20: Convergence trends for the primary variable ϕ^h.

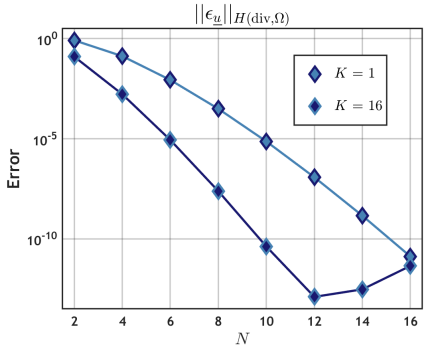

(a) p-convergence

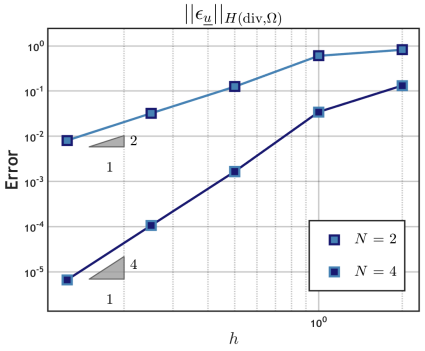

(b) h-convergence

Figure 4.21: Convergence trends for the secondary variable $\underline{u}^h$.

The different sparsity patterns from Figure 4.18 and Figure 4.19 shows that the smallest system arises from a primal-dual formulation using a *Gathering Matrix*. This approach is especially useful if the interest resides on the secondary variable since its interpolation does not require to compute any inverse mass matrices.

Finally, the error for both the primary and the secondary variable follow the optimal convergence of order N as shown in Figure 4.20 and Figure 4.21.

4.3.4 Neumann Problem: Square Domain

In this section, the Neumann problem for the Poisson equation is solved using a Direct Method. A manufactured solution is set as $\phi^{ex}(\boldsymbol{x}) = \cos(\pi x)\cos(\pi y)$ such that $\nabla\phi^{ex} = [\text{-}\pi\sin(\pi x)\cos(\pi y), \text{-}\pi\cos(\pi x)\sin(\pi y)]^{\mathrm{T}}$. The forcing function that matches the manufactured solution is $f(\boldsymbol{x}) = \text{-}2\pi^2\cos(\pi x)\cos(\pi y)$.

The problem is analyzed on the rectangular domain $\Omega = [0, 2] \times [\text{-}1, 1]$ and, due to the choice of the solution $\phi^{ex}(\boldsymbol{x})$, the term $\frac{\partial\phi}{\partial n}|_\Omega = 0$ is imposed. Since the solution is sought in the space $\phi \in H^1(\Omega)$, the term $\nabla\phi^h$ is required for the norm $||\epsilon_\phi||_{H^1(\Omega)}$ and it is also computed.

The domain is covered by a mesh of $K = 4$ elements with $K_x = 2$ elements in the x-direction and $K_y = 2$ elements in the y-direction. Additionally, a polynomial degree $N = 6$ is utilized. The problem is solved using a *Gathering Matrix* and a *Connectivity Matrix* which yield the same results. Examples of the sparsity of the systems for the different approaches are shown in Figure 4.24.

Finally, the convergence trends, Figure 4.25, follow the behavior from previous cases where optimal convergence is achieved under the appropriate error norm.

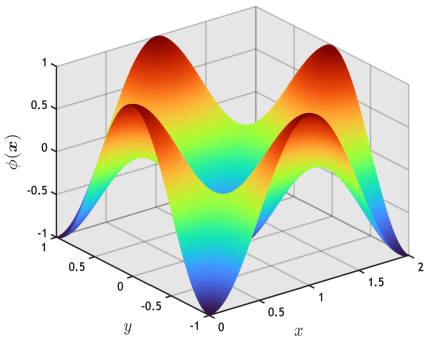

(a) $\phi^h = \Psi^0(\boldsymbol{x})\mathcal{N}^0(\phi^h)$

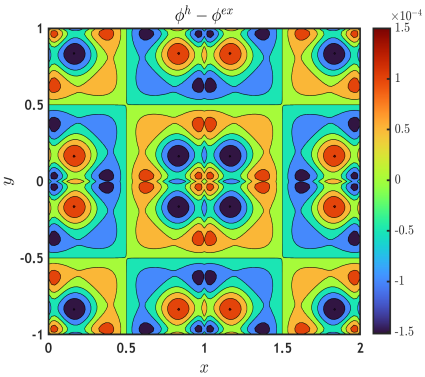

(b) Comparison between ϕ^h and ϕ^{ex}

Figure 4.22: Solution to $\nabla^2\phi = \text{-}f$ using $\frac{\partial\phi}{\partial n}|_{\partial\Omega} = 0$. Obtained using $N = 6$, $K_x = 2$, $K_y = 2$.

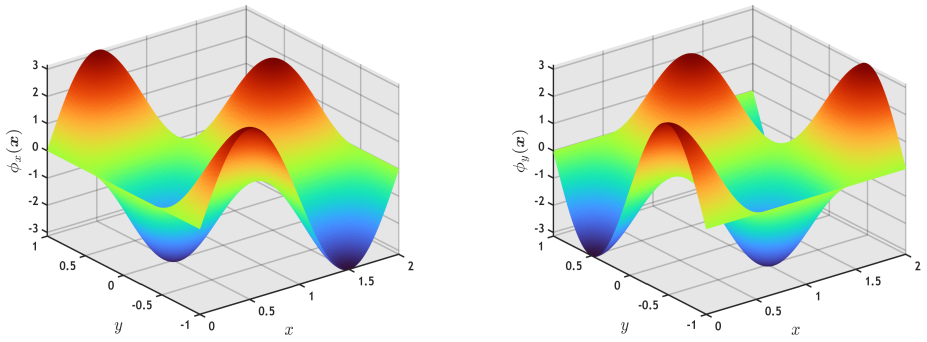

Figure 4.23: $\nabla\phi^h = \Psi^1(\boldsymbol{x})\mathbb{E}^{1,0}\mathcal{N}^0(\phi^h)$. To the left, $\phi^h_x(\boldsymbol{x})$ and $\phi^h_y(\boldsymbol{x})$ to the right.

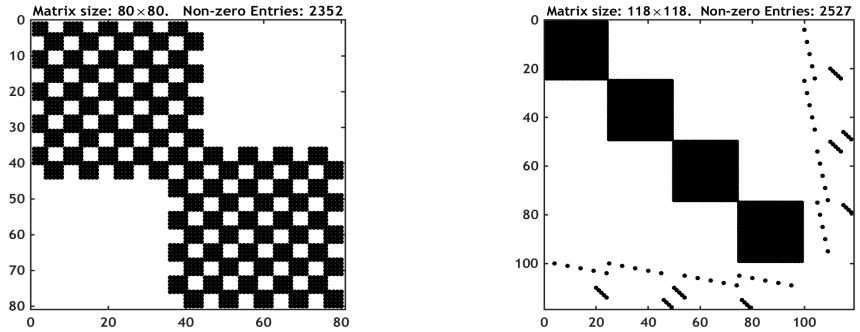

(a) Gathering Matrix

(b) Connectivity Matrix $\mathbb{N}$

Figure 4.24: Sparsity patterns after imposing $\phi(a, c) = \cos(a\pi)\cos(c\pi)$. $N = 4$, $K_x = 2$, $K_y = 2$.

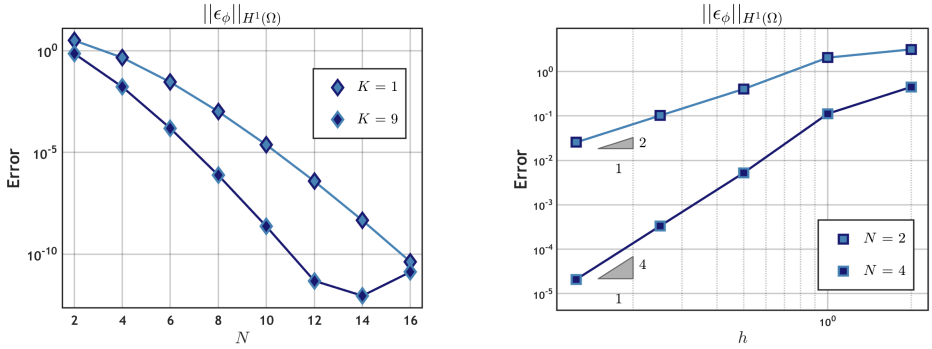

(a) p-convergence

(b) h-convergence

Figure 4.25: Convergence trends Poisson problem using $\frac{\partial\phi}{\partial n}|_{\partial\Omega} = 0$ in $\Omega = [0, 2] \times [-1, 1]$.

5

Scalar Eigenvalue Problems

Throughout this chapter, the Mimetic Spectral Element Method will be applied to eigenvalue problems related to the Laplacian operator. In Section 5.1, a short introduction is given about the so-called *Generalized Eigenvalue Problems* while Section 5.2 deals with problems on $a < x < b$. In Section 5.3, eigenvalue problems in $\mathbb{R}^2$ are explored in square, L-shape and cracked domains.

5.1 Generalized Eigenvalue Problems

The problems examined in this chapter are known as *Generalized Eigenvalue Problems* and have the form $\mathrm{A}\,\underline{x} = \lambda\,\mathrm{B}\,\underline{x}$. In the latter equation, A and B are both $n \times n$ matrices and the pair (A, B) is usually named *pencil* [37]. Then, the objective of the problem becomes to define the eigenpairs $(\lambda, \underline{x})$ to the pencil (A, B).

The more generally known standard eigenvalue problem is retrieved when $\mathrm{B} = \mathbb{I}$ such that the problem reduces to $\mathrm{A}\,\underline{x} = \lambda\,\underline{x}$. On the other hand, if $\mathrm{A} = \mathbb{I}$, then the standard problem $\hat{\lambda}\,\underline{x} = \mathrm{B}\,\underline{x}$ is obtained where $\hat{\lambda} = \frac{1}{\lambda}$. If B were to be different from the identity matrix, the standard problem can be obtained by multiplying both sides of the equation by B^{-1}, if it exists, such that,

$$\mathrm{A}\,\underline{x} = \lambda\,\mathrm{B}\,\underline{x} \quad \rightarrow \quad \mathrm{B}^{-1}\mathrm{A}\,\underline{x} = \lambda\,\underline{x} \quad \xrightarrow{\mathrm{C} = \mathrm{B}^{-1}\mathrm{A}} \quad \mathrm{C}\,\underline{x} = \lambda\,\underline{x}$$

and, if the inversion is not possible, a bit of a *dirty* numeric *hack* can be implemented by replacing B with $\mathrm{B}_s = \mathrm{B} + \varepsilon\mathbb{I}$ as to strengthen the main diagonal and make it

full rank with, maybe, $\varepsilon \approx 10^{-5}$. Unfortunately, by doing this, the matrix C will be neither symmetric nor sparse and the procedure is not recommended when $\mathrm{B}^{-1}\mathrm{A}$ has to be formed explicitly or the components of the pencil (A, B) are sparse [76].

An alternative to the burden of computing B^{-1} relies on applying the Cholesky factorization to either A or B to solve an equivalent problem with easier inversions,

$$\mathrm{B} = U_{\mathrm{B}}^{\mathrm{T}} U_{\mathrm{B}} \longrightarrow \left(U_{\mathrm{B}}^{-\mathrm{T}} \mathrm{A}\, U_{\mathrm{B}}^{-1}\right)\left(U_{\mathrm{B}}\, \underline{x}\right) = \lambda \left(U_{\mathrm{B}}\, \underline{x}\right) \longrightarrow \mathcal{A}\underline{\mathcal{U}} = \lambda \underline{\mathcal{U}}$$

$$\mathrm{A} = U_{\mathrm{A}}^{\mathrm{T}} U_{\mathrm{A}} \longrightarrow \left(U_{\mathrm{A}}^{-\mathrm{T}} \mathrm{B}\, U_{\mathrm{A}}^{-1}\right)\left(U_{\mathrm{A}}\, \underline{x}\right) = \frac{1}{\lambda} \left(U_{\mathrm{B}}\, \underline{x}\right) \longrightarrow \mathcal{B}\underline{\mathcal{V}} = \hat{\lambda} \underline{\mathcal{V}}$$

where U indicates an upper triangular matrix, the subindices specify the part of the stencil that is being rewritten and, abusing notation, $^{-\mathrm{T}}$ indicates both transposition and inversion. In a similar manner, the procedure above can be repeated with lower triangular matrices $\varsigma = L\, L^{\mathrm{T}}$ to obtain formulations for either λ or $\hat{\lambda}$.

Discussing all the variety of methods available to solve these type of problems is out of the scope of this thesis, however, the interested reader should definitely explore *The Symmetric Eigenvalue Problem* by Parlett [73]. The latter explores the basics required to compute eigenvalues of real symmetric systems while also discussing algorithms explaining its pros and cons.

In the present work, the standard MATLAB function *eig*[12] was utilized. This function uses either a Cholesky factorization on B to solve systems similar to the ones shown above or a QZ-algorithm (generalized Schur decomposition) which, much to Parlett's misfortune, ignores the symmetry of the input matrices but is impervious to hazards such as B being singular or even indefinite [73]. For additional information about the QZ-algorithm, Kressner [59, Chapter 2] is recommended.

5.2 Laplacian Eigenvalue Problems in $\mathbb{R}^1$

The problem discussed in this section is given by:

$$\frac{\mathrm{d}^2\phi}{\mathrm{d}x^2} = -\lambda\phi, \quad I \in [a, b]$$

where either homogeneous Dirichlet or Neumann boundary conditions are imposed at ∂I. The algebraic systems obtained will be quite similar as the ones observed in Section 4.1 so that the formulations will be more swiftly introduced.

In [9, p. 7], Boffi analyzes this problem and deduces the optimal approximation estimates using polynomials of degree p for eigenfunctions and eigenvalues as:

[12] MATLAB Documentation for *eig*: https://www.mathworks.com/help/matlab/ref/eig.html

$$||u^{(k)} - u_h^{(k)}||_V = \mathcal{O}(h^p) \qquad |\lambda^{(k)} - \lambda_h^{(k)}| = \mathcal{O}(h^{2p}) \tag{5.1}$$

where the function space V is selected according to the space in which the solution is sought. Therefore, the approximation rate for λ_i doubles with respect to the one at which their corresponding eigenfunctions are approximated [9]. Another result comes from the so-called *min-max property* which establishes the following bounds:

$$\lambda^{(k)} \leq \lambda_h^{(k)} \leq \lambda^{(k)} + C(k)h^{2p}$$

where $C(k)$ is a positive function depending on the eigenvalue. This statement implies that the numerical eigenvalues are all approximated from above. More detailed information about this property can be found in [9, Proposition 7.2]

5.2.1 Dirichlet Problem

For the Dirichlet problem, a mixed formulation is utilized. The weak form is,

$$\begin{aligned} (p,\, u)_I &= -\,(p', \phi)_I \qquad \forall\ p \in H_0^1(I) \\ (q, u')_I &= -\lambda\,(q, \phi)_I \qquad \forall\ q \in L^2(I) \end{aligned}$$

such that its associated discrete algebraic system is written as,

$$\begin{bmatrix} \mathbb{M}^{(0)} & \left(\mathbb{E}^{1,0}\right)^{\mathrm{T}}\mathbb{M}^{(1)} \\ \mathbb{M}^{(1)}\,\mathbb{E}^{1,0} & 0 \end{bmatrix} \begin{pmatrix} \mathcal{N}^0(u^h) \\ \mathcal{N}^1(\phi^h) \end{pmatrix} = -\lambda \begin{bmatrix} 0 & 0 \\ 0 & \mathbb{M}^{(1)} \end{bmatrix} \begin{pmatrix} \mathcal{N}^0(u^h) \\ \mathcal{N}^1(\phi^h) \end{pmatrix} \tag{5.2}$$

where the functions were expanded as shown in Section 4.1.2. In this case, a *true* primal-dual formulation cannot be built by following the ideas from Chapter 4 since the inverse of $\mathbb{M}^{(1)}$ would appear on the right-hand side but doing so would lead to a much more sparse left-hand side matrix and is, definitely, an option to consider.

Avoiding the appearance of inverse matrices on the formulation could be done by multiplying the second row by $\mathrm{inv}\left(\mathbb{M}^{(1)}\right)$ such that $\mathbb{M}^{(1)}\mathbb{E}^{1,0}$ becomes $\mathbb{E}^{1,0}$. Alternatively, $\widetilde{\mathcal{N}}^0(\phi^h)$ could be used such that $\left(\mathbb{E}^{1,0}\right)^{\mathrm{T}}\mathbb{M}^{(1)}$ becomes $\left(\mathbb{E}^{1,0}\right)^{\mathrm{T}}$ on the first row. In both cases, the term $\mathbb{M}^{(1)}$ from the right-hand side becomes $\mathbb{I}$.

Another idea worth considering would be to use the so-called *Schur Complement Method* (SCM), discussed in Appendix B, such that the following system is obtained:

$$\mathbb{E}^{(1,0)}\,\widetilde{\mathbb{M}}^{(1)}\left(\mathbb{E}^{(1,0)}\right)^{\mathrm{T}}\widetilde{\mathcal{N}}^0(\phi^h) = \lambda\,\widetilde{\mathbb{M}}^{(0)}\widetilde{\mathcal{N}}^0(\phi^h) \tag{5.3}$$

If one spectral element were to be used, the unknowns would reduce from $2N+1$ to N at the cost of computing inverse matrices. This is not limited to eigenvalue

problems and could be implemented, for example, to the problems from Section 4.3.

The eigenvalues in $I \in [a, b]$ are known to be $\lambda_m = \left(\frac{m\pi}{L}\right)^2$ for $m \in \mathbb{N}$ while the eigenfunctions are $\phi_m(x) = \sin\left(\frac{m\pi}{L}x\right)$ with $L = b - a$. For simplicity, the formulation is tested in $I = [0, \pi]$ such that the eigenvalues are the integers squared.

After setting up the system, the first step consists on solving for either $\mathcal{N}^1(\phi_m^h)$ or $\widetilde{\mathcal{N}}^0(\phi_m^h)$. The latter is done by using the eigenvectors associated to a specific eigenvalue or, equivalently, finding the null space of the discrete system after fixing λ_m^h. Once the degrees of freedom are known, interpolation is possible by computing either $\phi_m^h(x) = \Psi^1(x)\mathcal{N}^1(\phi_m^h)$ or $\phi_m^h(x) = \widetilde{\Psi}^0(x)\widetilde{\mathcal{N}}^0(\phi_m^h)$.

Before comparing ϕ_m^h and ϕ_m, the amplitudes of both have to be matched which is done by finding a constant c_m that forces ϕ_m^h to follow ϕ_m. In this case, a least-squares approach was used to determine c_m such that the error between ϕ_m^h and ϕ_m was minimized. Other criteria could be used such as finding the absolute maximum of the approximation and match it to an amplitude of unity, however, this method proved to not always be accurate since the functions would occasionally be flipped.

The fact that such step has to be done comes as no surprise since the null space of the algebraic system is different from the zero vector which means the eigenvectors are not unique. The process of multiplying by a constant to perform the *matching* is entirely justified by the fact that the null space is closed under scalar multiplication [82, p. 60] meaning that a multiple of any eigenvector is still an eigenvector.

With the *matching* complete, comparisons between $c_m\phi_m^h$ and ϕ_m^{ex} can be performed. In order to minimize notation, numerical eigenfunctions will be denoted only by ϕ_m^h since the constant c_m lacks importance.

In Figure 5.1, $\phi_6^h(x)$ and $\phi_7^h(x)$ are plotted using $N = 6$ and $K = 3$. With this parameters, $\phi_6^{ex}(x)$ is precisely followed by its approximation. For $\phi_7^{ex}(x)$, the amplitudes of the numerical eigenfunction are a bit off near $x = \frac{\pi}{2}$. As $m \to \infty$, ϕ_m^{ex} presents more oscillations which require an increase of mesh/polynomial refinement to keep up with the quality of the approximation. The fact that an eigenvalue is quite close to its true value should not be considered as an indication that its eigenfunction will also be since the former converges twice as fast.

The convergence properties for the eigenfunctions ϕ_6^h and ϕ_7^h are shown in Figure 5.2 and Figure 5.3 where optimal convergence is observed for the eigenfunctions as the slopes of the mesh refinement plots match the polynomial degree of approximation N confirming the error estimates shown in (5.1).

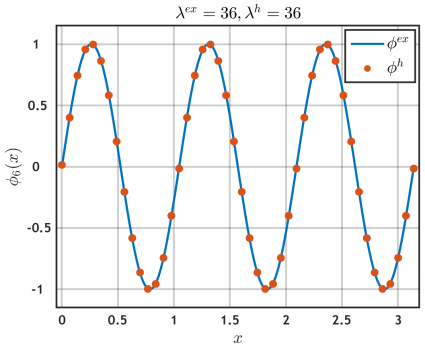

(a) Comparison between ϕ_6^{ex} and ϕ_6^h

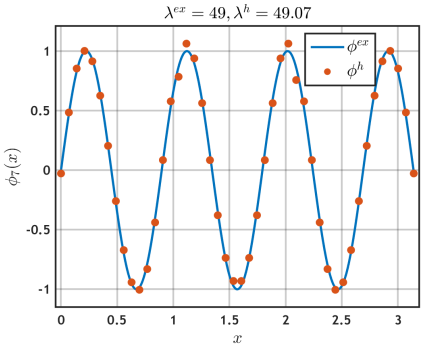

(b) Comparison between ϕ_7^{ex} and ϕ_7^h

Figure 5.1: Eigenfunctions ϕ_6^h and ϕ_7^h for the Dirichlet Problem. $N = 6$, $K = 3$.

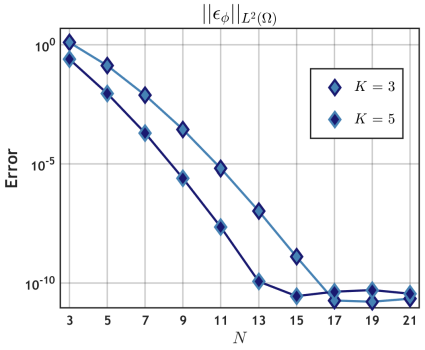

(a) p-convergence

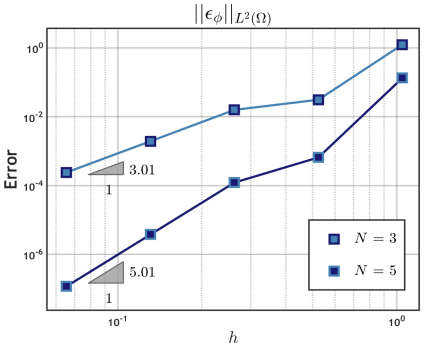

(b) h-convergence

Figure 5.2: Convergence trends for ϕ_6^h

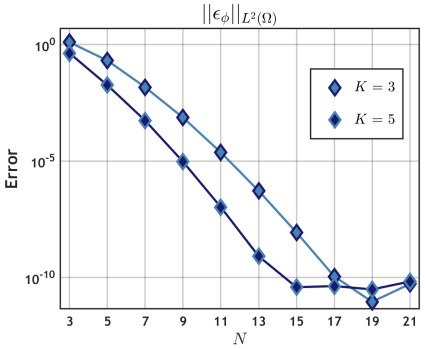

(a) p-convergence

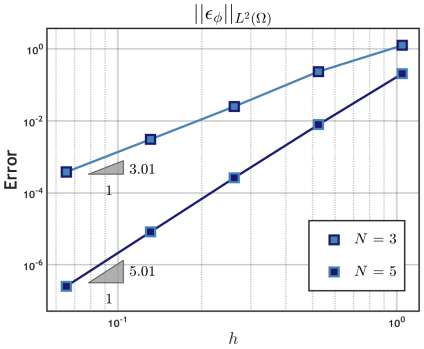

(b) h-convergence

Figure 5.3: Convergence trends for ϕ_7^h

Table 5.1: Order of Convergence for λ_3, λ_4, λ_5 and λ_6. Dirichlet Problem in $\mathbb{R}^1$.

h	λ^{ex}	$N=1$		$N=3$		$N=5$	
		λ^h	OC	λ^h	OC	λ^h	OC
$\frac{\pi}{5}$	9	11.765152	—	9.003532	—	$9+5\times10^{-7}$	—
	16	23.084931	—	16.031954	—	16.000013	—
	25	30.396355	—	25.013614	—	25.000006	—
	36	—	—	36.642306	—	36.001513	—
$\frac{\pi}{10}$	9	9.683821	2.01	9.000060	5.86	$9+5\times10^{-10}$	9.92
	16	18.192473	1.69	16.000591	5.76	$16+2\times10^{-8}$	9.85
	25	30.396355	0	25.003415	2.03	$25+2\times10^{-7}$	9.94
	36	47.060609	—	36.014128	5.51	36.000001	9.66
$\frac{\pi}{18}$	9	9.207440	2.02	9.000001	5.96	$9+1\times10^{-12}$	10.33
	16	16.659836	2.04	16.000018	5.93	$16+4\times10^{-11}$	9.94
	25	26.623231	2.04	25.000106	5.90	$25+6\times10^{-10}$	9.93
	36	39.393676	2.01	36.000453	5.85	$36+5\times10^{-9}$	9.91

Table 5.2: First 11 eigenvalues of the Dirichlet Laplacian Eigenvalue Problem in $\mathbb{R}^1$.

h	λ^{ex}	$N=3$	$N=5$	$N=7$	Trend
		λ^h	λ^h	λ^h	
$\frac{\pi}{4}$	1	1.000002	$1+9\times10^{-12}$	$1+6\times10^{-14}$	↙
	4	4.000546	$4+3\times10^{-8}$	$4+6\times10^{-13}$	↙
	9	9.012545	9.000004	$9+3\times10^{-10}$	↙
	16	16.008905	16.000004	$16+5\times10^{-10}$	↙
	25	25.548281	25.001538	$25+9\times10^{-7}$	↙
	36	37.920473	36.011740	36.000014	↙
	49	54.033661	49.061864	49.000153	↙
	64	97.268336	64.464376	64.002139	↙
	81	123.637761	81.807848	81.006140	↙
	100	176.932736	102.176611	100.027052	↙
	121	241.732546	125.968059	121.098843	↙

As an aside note, the multi-element approach was implemented with a *Gathering Matrix*. Using a *Connectivity Matrix* leads to the same result for ϕ_m^h, however, $2(K-1)$ eigenvalues $\lambda = 1$ are added to the system. The number of *spurious* eigenvalues coincides with the number of non-zero entries in $\mathbb{N}$. This proved to be true for all the cases and only *Gathering Matrices* are utilized from here onwards.

In Table 5.1, the order of convergence for some eigenvalues is shown to be *almost* the double of the predicted convergence of ϕ_m confirming, once again, the estimates from (5.1). For the cases $N = 3$ and $N = 5$, this value is either very close to $2N$ estimate or shows an increasing trend. The actual value might be reached by further

element refinement. The information from Table 5.2 shows the approximations for the first 11 eigenvalues which all show a decreasing tendency which confirms the fact that all λ_m^h are being approached from above.

5.2.2 Neumann Problem

A direct method is utilized as to incorporate the prescribed values at the boundary conditions easily. The weak form is found to be,

$$\left(\tilde{\phi}', \phi'\right)_I = \lambda \left(\tilde{\phi}, \phi\right)_I, \quad \forall\ q \in H^1(I)$$

such that its associated discrete algebraic system is given by,

$$\left(\mathbb{E}^{1,0}\right)^{\mathrm{T}}\ \mathbb{M}^{(1)}\mathcal{N}^0(\phi) = \lambda\, \mathbb{M}^{(0)}\mathcal{N}^0(\phi) \tag{5.4}$$

the problem, just as before, has an infinite countable set of solutions $(\phi_m, \lambda_m, m \in \mathbb{N})$ with $\lambda_m \to \infty$ as m increases. This result is attributed to the compact inclusion of $H^1(I)$ into $L^2(I)$ [10]. For an arbitrary domain $I \in [a, b]$, the eigenvalues are given by $\lambda_m = \left(\frac{m\pi}{L}\right)^2$ for $m \in \mathbb{Z}^*$ (non-negative integers) while the associated eigenfunctions are given by $\phi_m(x) = \cos\left(\frac{m\pi}{L}x\right)$.

Solving the Neumann problem follows the same logic used for the Dirichlet problem. However, since the eigenfunction is sought on the function space $\phi \in H^1(I)$, some extra steps are required. The general procedure is synthesized below:

- For simplicity, the formulation is tested on $I \in [0, \pi]$ such that the eigenvalues become the set of natural numbers squared and $\phi_m = \cos(mx)$.
- The eigenvectors associated to each λ_m^h are used to define $\mathcal{N}^0(\phi_m^h)$.
- The eigenfunctions are interpolated as $\phi_m^h(x) = \Psi^0(x)\mathcal{N}^0(\phi_m^h)$.
- The functions $\phi_m^h(x)$ are matched to $\phi_m(x)$ with a constant c_m. Since the analytic functions are now cosines, the *matching* is made simpler by using the fact that $\phi_m(0) = 1,\ \forall\, m \in \mathbb{Z}^*$. As a result, $c_m = \frac{1}{\phi_m^h(0)}$.
- The derivative of the eigenfunctions is computed as $\phi_m^h = \Psi^1(x)\mathbb{E}^{1,0}\mathcal{N}^0(\phi_m^h)$.
- The functions $\frac{\mathrm{d}\phi_m^h}{\mathrm{d}x}$ are matched to their analytical counterparts. Since the functions are now sines which are always zero at the boundaries, the matching constants are obtained as explained in Section 5.2.1 for the Dirichlet problem.
- Convergence plots are computed for $\phi_m^h(x)$ using the norm $||\epsilon_\phi||_{H^1(I)}$.
- The order of convergence for λ_m^h is computed for several N and K.

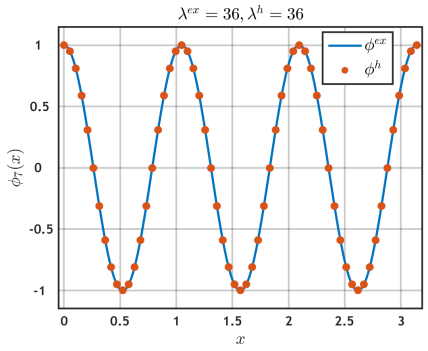

(a) Comparison between ϕ_7^{ex} and ϕ_7^h

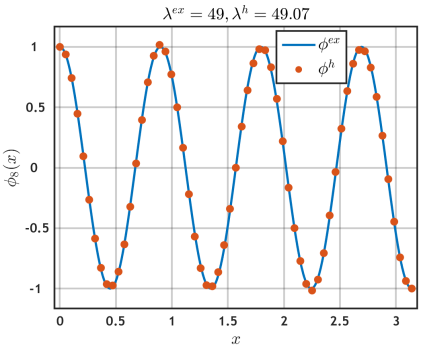

(b) Comparison between ϕ_8^{ex} and ϕ_8^h

Figure 5.4: Eigenfunctions ϕ_7^h & ϕ_8^h for the Neumann Problem. $N = 6$ & $K = 3$.

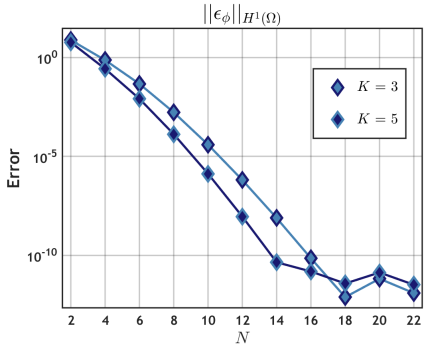

(a) p-convergence

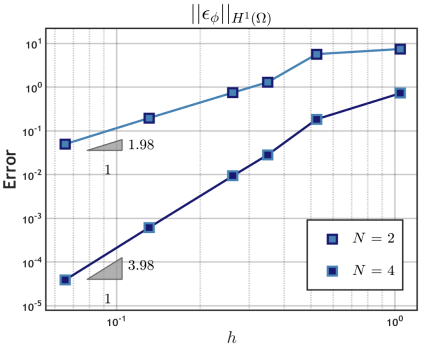

(b) h-convergence

Figure 5.5: Convergence trends for ϕ_7^h

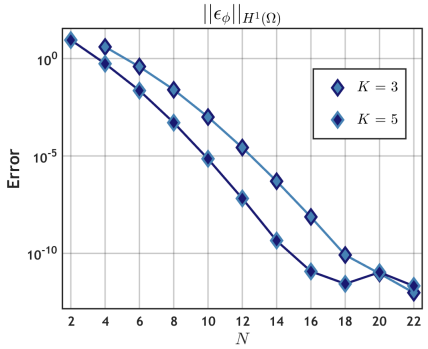

(a) p-convergence

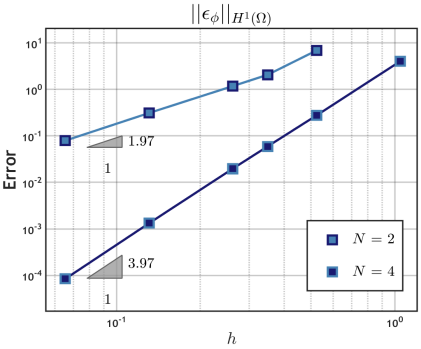

(b) h-convergence

Figure 5.6: Convergence trends for ϕ_8^h

Table 5.3: Order of Convergence for λ_4, λ_5, λ_6 & λ_7. Neumann problem in $I = [0, \pi]$.

h	λ^{ex}	$N=1$		$N=2$		$N=4$	
		λ^h	OC	λ^h	OC	λ^h	OC
$\frac{\pi}{5}$	9	11.765152	—	9.134005	—	9.000051	—
	16	23.084931	—	16.663257	—	16.000844	—
	25	30.396355	—	30.396355	—	25.013914	—
	36	—	—	43.889597	—	36.039171	—
$\frac{\pi}{10}$	9	9.683821	1.69	9.009431	3.69	$9+2\times10^{-7}$	7.81
	16	18.192473	1.70	16.051295	4.84	16.000003	8.67
	25	30.396355	0	25.188058	3.88	25.000034	7.58
	36	47.060609	—	36.536021	3.79	36.000205	7.42
$\frac{\pi}{20}$	9	9.167753	2.04	9.000609	3.92	$9+8\times10^{-10}$	7.95
	16	16.533007	2.04	16.003393	3.88	$16+1\times10^{-8}$	7.93
	25	26.309671	2.02	25.012803	3.83	$25+1\times10^{-7}$	7.90
	36	38.735287	1.92	36.037726	3.77	$36+8\times10^{-7}$	7.86
$\frac{\pi}{30}$	9	9.074263	2.02	9.000121	3.97	$9+3\times10^{-11}$	7.98
	16	16.235289	2.02	16.000677	3.96	$16+6\times10^{-10}$	7.98
	25	25.576224	2.03	25.002573	3.94	$25+5\times10^{-9}$	7.97
	36	37.199266	2.04	36.007636	3.92	$36+3\times10^{-8}$	7.96

Table 5.4: First 12 eigenvalues of the Neumann Laplacian Eigenvalue Problem in $I = [0, \pi]$.

h	λ^{ex}	$N=2$	$N=4$	$N=6$	Trend
		λ^h	λ^h	λ^h	
$\frac{\pi}{4}$	0	-6.17×10^{-15}	4.95×10^{-15}	-7.66×10^{-15}	-
	1	1.000512	$1+5\times10^{-9}$	$1+1\times10^{-14}$	↙
	4	4.030089	$4+5\times10^{-6}$	$4+1\times10^{-10}$	↙
	9	9.299730	9.000289	$9+4\times10^{-8}$	↙
	16	16.453667	16.008905	16.000004	↙
	25	31.232513	25.036454	25.000043	↙
	36	52.169393	36.186675	36.000494	↙
	49	80.529469	49.692788	49.003662	↙
	64	97.268336	64.464376	64.002139	↙
	81	—	86.794054	81.083580	↙
	100	—	112.514094	100.287822	↙
	121	—	143.871848	121.833099	↙

In Table 5.3, the order of convergence gets closer to the optimal values since further mesh refinements were utilized. The values λ_m^h in Table 5.4 approach λ_m^{ex} from above except for the zero eigenvalue which bounces between positive and negative values. However, the values are within machine precision. Thus, by choosing $V = H^1(I)$ in (5.1) the error estimates for the eigenfunctions and the eigenvectors turn out to be the expected ones.

5.3 Laplacian Eigenvalue Problems in $\mathbb{R}^2$

The problem discussed in this section is given by:

$$\nabla^2\phi = -\lambda\phi$$

which is referred to as *Helmholtz* equation whenever λ is a prescribed parameter rather than an eigenvalue. Dirichlet and Neumann conditions on a square are considered and then Neumann conditions on L-shape and cracked domain are explored.

For the square geometries, both the eigenfunctions and the eigenvalues will be compared to the analytical results. On the other hand, the L-shape domain together with the cracked domain will be compared to benchmarks[13] to assess their validity.

5.3.1 Dirichlet Problem: Square Domain

Pairing $\nabla^2\phi$ = -$\lambda\phi$ with $\phi|_{\partial\Omega} = 0$ leads to problems often found in science. For instance, if the domain were a membrane, then λ and $\phi(\boldsymbol{x})$ would be related to frequencies of vibration and shape of modes [60], respectively. If, however, Ω portrayed a waveguide, $\phi(\boldsymbol{x})$ would correspond to TM-modes and λ would be associated to a cut-off frequency [47, p. 298]. Thus, even when elementary, appropriate solutions of this problem have a wide range of applications.

Similarly to the $\mathbb{R}^1$ case, a mixed formulation is implemented as to easily incorporate the boundary conditions. In doing so, the weak formulation becomes:

$$\begin{aligned} (\boldsymbol{p},\boldsymbol{u})_\Omega &= -(\nabla\cdot\boldsymbol{p},\phi)_\Omega\,, \quad && \forall\, p\in H_0(\mathrm{div},\Omega) \\ (q,\nabla\cdot\boldsymbol{u})_\Omega &= -\lambda\,(q,\phi)_\Omega\,, && \forall\, q\in L^2(\Omega) \end{aligned}$$

By expanding the functions $\boldsymbol{u}$, $\boldsymbol{p}$ with the basis $\Psi^1(\boldsymbol{x})$ and ϕ, q with the basis $\Psi^2(\boldsymbol{x})$, the following system is obtained:

$$\begin{bmatrix} \mathbb{M}^{(1)} & \left(\mathbb{E}^{2,1}\right)^{\mathrm{T}}\mathbb{M}^{(2)} \\ \mathbb{M}^{(2)}\,\mathbb{E}^{2,1} & 0 \end{bmatrix} \begin{pmatrix} \mathcal{N}^1(u^h) \\ \mathcal{N}^2(\phi^h) \end{pmatrix} = -\lambda \begin{bmatrix} 0 & 0 \\ 0 & \mathbb{M}^{(2)} \end{bmatrix} \begin{pmatrix} \mathcal{N}^1(u^h) \\ \mathcal{N}^2(\phi^h) \end{pmatrix} \tag{5.5}$$

where SCM can be used to further reduce the size of the system.

In a general rectangular domain, the eigenvalues can be analytically computed to be $\lambda_{m,n} = \left(\frac{m\pi}{L_x}\right)^2 + \left(\frac{n\pi}{L_y}\right)^2$ for $(m,n)\in\mathbb{N}$ where L_x and L_y denote the lengths of the rectangle. For simplicity, the problem to be analyzed is set on $\Omega = [0,\pi]^2$ such that $\lambda_{m,n} = m^2 + n^2$ with associated eigenfunctions $\phi_{m,n}(x,y) = \sin(mx)\sin(ny)$.

[13] https://perso.univ-rennes1.fr/monique.dauge/benchmax.html, hosted by *Université de Rennes*

The logic of the solution procedure does not differ from the $\mathbb{R}^1$ case. With the domain defined and the solutions $\lambda^{ex}_{m,n}$ and $\phi^{ex}_{m,n}(\boldsymbol{x})$ known, the next step is to find the eigenvalues of the system in order to define its associated eigenvectors. Once the latter is done, the eigenfunctions are interpolated as $\phi^h_{m,n} = \Psi^0(\boldsymbol{x})\mathcal{N}^0(\phi^h_{m,n})$ and then matched to $\phi^{ex}_{m,n}(\boldsymbol{x})$. As last step, the convergence properties for both $\lambda^h_{m,n}$ and $\phi^h_{m,n}(\boldsymbol{x})$ are computed.

The eigenfunctions $\phi^h_{1,1}$ and $\phi^h_{2,2}$ are shown in Figure 5.7 and Figure 5.8, respectively, where they are compared to the exact results. In Figure 5.9, the convergence for h- and p-refinements was computed for $\phi^h_{1,1}$ while the same is true for $\phi^h_{2,2}$ in Figure 5.10. In both, the order of convergence for h-refinements would stabilize towards the optimal values of N had further mesh elements been used.

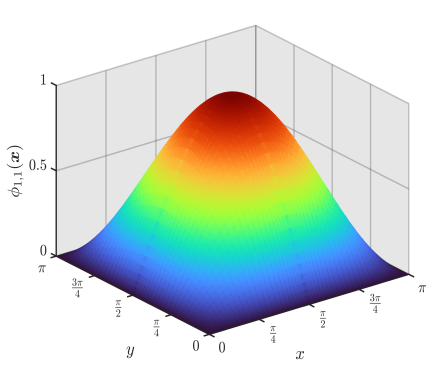

(a) $\phi^h_{1,1} = \Psi^2(\boldsymbol{x})\mathcal{N}^2(\phi^h_{1,1})$

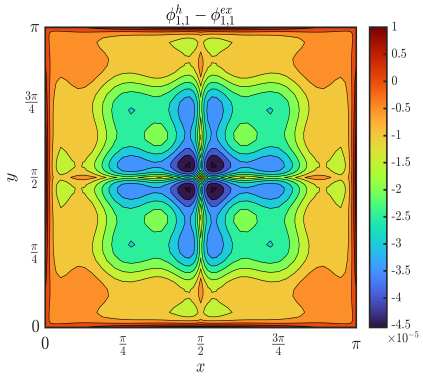

(b) Comparison between $\phi^h_{1,1}$ and $\phi^{ex}_{1,1}$

Figure 5.7: Eigenfunction $\phi^h_{1,1}(\boldsymbol{x})$. Computed using $N = 6$, $K_x = 2$, $K_y = 2$.

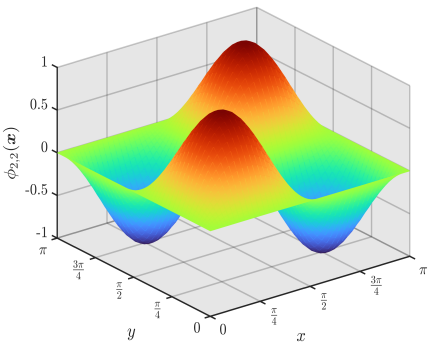

(a) $\phi^h_{2,2} = \Psi^2(\boldsymbol{x})\mathcal{N}^2(\phi^h_{2,2})$

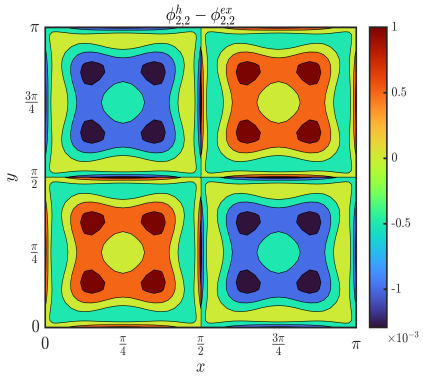

(b) Comparison between $\phi^h_{2,2}$ and $\phi^{ex}_{2,2}$

Figure 5.8: Eigenfunction $\phi^h_{2,2}(\boldsymbol{x})$. Computed using $N = 6$, $K_x = 2$, $K_y = 2$.

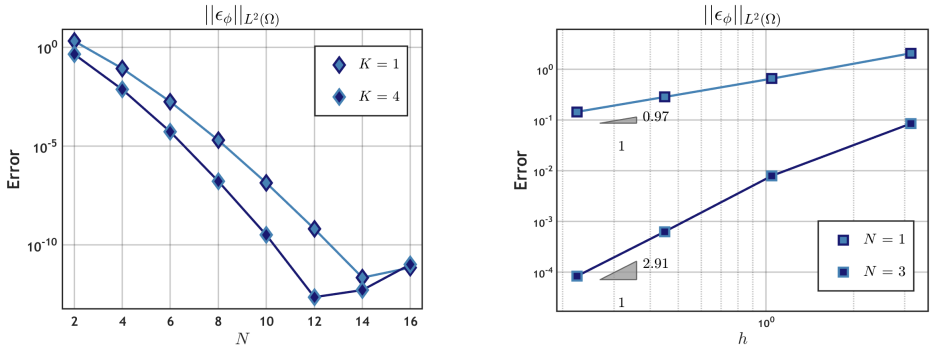

(a) p-convergence (b) h-convergence

Figure 5.9: Convergence trends for $\phi^h_{1,1}$

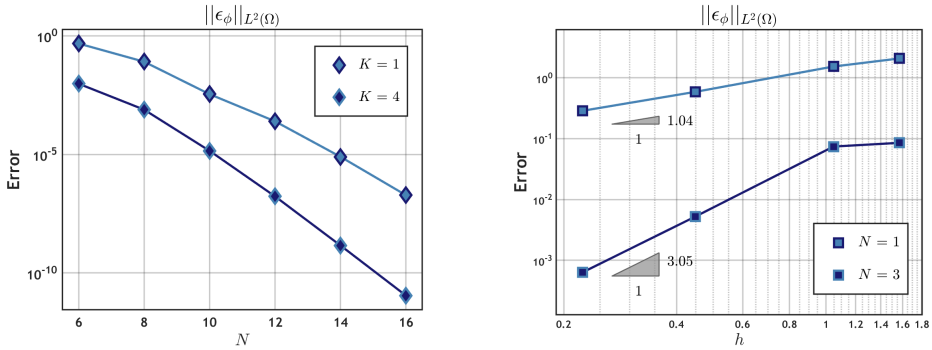

(a) p-convergence (b) h-convergence

Figure 5.10: Convergence trends for $\phi^h_{2,2}$

The convergence properties for $\lambda^h_{m,n}$ are shown in Table 5.5 and Table 5.6. Unlike the $\mathbb{R}^1$ case where all λ were *unique*, this problem has eigenvalues with multiplicity $\mathrm{M} > 1$. For general domains, this value is obtained by observing the number of times a specific λ repeats itself. For this choice of Ω, however, $\mathrm{M} \geq 2$ whenever $m \neq n$ and the the multiplicity can be obtained by decomposing each $\lambda_{m,n}$ into its prime components and applying the formulae in [60, pp. 169-170].

The eigenvalues are sorted from smallest to largest and matched according to their multiplicities. Consider, for example, λ^h in Table 5.6 for $N = 3$. Had M^h not been taken into account, $\lambda^h = 34.47$ would be the approximation to $\lambda = 17$. Moreover, it would be *spurious* as it would approximate an eigenvalue with a distinct multiplicity. Instead, it is set as the estimate of $\lambda = 18$. This is because 18 is the next smallest eigenvalue that matches the multiplicity of λ^h after $\lambda = 13$.

A similar procedure is shown in [9, pp. 39-43] where the rearrangement aims to have a better understanding of the convergence of spurious eigenvalues arising from the approximation of Maxwell Eigenvalue Problem with a nodal basis. However, it was deemed appropriate to use it in this setting.

Table 5.5: Order of Convergence for $\lambda_{1,1}$, $\lambda_{2,2}$, $\lambda_{1,4} = \lambda_{4,1}$ and $\lambda_{5,5}$ for the Dirichlet problem in $\Omega = [0, \pi]^2$.

h	λ^{ex}	$N=1$		$N=3$		$N=5$	
		λ^h	OC	λ^h	OC	λ^h	OC
π	2	2.431708	—	2.001113	—	2+5×10^{-7}	—
	8	—	—	12.158542	—	8.058047	—
	17	—	—	—	—	39.525873	—
	25	—	—	—	—	47.768944	—
$\frac{\pi}{3}$	2	2.188537	0.75	2.000025	3.45	2+3×10^{-10}	6.78
	8	10.942687	—	8.005735	5.99	8.000001	9.84
	17	—	—	17.484064	—	17.001788	8.59
	25	—	—	25.489060	—	25.001791	8.60
$\frac{\pi}{6}$	2	2.046097	2.03	2+4×10^{-7}	5.96	2	6.71
	8	8.754150	1.96	8.000100	5.83	8+1×10^{-9}	9.89
	17	22.908424	—	17.011470	5.40	17.000002	9.57
	25	32.828063	—	25.012699	5.27	25.000002	9.53
$\frac{\pi}{10}$	2	2.016502	2.01	2+2×10^{-8}	5.99	2	2.36
	8	8.266503	2.04	8.000004	5.95	8+1×10^{-11}	8.46
	17	19.200724	1.93	17.000591	5.80	17+1×10^{-8}	9.88
	25	27.876295	1.96	25.000651	5.81	25+1×10^{-8}	9.88

Table 5.6: First 12 eigenvalues of the Dirichlet Laplacian Eigenvalue Problem in $\Omega = [0, \pi]^2$.

h	λ^{ex}	M^{ex}	$N=3$		$N=5$		$N=7$		Trend
			λ^h	M^h	λ^h	M^h	λ^h	M^h	
π	2	1	2.001113	1	2+5×10^{-7}	1	2+6×10^{-11}	1	↙
	5	2	7.079827	2	5.029023	2	5.000133	2	↙
	8	1	12.158542	1	8.058047	1	8.000267	1	↙
	10	2	18.237813	2	10.243071	2	10.003785	2	↙
	13	2	23.316527	2	13.272094	2	13.003918	2	↙
	17	2	—	—	39.528738	2	18.013568	2	↙
	18	1	34.474512	1	18.486142	1	18.000757	1	↙
	20	2	—	—	49.692788	2	21.013702	2	↙
	25	2	—	—	64.464376	2	26.017354	2	↙
	26	2	—	—	86.794054	2	28.941313	2	↙
	29	2	—	—	143.871848	2	31.941447	2	↙
	32	1	—	—	112.514094	1	34.027137	1	↙

5.3.2 Neumann Problem: Square Domain

A direct formulation is implemented as to easily incorporate the boundary conditions. In doing so, the weak form for the eigenvalue problem reads,

$$\left(\nabla\tilde{\phi},\,\nabla\phi\right)_{\Omega} = \lambda\left(\tilde{\phi},\,\phi\right)_{\Omega}, \quad \forall\,\tilde{\phi} \in H^1(\Omega)$$

and, by expanding ϕ and $\tilde{\phi}$ with $\Psi^0(\boldsymbol{x})$, the algebraic system to solve becomes,

$$\left(\mathbb{E}^{1,0}\right)^{\mathrm{T}}\,\mathbb{M}^{(1)}\,\mathbb{E}^{1,0}\,\mathcal{N}^0(\phi^h) = \lambda\,\mathbb{M}^{(0)}\mathcal{N}^0(\phi^h) \tag{5.6}$$

Similarly to the Dirichlet problem, in a general rectangular domain the eigenvalues are given by $\lambda_{m,n} = \left(\frac{m\pi}{L_x}\right)^2 + \left(\frac{n\pi}{L_y}\right)^2$ where L_x and L_y still denote the lengths of the rectangle. However, the pair (m,n) belongs to non-negative integers $\mathbb{Z}^*$ instead of the natural numbers.

For simplicity, the problem to be analyzed is set on $\Omega = [0,\pi]^2$ such that $\lambda_{m,n} = m^2 + n^2$ with associated eigenfunctions $\phi_{m,n}(x,y) = \cos(mx)\cos(ny)$. Similarly to its $\mathbb{R}^1$ counterpart, the solution method follows the same step-by-step procedure and only certain steps are pointed out:

- Since $\phi_{m,n} \in H^1(\Omega)$, the norm $||\epsilon_{\phi_{m,n}}||_{H^1(\Omega)}$ requires $\nabla\phi_{m,n}$ to be computed. Thus, a complete error analysis per pair (m,n) requires the computation of 3 functions. The gradient is obtained from $\nabla\phi^h_{m,n} = \Psi^1(\boldsymbol{x})\,\mathbb{E}^{1,0}\,\mathcal{N}^0(\phi^h_{m,n})$.
- The fact that $\phi_{m,n}(0,0) = 1,\ \forall\,(m,n) \in \mathbb{Z}^*$ is used to match $\phi^h_{m,n}$ to $\phi^{ex}_{m,n}$ by using a constant $c_{m,n} = \frac{1}{\phi^h_{m,n}(0,0)}$. Thus, the numerical eigenfunction becomes $\hat{\phi}^h_{m,n} = c_{m,n}\phi^h_{m,n}$. In an attempt to minimize notation, the normalized approximation is still identified as $\phi^h_{m,n}$ since $c_{m,n}$ lacks importance.
- The components of $\nabla\phi^h_{m,n}$ are matched to $\nabla\phi^{ex}_{m,n}$.
  - For $\frac{\partial}{\partial x}\phi^h_{m,n}$, a matching constant $c^x_{m,n} = \frac{m}{\max(|\frac{\partial}{\partial x}\phi^h_{m,n}|)}$ is utilized.
  - A new variable $\alpha = \max\left(\frac{\partial}{\partial x}\phi^{ex}_{m,n} - \frac{\partial}{\partial x}\phi^h_{m,n}\right)$ is introduced.
  - If $\alpha > 1$, then $c_{m,n}$ is multiplied by -1, otherwise it stays the same.
  - Thus, $\frac{\partial}{\partial x}\hat{\phi}^h_{m,n} = c^x_{m,n}\frac{\partial}{\partial x}\phi^h_{m,n}$ but still referred to as $\frac{\partial}{\partial x}\phi^h_{m,n}$.
  - The procedure is repeated for $\frac{\partial}{\partial y}\phi^h_{m,n}$ using $c^y_{m,n} = \frac{n}{\max(|\frac{\partial}{\partial y}\phi^h_{m,n}|)}$.
- The set of $\lambda^h_{m,n}$ are sorted following the ideas described in Section 5.3.1.
- The error analysis is then normally computed for both $\lambda^h_{m,n}$ and $\phi^h_{m,n}$.

The eigenfunctions $\phi_{1,1}(\boldsymbol{x})$ and $\phi_{3,3}(\boldsymbol{x})$ are represented in Figure 5.11 and Figure 5.12, respectively. The numerical approximations prove to be very close to the analytical results as evidenced by the coefficients on the color bars. The fact that $\phi^h_{1,1}(\boldsymbol{x})$ is much closer to its analytical counterpart than $\phi^h_{3,3}(\boldsymbol{x})$ is to $\phi^{ex}_{3,3}(\boldsymbol{x})$ can be understood as a consequence of the former corresponding to the fourth eigenvalue while the latter corresponds to the twentieth eigenvalue.

In Figure 5.13 and Figure 5.14 the convergence for $\phi^h_{1,1}(\boldsymbol{x})$ and $\phi^h_{3,3}(\boldsymbol{x})$ is shown. Even though the convergence rates for the h-refinement plots do not achieve the optimal rates of N, they are quite close. The disagreement between the values is attributed to the fact that mesh should have been refined with even a further number elements.

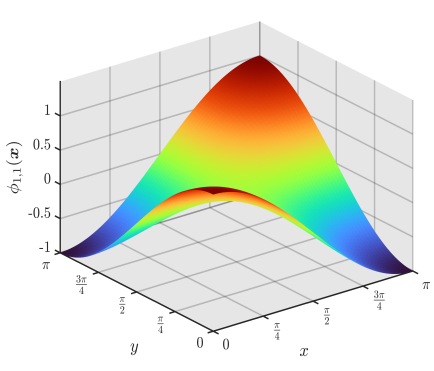

(a) $\phi^h_{1,1} = \Psi^0(\boldsymbol{x})\mathcal{N}^0(\phi^h_{1,1})$

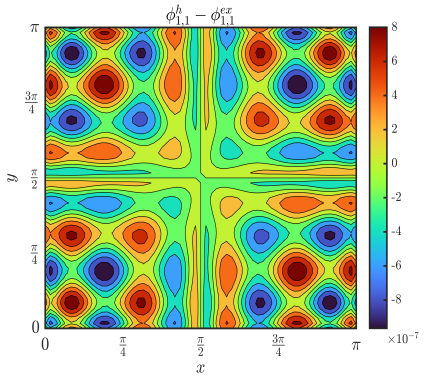

(b) Comparison between $\phi^h_{1,1}$ and $\phi^{ex}_{1,1}$

Figure 5.11: Eigenfunction $\phi_{1,1}(\boldsymbol{x})$. Computed using $N = 6$, $K_x = 2$, $K_y = 2$.

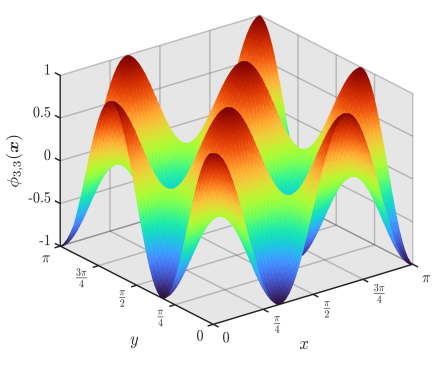

(a) $\phi^h_{3,3} = \Psi^0(\boldsymbol{x})\mathcal{N}^0(\phi^h_{3,3})$

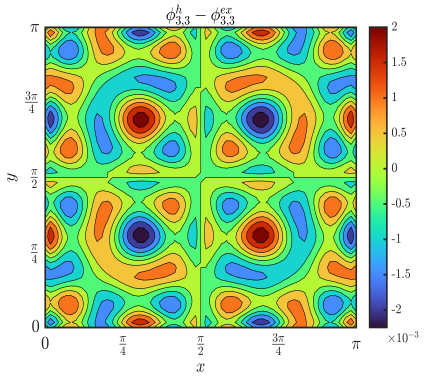

(b) Comparison between $\phi^h_{3,3}$ and $\phi^{ex}_{3,3}$

Figure 5.12: Eigenfunction $\phi_{3,3}(\boldsymbol{x})$. Computed using $N = 6$, $K_x = 2$, $K_y = 2$.

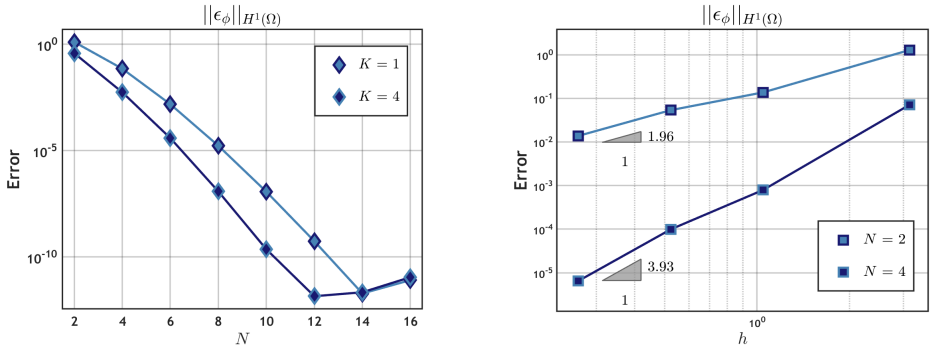

(a) p-convergence (b) h-convergence

Figure 5.13: Convergence trends for $\phi^h_{1,1}$

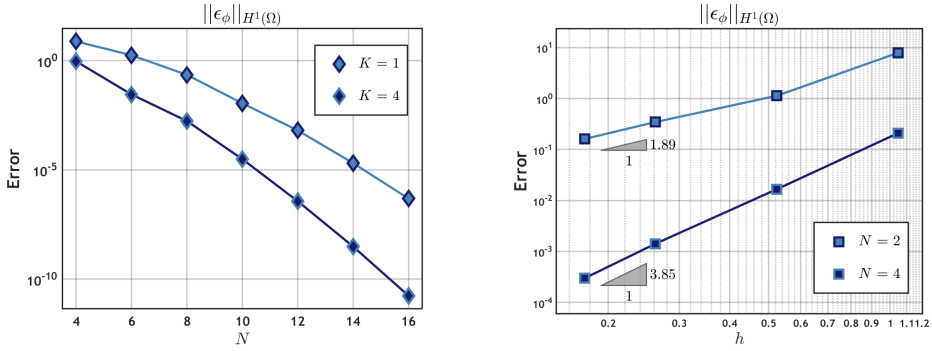

(a) p-convergence (b) h-convergence

Figure 5.14: Convergence trends for $\phi^h_{3,3}$

In Table 5.7 different values of $\lambda^h_{m,n}$ are obtained for a combination of mesh lengths and polynomial approximations. The order of convergence is observed to nearly match the predicted values of $2N$ where, once again, further mesh refinements would lead to the expected values. However, considering the fact that a rate of convergence of 1.96 was obtained for $\phi^h_{1,1}$ with $N = 2$, the value 3.98 for $\lambda^h_{1,1}$ seems to be a reasonable approximation.

In Table 5.8, it is confirmed that $\lambda^h_{m,n}$ approaches $\lambda^{ex}_{m,n}$ from above. Since $\lambda^h_{m,n} = \lambda^h_{n,m}$, the multiplicity of the eigenvalues is taken into account when they are sorted from smallest to largest. In this case, there is no need to use M^h to sort the eigenvalues for the case $N = 2$ since the discrete multiplicities match the exact multiplicities. Nevertheless, this is observed for $\lambda^h_{3,3}$ and $\lambda^h_{4,0} = \lambda^h_{0,4}$ in the $N = 4$ case where the approximations are swapped to match the exact multiplicities.

Had the latter not been done, 34.47 would have been the approximation to $\lambda_{4,0}^{ex}$ when using $N = 2$. In the end, this arrangement gives a better understanding of the early convergence for the discrete eigenvalues but the convergence rates are, nevertheless, reached when either the elements or the polynomial degree is increased.

Table 5.7: Order of Convergence for $\lambda_{1,1}$, $\lambda_{1,2} = \lambda_{2,1}$, $\lambda_{3,2} = \lambda_{2,3}$ & $\lambda_{4,0} = \lambda_{0,4}$ for the Neumann problem in $\Omega = [0, \pi]^2$.

h	λ^{ex}	$N=1$		$N=2$		$N=4$	
		λ^h	OC	λ^h	OC	λ^h	OC
π	2	2.431708	—	2.431708	—	2.001113	—
	5	—	—	7.295125	—	5.029580	—
	13	—	—	—	—	21.266280	—
	16	—	—	—	—	38.525873	—
$\frac{\pi}{3}$	2	2.188537	0.75	2.003162	4.48	$2+1\times10^{-7}$	8.39
	5	6.565612	—	5.089199	2.96	5.000051	5.78
	13	16.414031	—	15.030305	—	13.005060	6.73
	16	21.885375	—	20.924240	—	16.036842	5.83
$\frac{\pi}{6}$	2	2.046097	2.03	2.000205	3.94	$2+4\times10^{-10}$	7.97
	5	5.400124	1.97	5.006428	3.79	$5+2\times10^{-7}$	7.87
	13	15.319762	0.56	13.074026	4.78	13.000012	8.66
	16	21.885375	0	16.350471	3.81	16.000207	7.47
$\frac{\pi}{10}$	2	2.016502	2.01	2.000002	3.98	$2+7\times10^{-12}$	8.00
	5	5.141503	2.03	5.000861	3.93	$5+3\times10^{-9}$	7.96
	13	13.817073	2.04	13.010280	3.86	$13+2\times10^{-7}$	7.92
	16	18.192473	1.93	16.051295	3.86	16.000001	7.85

Table 5.8: First 12 eigenvalues of the Neumann Laplacian Eigenvalue Problem in $\Omega = [0, \pi]^2$.

h	λ^{ex}	M^{ex}	$N=2$		$N=4$		$N=6$		Trend
			λ^h	M^h	λ^h	M^h	λ^h	M^h	
π	0	1	-1.6×10^{-16}	1	-6.1×10^{-16}	1	9.83×10^{-16}	1	-
	1	2	1.215854	2	1.000556	2	$1+2\times10^{-7}$	2	↙
	2	1	2.431708	1	2.001113	1	$2+5\times10^{-7}$	1	↙
	4	2	6.079271	2	4.029023	2	4.000133	2	↙
	5	2	7.295125	2	5.029580	2	5.000133	2	↙
	8	1	12.158542	1	8.058047	1	8.000267	1	↙
	9	2	—	—	17.237256	2	9.243071	2	↙
	10	2	—	—	18.237813	2	10.243071	2	↙
	13	2	—	—	21.266280	2	13.243204	2	↙
	16	2	—	—	38.525873	2	17.013568	2	↙
	17	2	—	—	39.526430	2	18.013569	2	↙
	18	1	—	—	34.474512	1	18.486142	1	↙

5.3.3 Neumann Problem: L-shape Domain

A slight variation of the canonical domain is analyzed in this section where Ω is defined as $\Omega = [-1,1]^2 \setminus ([0,1]) \times [-1,0])$ and shown in Figure 5.15 where homogeneous Neumann conditions are applied at $\partial\Omega$.

The domain is divided into 3 subdomains as to guarantee that the mesh covers the geometry correctly. Each subdomain Ω_k can further be divided into additional subdomains which will be useful when testing the order of convergence of the eigenvalues when decreasing the element dimensions.

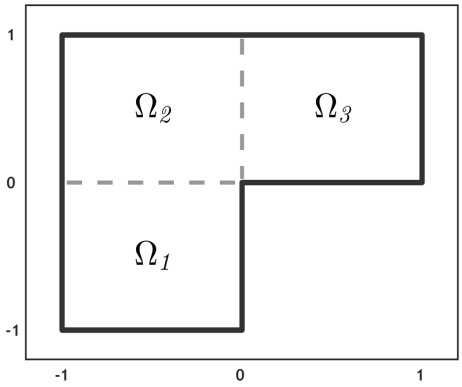

Figure 5.15: L-Shape domain with subdomains Ω_1, Ω_2 & Ω_3.

A direct method is utilized. The weak form and its associated algebraic system follows what was described in Section 5.3.2. The shape of the domain is taken into consideration in the discrete algebraic system by the *Gathering Matrix* which ensures the correct degrees of freedom are glued together.

A first look at the eigenvalues of the system is shown in Table 5.9. The data was obtained using 4 elements inside each subdomain Ω_k and rounded to 10 decimals for better visualization. The number of digits the approximation shares with the reference data is highlighted in orange.

Table 5.9: First 4 unique eigenvalues $\lambda > 0$ of $\nabla^2\phi = -\lambda\phi$ on the L-shape domain with Neumann boundary conditions. $\lambda_3 = \lambda_4$.

h	λ, Ref. [29]	M	$N=3$	$N=6$	$N=12$	Trend
			λ^h	λ^h	λ^h	
$\frac{1}{2}$	$\lambda_1 = 1.4756218239$	1	1.4806823505	1.4766193150	1.4758040123	↙
	$\lambda_2 = 3.5340313667$	1	3.5341855045	3.5340363069	3.5340315259	↙
	$\lambda_3 = 9.8696044010$	2	9.8709526500	9.8696044014	9.8696044010	↙
	$\lambda_5 = 11.3894793979$	1	11.3909756632	11.3894864072	11.3894796256	↙

It might come as a surprise that the first eigenvalue in Table 5.9 shows such a poor convergence. This is due to the fact that it is connected to a strong unbounded singularity [29]. The eigenvalue with multiplicity 2 is analytic with exact value π^2. The other two eigenvalues are linked to functions with rapid changes at the re-entrant corner which affects their convergence.

A more quantitative approach to the latter issue is shown in Table 5.10 where the order of convergence is computed for a series of parameters h and N.

Table 5.10: Order of Convergence for the first 4 unique eigenvalues $\lambda > 0$.
Neumann problem in $\Omega = [-1,1]^2 \setminus ([0,1] \times [-1,0])$.

h	λ, Ref. [29]	$N=3$		$N=4$		$N=6$	
		λ^h	OC	λ^h	OC	λ^h	OC
1	1.4756218239	1.4882540083	—	1.4821290680	—	1.4781256929	—
	3.5340313667	3.5355705135	—	3.5342665658	—	3.5340624602	—
	9.8696044010	9.8750975039	—	9.8750975039	—	9.8696070069	—
	11.3894793979	11.3969742650	—	11.3950366850	—	11.3895253478	—
$\frac{1}{2}$	λ_1	1.4806823505	1.31	1.4782275811	1.32	1.4766193150	1.32
	λ_2	3.5341855045	3.32	3.5340667750	2.73	3.5340363069	2.65
	λ_3	9.8709526500	2.03	9.8696178789	8.67	9.8696044015	12.6
	λ_5	11.3909756635	2.32	11.3895416689	6.48	11.3894864072	2.71
$\frac{1}{4}$	λ_1	1.4776315157	1.33	1.4766561029	1.33	1.4760176666	1.33
	λ_2	3.5340541285	2.76	3.5340369641	2.66	3.5340321453	2.66
	λ_3	9.8696268913	5.91	9.8696044564	7.93	9.8696044010	2.00
	λ_5	11.3895327936	4.81	11.3894873966	2.96	11.3894805098	2.65
$\frac{1}{7}$	λ_1	1.4765749004	1.33	1.4761122586	1.33	1.4758095221	1.33
	λ_2	3.5340364695	2.67	3.5340326268	2.66	3.5340315418	2.66
	λ_3	9.8696051955	5.97	9.8696044017	7.98	9.8696044010	—
	λ_5	11.3894874041	3.40	11.3894811971	2.67	11.3894796485	2.66
$\frac{1}{9}$	λ_1	1.4763035405	1.33	1.4759726161	1.33	1.4757560788	1.33
	λ_2	3.5340339780	2.67	3.5340320115	2.66	3.5340314563	2.66
	λ_3	9.8696045774	5.99	9.8696044011	8.02	9.8696044010	—
	λ_5	11.3894832862	2.87	11.3894803196	2.66	11.3894795262	2.66

A rate of convergence stabilizing at 1.33 is attained for λ_1 regardless of N or h caused by the strong singular behavior of $\nabla\phi$ at the re-entrant corner. For λ_2, the rate stabilizes at 2.66 which already indicates some sort of non-smoothness on the functions associated to the eigenvalue. For λ_5, the computed rates also stabilized towards 2.66 except for the $N = 3$ case. Had further mesh refinements been computed, the rate would have reached the specified value based on the fact that it shows a decreasing tendency. The eigenvalues have different speeds of convergence according to the different regularities of their associated eigenfunctions [9].

Even though it is not possible to know *a priori* if the convergence rate of an eigenvalue will be affected by the non-smoothness of its eigenfunction, it is known that the presence of corners leads to singular behavior regardless of the smoothness of the boundary conditions [75]. Methods such as the classical *Finite Element Method* or, in this case, a *Mimetic Spectral Method* can, obviously, still be utilized even when the global solution is not smooth. The price to pay is a lower convergence rate which, as seen in Table 5.10, manifests itself on the convergence of λ^h.

On the other hand, λ_3 and λ_4 converge at a rate of $2N$ since they are not associated to singularities anywhere in Ω. Their last computed rate of convergence is highlighted in gray in Table 5.10. For $N = 6$, the eigenvalue converges so fast that for $h = 1/4$, the rate decreases at 2 and then it reaches the reference value up to 10 decimal places. Previous to this, a rate of 12.6 is attained (highlighted in blue).

Finally, contours and surfaces for the functions $\phi(\boldsymbol{x})$ and $\nabla\phi(\boldsymbol{x})$ are shown in Appendix C for the five eigenvalues considered in this section where it can be observed that the eigenvalues with sub-optimal convergence rates are connected to functions where rapid changes occur at the *re-entrant* corner and its vicinity.

5.3.4 Neumann Problem: Cracked Domain

The analysis is now shifted to $\Omega = [-1, 1]^2 \setminus \{(x_1, x_2) \in \mathbb{R}^2 : 0 \leq x < 1,\ y = 0\}$ with Neumann conditions at $\partial\Omega$. The geometry is *pre-divided* into 4 subdomains Ω_k which can be further split into additional subdomains. This is shown in Figure 5.16.

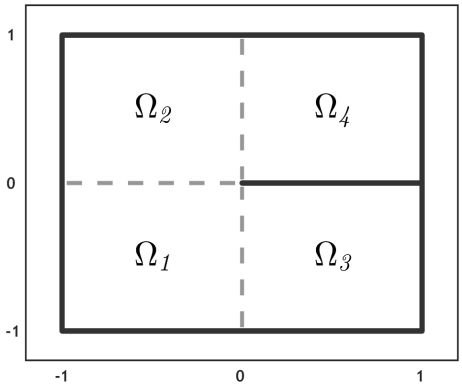

Figure 5.16: Cracked domain. Subdomains Ω_3 & Ω_4 are disconnected except at $(x, y) = (0, 0)$.

A direct method together with a *Gathering Matrix* is utilized. A first look at the eigenvalues of the system is shown in Table 5.11. The data was obtained using one element inside each subdomain Ω_k, hence, a total of 4 elements cover the whole

geometry. The values are truncated to 10 decimals for better visualization and the digits shared between the approximation and the reference are highlighted in orange.

Table 5.11: First 9 unique eigenvalues $\lambda > 0$ of the Laplacian Eigenvalue Problem on the Cracked domain from Figure 5.16 with Neumann boundary conditions.

h	λ, Ref. [29]	M	$N = 3$	$N = 6$	$N = 12$	Trend
			λ^h	λ^h	λ^h	
	1.0340740085	1	1.0790348792	1.0473612226	1.0377843991	↙
	2.4674011002	1	2.4677381625	2.4674011003	2.4674011002	↙
	4.0469252914	1	4.0483807778	4.0469413826	4.0469256263	↙
	9.8696044010	2	9.8750975039	9.8696070069	9.8696044010	↙
1	10.8448542781	1	10.8523145614	10.8448790789	10.8448547485	↙
	12.2648958490	1	12+0.34283566	12+0.31537842	12.2791265269	↙
	12.3370055014	1	12+0.44157406	12.3370081072	12.3370055014	↙
	19.7392088022	1	19.7501950079	19.7392140138	19.7392088022	↙
	21.2441074562	1	20+2.13741675	21+0.33478577	21.2696644450	↙

Once again, some eigenvalues approach faster to the reference data while others stagnate. The eigenvalues λ_2, $\lambda_4 = \lambda_5$, λ_8 and λ_9 are equal to $\pi^2/4$, π^2, $5\pi^2/4$ and $2\pi^2$, respectively [29], and, unsurprisingly, for $N = 12$ they already match the reference data up to 10 decimals. The latter *might* be already an indication that they are not associated to eigenfunctions with singularities. A more quantitative approach, however, is shown at Table 5.12 where the rates of convergence are computed.

The last computed order of convergence for λ_2, $\lambda_4 = \lambda_5$, λ_8 and λ_9 is highlighted in gray. For all the polynomial cases, the rates are basically the optimal value of $2N$. For $N = 6$, the approximations converge so fast that only after two iterations in h, this set of eigenvalues has already matched the reference data. The functions $\phi(\boldsymbol{x})$ and $\nabla\phi(\boldsymbol{x})$ related to these eigenvalues are continuous through the whole domain even when continuity is not enforced at the line $y = 0$ for $x > 0$.

All the other eigenvalues are split into two groups. The first group is associated to functions $\nabla\phi(\boldsymbol{x})$ which exhibit a peak at $(x, y) = (0, 0)$ while the second group consists of functions that are discontinuous at the cracked line. The former group shows a rate of convergence of unity while the latter stabilizes at a rate of 3 as seen in Table 5.12. This reinforces the fact that the convergence is attached to the regularity of the functions which, in this case, includes the gradient since $\phi \in H^1(\Omega)$.

Surfaces and contours for $\phi(\boldsymbol{x})$ and $\nabla\phi(\boldsymbol{x})$ can be found at Appendix D. In there, it can be visually proved that the eigenvalues λ_1, λ_7 and λ_{10} are associated to functions with a strong singular behavior at the origin. For λ_3 and λ_6, it can be noted that the associated functions are discontinuous at the cracked line and,

finally, the analytic eigenvalues are entirely continuous through Ω even when the *Gathering Matrix* **does not** impose continuity in that region of the domain.

Table 5.12: Order of Convergence for the first 9 unique eigenvalues $\lambda > 0$.
Neumann problem in $\Omega = [-1, 1]^2 \setminus \left\{(x_1, x_2) \in \mathbb{R}^2 : 0 \leq x < 1,\ y = 0\right\}$.

h	λ, Ref. [29]	$N = 3$		$N = 4$		$N = 6$	
		λ^h	OC	λ^h	OC	λ^h	OC
	1.0340740085	1.0790348792	—	1.0613797335	—	1.0473612226	—
	2.4674011002	2.4677381625	—	2.467404 4697	—	2.4674011002	—
	4.0469252914	4.0483807777	—	4.0470978345	—	4.0469413825	—
	9.8696044010	9.8750975039	—	9.87509750395	—	9.8696070068	—
1	10.8448542781	10.8523145613	—	10.8504241168	—	10.8448790789	—
	12.2648958490	12+0.34283566	—	12+0.34250197	—	12+0.31537842	—
	12.3370055014	12+0.44157406	—	12.3760785966	—	12.3370081072	—
	19.7392088022	19.7501950079	—	19.7501950079	—	19.7392140137	—
	21.2441074562	20+2.13741675	—	21+0.50434331	—	21+0.33478577	—
	λ_1	1.0565554926	0.99	1.0477298023	0.99	1.0407158352	1.00
	λ_2	2.4674067228	5.90	2.4674011141	7.92	2.4674011002	—
	λ_3	4.0470333920	3.75	4.0469443121	3.18	4.0469273200	2.98
	λ_4	9.8709526501	2.02	9.8696178789	8.67	9.8696044010	12.8
$\frac{1}{2}$	λ_6	10.8463125005	2.35	10.8448936732	7.14	10.8448571133	3.12
	λ_7	12+0.33835937	0.08	12+0.31676536	0.58	12.2903052571	0.99
	λ_8	12+0.35156571	2.84	12.3370189930	11.5	12.3370055014	12.9
	λ_9	19.7419053001	2.02	19.7392357579	8.67	19.7392088022	12.8
	λ_{10}	21+0.41565564	2.38	21+0.33741211	1.48	21.2897321268	0.99
	λ_1	1.0452577028	1.00	1.0408794896	1.00	1.0373893446	1.00
	λ_2	2.4674011895	5.97	2.4674011002	7.84	2.4674011002	—
	λ_3	4.0469372945	3.17	4.0469276742	2.99	4.0469255449	3.00
	λ_4	9.8696268913	5.90	9.8696044564	7.92	9.8696044010	—
$\frac{1}{4}$	λ_6	10.8448929075	5.23	10.8448576808	3.53	10.8448546359	2.98
	λ_7	12+0.30751256	0.78	12.2909267357	0.99	12.2776153091	0.99
	λ_8	12.3370280808	9.33	12.3370055567	7.92	12.3370055014	—
	λ_9	19.7392537826	5.90	19.7392089128	7.92	19.7392088022	—
	λ_{10}	21+0.32083659	1.16	21.2908475534	0.99	21.2669504751	0.99
	λ_1	1.0415163491	1.00	1.0386058247	1.00	1.0362829644	1.00
	λ_2	2.467401 1081	5.97	2.4674011002	—	2.4674011002	—
	λ_3	4.0469288132	3.17	4.0469259980	2.99	4.0469253665	3.00
	λ_4	9.8696063994	5.90	9.869604432	7.97	9.8696044010	—
$\frac{1}{6}$	λ_6	10.8448611829	5.23	10.8448552778	3.02	10.8448543844	2.99
	λ_7	12.2933465951	0.78	12.2822650492	0.99	12.2733777582	0.99
	λ_8	12.3370075075	9.33	12.337005535	8.02	12.3370055014	—
	λ_9	19.7392127988	5.90	19.739208865	7.98	19.7392088022	—
	λ_{10}	21.2952088630	1.16	21.2752999006	0.99	21.2593399257	0.99
	λ_1	1.0404497979	1.00	1.0379571403	1.00	1.0359670848	1.00
	λ_2	2.467401 1033	5.99	2.4674011002	—	2.4674011002	—
	λ_3	4.0469275067	3.00	4.0469257364	2.99	4.0469253387	2.99
	λ_4	9.8696051955	5.98	9.869604401 7	7.95	9.8696044010	—
$\frac{1}{7}$	λ_6	10.8448581779	3.70	10.8448549078	2.99	10.8448543451	2.99
	λ_7	12.2892927775	0.99	12.2797868062	0.99	12.2721665266	0.99
	λ_8	12.3370062989	5.98	12.337005502 0	8.24	12.3370055014	—
	λ_9	9.73921103911	5.98	19.739208803 4	8.07	19.7392088023	—
	λ_{10}	21.2879224554	0.99	21.2708499295	0.99	21.2571645328	0.99

6

Maxwell Eigenvalue Problem

The present chapter is devoted to the solution of the eigenvalue problem for the Maxwell equations. Specifically, the eigenvalue problem for the electric field will be tackled in conjunction with $\mathbf{n} \times \mathbf{E} = 0$ at $\partial\Omega$ (PEC boundary conditions). This part of the thesis is segmented as follows:

- In Section 6.1 the discrete variational formulation for the problem will be discussed and put together in terms of the mass and incidence matrices discussed back in Chapter 3. Furthermore, the addition of the linear constraint $\nabla \cdot \mathbf{D} = 0$ will be discussed and implemented.

- In Section 6.2, isotropic material properties will be utilized and the eigenvalue problem will be solved first in a square domain. Such results should resemble, up to certain extent, those from Section 5.3.2 and will be used as a guideline to verify that the implementation has been correctly executed. The methodology will then be utilized on domain with a unconnected boundary. Finally, the framework will be applied to a domain constituted by two different types of isotropic materials.

- In Section 6.3, anisotropic permittivity tensors will be used along with $\underline{\underline{\mu}} = \mathbb{I}$. A square domain will be analyzed first as to observe the influence of the off-diagonal entries of $\underline{\underline{\epsilon}}$ on λ. The analysis will then be shifted to an H-domain where a permittivity tensor with complex-valued entries will be utilized.

6.1 Mimetic Spectral Formulation

The first step in defining the sought discrete formulation consists on recalling the variational formulation shown in Equation 2.16 for the electric field $\mathbf{E}$. The equation is repeated below for convenience and reads,

$$\int_\Omega \left(\nabla \times \widetilde{\mathbf{E}}\right) \cdot \left(\underline{\underline{\mu}}^{-1} \nabla \times \mathbf{E}\right) \, \mathrm{d}\Omega = \omega^2 \int_\Omega \widetilde{\mathbf{E}} \, \underline{\underline{\epsilon}} \, \mathbf{E} \, \mathrm{d}\Omega, \quad \forall \, \widetilde{\mathbf{E}} \in H_0(\mathrm{curl}; \Omega) \tag{6.1}$$

where ω^2 and $\mathbf{E}$ are the sought eigenvalue and eigenfunction, respectively, while $\widetilde{\mathbf{E}}$ is the test function. Secondly, by using the Tonti diagram shown in Figure 2.7, it is observed that the spatial part of $\mathbf{E}$ is associated to inner oriented lines. Such orientation is inherited from its global variable *voltage* as explained in Section 2.2.3.

The latter suggests that the correct interpolation for the electric field is given by $\mathbf{E} = \Psi^1(\boldsymbol{x}) \mathcal{N}^1(\mathrm{E}^h)$ with a similar treatment for $\widetilde{\mathbf{E}}$. Constructing the curl operator is achieved with an incidence matrix as shown in (3.36). In the next section, these details are used to obtain the discrete system for the curl-curl problem.

6.1.1 Omission of Divergence-Free Condition

As established before, the electric field is associated to lines such that its set of basis functions is defined to be $\Psi^1(\boldsymbol{x})$ and, as a result, $\nabla \times \mathbf{E} = \Psi^2(\boldsymbol{x}) \, \mathbb{E}^{2,1}_{\mathrm{curl}} \mathcal{N}(\mathrm{E}^h)$. By inserting this information into (6.1), the following is obtained:

$$\int_\Omega \Psi^2(\boldsymbol{x}) \, \mathbb{E}^{2,1}_{\mathrm{curl}} \, \mathcal{N}^1(\tilde{\mathrm{E}}^h) \, \underline{\underline{\mu}}^{-1} \, \Psi^2(\boldsymbol{x}) \mathbb{E}^{2,1}_{\mathrm{curl}} \mathcal{N}^1(\mathrm{E}^h) \, \mathrm{d}\Omega = \cdots$$

$$\cdots = \omega^2 \int_\Omega \Psi^1(\boldsymbol{x}) \, \mathcal{N}^1(\tilde{\mathrm{E}}^h) \, \underline{\underline{\epsilon}} \, \Psi^1(\boldsymbol{x}) \, \mathcal{N}^1(\mathrm{E}^h) \, \mathrm{d}\Omega$$

In a following step, some terms are rearranged as follows:

$$\left(\mathbb{E}^{2,1}_{\mathrm{curl}}\right)^{\mathrm{T}} \left(\int_\Omega \Psi^2(\boldsymbol{x})^{\mathrm{T}} \underline{\underline{\mu}}^{-1} \, \Psi^2(\boldsymbol{x}) \, \mathrm{d}\Omega \right) \mathbb{E}^{2,1}_{\mathrm{curl}} \, \mathcal{N}^1(\mathrm{E}^h) = \cdots$$

$$\cdots = \omega^2 \left(\int_\Omega \Psi^1(\boldsymbol{x})^{\mathrm{T}} \underline{\underline{\epsilon}} \, \Psi^1(\boldsymbol{x}) \, \mathrm{d}\Omega \right) \mathcal{N}^1(\mathrm{E}^h)$$

where the first and second integral are renamed as $\mathbb{M}^{(2)}_{\underline{\underline{\mu}}^{-1}}$ and $\mathbb{M}^{(1)}_{\underline{\underline{\epsilon}}}$, respectively. In fact, both matrices reduce to the ones used in the 2D problems from Chapter 4 and Chapter 5 whenever the material parameters are equal to the identity tensor.

6.1.2 Linear Constraint $\nabla \cdot \mathbf{D} = 0$

As specified in Section 2.5.3, failing to couple the curl-curl problems with their respective divergence-free conditions has the potential to generate non-physical solutions. A possible remedy relies on utilizing *penalty methods* which employ formulations as the ones presented in (2.19) and (2.20). However, this approach will not be explored in this thesis. Alternatively, the *Kikuchi formulation* [56] shown in (2.18) can be utilized. Even though the latter was deduced for $\underline{\underline{\epsilon}} = \underline{\underline{\mu}} = \mathbb{I}$, introducing general material properties is trivial as shown below,

$$\Big(\operatorname{curl}\tilde{\mathrm{E}}, \underline{\underline{\mu}}^{-1}\operatorname{curl}\mathrm{E}\Big) + \Big(\underline{\underline{\epsilon}}\,\tilde{\mathrm{E}}, \operatorname{grad} p\Big) = \lambda\Big(\tilde{\mathrm{E}}, \underline{\underline{\epsilon}}\,\mathrm{E}\Big), \quad \forall\, \tilde{\mathrm{E}} \in H_0(\operatorname{curl};\Omega) \tag{6.2a}$$

$$\Big(\operatorname{grad} q, \underline{\underline{\epsilon}}\,\mathrm{E}\Big) = 0, \qquad \forall\, q \in H_0^1(\Omega) \tag{6.2b}$$

where the objective is to find $(\lambda, \mathrm{E}, p) \in \mathbb{R}^1 \times H_0(\operatorname{curl};\Omega) \times H_0^1(\Omega)$ with p acting as a dummy variable (*Lagrange Multiplier*) that has no physical meaning.

At this point, the main focus is to discretize the variables paired with the *gradient* operators. Based on the Neumann Poisson problems solved in previous chapters, it is clear that such variables are associated to nodes. However, the degrees of freedom could belong to either the primal or, possibly, the dual mesh.

Such dilemma can be solved by recalling that the number of spurious zero eigenvalues is equal to the number of internal nodes in the mesh when $\partial\Omega$ is simply connected [80, p. 127]. Thus, the system (6.2) is solved in the mesh from Figure 6.1 with $p = q = 0$ such that the curl-curl problem is retrieved without the divergence constraint. Such domain discretization can be achieved by either 9 elements with $N = 1$ or one element with $N = 3$. In order to avoid dealing with multi-element formulations for the initial testing, the latter option is chosen.

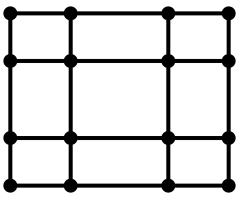

Figure 6.1: Primal Mesh for the Maxwell Eigenvalue Problem with 4 internal nodes.

Since this test is only used to determine the number of zero eigenvalues the formulation would generate, the size of the domain is irrelevant. For the selected mesh, the multiplicity of the zero eigenvalue was found to be 4 which equals the number of internal nodes of the mesh. Hence, the variables associated to the gradient

in the system (6.2) belong to the same mesh as the field $\mathbf{E}$. The nodes at the boundary are not taken into account since $p \in H_0^1(\Omega)$.

The *Kikuchi formulation* with general material parameters can now be discretized by using $p = \Psi^0(\boldsymbol{x})\mathcal{N}^0(p^h)$ which means that $\nabla p = \Psi^1(\boldsymbol{x})\mathbb{E}^{1,0}_{\text{grad}}\mathcal{N}^0(p^h)$ with the test function q undergoing the same treatment. Thence, the discretized mixed formulation becomes:

$$\underbrace{\begin{bmatrix} \left(\mathbb{E}^{2,1}_{\text{curl}}\right)^{\mathrm{T}} \mathbb{M}^{(2)}_{\underline{\underline{\mu}}^{-1}} \mathbb{E}^{2,1}_{\text{curl}} & \mathbb{M}^{(1)}_{\underline{\underline{\epsilon}}} \mathbb{E}^{1,0}_{\text{grad}} \\ \left(\mathbb{E}^{1,0}_{\text{grad}}\right)^{\mathrm{T}} \mathbb{M}^{(1)}_{\underline{\underline{\epsilon}}} & 0 \end{bmatrix}}_{\text{LHS}} \begin{pmatrix} \mathcal{N}^1(\mathrm{E}^h) \\ \mathcal{N}^0(p^h) \end{pmatrix} = \lambda \underbrace{\begin{bmatrix} \mathbb{M}^{(1)}_{\underline{\underline{\epsilon}}} & 0 \\ 0 & 0 \end{bmatrix}}_{\text{RHS}} \begin{pmatrix} \mathcal{N}^1(\mathrm{E}^h) \\ \mathcal{N}^0(p^h) \end{pmatrix} \tag{6.3}$$

With this formulation, the large null space of the curl-curl operator is removed and for the mesh from Figure 6.1 it means that the zero eigenvalue with multiplicity 4 disappears as a solution. This does not signify that the sole purpose of (6.3) is to eliminate zero eigenvalues. In some cases, $\lambda = 0$ could be an acceptable solution and the formulation should allow for such. This will be tested in Section 6.2.2.

6.2 Isotropic Permitivity Tensor

In this section, a permittivity tensor of the form $\underline{\underline{\epsilon}} = \mathbb{I}$ will be utilized. A bit more general tensor such as $\varepsilon\,\mathbb{I}$ with $\varepsilon \in \mathbb{R}_{>0}$ could be utilized but it does not lead to a more general situation. This claim is easily verified by considering the vector differential equation for the Maxwell Eigenvalue Problem for the field $\mathbf{E}$ with $\underline{\underline{\epsilon}} = \varepsilon\,\mathbb{I}$:

$$\nabla \times \left(\underline{\underline{\mu}}^{-1} \nabla \times \mathbf{E}\right) = \omega^2\,\varepsilon\,\mathbb{I}\,\mathbf{E} \quad \xrightarrow{\Lambda = \omega^2\,\varepsilon} \quad \nabla \times \left(\underline{\underline{\mu}}^{-1} \nabla \times \mathbf{E}\right) = \Lambda\,\mathbf{E}$$

which immediately suggests that multiplying the permittivity tensor by a scalar is the same as solving the eigenvalue problem for a modified eigenvalue with the permittivity being equal to the identity tensor.

6.2.1 Square Domain

The domain $\Omega = [0,\,\pi]^2$ is considered. Non-trivial solutions for the field $\mathbf{E}$ satisfying the Maxwell Eigenvalue Problem are sought when $\underline{\underline{\epsilon}}$ and $\underline{\underline{\mu}}$ are equal to the identity tensor. Under such conditions, the analytical eigenfunctions are computed from $\mathbf{E}_{m,n}(\boldsymbol{x}) = \text{curl}(\phi_{m,n})$ with $\phi_{m,n}(\boldsymbol{x}) = \cos(mx)\cos(ny)$ while the eigenvalues are given by $\lambda^2_{m,n} = m^2 + n^2$ with $(m, n) \in \mathbb{Z}^*$. However, the combination $(m, n) = (0, 0)$ is not allowed since it leads to $\mathbf{E}(\boldsymbol{x}) = 0$ due to the constraint $\nabla \cdot \mathbf{D} = 0$ and the boundary condition $\mathbf{n} \times \mathbf{E} = 0$.

The main difference from the problems discussed in Chapter 5, despite the unknown being a vector-valued function, relies on the fact that $\mathbf{E} \in H_0(\text{curl};\Omega)$ which implies that the norm $||\epsilon_{\mathbf{E}_{m,n}}||_{H(\text{curl};\Omega)}$ has to be used. Thus, a complete error analysis per pair (m,n) requires the components of $\mathbf{E}$ in addition to $\nabla \times \mathbf{E}$.

Additionally, each computed function has to be matched to its analytical counterpart such that the error norm can be correctly determined. This process follows exactly the course of action described thoroughly in Section 5.3.2 and, hence, not repeated here. The only comments worth mentioning are the ones related to the matching constants $c_{m,n}$ since those differ from the ones of previous examples.

- The matching constant $c^x_{m,n} = \frac{n}{\max\left(\left|\left(\mathrm{E}^h_x\right)_{m,n}\right|\right)}$ was defined for E_x.
- The matching constant $c^y_{m,n} = \frac{m}{\max\left(\left|\left(\mathrm{E}^h_y\right)_{m,n}\right|\right)}$ was defined for E_y.
- For $\nabla \times \mathbf{E}^h$, the already normalized components E^h_x and E^h_y are utilized.
- The term $|\mathbf{E}^h|$ was also computed but it was matched to an amplitude of unity.
- The numerical functions used for the error computation would then be the matching constant multiplied by their corresponding function.

In Figure 6.2, the components of the field $\mathbf{E}$ are plotted for $\lambda_{1,1}$. In order to assess how well they represent the actual solution, $|\mathbf{E}^h_{1,1}|$ was compared to $|\mathbf{E}^{ex}_{1,1}|$ as shown in Figure 6.3. Similarly, in Figure 6.4, $\nabla \times \mathbf{E}^h_{1,1}$ and its analytical counterpart are contrasted. The numerical approximations were computed with $N = 8$ and 4 spectral elements. The same type of comparisons can be found in Figure 6.5, Figure 6.6 and Figure 6.7 for $\lambda_{4,4}$.

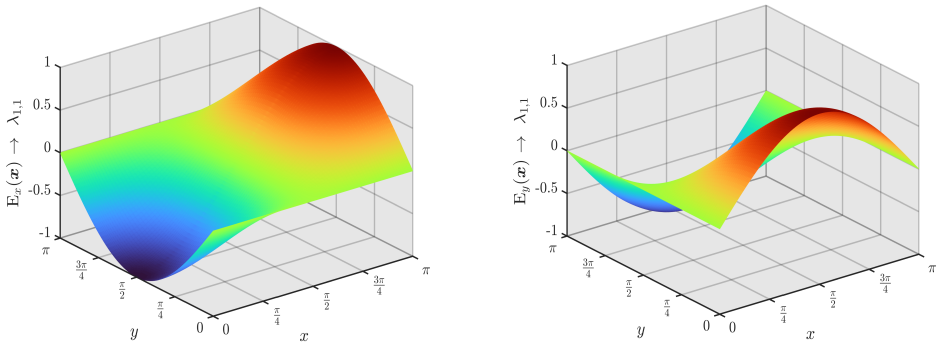

(a) E^h_x (b) E^h_y

Figure 6.2: Components of $\mathbf{E}^h_{1,1}(\boldsymbol{x}) = \Psi^1(\boldsymbol{x})\mathcal{N}^1(\mathrm{E}^h)$. Computed using $N = 8$, $K_x = 2$, $K_y = 2$.

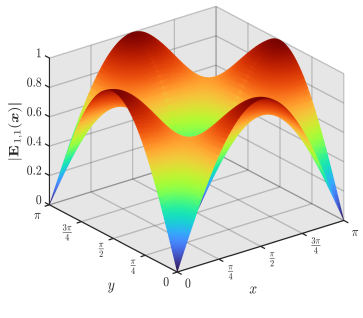

(a) $|\mathbf{E}^h| = \sqrt{(\mathrm{E}_x^h)^2 + (\mathrm{E}_y^h)^2}$

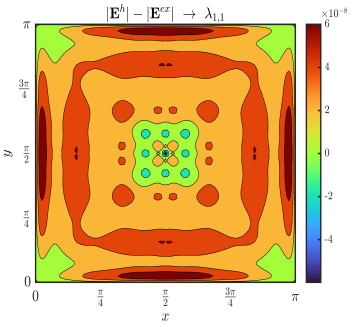

(b) Comparison between $|\mathbf{E}^h|$ and $|\mathbf{E}^{ex}|$

Figure 6.3: Norm $\left|\mathbf{E}_{1,1}^h\right|$ (*left*) and its comparison to the analytical solution (*right*). Discrete system solved with $N = 8$, $K_x = 2$, $K_y = 2$.

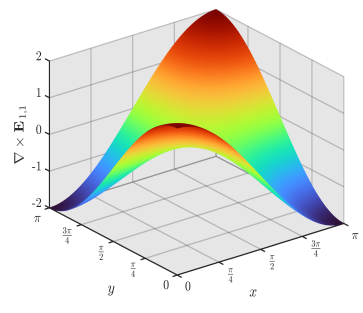

(a) $\nabla \times \mathbf{E}^h = \Psi^2(\boldsymbol{x})\,\mathbb{E}^{2,1}\,\mathcal{N}^1(\mathrm{E}^h)$

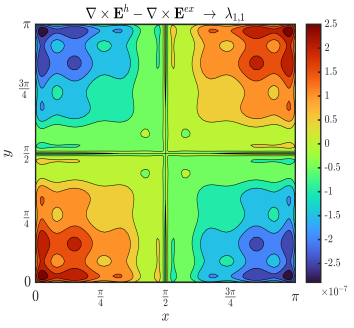

(b) Comparison between $\nabla \times \mathbf{E}^h$ and $\nabla \times \mathbf{E}^{ex}$

Figure 6.4: Function $\nabla \times \mathbf{E}_{1,1}^h$ (*left*) and its comparison to the analytical solution (*right*). Discrete system solved with $N = 8$, $K_x = 2$, $K_y = 2$.

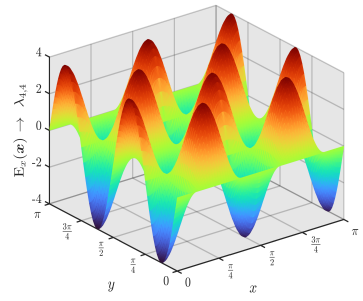

(a) E_x^h

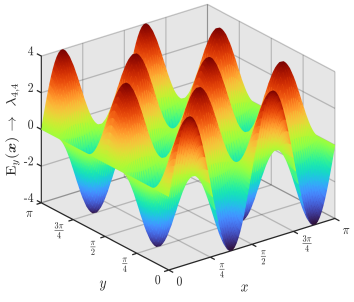

(b) E_y^h

Figure 6.5: Components of $\mathbf{E}_{4,4}^h(\boldsymbol{x}) = \Psi^1(\boldsymbol{x})\mathcal{N}^1(\mathrm{E}^h)$. Computed using $N = 10$, $K_x = 2$, $K_y = 2$.

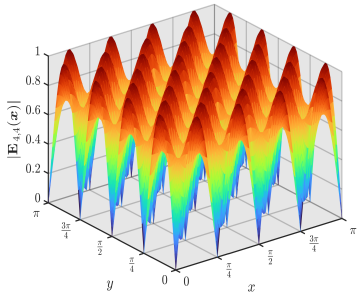

(a) $|\mathbf{E}^h| = \sqrt{(\mathrm{E}_x^h)^2 + (\mathrm{E}_y^h)^2}$

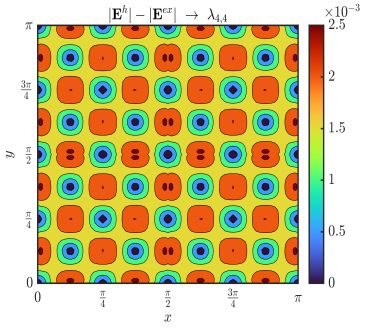

(b) Comparison between $|\mathbf{E}^h|$ and $|\mathbf{E}^{ex}|$

Figure 6.6: Norm $\left|\mathbf{E}_{4,4}^h\right|$ (*left*) and its comparison to the analytical solution (*right*). Discrete system solved with $N = 10$, $K_x = 2$, $K_y = 2$.

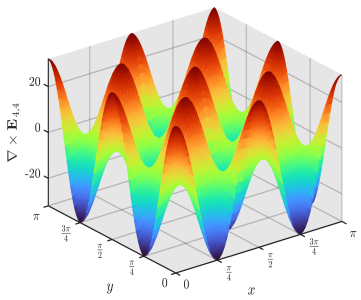

(a) $\nabla \times \mathbf{E}^h = \Psi^2(\boldsymbol{x})\, \mathbb{E}^{2,1}\, \mathcal{N}^1(\mathrm{E}^h)$

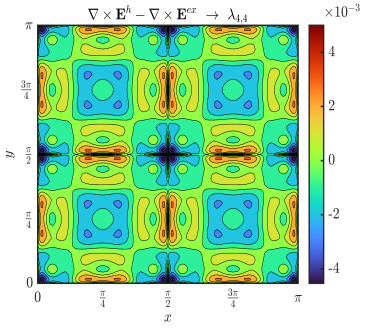

(b) Comparison between $\nabla \times \mathbf{E}^h$ and $\nabla \times \mathbf{E}^{ex}$

Figure 6.7: Function $\nabla \times \mathbf{E}_{4,4}^h$ (*left*) and its comparison to the analytical solution (*right*). Discrete system solved with $N = 10$, $K_x = 2$, $K_y = 2$.

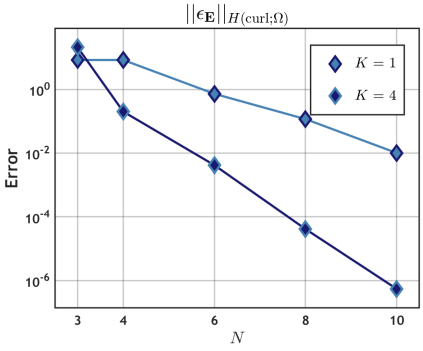

(a) p-convergence

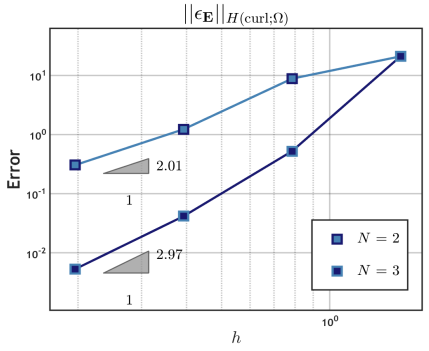

(b) h-convergence

Figure 6.8: Convergence trends for $\mathbf{E}_{2,2}^h$

In Figure 6.8, the convergence for h- and p-refinements is shown for the eigenfunction $\mathbf{E}^h_{2,2}$. For the h-refinement it is observed that the convergence rates match the degree of polynomial approximation N while the p-convergence plot exhibits the exponential convergence. Since all the eigenfunctions on this geometry are smooth, similar behavior is observed for any other eigenfunction.

Information about $\lambda^h_{m,n}$ with varying polynomial degree can be found in Table 6.1 where it is observed that the approximations approach the actual solution from above. Similar to Section 5.3.2, the multiplicity of the eigenvalues was taken into account when distributing them on the table as depicted by the ones shaded in gray. For $N = 4$, $\lambda = 16$ and $\lambda = 17$ are not approximated at all while for $N = 6$ its discrete counterparts are not as accurately predicted as $\lambda = 18$ is. Since $\lambda_{3,3}$ has already been approximated by the lower polynomial degrees, it makes sense that it is much closer to its analytical value for $N = 8$ when compared to $\lambda_{4,0} = \lambda_{0,4}$ or $\lambda_{4,1} = \lambda_{1,4}$ as shown by the blue shaded cells.

In Table 6.2 the multiplicity also played a role in the gray shaded eigenvalues when ordering them from lowest to highest. Additionally, the actual rates of convergence are shown for the first 11 unique Maxwell eigenvalues where it is observed that such rates are equal (or very close to being equal) to $2N$. The latter comes as no surprise since this was also the result obtained in the square domains from Chapter 5 regardless of the boundary conditions utilized. With these results it can be established that the eigenvalues for this geometry and material properties converge twice as fast as their corresponding eigenfunctions when varying the polynomial degree N.

Table 6.1: First 11 Maxwell eigenvalues in $\Omega = [0, \pi]^2$ with isotropic material properties.

h	λ^{ex}	M^{ex}	$N = 4$		$N = 6$		$N = 8$		Trend
			λ^h	M^h	λ^h	M^h	λ^h	M^h	
π	1	2	1.0000147138	2	1.0000000034	2	1	2	↙
	2	1	2.0000294277	1	2.0000000068	1	2	1	↙
	4	2	4.2554897129	2	4.0023440864	2	4.0000056527	2	↙
	5	2	5.2555044268	2	5.0023440898	2	5.0000056527	2	↙
	8	1	8.5109794259	1	8.0046881728	1	8.0000113054	1	↙
	9	2	10.3479578540	—	9.0351770978	2	9.0003068577	2	↙
	10	2	11.3479725679	—	10.0351771012	2	10.0003068577	2	↙
	13	2	14.6034475670	—	13.0375211842	2	13.0003125105	2	↙
	16	2	—	—	20.3147399877	2	16.2105702559	2	↙
	17	2	—	—	21.3147399911	2	17.2105702559	2	↙
	18	1	20.6959157081	1	18.0703541956	1	18.0006137155	1	↙

Table 6.2: Order of Convergence for the first 11 unique Maxwell eigenvalues in $\Omega = [0, \pi]^2$ with $\underline{\underline{\epsilon}} = \underline{\underline{\mu}} = \mathbb{I}$.

h	λ^{ex}	$N=1$		$N=2$		$N=3$	
		λ^h	OC	λ^h	OC	λ^h	OC
	1	1.2158542037	—	1.0075223273	—	1.0001366061	—
	2	2.4317084074	—	2.0150446547	—	2.0002732123	—
	4	—	—	4.0528473456	—	4.0528473456	—
	5	—	—	5.0603696730	—	5.0529839518	—
	8	—	—	8.1056946913	—	8.1056946913	—
$\pi/2$	9	—	—	13.0423484710	—	9.4801183744	—
	10	—	—	14.0498707984	—	10.4802549806	—
	13	—	—	17.0951958167	—	13.5329657201	—
	16	—	—	—	—	17.0219588519	—
	17	—	—	—	—	18.0220954580	—
	18	—	—	26.0846969420	—	18.9602367489	—
	1	1.0523868620	2.04	1.0005121405	3.88	1.0000022787	5.91
	2	2.1047737240	2.04	2.0010242810	3.88	2.0000045574	5.91
	4	4.8634168148	—	4.0300893095	0.81	4.0005464247	6.60
	5	5.9158036768	—	5.0306014500	0.98	5.0005487034	6.59
	8	9.7268336296	—	8.0601786190	0.81	8.0010928494	6.60
$\pi/4$	9	12.8430897517	—	9.2997308006	3.75	9.0125456057	5.26
	10	13.8954766138	—	10.3002429412	3.75	10.0125478845	5.26
	13	17.7065065666	—	13.3298201101	3.63	13.0130920305	5.35
	16	—	—	16.2113893827	—	16.2113893827	2.27
	17	—	—	17.2119015233	—	17.2113916615	2.27
	18	25.6861795035	—	18.5994616013	3.75	18.0250912115	5.26
	1	1.0129160450	2.02	1.0000327660	3.97	1.0000000361	5.98
	2	2.0258320901	2.02	2.0000655321	3.97	2.0000000723	5.98
	4	4.2095474481	2.04	4.0020485621	3.88	4.0000091149	5.91
	5	5.2224634932	2.04	5.0020813282	3.88	5.0000091511	5.91
	8	8.4190948963	2.04	8.0040971243	3.88	8.0000182298	5.91
$\pi/8$	9	10.0802909335	1.83	9.0224868867	3.74	9.0002273446	5.79
	10	11.0932069786	1.83	10.0225196528	3.74	10.0002273808	5.79
	13	14.2898383817	1.87	13.0245354489	3.75	13.0002364596	5.79
	16	19.4536672593	—	16.1203572380	0.81	16.0021856989	6.60
	17	20.4665833043	—	17.1203900041	0.82	17.0021857351	6.60
	18	20.1605818671	1.83	18.0449737734	3.74	18.0004546893	5.79
	1	1.0032168743	2.01	1.0000020602	3.99	1.0000000005	5.99
	2	2.0064337487	2.01	2.0000041204	3.99	2.0000000011	5.98
	4	4.0516641802	2.02	4.0001310643	3.97	4.0000001447	5.91
	5	5.0548810545	2.02	5.0001331245	3.97	5.0000001453	5.91
	8	8.1033283604	2.02	8.0002621286	3.97	8.0000002895	5.91
$\pi/16$	9	9.2631305555	2.04	9.0014782540	3.93	9.0000036848	5.79
	10	10.2663474299	2.04	10.0014803142	3.93	10.0000036853	5.79
	13	13.3147947357	2.03	13.0016093183	3.93	13.0000038295	5.79
	16	16.8381897926	2.04	16.0081942486	3.88	16.0000364597	6.60
	17	17.8414066669	2.04	17.0081963088	3.88	17.0000364603	6.60
	18	18.5262611110	2.03	18.0029565080	3.93	18.0000073696	5.79

6.2.2 Doubly Connected Domain

This section aims to determine if the previously discussed formulation can detect an actual physical zero eigenvalue which can be verified by testing any geometry with a hole. The presented problem, from [21], has a domain $\Omega = [0,4]^2 \setminus (1,3)^2$ and is depicted in Figure 6.9 where the geometry has been split into 8 segments which can be further divided into more elements.

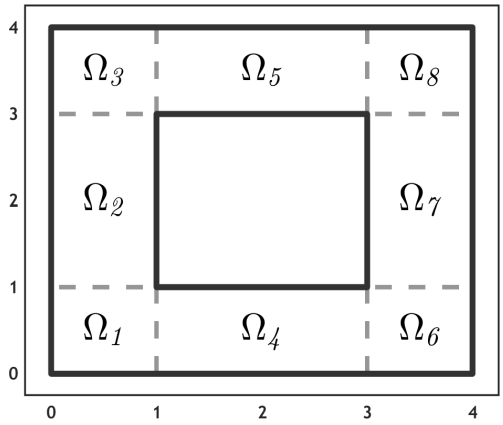

Figure 6.9: Double connected domain

In [21], 3 different Maxwell eigensolvers are explored. Two of them are classical non-conforming approximations while the other is an interior penalty discontinuous Galerkin method. All solvers are designed around the space $H_0(\mathrm{curl};\Omega) \cap H(\mathrm{div};\Omega)$ such that the divergence-free conditions of the Maxwell eigenproblem can be tackled.

For the doubly connected domain, the benchmark uses a solver that enforces the divergence-free constraint through penalizing the divergence term and does so with meshes that are graded around the re-entrant corners of the geometry. For geometries where $\lambda = 0$ is a solution, standard interior penalty methods will generate several zero eigenvalues among which the true Maxwell eigenvalue zero will be *surrounded* by plenty of non-physical zero eigenvalues [21, p. 70]. The method from the benchmark attempts to correct such behavior.

In Table 6.3, the first five eigenvalues of the Maxwell eigenproblem on the doubly connected domain are presented. It is noted, however, that λ_1^h is not incredibly close to being zero in the most refined mesh. In fact, it could easily be confused for a very small non-zero eigenvalue and, to avoid such situation, further mesh refinement should be applied. Unfortunately, $h = 1/64$ was the most refined mesh utilized. On the bright side, it did eliminate all the spurious zero eigenvalues.

Table 6.3: First 5 Maxwell eigenvalues in $\Omega = [0,4]^2 \setminus (1,3)^2$ with $\underline{\underline{\epsilon}} = \underline{\underline{\mu}} = \mathbb{I}$ from [21, Table 5].

h	Benchmark Eigenvalue Approximations				
	λ_1^h	λ_2^h	λ_3^h	λ_4^h	λ_5^h
$1/2$	0.716	0.925	0.925	1.301	2.896
$1/4$	0.396	0.661	0.661	1.146	2.200
$1/8$	0.175	0.471	0.471	1.080	1.784
$1/16$	0.063	0.373	0.373	1.054	1.586
$1/32$	0.020	0.335	0.335	1.045	1.511
$1/64$	0.006	0.322	0.322	1.042	1.486
Trend	Decreasing	Decreasing	Decreasing	Decreasing	Decreasing

In Table 6.4, the first 5 eigenvalues for the Maxwell problem computed with the formulation (6.3) are shown. Since not all elements have the same length, the measure h was computed as an *average* of the lengths of all the elements. The value $h = 1.25$ is indicative of using one spectral element in each subdomain Ω_k.

Perhaps the most noticeable feature of the aforementioned table is the fact that the zero eigenvalue is approximated up to machine precision even for $N = 2$. Even using 2 spectral elements for each subdomain Ω_k paired with the lowest degree approximation produces $\lambda_1^h = 1 \times 10^{-15}$ as an eigenvalue which is completely superior to the result from the interior penalty method from the benchmark.

Comparing the other eigenvalues leads to a good agreement between both methods. Since the results from [21] are overestimated, it could be stated that the true values should be smaller. This is based on the fact that λ_h^1 is slightly positive instead of zero and assuming such behavior spreads to the other data. Thus, the results obtained with (6.3) are *better* than the ones of the benchmark since all λ^h are slightly smaller. The fact that the results are more accurate can be attributted to the fact that the utilized dimensional function spaces satisfy a De Rham sequence.

Table 6.4: First 5 Maxwell eigenvalues in $\Omega = [0,4]^2 \setminus (1,3)^2$ with $\underline{\underline{\epsilon}} = \underline{\underline{\mu}} = \mathbb{I}$ computed using (6.3).

h	$\lambda^h \rightarrow \left\{ \begin{smallmatrix} N=14 \\ K=8 \end{smallmatrix} \right\}$	$N = 2$	$N = 4$	$N = 8$	Trend
		λ^h	λ^h	λ^h	
1.25	3×10^{-15}	3×10^{-15}	-2×10^{-15}	4×10^{-15}	—
	0.316216510716555	0.312116881028890	0.315349870315529	0.316091573033414	↗
	0.316216510716575	0.312116881028896	0.315349870315529	0.316091573033531	↗
	1.041521635153060	1.041475510300464	1.041493602902615	1.041519673068677	↗
	1.475228532358697	1+0.5104014151426	1.486727459719769	1.473996828071681	↙

Even though the approximation for some of the eigenvalues shows an increasing tendency, the values are still below the ones from the benchmark. Consider, for example, λ_4^h from Table 6.4 which settles at 1.0415 while the benchmark provides 1.0420. Similar reasoning can be applied to the other non-zero eigenvalues.

In Table 6.5, the rates of convergence for the eigenvalues can be found where $\lambda = 0$ is omitted since it is always approximated up to an order of $\pm 10^{-15}$ and only λ_2^h is shown since it is equal to λ_3^h. The number of spectral elements used were 1, 2, 3 and 4 for each Ω_k such that the first column in the latter table was obtained.

Similarly to the cases explored in Section 5.3.3 and Section 5.3.4, there is a sub-optimal convergence rate for the eigenvalues which signals to the fact the eigenfunctions exhibit some sort of singularity. Estimating the behavior of $\mathbf{E}_{\lambda=0}$ is, at this moment, impossible since its eigenvalue converges for any given N.

For λ_2^h and λ_5^h, the rates of convergence are below 2 for all the evaluated N while rates oscillate around 2.5 for λ_4^h. Irregular data was obtained for $N = 2$ where the convergence rate for the latter eigenvalue varied tremendously from $1.5 \to 4.3 \to 0.6$ for which no good explanation was found. However, the rest of the data is consistent and it is clear that the eigenfunctions linked to $\mathbf{E}_{\lambda_4^h}$ are smoother than $\mathbf{E}_{\lambda_2^h}$ and $\mathbf{E}_{\lambda_5^h}$.

In Appendix E, the eigenfunctions for this problem are plotted where it is shown that λ_0^h, $\lambda_2^h = \lambda_3^h$ and λ_5^h are associated to eigenfunctions with highly singular behavior. On the other side, the eigenfunction related to λ_4^h, exhibits non-smoothness at the re-entrant corners which is not as *dramatic* as the one from the other eigenfunctions, hence, its higher rate of convergence.

Table 6.5: Order of Convergence for λ_2^h, λ_4^h and λ_5^h in $\Omega = [0,4]^2 \setminus (1,3)^2$ using $\underline{\underline{\epsilon}} = \underline{\underline{\mu}} = \mathbb{I}$.

h	$\lambda^h \to \left\{ \begin{smallmatrix} N=14 \\ K=8 \end{smallmatrix} \right\}$	$N=2$		$N=3$		$N=4$	
		λ^h	OC	λ^h	OC	λ^h	OC
1.250	0.3162165107	0.3121168810	—	0.3146037409	—	0.3153498703	—
	1.0415216351	1.0414755103	—	1.0418452015	—	1.0414736029	—
	1.4752285323	1+0.51040141	—	1.4621842886	—	1.4667274597	—
0.6250	λ_2^h	0.3145369392	1.29	0.3155732529	1.33	0.3159093612	1.50
	λ_4^h	1.0416548699	1.53	1.0414798102	2.95	1.0415088575	1.91
	λ_5^h	1.4637827891	1.62	1.4693334465	1.15	1.4723941499	1.58
0.4166	λ_2^h	0.3152495820	1.36	0.3158597608	1.45	0.3160548967	1.58
	λ_4^h	1.0414986015	4.33	1.0415046246	2.22	1.0415173205	2.68
	λ_5^h	1.4671787527	0.87	1.4719510114	1.45	1.4737449099	1.60
0.3125	λ_2^h	0.3155698637	1.40	0.3159865588	1.53	0.3161194308	1.77
	λ_4^h	1.0414942612	0.60	1.0415135147	2.57	1.0415197026	2.79
	λ_5^h	1.4695532952	1.21	1.4731149266	1.52	1.4743422789	1.79

6.2.3 Piecewise Constant Permittivity

In this section, a problem described in [29] is discussed. The domain is given by $\Omega = [\text{-}1, 1]^2$ where two different materials are utilized in a check pattern as shown in Figure 6.10. For Ω_1 and Ω_4, the permittivity is given by $\underline{\underline{\epsilon_1}} = \mathbb{I}$ while for Ω_2 and Ω_3 the value $\underline{\underline{\epsilon_2}} = 0.01\,\mathbb{I}$ is utilized.

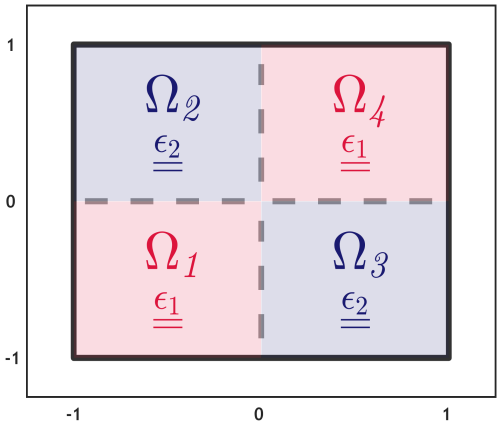

Figure 6.10: Domain $\Omega = [\text{-}1, 1]^2$ split into 4 subdomains and two different materials.

For this problem, the system to solve is constructed as $\mathbb{LHS}\,\underline{x} = \mathbb{RHS}$ where $\mathbb{LHS} = \text{diag}(\text{LHS}_{\Omega_1}, \cdots, \text{LHS}_{\Omega_4})$ and $\mathbb{RHS} = \text{diag}(\text{RHS}_{\Omega_1}, \cdots, \text{RHS}_{\Omega_4})$. In the latter constructions, both LHS_{Ω_k} and RHS_{Ω_k} follow the definitions established in (6.3). Finally, the vector $\underline{x} = \left[\mathcal{N}^1_{\Omega_1}(\text{E}^h)\,\mathcal{N}^0_{\Omega_1}(p^h)\ \cdots\ \mathcal{N}^1_{\Omega_4}(\text{E}^h)\,\mathcal{N}^0_{\Omega_4}(p^h)\right]^{\text{T}}$ contains the degrees of freedom. Since some unknowns in $\underline{x}$ are shared between elements, a *Gathering Matrix* is utilized to glue all the components together and, after applying the boundary conditions, the system $\widehat{\mathbb{LHS}}\,\hat{\underline{x}} = \widehat{\mathbb{RHS}}$ is obtained.

From the benchmark [29], for the first 10 eigenvalues it is indicated the number of digits which are expected to be correct. The latter was done by successively refining the approximation and verifying the number of digits that remained unchanged after each refinement. The best approximations given by the benchmark were obtained with polynomials of degree 10 and a mesh refined near the center consisting of 10 layers with ratio four. However, even with such discretization the number of *correct* digits for λ^h_3 and λ^h_7 was estimated to be **3** while for all the other λ^h this value was above ten. The latter might be already an indication that the eigenfunctions for those eigenvalues are highly singular. In fact, in Appendix F such plots are presented where it can be clearly observed that both $\mathbf{E}_3$ and $\mathbf{E}_7$ exhibit a strong singularity at the origin.

In Table 6.6, the order of convergence for selected eigenvalues is shown. The number of spectral elements used per subdomain can be calculated as $1/h^2$ meaning that the lowest approximation used one element in Ω_k while the best one utilized 64. Perhaps, the most significant result is just how slow the convergence is for λ_3^h when compared to the other *well-behaved* eigenvalues λ_1^h, λ_5^h and λ_9^h which achieve their optimal rates of convergence.

As a additional comment, the eigenvalues associated to highly singular eigenfunctions (i.e., λ_3^h and λ_7^h) are being approached from below while the rest of them are being approached from above.

Table 6.6: Maxwell eigenvalues in $\Omega = [-1, 1]^2$ with piecewise constant permittivity.

h	λ, Ref.[29]	$N = 2$		$N = 3$	
		λ^h	OC	λ^h	OC
1	4.8931933248	4+0.92927625	—	4.8938081893	—
	15.5369816531	7.2715751619	—	7.3926138597	—
	24.4874560134	33.8811148480	—	25.6535605710	—
	44.4352169342	65.5359892288	—	46.7909978279	—
$1/2$	λ_1^h	4.8956176593	3.90	4.8932010168	6.32
	λ_3^h	7.4495434032	0.03	8.4211962203	5.31
	λ_5^h	20+5.2174105	3.69	20+7.8155503	1.80
	λ_9^h	40+5.8969861	3.85	44+0.50142623	5.15
$1/4$	λ_1^h	4.8933460602	3.99	4.8931932722	7.19
	λ_3^h	8.4632698809	0.20	9.3538944194	0.21
	λ_5^h	24+0.5416728	3.75	24.4879904721	5.78
	λ_9^h	44+0.5474212	3.70	44.4363812680	5.83
$1/8$	λ_1^h	4.8932027638	4.02	4.8931933118	2.01
	λ_3^h	9.3917671869	0.21	10.1894832623	0.22
	λ_5^h	24.4910132882	3.93	24.4874644786	5.98
	λ_9^h	44.4426041814	3.92	44.4352357857	5.95

Back in Section 6.2.2, for the doubly connected domain, the lower rates of convergence of the eigenvalues were attributed to the geometry not being *nice* enough even when the whole domain was constituted by a single material. For the present case, however, the geometry is beyond simple as well as the permittivity tensors but the distribution of materials within the domain causes the singularities for some of the eigenfunctions. This is a clear example that even isotropic material properties on a simple geometry can lead to singular solutions depending on the distribution of the materials.

6.3 Anisotropic Permittivity Tensor

The final benchmarks are done for anisotropic permittivity tensors $\underline{\underline{\epsilon}}$. For the 2D problems considered in this section, the notation of [53] is followed in which the relative permittivity and permeability tensors are defined as,

$$\underline{\underline{\epsilon}} = \begin{bmatrix} \underline{\underline{\epsilon_{rt}}} & 0 \\ 0 & \epsilon_{rz} \end{bmatrix}, \qquad \underline{\underline{\mu}} = \begin{bmatrix} \underline{\underline{\mu_{rt}}} & 0 \\ 0 & \mu_{rz} \end{bmatrix}$$

where both $\underline{\underline{\epsilon_{rt}}}$ and $\underline{\underline{\mu_{rt}}}$ are 2×2 tensors describing the *in-plane* relative permittivity and permeability, respectively, with the scalars representing the zz components of each material property. Thus, the 2D Maxwell eigenproblem for $\mathbf{E}$ would read,

$$\begin{aligned} \nabla \times \left(\mu_{rz}^{-1} \nabla \times \mathbf{E} \right) &= \omega^2 \underline{\underline{\epsilon_{rt}}}\, \mathbf{E} \quad \text{in} \quad \Omega \\ \nabla \cdot \left(\underline{\underline{\epsilon_{rt}}}\, \mathbf{E} \right) &= 0 \quad \text{in} \quad \Omega \\ \mathbf{n} \times \mathbf{E} &= 0 \quad \text{in} \quad \partial\Omega \end{aligned}$$

The upcoming sections will utilize second order positive tensors $\underline{\underline{\epsilon_{rt}}}$ paired with the scalar $\mu_{rz} = 1$. For the formulation expressed in (6.3), the latter means that $\mathbb{M}^{(2)}_{\underline{\underline{\mu^{-1}}}}$ reduces to the regular $\mathbb{M}^{(2)}$ used in previous chapters while $\mathbb{M}^{(1)}_{\underline{\underline{\epsilon}}}$ remains as general as it was. Evaluating such matrix for a full 2×2 tensor is shown below:

$$\mathbb{M}^{(1)}_{\underline{\underline{\epsilon}}} = \int_\Omega \Psi^1(\boldsymbol{x})^{\mathrm{T}} \underline{\underline{\epsilon}}\, \Psi^1(\boldsymbol{x})\, \mathrm{d}\Omega = \int_\Omega \begin{bmatrix} \Psi^1_x & 0 \\ 0 & \Psi^1_y \end{bmatrix}^{\mathrm{T}} \begin{bmatrix} \epsilon_1 & \epsilon_2 \\ \epsilon_3 & \epsilon_4 \end{bmatrix} \begin{bmatrix} \Psi^1_x & 0 \\ 0 & \Psi^1_y \end{bmatrix} \mathrm{d}\Omega =$$

$$= \int_\Omega \begin{bmatrix} \left(\Psi^1_x\right)^{\mathrm{T}} & 0 \\ 0 & \left(\Psi^1_y\right)^{\mathrm{T}} \end{bmatrix} \begin{bmatrix} \epsilon_1 \Psi^1_x & \epsilon_2 \Psi^1_y \\ \epsilon_3 \Psi^1_x & \epsilon_4 \Psi^1_y \end{bmatrix} \mathrm{d}\Omega = \int_\Omega \begin{bmatrix} \epsilon_1 \left(\Psi^1_x\right)^{\mathrm{T}} \Psi^1_x & \epsilon_2 \left(\Psi^1_x\right)^{\mathrm{T}} \Psi^1_y \\ \epsilon_3 \left(\Psi^1_y\right)^{\mathrm{T}} \Psi^1_x & \epsilon_4 \left(\Psi^1_y\right)^{\mathrm{T}} \Psi^1_y \end{bmatrix} \mathrm{d}\Omega$$

where the index in the basis functions indicates the spatial component in which nodal expansions are used as shown in (3.14). Additionally, it can be observed that whenever the off-diagonal terms of the tensor are equal to zero, the mass matrix reduces to the regular one used throughout Chapter 4 and Chapter 5.

6.3.1 Square Domain

The present problem is taken from [53, Section 4.1] where a domain $\Omega = [0, \pi]^2$ is analyzed along with a permittivity tensor $\underline{\underline{\epsilon_{rt}}} = \left[\begin{smallmatrix} 2 & 1 \\ 1 & 2 \end{smallmatrix}\right]$ and $\mu_{rz} = 1$ using first order edge-based vector elements on a mesh created by triangles. The approximations of the benchmark are shown in Table 6.7 where h is indicative of the longest edge within the tessellation. The best approximations are highlighted in blue.

Table 6.7: First 5 Maxwell eigenvalues in $\Omega = [0, \pi]^2$ with $\underline{\underline{\epsilon_{rt}}} = \begin{bmatrix} 2 & 1 \\ 1 & 2 \end{bmatrix}$, $\mu_{rz} = 1$ from [53, Table 3].

h	Benchmark Eigenvalue Approximations				
	λ_1^h	λ_2^h	λ_3^h	λ_4^h	λ_5^h
$\sqrt{2}\pi/8$	0.360110	0.851986	0.901434	1.935574	2.205845
$\sqrt{2}\pi/16$	0.361843	0.879173	0.892018	1.907659	2.354616
$\sqrt{2}\pi/32$	0.362324	0.886427	0.889671	1.901324	2.397779
$\sqrt{2}\pi/64$	0.362450	0.888271	0.889084	1.899822	2.409096
$\sqrt{2}\pi/128$	0.362483	0.888734	0.888938	1.899455	2.411969
Trend	Increasing	Increasing	Decreasing	Decreasing	Increasing

The results obtained with the mimetic spectral formulation (6.3) are shown in Table 6.8 and Table 6.9. The rates of convergence for the first 5 eigenvalues show optimal speeds equal to $2N$ which is already expresses that the associated eigenfunctions are smooth within Ω. Such eigenfunctions are shown in Appendix G.

Table 6.8: Order of Convergence for the first 5 Maxwell eigenvalues in $\Omega = [0, \pi]^2$ using $\underline{\underline{\epsilon_{rt}}} = \begin{bmatrix} 2 & 1 \\ 1 & 2 \end{bmatrix}$ and $\mu_{rz} = 1$.

h	$\lambda^h \rightarrow \begin{Bmatrix} N{=}20 \\ K{=}4 \end{Bmatrix}$	$N=1$		$N=2$		$N=4$	
		λ^h	OC	λ^h	OC	λ^h	OC
$\frac{\pi}{2}$	0.3624937135	0.4421288013	—	0.3627564111	—	0.3624796541	—
	0.8888888888	0.9726833629	—	0.9016309905	—	0.8888953998	—
	0.8888888888	1.2158542037	—	0.9021334277	—	0.8888977872	—
	1.8993341127	-	—	1+0.97045007	—	1.8994657582	—
	2.4129318259	-	—	2.4164548547	—	2.4130413740	—
$\frac{\pi}{4}$	λ_1^h	0.3801768523	2.17	0.3624712013	3.54	0.3624919355	2.98
	λ_2^h	0.9194178460	1.46	0.8897468741	3.89	0.8888953998	7.72
	λ_3^h	0.9662498371	2.08	0.8899096774	3.70	0.8888977872	8.00
	λ_4^h	2.3296911976	—	1+0.90905864	2.87	1.8994657582	3.55
	λ_5^h	2+0.82846091	—	2.4287541101	2.17	2.4130413740	1.90
$\frac{\pi}{8}$	λ_1^h	0.3667591504	2.05	0.3624863555	1.61	0.3624934922	3.01
	λ_2^h	0.8970492724	1.90	0.8889441901	3.96	0.8888889197	7.95
	λ_3^h	0.9077920246	2.03	0.8889556770	3.93	0.8888889236	8.00
	λ_4^h	1+0.99783202	2.13	1.8999615077	3.95	1.8993346562	7.92
	λ_5^h	2+0.52264730	1.92	2.4139349932	3.98	2.4129322508	8.01
$\frac{\pi}{12}$	λ_1^h	0.3643734716	2.02	0.3624910639	2.52	0.3624937144	7.86
	λ_2^h	0.8925578348	1.97	0.8888998789	3.99	0.8888888888	8.55
	λ_3^h	0.8972519612	2.01	0.8889021934	3.98	0.8888888888	9.07
	λ_4^h	1+0.94233508	2.04	1.8994517896	4.13	1.8993341339	7.99
	λ_5^h	2.4618023772	1.99	2.4131120250	4.23	2.4129318426	7.98

Table 6.9: First 5 Maxwell eigenvalues in $\Omega = [0, \pi]^2$: $\underline{\underline{\epsilon_{rt}}} = \left[\begin{smallmatrix} 2 & 1 \\ 1 & 2 \end{smallmatrix}\right]$, $\mu_{rz} = 1$.

h	$\lambda^h \rightarrow \left\{ \begin{smallmatrix} N=20 \\ K=4 \end{smallmatrix} \right\}$	$N = 2$	$N = 4$	$N = 8$	Trend
		λ^h	λ^h	λ^h	
	0.362493713534222	0.362756411108870	0.362479654178890	0.362493406420269	↙
	0.888888888888976	0.901630990523142	0.888895399835800	0.888888888888904	↙
$\pi/2$	0.888888888890293	0.902133427739300	0.888897787263535	0.888888888888908	↙
	1.899334112725240	1+0.9704500737540	1.899465758293698	1.899331885960170	↙
	2.412931825959713	2.416454854719386	2.413041374054393	2.412925952684026	↙

The most accurate results from the benchmark and the mimetic spectral method are highlighted in blue in Table 6.8 and Table 6.9, respectively. In fact, the results from both methods are in very good agreement as detailed below:

- For λ_1^h, the benchmark estimates 0.362483 with an *increasing* trend, thus, it is a lower bound. The MSEM gives 0.362493 which is above the latter value.
- For λ_2^h, the benchmark acts as a lower bound since the eigenvalue 0.888734 tends to *increase*. The MSEM gives 0.888888 which is above such bound.
- For λ_3^h a *decreasing* tendency is detailed by the benchmark from a value of 0.888938. The MSEM stays below this upper bound at 0.888888.
- For λ_4^h, the value 1.899455 has a *decreasing* tendency which is consistent with the MSEM approximation of 1.899334.
- For λ_5^h, the benchmark expects 2.411969 to *increase* which is congruent with the MSEM approximation of 2.412931.

Had the formulation (6.3) not been utilized and only the curl-curl equation been considered, plenty of unwanted zero eigenvalues would have polluted the spectra. Whenever a solution wants to be deemed as physical or non-physical, the term $\nabla \cdot \mathbf{D}$ has to be computed. Accepting a solution as physical, requires such term to vanish in Ω, otherwise, it has to be catalogued as *spurious*.

Within the MSEM framework, verifying $\nabla \cdot \mathbf{D}$ would be done as follows. In Figure 2.7 is shown that both fields $\mathbf{D}$ and $\mathbf{E}$ belong to edges but on different grids. By recalling the concepts from Section 3.3.3, the degrees of freedom for $\mathbf{D}$ are written as $\mathcal{N}^1(\mathrm{D}^h) = \mathbb{M}_{\underline{\underline{\epsilon}}}^{(1)} \mathcal{N}^1(\mathrm{E}^h)$. The divergence requires surface degrees of freedom for which the transpose of $\mathbb{E}_{\text{grad}}^{1,0}$ is used along with the appropriate basis for 2D volumes $\widetilde{\Psi}^2(\boldsymbol{x})$. All pieces put together allow to interpolate $\nabla \cdot \mathbf{D}$ in Ω.

Due to the formulation being utilized in this section, there is no need to check the veracity of the eigenvalues. However, it will be shown how non-physical solutions

fail to satisfy $\nabla \cdot \mathbf{D} = 0$. In Figure 6.12a, the function $\mathbf{E}_{\lambda=0}(\boldsymbol{x})$ clearly violates the constraint. On the other hand, true solutions satisfy it **pointwise** as shown in Figure 6.12b through Figure 6.12f. The plots were obtained with $K_x = K_y = 1$ and $N = 8$ but identical behavior is achieved with lower degree polynomials. This procedure allows to *manually* find solutions $\mathbf{E} \in H_0(\mathrm{curl}; \Omega)$ and $\mathbf{D} \in H(\mathrm{div}; \Omega)$ when formulations neglecting the divergence constraint are opted for.

A byproduct of the formulation (6.3) is the so-called Lagrange Multiplier p which has no physical significance but is shown for completeness in Figure 6.11.

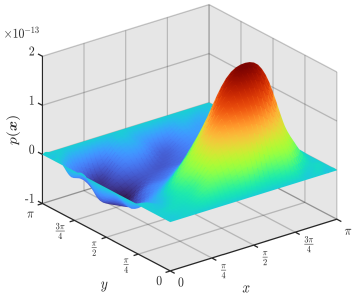

(a) Lagrange Multiplier p for λ_1^h

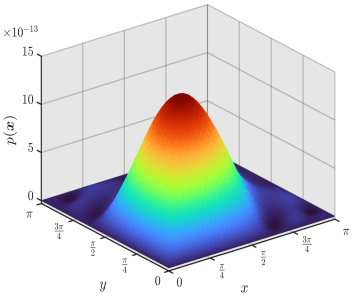

(b) Lagrange Multiplier p for λ_5^h

Figure 6.11: Lagrange Multiplier computed as $p^h = \Psi^0(\boldsymbol{x})\mathcal{N}^0(p^h)$ using $N = 8$, $K_x = 1$, $K_y = 1$.

The effect of the off-diagonal terms of $\underline{\underline{\epsilon_{rt}}}$ on λ is shown in Table 6.10 where the eigenvalues with M > 1 in the isotropic case have now split. For the current problem, λ_2^h and λ_3^h seem to merge, however, in Table 6.8 the MSEM shows that they are different even when sharing several decimals. Additionally, the benchmark approximates both values from different directions. Had the eigenvalues been equal, the latter would not be the case. There might be anisotropic tensors that merge some eigenvalues back together but for the presented example this does not occur.

Table 6.10: Effect of the off-diagonal terms of $\underline{\underline{\epsilon_{rt}}}$ on eigenvalues in $\Omega = [0, \pi]^2$.

$\underline{\underline{\epsilon_{rt}}}$	λ_1	λ_2	λ_3	λ_4	λ_5
$\begin{bmatrix} 2 & 0 \\ 0 & 2 \end{bmatrix}$	0.5	0.5	1	2	2
$\begin{bmatrix} 2 & 0.5 \\ 0.5 & 2 \end{bmatrix}$	0.41	0.63	0.96	1.98	2.16
$\begin{bmatrix} 2 & 1 \\ 1 & 2 \end{bmatrix}$	0.36	0.88	0.88	1.89	2.41
Trend	Decreasing	Increasing	—	Decreasing	Increasing

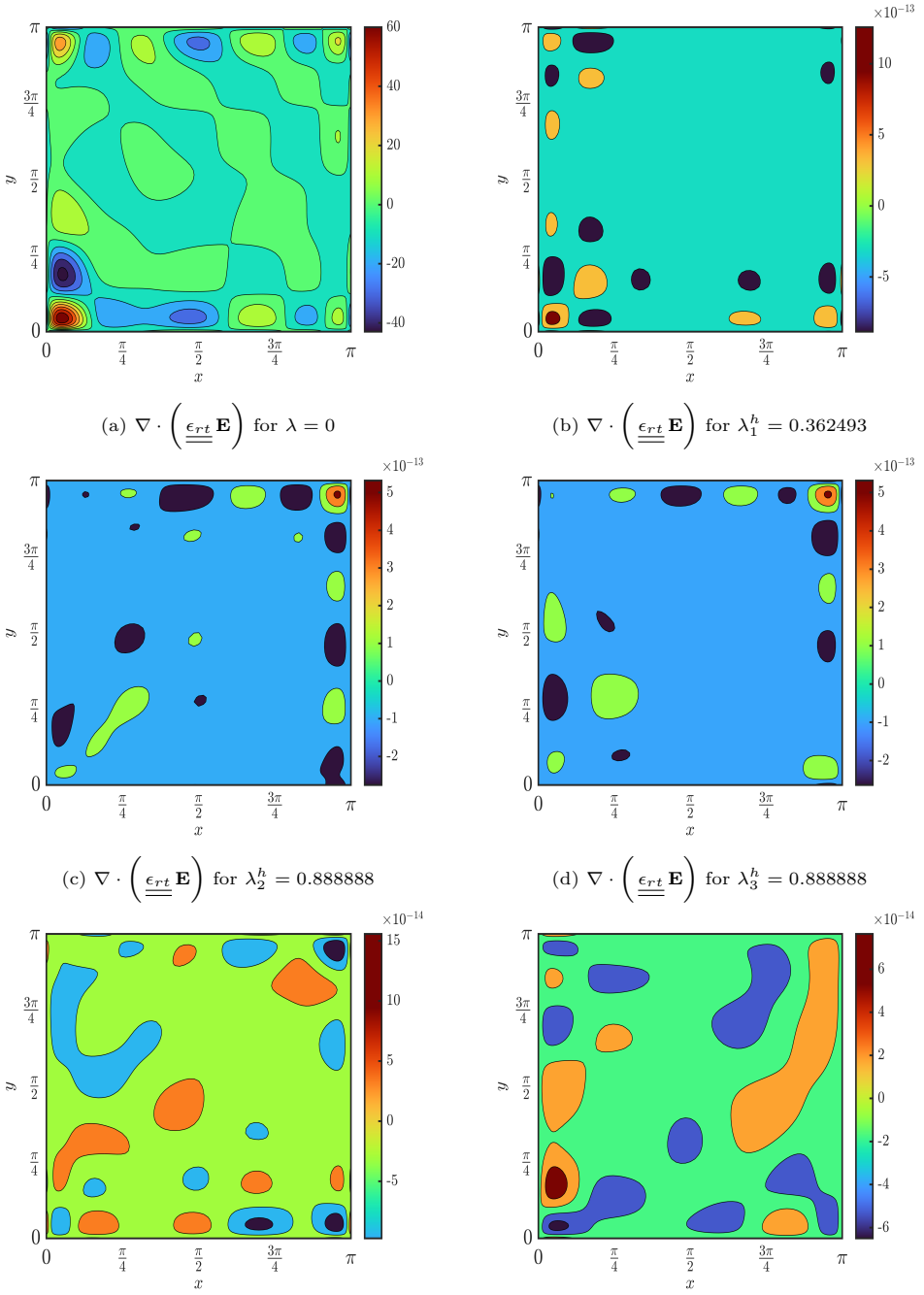

(a) $\nabla \cdot \left(\underline{\underline{\epsilon_{rt}}}\, \mathbf{E} \right)$ for $\lambda = 0$

(b) $\nabla \cdot \left(\underline{\underline{\epsilon_{rt}}}\, \mathbf{E} \right)$ for $\lambda_1^h = 0.362493$

(c) $\nabla \cdot \left(\underline{\underline{\epsilon_{rt}}}\, \mathbf{E} \right)$ for $\lambda_2^h = 0.888888$

(d) $\nabla \cdot \left(\underline{\underline{\epsilon_{rt}}}\, \mathbf{E} \right)$ for $\lambda_3^h = 0.888888$

(e) $\nabla \cdot \left(\underline{\underline{\epsilon_{rt}}}\, \mathbf{E} \right)$ for $\lambda_4^h = 1.899334$

(f) $\nabla \cdot \left(\underline{\underline{\epsilon_{rt}}}\, \mathbf{E} \right)$ for $\lambda_5^h = 2.412931$

Figure 6.12: Divergence constraints computed as $\nabla \cdot \mathbf{D}^h = \widetilde{\Psi}^2(\boldsymbol{x}) \left(\mathbb{E}_{\text{grad}}^{1,0} \right)^{\mathrm{T}} \mathbb{M}_{\underline{\underline{\epsilon}}}^{(1)} \mathcal{N}^1(\mathrm{E}^h)$.

6.3.2 H-Domain

This section focuses on the problem described in [53, Section 4.2] in which the Maxwell eigenproblem is analyzed with $\underline{\underline{\epsilon_{rt}}} = \left[\begin{smallmatrix} 1 & -j \\ j & 4 \end{smallmatrix}\right]$ inside a so-called H-domain. For the purposes of the discretization using the MSEM finite elements, the geometry was divided in 7 subdomains Ω_k as to facilitate the meshing of the domain. The partitions as well as the exact dimensions of the domain are depicted in Figure 6.13.

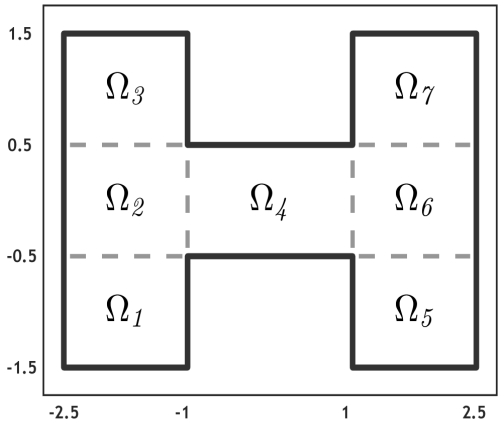

Figure 6.13: H-domain

As opposed to the previous cases, in this problem the right-hand side block matrix from (6.3) will be complex valued due to the choice of the permittivity tensor. This, however, does not change the methodology used to obtain the eigenvalues but does modify the way in which the eigenfunctions are obtained and presented.

The eigenvalues are still the result of the *generalized eigenvalue problem* for which MATLAB is used once the discrete system has been properly assembled. Defining the eigenfunctions requires first to compute the eigenvectors. This is done by feeding each λ^h back into the discrete formulation and then calculating the null space of the system. In doing so, all the degrees of freedom $\mathcal{N}^1(\mathrm{E}^h)$ and $\mathcal{N}^0(p^h)$ are obtained.

The eigenfunctions cannot be immediately reconstructed because the degrees of freedom are complex-valued. Hence, $\mathcal{N}^1(\mathrm{E}^h)$ is split into $\mathcal{N}^1_{\mathrm{Re}}(\mathrm{E}^h) = \mathrm{Re}\left(\mathcal{N}^1(\mathrm{E}^h)\right)$ and $\mathcal{N}^1_{\mathrm{Im}}(\mathrm{E}^h) = \mathrm{Im}\left(\mathcal{N}^1(\mathrm{E}^h)\right)$ which denote the real and imaginary parts, respectively. Finally, the eigenfunctions are interpolated as $\mathrm{Re}(\mathbf{E}^h) = \Psi^1(\boldsymbol{x})\,\mathcal{N}^1_{\mathrm{Re}}(\mathrm{E}^h)$ and $\mathrm{Im}(\mathbf{E}^h) = \Psi^1(\boldsymbol{x})\mathcal{N}^1_{\mathrm{Im}}(\mathrm{E}^h)$. In Appendix H, the eigenfunctions for the first 5 eigenvalues of the problem are shown in which $\mathrm{Re}(|\mathbf{E}^h|)$ and $\mathrm{Im}(|\mathbf{E}^h|)$ were also included.

The results from the benchmark were obtained with first order edge-based vector elements and are shown in Table 6.11. Those values are only used as a reference to

verify if the data obtained with the formulation (6.3) is leading towards the right values. Nevertheless, they are not utilized for computing the order of convergence. This is because the most accurate data was obtained with the MSEM formulation utilizing polynomials of degree 8 and 9 spectral elements per subdomain Ω_k.

Table 6.11: First 5 Maxwell eigenvalues in H-domain: $\underline{\underline{\epsilon_{rt}}} = \begin{bmatrix} 1 & -j \\ j & 4 \end{bmatrix}$, $\mu_{rz} = 1$. From [53, Table 4].

h	Benchmark Eigenvalue Approximations				
	λ_1^h	λ_2^h	λ_3^h	λ_4^h	λ_5^h
0.293524	0.040378	0.388638	0.781945	0.982714	1.606289
0.146762	0.040884	0.395901	0.784755	0.992164	1.626574
0.073381	0.041091	0.398877	0.785987	0.996140	1.634283
0.036690	0.041173	0.400074	0.786498	0.997754	1.637230
0.018345	0.041206	0.400552	0.786704	0.998401	1.638369
Trend	Increasing	Increasing	Increasing	Increasing	Increasing

Table 6.12: Order of Convergence for the first 5 Maxwell eigenvalues in the H-domain from Figure 6.13 using $\underline{\underline{\epsilon_{rt}}} = \begin{bmatrix} 1 & -j \\ j & 4 \end{bmatrix}$ and $\mu_{rz} = 1$.

h	$\lambda^h \rightarrow \begin{Bmatrix} N=8 \\ K=63 \end{Bmatrix}$	$N=2$		$N=3$		$N=4$	
		λ^h	OC	λ^h	OC	λ^h	OC
1.28	0.041216865	0.0396707306	—	0.0406801227	—	0.0409696465	—
	0.400706061	0.3953658283	—	0.3932724910	—	0.3970738192	—
	0.786771968	0.7785410562	—	0.7884045525	—	0.7850417013	—
	0.998611654	1.0281485790	—	0.9919999493	—	0.9947379885	—
	1.638737663	1.6820897703	—	1.6934295918	—	1.6326385780	—
0.64	λ_1^h	0.0407193554	1.64	0.0410345792	1.56	0.0411279062	1.47
	λ_2^h	0.3946063576	0.19	0.3980808021	1.50	0.3994133095	1.49
	λ_3^h	0.7860229303	3.46	0.7856795488	0.58	0.7862316756	1.68
	λ_4^h	0.9926180776	2.30	0.9953204192	1.01	0.9969007788	1.18
	λ_5^h	1.6655332060	0.69	1.6334015517	3.36	1.6359072877	1.11
0.42	λ_1^h	0.0409485973	1.52	0.0411166029	1.47	0.0411702656	1.59
	λ_2^h	0.3970690808	1.28	0.3992561123	1.46	0.4000290051	1.60
	λ_3^h	0.7855912681	1.12	0.7861634217	1.44	0.7864867489	1.58
	λ_4^h	0.9943203671	0.82	0.9967007607	1.34	0.9977094534	1.58
	λ_5^h	1.6552530219	1.19	1.6355926076	1.30	1.6372151559	1.53

In Table 6.11, the values $h = \{1.285, 0.642, 0.428\}$ are indicative of using 1, 4 and 9 spectral elements per subdomain Ω_k. By looking at the eigenfunctions from Appendix H, it would be difficult to suggest that optimal convergence rates could be achieved since the plots depict rapid changes at the internal corners of the geometry. It is observed, however, that for the cases $N = \{2, 3\}$ the order of

convergence stabilizes between 1.30 and 1.60. The same behavior should be expected even if the polynomial degree is increased.

Similarly to the benchmark, the MSEM formulation approximates the first 3 eigenvalues from below. Nonetheless, λ_h^4 and λ_h^5 are approached from above. According to Boffi [9], determining if eigenvalue approximations are approached from either above or below has not been given a conclusive response but the general consensus seems to be that *conforming* approximations are above the exact solutions while *non-conforming* ones are below. Even the same eigenvalue approximation can become a lower or upper bound depending on the chosen mesh.

For the collection of problems in this chapter, eigenvalues associated to smooth eigenfunctions were always approached from above while highly singular solutions, such as the ones obtained from the domain with two materials, were approached from below. For eigenvalues/eigenfunctions in between these two extremes, the approximations have the possibility to be approached from either direction.

6.4 Additional Remarks

In [39], the framework utilized along this thesis is applied to a series of problems related to the Darcy flow equations. Particularly relevant is the so-called *Sand-Shale System* solved on $\Omega = [\text{-}1,\ 1]^2$ with both a direct and a mixed formulation where, in a post-processing step, the net flux through the left boundary of the domain is computed. In doing so, it is observed that the **direct formulation** approaches the net flux value from **above** while the **mixed formulation** does it from **below**.

For the problems presented in this chapter, the quantity to analyze will be the electrostatic field energy $\mathrm{U_E} = \frac{1}{2}\int_\Omega \mathbf{E}\cdot\mathbf{D}\,\mathrm{d}\Omega$. Specifically, this will be tested for the eigenproblem presented in Section 6.2.1 and Section 6.3.1.

6.4.1 The De Rham Complex in $\mathbb{R}^2$

Before defining the weak form, it should be recalled that in $\mathbb{R}^2$, there are two sets of function spaces that obey the De Rham cohomology [51] such that a double De Rham sequence can be built as follows:

$$\begin{array}{ccccc} H^1(\Omega) & \xrightarrow{\text{grad}} & H(\text{curl};\Omega) & \xrightarrow{\text{curl}} & L^2(\Omega) \\ \star\updownarrow & & \star\updownarrow & & \star\updownarrow \\ \widetilde{L}^2(\Omega) & \xleftarrow{\text{div}} & \widetilde{H}(\text{div};\Omega) & \xleftarrow{\text{curl}} & \widetilde{H}(\text{curl};\Omega) \end{array}$$

where the curl operator on the first row acts on vector fields whereas the one on the second row does it on scalar fields. The symbol $\star$ represents the Hodge operator.

Since Tonti diagrams are quite closely related to the De Rham sequences, the eigenvalue problem can be accommodated in this type of structure. There are 3 main terms to consider: (1) $\mathbf{D} = \underline{\underline{\epsilon}}\,\mathbf{E}$, (2) $\nabla \times \left(\underline{\underline{\mu}}^{-1} \times \mathbf{E}\right)$ and (3) $\omega^2\,\underline{\underline{\epsilon}}\,\mathbf{E}$ for which the following constructions are helpful,

$$\begin{array}{ccc} -\phi & \xrightarrow{\text{grad}} & \mathbf{E} \\ & & \downarrow \star_{\underline{\underline{\epsilon}}} \\ 0 & \xleftarrow{\text{div}} & \mathbf{D} \end{array} \qquad \text{and} \qquad \begin{array}{ccc} \mathbf{E} & \xrightarrow{\text{curl}} & \gamma \\ & & \downarrow \star_{\underline{\underline{\mu}}^{-1}} \\ \mathbf{F} & \xleftarrow{\text{curl}} & \widetilde{\gamma} \end{array} \tag{6.4}$$

where the vertical arrow for the electric potential is excluded since there is no constitutive equation relating ϕ and the electric charge density ρ (set to zero for the eigenproblem). By the same argument, $\mathbf{E}$ and $\mathbf{F}$ are not connected. The remaining vertical links are kept since they rely on the material parameters $\underline{\underline{\epsilon}}$ and $\underline{\underline{\mu}}$.

The electric potential, even when not used in the formulation, is shown since it shares the same function space as the Lagrange Multiplier p used to impose $\nabla \cdot \mathbf{D} = 0$.

6.4.2 Mixed Formulation for the Maxwell Eigenproblem

The formulation presented in (6.3) is certainly not unique. An alternative system for the Maxwell eigenproblem could be obtained if, for example, the curl-curl operator is split by introducing additional variables. This is the same principle used in the mixed formulations of the scalar Poisson problem from Chapter 4 and Chapter 5.

Since the main focus is to split the curl-curl operator, the attention is centered on the right diagram from (6.4). The equations to be used are constructed by *following the arrows* in such diagram which leads to the following system:

$$\gamma = \nabla \times \mathbf{E} \tag{6.5a}$$

$$\widetilde{\gamma} = \star_{\underline{\underline{\mu}}^{-1}} \gamma \tag{6.5b}$$

$$\mathbf{F} = \nabla \times \widetilde{\gamma} = \omega^2\,\underline{\underline{\epsilon}}\,\mathbf{E} \tag{6.5c}$$

where γ belongs to primal surfaces, $\widetilde{\gamma}$ belongs to dual nodes and $\mathbf{E}$ belongs to primal edges. The term $\mathbf{F}$ was just a dummy variable to avoid introducing $\omega^2\,\underline{\underline{\epsilon}}\,\mathbf{E}$ into the diagrams above. Discretizing the equations is now straightforward. In (6.5a), the equation is topological and requires only incidence matrices. On the contrary, in (6.5b) primal surface degrees of freedom are transformed into unknowns on dual

nodes for which a mass matrix is required. The equation (6.5c) requires a bit of work which starts by multiplying by a test function $\boldsymbol{v}$ defined on primal edges:

$$\int_\Omega \boldsymbol{v}\,(\nabla\times\widetilde{\gamma})\;\mathrm{d}\Omega = \int_\Omega\;(\nabla\times\boldsymbol{v})\,\widetilde{\gamma}\;\mathrm{d}\Omega = \omega^2\int_\Omega v\,\underline{\underline{\epsilon}}\,\mathbf{E}\;\mathrm{d}\Omega$$

where the boundary term disappears because $\boldsymbol{v}\in H_0(\mathrm{curl};\Omega)$. The terms in the equation above are expanded as $\nabla\times\boldsymbol{v}=\Psi^2(\boldsymbol{x})\,\mathbb{E}^{2,1}_{\mathrm{curl}}\,\mathcal{N}^1(v^h)$, $\widetilde{\gamma}=\widetilde{\Psi}^0(\boldsymbol{x})\widetilde{\mathcal{N}}^0\left(\widetilde{\gamma}^h\right)$ and $\mathbf{E}=\Psi^1(\boldsymbol{x})\mathcal{N}^1(\mathrm{E}^h)$. The test function is expanded in the same way as the electric field. By putting all together, the following is obtained:

$$\left(\mathbb{E}^{2,1}_{\mathrm{curl}}\right)^{\mathrm{T}}\underbrace{\left[\int_\Omega \Psi^2(\boldsymbol{x})\widetilde{\Psi}^0(\boldsymbol{x})\;\mathrm{d}\Omega\right]}_{\mathbb{I}}\widetilde{\mathcal{N}}^0\left(\widetilde{\gamma}^h\right)=\omega^2\,\mathbb{M}^{(1)}_{\underline{\underline{\epsilon}}}\,\mathcal{N}^1(\mathrm{E}^h)$$

where the fact that the bases $\widetilde{\Psi}^{(n-d)}(\boldsymbol{x})$ and $\Psi^{(d)}(\boldsymbol{x})$ are bi-orthogonal with respect to each other has been used [51, Lemma 2] such that the identity matrix remains. The parameter n describes the dimension of the embedding space.

Thus, the discretized equations correspondent to the system (6.5a)-(6.5c) are:

$$\mathcal{N}^2(\gamma^h) \;=\; \mathbb{E}^{2,1}_{\mathrm{curl}}\,\mathcal{N}^1(\mathrm{E}^h) \tag{6.6a}$$

$$\widetilde{\mathcal{N}}^0\left(\widetilde{\gamma}^h\right) \;=\; \mathbb{M}^{(2)}_{\underline{\underline{\mu^{-1}}}}\,\mathcal{N}^2(\gamma^h) \tag{6.6b}$$

$$\left(\mathbb{E}^{2,1}_{\mathrm{curl}}\right)^{\mathrm{T}}\widetilde{\mathcal{N}}^0\left(\widetilde{\gamma}^h\right) \;=\; \omega^2\,\mathbb{M}^{(1)}_{\underline{\underline{\epsilon}}}\,\mathcal{N}^1(\mathrm{E}^h) \tag{6.6c}$$

A more compact system is obtained by substituting (6.6b) into (6.6c):

$$\mathcal{N}^2(\gamma^h) \;=\; \mathbb{E}^{2,1}_{\mathrm{curl}}\,\mathcal{N}^1(\mathrm{E}^h) \tag{6.7a}$$

$$\left(\mathbb{E}^{2,1}_{\mathrm{curl}}\right)^{\mathrm{T}}\mathbb{M}^{(2)}_{\underline{\underline{\mu^{-1}}}}\,\mathcal{N}^2(\gamma^h) \;=\; \omega^2\,\mathbb{M}^{(1)}_{\underline{\underline{\epsilon}}}\,\mathcal{N}^1(\mathrm{E}^h) \tag{6.7b}$$

By including the divergence constraint, the complete system is written as:

$$\begin{bmatrix} \mathbb{I} & -\mathbb{E}^{2,1}_{\mathrm{curl}} & 0 \\ \left(\mathbb{E}^{2,1}_{\mathrm{curl}}\right)^{\mathrm{T}}\mathbb{M}^{(2)}_{\underline{\underline{\mu^{-1}}}} & 0 & \mathbb{M}^{(1)}_{\underline{\underline{\epsilon}}}\mathbb{E}^{1,0}_{\mathrm{grad}} \\ 0 & \left(\mathbb{E}^{1,0}_{\mathrm{grad}}\right)^{\mathrm{T}}\mathbb{M}^{(1)}_{\underline{\underline{\epsilon}}} & 0 \end{bmatrix}\underline{X}=\lambda\begin{bmatrix} 0 & 0 & 0 \\ 0 & \mathbb{M}^{(1)}_{\underline{\underline{\epsilon}}} & 0 \\ 0 & 0 & 0 \end{bmatrix}\underline{X} \tag{6.8}$$

where λ replaced ω^2 as the eigenvalue and $\underline{X}=\left[\mathcal{N}^2(\gamma^h)\;\;\mathcal{N}^1(\mathrm{E}^h)\;\;\mathcal{N}^0(p^h)\right]^{\mathrm{T}}$.

6.4.3 Electrostatic Field Energy

The motivation of writing a mixed formulation for the Maxwell Eigenproblem was to investigate if λ^h would be approximated from a different direction when compared to (6.3). Since this did not occur, the analysis was shifted to the convergence of integral quantities as to verify if the behavior from [39] could be replicated.

The term to be analyzed is the electrostatic field energy $\mathrm{U_E} = \frac{1}{2}\int_\Omega \mathbf{E}\cdot\mathbf{D}\,\mathrm{d}\Omega$. In both (6.3) and (6.8), $\mathbf{E}$ belongs to primal edges while $\mathbf{D}$ belongs to dual edges. By using this information, the approximation for the energy becomes:

$$\mathrm{U_E} = \frac{1}{2}\left(\mathcal{N}^1(\mathrm{E}^h)\right)^{\mathrm{T}} \underbrace{\left[\int_\Omega \Psi^1(\boldsymbol{x})^{\mathrm{T}}\,\widetilde{\Psi}^1(\boldsymbol{x})\,\mathrm{d}\Omega\right]}_{\mathbb{I}} \mathcal{N}^1(\mathrm{D}^h) = \frac{1}{2}\left(\mathcal{N}^1(\mathrm{E}^h)\right)^{\mathrm{T}} \mathcal{N}^1(\mathrm{D}^h)$$

where the bi-orthogonality of the primal and dual functions was used. The degrees of freedom for the electric displacement $\mathcal{N}^1(\mathrm{D}^h)$ are computed by using the constitutive equation $\mathbf{D} = \star_{\underline{\underline{\epsilon}}}\mathbf{E}$ from (6.4) which leads to $\mathcal{N}^1\left(\mathrm{D}^h\right) = \mathbb{M}^{(1)}_{\underline{\underline{\epsilon}}}\mathcal{N}^1\left(\mathrm{E}^h\right)$. In fact, such definition had already been used in Section 6.3.1 to compute the $\nabla\cdot\mathbf{D}^h = 0$ to verify if the resulting eigenfunctions were spurious solutions or not. With this last piece of information, the energy is computed as:

$$\mathrm{U_E} = \frac{1}{2}\left(\mathcal{N}^1(\mathrm{E}^h)\right)^{\mathrm{T}} \mathbb{M}^{(1)}_{\underline{\underline{\epsilon}}}\mathcal{N}^1(\mathrm{E}^h) \tag{6.9}$$

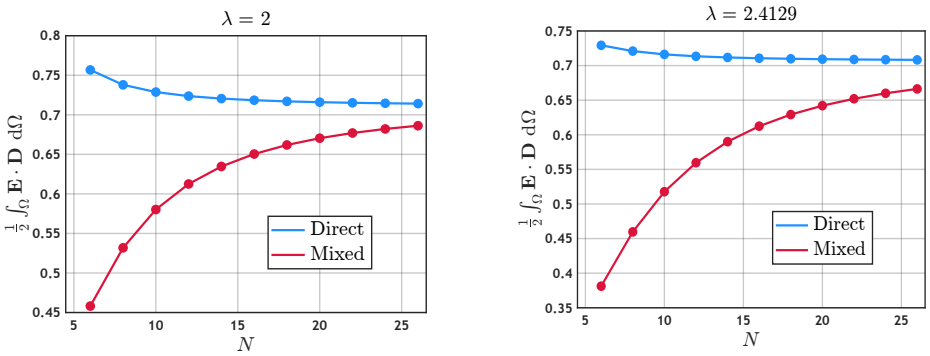

(a) $\underline{\underline{\epsilon}} = \underline{\underline{\mu}} = \mathbb{I}$ (b) $\underline{\underline{\epsilon_{rt}}} = \begin{bmatrix} 2 & 1 \\ 1 & 2 \end{bmatrix}$ and $\mu_{rz} = 1$

Figure 6.14: Convergence of $\mathrm{U_E}$ on $K = [0,\pi]^2$ when using a direct and a mixed formulation.

The convergence for $\mathrm{U_E}$ is shown in Figure 6.14a for the eigenfunction related to $\lambda = 2$ from the problem described in Section 6.2.1. Additionally, in Figure 6.14b the same plot is presented for the eigenfunction related to $\lambda = 2.41$ of the anisotropic

square case from Section 6.3.1. In both instances, the mixed method approximates the energy from below while the direct method does it from above such that the some conclusion found in [39] is obtained.

The most important reflection from this section is that if the energy U_E were to be a quantity of extreme interest, then using both types of formulations would effectively create a lower and upper bound for such variable. In Figure 6.14, the approximation was only performed with one spectral element but increasing this value should allow for more precise bounds of U_E.

7

Conclusions

In this thesis, a mimetic spectral element framework has been successfully applied to a collection of problems in $\mathbb{R}^1$ and $\mathbb{R}^2$ using the Whitney Map described in [51].

Most of the present work deals with simple problems such as the classic Poisson equation and eigenvalue problems for the Laplacian operator in diverse geometries and subject to different boundary conditions. Each of these cases, despite being basic, had as a purpose to slowly build up knowledge and experience in applying the MSEM framework. Ultimately, this was beneficial since it allowed to more confidently explore the *main dish* of this thesis, the Maxwell Eigenvalue Problem.

The only case that, perhaps, is a complete outlier in the present work is the problem related to the Hartmann Flow system. Its inclusion in this thesis was motivated mainly by curiosity in how to apply this framework to ordinary differential equations that included the first derivative. In doing so, a matrix $\mathbb{C}^{0,1}$ was obtained which was found to be effective in *changing* degrees of freedom attached to lines into degrees of freedom defined on nodes.

In fact, a *minor* research question in this thesis was related to the possibility of modifying the mimetic framework to accommodate to what was described above. After the results obtained in Section 4.2.2, it can be stated that the methodology was properly modified and the application of $\mathbb{C}^{0,1}$ lead to optimal convergence rates. A next step, maybe, would be to extend the idea to PDEs.

The *major* research questions were related to the Maxwell Eigenproblem. The first one was focused on the possibility of developing a formulation that could avoid

spurious solutions and provide faster rates of convergence than traditional FEM.

Creating a formulation that gets rid of spurious solutions is entirely possible when the *correct* equations are involved. In Chapter 6, the attention was focused on the eigenvalue problem for the electric field and it was mentioned that failing to couple the curl-curl equation with the appropriate divergence-free condition would inevitably lead to spurious solutions. This could be somehow circumvented if *special* elements based on $H_0(\text{curl};\Omega) \cap H(\text{div};\Omega)$ were utilized as was the case of the benchmark in Section 6.2.2.

For the finite elements used in this thesis, a spurious free formulation was developed by following the work done by Kikuchi [56] and consisted in adding a Lagrange Multiplier that would force the field $\mathbf{E}$ to be orthogonal to gradients. Additionally, optimal rates of convergence of N and $2N$ were obtained for eigenfunctions and eigenvalues, respectively, when smooth solutions were expected. When the latter condition was met, the presented methodology was indeed faster than traditional FEM since in this framework the polynomial degree can be changed at will.

Another research question was related to the analysis of geometries with an arbitrary Betti number b_1. This was particularly aimed at the fact that geometries with holes do allow for $\lambda = 0$ as a solution. This was tested for a *Doubly Connected Domain* in which $b_1 = 1$ and it was found that the formulation based on [56] did allow to capture the zero eigenvalue as a solution. Even though this does not classify as a geometry with an *arbitrary* number b_1, it should be expected that the formulation behaves adequately for any other domain with holes.

The final research question focused on the effect of anisotropy and geometry on the convergence rates of eigenvalues. It was observed that for nice, simple geometries such as the square, the anisotropy did not modify the order of convergence of the eigenvalues. For the H-domain explored in Section 6.3.2, sub-optimal rates of convergence were obtained but the case could be made that the shape of the domain had more weight on that issue. In that sense, the answer is not conclusive. However, it was noticed that even isotropic material properties on simple geometries led to sub-optimal convergence rates when materials with different properties are found sharing the same domain.

Besides what has already been mentioned, it is worth indicating that with the current MSEM methodology, it was *extremely* easy to identify solutions that did not satisfy $\nabla \cdot \mathbf{D} = 0$. Additionally, for those eigenfunctions that did fulfill such constraint, it was found that the solutions satisfy it **pointwise**. This characteristic would be quite relevant for problems with non-zero sources $\mathbf{J}$ with the field $\mathbf{H}$ since the equation $\nabla \cdot \mathbf{B}$ is always mapped to zero.

As an extra feature, it was found how to compute upper and lower bounds for integral quantities by using a direct method and a mixed formulation which, in this case, was used for the term $\frac{1}{2}\int_{\Omega} \mathbf{E}\cdot\mathbf{D}\,\mathrm{d}\Omega$.

Had the work on this thesis needed to continue, the next step would have certainly been to work with the complete time-harmonic system by including non-zero electric current density $\mathbf{J}$ and non-homogeneous boundary conditions. Perhaps, working with the formulation for the field $\mathbf{H}$ shown in (2.11) would have been appropriate as to deal with the constitutive equation $\mathbf{B} = \underline{\underline{\mu}}\,\mathbf{H}$ and the divergence-free condition $\nabla\cdot\mathbf{B} = 0$ and take advantage of the fact that such topological relation can be satisfied pointwise.

Bibliography

[1] James H Adler et al. “A Stable Mimetic Finite-Difference Method for Convection-Dominated Diffusion Equations”. Aug. 2022.

[2] James H. Adler et al. “A finite-element framework for a mimetic finite-difference discretization of Maxwell’s equations”. In: *SIAM Journal on Scientific Computing* 43 (4 2021), A2638–A2659. ISSN: 10957197. DOI: 10.1137/20M1382568.

[3] Douglas Arnold, Richard Falk, and Ragnar Winther. “Finite element exterior calculus: from Hodge theory to numerical stability”. In: *Bulletin of the American Mathematical Society* 47.2 (Jan. 2010), pp. 281–354. DOI: 10.1090/s0273-0979-10-01278-4.

[4] Douglas N. Arnold. “Mixed Finite Element Methods for Elliptic Problems”. In: *Computer Methods in Applied Mechanics and Engineering* 82 (1 1990), pp. 281–300. ISSN: 0045-7825. DOI: 10.1016/0045-7825(90)90168-L.

[5] C.A. Balanis. *Advanced Engineering Electromagnetics*. CourseSmart Series. Wiley, 2012. ISBN: 9780470589489.

[6] “Basic Concepts”. In: *The Mathematical Theory of Finite Element Methods*. New York, NY: Springer New York, 2008, pp. 1–22. ISBN: 978-0-387-75934-0. DOI: 10.1007/978-0-387-75934-0_1.

[7] P. Bochev. “A discourse on variational and geometric aspects of stability of discretizations”. In: *33rd Computational Fluid Dynamics Lecture Series, VKI LS* 5 (2003).

[8] P. Bochev and James M. Hyman. “Principles of Mimetic Discretizations of Differential Operators”. In: vol. 142. Springer New York, Jan. 2007, pp. 89–119. ISBN: 978-0-387-30916-3. DOI: 10.1007/0-387-38034-5_5.

[9] D. Boffi. “Finite element approximation of eigenvalue problems”. In: *Acta Numerica* 19 (May 2010), pp. 1–120. ISSN: 0962-4929.

[10] D. Boffi, F. Brezzi, and M. Fortin. *Mixed Finite Element Methods and Applications*. Vol. 44. Springer Science & Business Media, 2013. ISBN: 978-3-642-36519-5. DOI: 10.1007/978-3-642-36519-5.

[11] A. Bossavit. “Whitney forms: A class of finite elements for three-dimensional computations in electromagnetism”. In: *Article in Science, Measurement and Technology* (1988).

[12] A. Bossavit. “Solving Maxwell equations in a closed cavity, and the question of ‘spurious modes’”. In: *IEEE Transactions on Magnetics* 26 (2 1990), pp. 702–705. ISSN: 19410069. DOI: 10.1109/20.106414.

[13] A. Bossavit. “Mixed methods and the marriage between “mixed” finite elements and boundary elements”. In: *Numerical Methods for Partial Differential Equations* 7.4 (1991), pp. 347–362. DOI: 10.1002/num.1690070405.

[14] A. Bossavit. “Building a finite-dimensional "Maxwell’s house"”. In: *Journal of Japanese Society of Applied Electromagnetism and Mechanics* (1998).

[15] A. Bossavit. *Computational Electromagnetism: Variational Formulations, Complementarity, Edge Elements*. Academic Press, 1998.

[16] A. Bossavit. “Japanese Papers”. 1998. URL: https://faculty.washington.edu/seattle/physics544/2011-lectures/bossavit.pdf.

[17] A. Bossavit. “On the geometry of electromagnetism”. In: *Journal of Japanese Society of Applied Electromagnetism and Mechanics* (1998), pp. 17–28.

[18] A. Bossavit. “Generating Whitney forms of polynomial degree one and higher”. In: *IEEE Transactions on Magnetics* 38 (2 I Mar. 2002), pp. 341–344. ISSN: 00189464. DOI: 10.1109/20.996092.

[19] A. Bossavit. “A uniform rationale for Whitney forms on various supporting shapes”. In: *Mathematics and Computers in Simulation* 80 (8 Apr. 2010), pp. 1567–1577. ISSN: 03784754. DOI: 10.1016/j.matcom.2008.11.005.

[20] A. Bossavit and J.-C. Verite. “A mixed fem-biem method to solve 3-D eddy-current problems”. In: *IEEE Transactions on Magnetics* 18.2 (1982), pp. 431–435. DOI: 10.1109/TMAG.1982.1061847.

[21] Sussane C. Brenner, Fengyan Li, and Li-yeung Sung. “Nonconforming Maxwell eigensolvers”. In: *Journal of Scientific Computing* 40 (1-3 July 2009), pp. 51–85. ISSN: 08857474. DOI: 10.1007/s10915-008-9266-9.

[22] F. Brezzi. “On the existence, uniqueness and approximation of saddle-point problems arising from lagrangian multipliers”. In: *ESAIM: Mathematical Modelling and Numerical Analysis - Modélisation Mathématique et Analyse Numérique* 8.R2 (1974), pp. 129–151.

[23] Franco Brezzi and Annalisa Buffa. “Innovative mimetic discretizations for electromagnetic problems”. In: vol. 234. Aug. 2010, pp. 1980–1987. DOI: 10.1016/j.cam.2009.08.049.

[24] C. Canuto et al. *Spectral Methods: Evolution to Complex Geometries and Applications to Fluid Dynamics*. Springer-Verlag Berlin, Heidelberg, 2007. ISBN: 978-3-540-30727-3.

[25] J. Clerk-Maxwell. "Remarks on the Mathematical Classification of Physical Quantities," in: *Proceedings of the London Mathematical Society* s1-3.1 (1869), pp. 224–233.

[26] B. Cockburn. "Static Condensation, Hybridization, and the Devising of the HDG Methods". In: *Building Bridges: Connections and Challenges in Modern Approaches to Numerical Partial Differential Equations*. Ed. by Gabriel R. Barrenechea et al. Cham: Springer International Publishing, 2016, pp. 129–177. ISBN: 978-3-319-41640-3. DOI: 10.1007/978-3-319-41640-3_5.

[27] G. Cohen and M. Durufle. *Benchmark computations for Maxwell equations for the approximation of highly singular solutions: Results from Inria Rocquencourt*. Université de Rennes. URL: https://www.math.u-bordeaux.fr/~durufle/eigenvalue.php.

[28] G. Cohen and S. Pernet. *Finite Element and Discontinuous Galerkin Methods for Transient Wave Equations*. Ed. by Chattot J.J. et al. Springer Science + Business Media B.V., 2017. ISBN: 978-94-017-7761-2. DOI: 10.1007/978-64-017-7761-2.

[29] M. Dauge. *Benchmark computations for Maxwell equations for the approximation of highly singular solutions*. Université de Rennes. 2004. URL: https://perso.univ-rennes1.fr/monique.dauge/benchmax.html.

[30] G.A. Deschamps. "Electromagnetics and differential forms". In: *Proceedings of the IEEE* 69.6 (1981), pp. 676–696. DOI: 10.1109/PROC.1981.12048.

[31] G.A. Deschamps, E. Roubine, and Unesco. *Mathematics Applied to Physics*. Teaching of basic sciences. Springer-Verlag, 1970. ISBN: 9780387049656.

[32] Jozef Dodziuk. "Finite-Difference Approach to the Hodge Theory of Harmonic Forms". In: *American Journal of Mathematics* 98.1 (1976), pp. 79–104. ISSN: 00029327, 10806377. URL: http://www.jstor.org/stable/2373615.

[33] Huoyuan Duan et al. "New Mixed Elements for Maxwell Equations". In: *SIAM Journal on Numerical Analysis* 57.1 (2019), pp. 320–354. DOI: 10.1137/18M1168054.

[34] A. Ern and J.L. Guermond. *Finite Elements II: Galerkin Approximation, Elliptic and Mixed PDEs*. Vol. 2. Springer Nature Switzerland AG, 2021. ISBN: 978-3-030-56923-5. DOI: 10.1007/978-3-030-56923-5.

[35] Richard P. Feynman, Robert B. Leighton, and Matthew Sand. *The Feynman Lectures on Physics: New Millenium Edition. Volume II*. Vol. 2. Basic Books, Perseus Books Group, 1964. ISBN: 2010938208.

[36] H. Flanders. *Differential forms : with applications to the physical sciences*. Academic Press, Inc., 1963. ISBN: 0-486-66169-5.

[37] F.R. Gantmacher. *The Theory of Matrices*. Vol. 1. Chelsea Publishing Company, New York, 1959.

[38] M. Gerritsma. "Edge Functions for Spectral Element Methods". In: *Spectral and High Order Methods for Partial Differential Equations* 76 (2011). Ed. by Jan S. Hesthaven and Einar M. Rønquist, pp. 199–207. DOI: 10.1007/978-3-642-15337-2.

[39] M. Gerritsma et al. "Mimetic Spectral Element Method for Anisotropic Diffusion". In: *Numerical Methods for PDEs: State of the Art Techniques*. Ed. by Daniele Antonio Di Pietro, Alexandre Ern, and Luca Formaggia. Cham: Springer International Publishing, 2018, pp. 31–74. ISBN: 978-3-319-94676-4. DOI: 10.1007/978-3-319-94676-4_3.

[40] W.C. Gibson. *The Method of Moments in Electromagnetics*. Taylor & Francis, 2014. ISBN: 9781482235791.

[41] W.J. Gordon and C.A. Hall. "Transfinite Element Methods: Blending-Function Interpolation over Arbitrary Curved Element Domains". In: *Numer. Math* 21 (1973), pp. 109–129.

[42] V. Gradinaru and R. Hiptmair. "Whitney Elements on Pyramids". In: *Electronic Transactions on Numerical Analysis* 8 (1999), pp. 154–168. ISSN: 1068-9613.

[43] M. Hara et al. "A three dimensional analysis of RF electromagnetic fields by the finite element method". In: *IEEE Transactions on Magnetics* 19.6 (1983), pp. 2417–2420. DOI: 10.1109/TMAG.1983.1062816.

[44] R.F. Harrington, IEEE Antennas, and Propagation Society. *Field Computation by Moment Methods*. An IEEE / OUP classic reissue. Wiley-IEEE Press, 1993. ISBN: 9780198592174.

[45] R. Hiptmair. "Discrete Hodge operators". In: *Numerische Mathematik* 90 (2 Dec. 2001), pp. 265–289. ISSN: 0029599X. DOI: 10.1007/s002110100295.

[46] R. Hiptmair. "Maxwell's Equations: Continuous and Discrete". In: *Computational Electromagnetism: Cetraro, Italy 2014*. Ed. by Alfredo Bermúdez de Castro and Alberto Valli. Cham: Springer International Publishing, 2015, pp. 1–58. ISBN: 978-3-319-19306-9. DOI: 10.1007/978-3-319-19306-9_1.

[47] S. Hoole. *Finite Elements, Electromagnetics and Design*. Elsevier, 1995. ISBN: 978-0-444-89563-9. DOI: 10.1016/B978-0-444-89563-9.X5019-2.

[48] Ronald H W Hoppe. "A Penalty Method for the Approximate Solution of Stationary Maxwell Equations". In: *Numerische Mathematik* 36 (1981), pp. 389–403.

[49] Kaibo Hu et al. "Spurious solutions for high-order curl problems". In: *IMA Journal of Numerical Analysis* (June 2022). ISSN: 0272-4979. DOI: 10.1093/imanum/drac024.

[50] James M Hyman and Mikhail Shashkov. "Mimetic Discretizations for Maxwell's Equations". In: *Journal of Computational Physics* 151 (1999), pp. 881–909.

[51] V. Jain et al. "Construction and application of algebraic dual polynomial representations for finite element methods on quadrilateral and hexahedral meshes". In: *Computers and Mathematics with Applications* 95 (Aug. 2021), pp. 101–142. ISSN: 08981221. DOI: 10.1016/j.camwa.2020.09.022.

[52] Claude Le Bris Jean F. Gerbeau and Tony Lelièvre. *Mathematical methods for the magnetohydrodynamics of liquid metals*. Oxford University Press, 2006. ISBN: 978-0-19-856665-6.

[53] W. Jiang et al. "Mixed Finite Element Method for 2D Vector Maxwell's Eigenvalue Problem in Anisotropic Media". In: *Progress In Electromagnetics Research* 148 (2014), pp. 159–170. ISSN: 10704698. DOI: 10.2528/PIER14052608.

[54] Jian-Ming Jin. *The Finite Element Method in Electromagnetics*. 2nd. Wiley, 2002. ISBN: 0471438189.

[55] Jian-Ming Jin. *Theory and Computation of Electromagnetic Fields*. 2nd ed. Vol. 51. John Wiley & Sons, Incorporated, 2015. ISBN: 978-1-119-10804-7.

[56] F. Kikuchi. "Mixed and Penalty Formulations for Finite Element Analysis of an Eigenvalue Problem in Electromagnetism". In: *Computer Methods In Applied Mechanics and Engineering* 64 (1987), pp. 509–521.

[57] A. Konrad. "On the Reduction of the Number of Spurious Modes in the Vectorial Finite-Element Solution of Three-Dimensional Cavities and Waveguides". In: *IEEE Transactions on Microwave Theory and Techniques* 34.2 (1986), pp. 224–227. DOI: 10.1109/TMTT.1986.1133315.

[58] Jasper Kreeft and Marc Gerritsma. "Mixed mimetic spectral element method for Stokes flow: A pointwise divergence-free solution". In: *Journal of Computational Physics* 240 (2013), pp. 284–309. ISSN: 0021-9991. DOI: 10.1016/j.jcp.2012.10.043.

[59] D. Kressner. *Numerical Methods for General and Structured Eigenvalue Problems. Lecture Notes in Computational Science and Engineering*. Springer Berlin, Heidelberg, 2005. ISBN: 978-3-540-28502-1.

[60] J.R. Kuttler and V.G. Sigillito. "Eigenvalues of the Laplacian in Two Dimensions". In: *SIAM Review* 26 (2 Apr. 1984), pp. 163–193.

[61] Andrei V. Lavrinenko et al. *Numerical Methods in Photonics*. CRC Press, Taylor & Francis Group, LLC, 2015, pp. 293–294. ISBN: 9781466563896.

[62] D. Lee, A. Palha, and M. Gerritsma. "Discrete conservation properties for shallow water flows using mixed mimetic spectral elements". In: *Journal of Computational Physics* 357 (2018), pp. 282–304. ISSN: 0021-9991. DOI: 10.1016/j.jcp.2017.12.022.

[63] K. Lipnikov et al. "The mimetic finite difference method for the 3D magnetostatic field problems on polyhedral meshes". In: *Journal of Computational Physics* 230 (2 Jan. 2011), pp. 305–328. ISSN: 10902716. DOI: 10.1016/j.jcp.2010.09.007.

[64] Konstantin Lipnikov, Gianmarco Manzini, and Mikhail Shashkov. "Mimetic finite difference method". In: *Journal of Computational Physics* 257 (PB Jan. 2014), pp. 1163–1227. ISSN: 10902716. DOI: 10.1016/j.jcp.2013.07.031.

[65] Jonni Lohi and Lauri Kettunen. "Whitney forms and their extensions". In: *Journal of Computational and Applied Mathematics* 393 (2021), p. 113520. ISSN: 0377-0427. DOI: https://doi.org/10.1016/j.cam.2021.113520.

[66] Claudio Mattiussi. "The finite volume, finite element, and finite difference methods as numerical methods for physical field problems". In: ed. by Peter W. Hawkes. Vol. 113. Advances in Imaging and Electron Physics. Elsevier, 2000, pp. 1–146. DOI: 10.1016/S1076-5670(00)80012-9.

[67] Peter Monk. *Finite Element Methods for Maxwell's Equations*. Clarendon Press, 2003.

[68] J C Nedelec. "Mixed finite elements in $\mathbb{R}^3$". In: *Numerische Mathematik* 35 (1980), pp. 315–341. DOI: 10.1007/BF01396415.

[69] A.V. Osipov and S.A. Tretyakov. *Modern Electromagnetic Scattering Theory with Applications*. Wiley, 2017. ISBN: 9781119293286.

[70] A. Palha and M. Gerritsma. "A mass, energy, enstrophy and vorticity conserving (MEEVC) mimetic spectral element discretization for the 2D incompressible Navier–Stokes equations". In: *Journal of Computational Physics* 328 (2017), pp. 200–220. ISSN: 0021-9991. DOI: 10.1016/j.jcp.2016.10.009.

[71] A. Palha, B. Koren, and F. Felici. "A mimetic spectral element solver for the Grad-Shafranov equation". In: *Journal of Computational Physics* 316 (July 2016), pp. 63–93. ISSN: 10902716. DOI: 10.1016/j.jcp.2016.04.002.

[72] Artur Palha et al. "Physics-compatible discretization techniques on single and dual grids, with application to the Poisson equation of volume forms". In: *Journal of Computational Physics* 257 (PB Jan. 2014), pp. 1394–1422. ISSN: 10902716. DOI: 10.1016/j.jcp.2013.08.005.

[73] Beresford N. Parlett. *The Symmetric Eigenvalue Problem*. Prentice-Hall, 1980. ISBN: 0-89871-402-8.

[74] J. Blair Perot. "Discrete Conservation Properties of Unstructured Mesh Schemes". In: *Annual Review of Fluid Mechanics* 43.1 (2011), pp. 299–318. DOI: 10.1146/annurev-fluid-122109-160645.

[75] G. Pierre. *Elliptic Problems in Nonsmooth Domains*. Pitman Advanced Publishing Program, 1985. ISBN: 9780273086475.

[76] S. Pissanetzky. *Sparse Matrix Technology*. Academic Press, Harcourt Brace Jovanovich Publishers, 1984.

[77] F. Rapetti and A. Bossavit. "Whitney Forms of Higher Degree". In: *SIAM Journal on Numerical Analysis* 47 (3 Jan. 2009), pp. 2369–2386. ISSN: 0036-1429. DOI: 10.1137/070705489.

[78] P. A. Raviart and J. M. Thomas. "A mixed finite element method for 2-nd order elliptic problems". In: *Mathematical Aspects of Finite Element Methods*. Ed. by Ilio Galligani and Enrico Magenes. Berlin, Heidelberg: Springer Berlin Heidelberg, 1977, pp. 292–315. ISBN: 978-3-540-37158-8.

[79] Nicolas Robidoux and Stanly Steinberg. "A Discrete Vector Calculus in Tensor Grids". In: *Computational Methods in Applied Mathematics* 1 (2001), pp. 1–44.

[80] T. Rylander, P. Ingelström, and A. Bondeso. *Computational Electromagnetics*. 2nd ed. Vol. 51. Springer New York, 2013. ISBN: 978-1-4614-5351-2. DOI: 10.1007/978-1-4614-5351-2.

[81] Levent Sevgi. *Electromagnetic Modeling and Simulation*. Wiley-IEEE Press Series on Electromagnetic Wave Theory, 2014.

[82] A. Sheldon. *Linear Algebra Done Right*. Springer International Publishing, 2015. ISBN: 978-3-319-11080-6. DOI: 10.1007/978-3-319-11080-6_3.

[83] J.A. Shercliff. *A Textbook of Magnetohydrodynamics*. Pergamon Press, 1965. ISBN: 9780082016984. URL: http://www.springer.com/series/718.

[84] Din Sun et al. “Spurious modes in finite-element methods”. In: *IEEE Antennas and Propagation Magazine* 37.5 (1995), pp. 12–24. DOI: 10.1109/74.475860.

[85] A. Taflove. *Computational Electrodynamics: The Finite-difference Time-domain Method*. Antennas and Propagation Library. Artech House, 1995. ISBN: 9780890067925.

[86] K.T Tang. *Mathematical Methods for Engineers and Scientists 3: Fourier Analysis, Partial Differential Equations and Variational Methods*. Springer-Verlag Berlin, Heidelberg, 2007. ISBN: 978-3-642-07947-4.

[87] Timo Tarhasaari, Lauri Kettunen, and Alain Bossavit. “Some realizations of a discrete Hodge operator: A reinterpretation of finite element techniques”. In: *IEEE Transactions on Magnetics* 35 (3 PART 1 1999), pp. 1494–1497. ISSN: 00189464. DOI: 10.1109/20.767250.

[88] Enzo Tonti. “Sulla Struttura Formale delle Teorie Fisiche”. In: *Rendiconti del Seminario Matematico e Fisico di Milano* 46 (Dec. 1976), pp. 163–257. DOI: 10.1007/BF02925692.

[89] Enzo Tonti. *The Mathematical Structure of Classical and Relativistic Physics: A General Classification Diagram*. Birkhäuser, 2013. ISBN: 9781461474227. DOI: 10.1007/978-1-4614-7422-7.

[90] Enzo Tonti. “Why starting from differential equations for computational physics?” In: *Journal of Computational Physics* 257 (PB Jan. 2014), pp. 1260–1290. ISSN: 10902716. DOI: 10.1016/j.jcp.2013.08.016.

[91] Lourenço Beirão da Veiga, Konstantin Lipnikov, and Gianmarco Manzini. *The Mimetic Finite Difference Method for Elliptic Problems*. 1st ed. Vol. 11. Springer Cham, 2014, pp. 1–389. DOI: 10.1007/978-3-319-02663-3.

[92] Kane S. Yee. “Numerical Solution of Initial Boundary Value Problems Involving Maxwell’s Equations in Isotropic Media”. In: *IEEE Transactions on Antennas and Propagation* 14 (3 1966), pp. 302–307. ISSN: 15582221. DOI: 10.1109/TAP.1966.1138693.

[93] Yi Zhang, Joël Fisser, and Marc Gerritsma. “A hybrid mimetic spectral element method for three-dimensional linear elasticity problems”. In: *Journal of Computational Physics* 433 (2021), p. 110179. ISSN: 0021-9991. DOI: 10.1016/j.jcp.2021.110179.

A

Hybrid Systems

Consider to following problem:

$$\begin{bmatrix} A & B^{\mathrm{T}} & C^{\mathrm{T}} \\ B & 0 & 0 \\ C & 0 & 0 \end{bmatrix} \begin{pmatrix} x \\ y \\ \Lambda \end{pmatrix} = \begin{pmatrix} F \\ G \\ 0 \end{pmatrix}$$

in which the first row is used to solve for the unknown vector x as:

$$x = A^{-1}\Big(F - B^{\mathrm{T}}y - C^{\mathrm{T}}\Lambda\Big)$$

such that a new reduced system is obtained:

$$\begin{bmatrix} -BA^{-1}B^{\mathrm{T}} & -BA^{-1}C^{\mathrm{T}} \\ -CA^{-1}B^{\mathrm{T}} & -CA^{-1}C^{\mathrm{T}} \end{bmatrix} \begin{pmatrix} y \\ \Lambda \end{pmatrix} = \begin{pmatrix} G - BA^{-1}F \\ -CA^{-1}F \end{pmatrix}$$

which can be rewritten as:

$$\begin{bmatrix} \hat{A} & \hat{B}^{\mathrm{T}} \\ \hat{B} & \hat{D} \end{bmatrix} \begin{pmatrix} y \\ \Lambda \end{pmatrix} = \begin{pmatrix} \hat{G} \\ \hat{F} \end{pmatrix}$$

where the terms $\hat{A} = -BA^{-1}B^{\mathrm{T}}$, $\hat{B} = -CA^{-1}B^{\mathrm{T}}$, $\hat{D} = -CA^{-1}C^{\mathrm{T}}$, $\hat{G} = G - BA^{-1}F$ and $\hat{F} = -CA^{-1}F$ are introduced to simplify the writing of the system.

The new system is solved for y which leads to:

$$y = \hat{A}^{-1}\left(\hat{G} - \hat{B}^{\mathrm{T}}\Lambda\right)$$

which is used to solve for the variable Λ as:

$$\hat{B}\hat{A}^{-1}\left(\hat{G} - \hat{B}^{\mathrm{T}}\Lambda\right) + \hat{D}\Lambda = \hat{F}$$

$$\underbrace{\left(\hat{D} - \hat{B}\hat{A}^{-1}\hat{B}^{\mathrm{T}}\right)}_{\mathrm{K}}\Lambda = \underbrace{\hat{F} - \hat{B}\hat{A}^{-1}\hat{G}}_{f}$$

If the formulation presented at the beginning were to be the primal-primal Poisson problem in $\mathbb{R}^n$ with Homogeneous Dirichlet boundary conditions, then $F = 0$, $A = \mathbb{M}^{(n-1)}$, $B = \mathbb{M}^{(n)}\,\mathbb{E}^{n,n-1}$, $G = \underline{\mathrm{F}}$ and $C = \mathbb{N} \rightarrow$ Connectivity matrix (Section 3.6.2). The unknown vectors for such problem would be $x = \mathcal{N}^{(n-1)}(u^h)$, $y = \mathcal{N}^{n}(\phi^h)$ while Λ would be the multipliers at the element intersections. The same association can be done for the variables of the primal-dual problem.

Thus, by solving for the multipliers Λ from the system $\mathrm{K}\Lambda = f$, the solution for the main variable $\mathcal{N}^{n}(\phi^h)$ can be obtained as $\mathcal{N}^{n}(\phi^h) = \hat{A}^{-1}\left(\hat{G} - \hat{B}^{\mathrm{T}}\Lambda\right)$. The advantage of this procedure is that the system for the main variable is way smaller than the one of the original formulation. Additionally, the solution for $\mathcal{N}^{n}(\phi^h)$ can be computed all at the same time since the problem is now effectively decoupled.

Additional information about this procedure can be found in [26].

B

Schur Complement Method

The main idea is to use block Gaussian elimination to solve a system of linear equations that can be written out in the following form:

$$\begin{bmatrix} A_1 & A_2 \\ A_3 & A_4 \end{bmatrix} \begin{pmatrix} x_1 \\ x_2 \end{pmatrix} = \begin{pmatrix} F_1 \\ F_2 \end{pmatrix} \tag{B.1}$$

The first step consists on using the equation from the first row and solve for x_1:

$$x_1 = A_1^{-1}(F_1 - A_2 x_2) \tag{B.2}$$

and this result is used on the second row to obtain an equation for x_2 only:

$$A_3\, A_1^{-1}\left(F_1 - A_2 x_2\right) + A_4\, x_2 = F_2 \quad \rightarrow \quad \left(A_4 - A_3\, A_1^{-1}\, A_2\right) x_2 = F_2 - A_3\, A_1^{-1}\, F_1 \tag{B.3}$$

which immediately imposes a condition on the existence of the inverse of both A_1 and $A_4 - A_3\, A_1^{-1}\, A_2$ for a solution to exist. To be more compact on the notation, the variables S and F are introduced such that,

$$S\, x_2 = F \quad \begin{cases} S = A_4 - A_3\, A_1^{-1}\, A_2 \\ B = F_2 - A_3\, A_1^{-1}\, F_1 \end{cases} \tag{B.4}$$

Thus, it is only a matter of defining the terms S and B for different formulations. Consider now, for example, the discrete system arising from the primal-primal mixed

formulation of the Poisson equation in $\Omega \in \mathbb{R}^n$:

$$\begin{bmatrix} \mathbb{M}^{(n-1)} & \left(\mathbb{E}^{(n,n-1)}\right)^{\mathrm{T}} \mathbb{M}^{(n)} \\ \mathbb{M}^{(n)}\,\mathbb{E}^{(n,n-1)} & 0 \end{bmatrix} \begin{pmatrix} \mathcal{N}^{(n-1)}(u^h) \\ \mathcal{N}^{(n)}(\phi^h) \end{pmatrix} = \begin{pmatrix} \mathbb{B} \\ \underline{\mathrm{F}} \end{pmatrix} \tag{B.5}$$

For $n = 1$, the system is equivalent to the one in Section 4.1.2 while for $n = 2$ it resembles the one found in Section 4.3.2. By applying the *Schur Complement Method* (SCM), it is possible to solve for $\mathcal{N}^{(n)}(\phi^h)$ with S and B defined as:

$$S = -\left(\mathbb{M}^{(n)}\,\mathbb{E}^{(n,n-1)}\right)\left(\mathbb{M}^{n-1}\right)^{-1}\left(\left(\mathbb{E}^{(n,n-1)}\right)^{\mathrm{T}} \mathbb{M}^{(n)}\right) \tag{B.6}$$

$$B = \underline{\mathrm{F}} - \left(\mathbb{M}^{(n)}\,\mathbb{E}^{(n,n-1)}\right)\left(\mathbb{M}^{n-1}\right)^{-1}\mathbb{B} \tag{B.7}$$

For the primal-dual formulation of the Poisson equation in $\Omega \in \mathbb{R}^n$:

$$\begin{bmatrix} \mathbb{M}^{(n-1)} & \left(\mathbb{E}^{(n,n-1)}\right)^{\mathrm{T}} \\ \mathbb{E}^{(n,n-1)} & 0 \end{bmatrix} \begin{pmatrix} \mathcal{N}^{(n-1)}(u^h) \\ \widetilde{\mathcal{N}}^{0}(\phi^h) \end{pmatrix} = \begin{pmatrix} \mathbb{B} \\ -\mathcal{N}^{(n)}(f^h) \end{pmatrix} \tag{B.8}$$

hence, it can be solved directly for $\widetilde{\mathcal{N}}^{0}(\phi^h)$ by using,

$$S = -\mathbb{E}^{(n,n-1)}\left(\mathbb{M}^{n-1}\right)^{-1}\left(\mathbb{E}^{(n,n-1)}\right)^{\mathrm{T}} \tag{B.9}$$

$$B = -\mathcal{N}^{(n)}(f^h) - \mathbb{E}^{(n,n-1)}\left(\mathbb{M}^{n-1}\right)^{-1}\mathbb{B} \tag{B.10}$$

For eigenvalue problems, the application is also straightforward:

$$\begin{bmatrix} \mathbb{M}^{(n-1)} & \left(\mathbb{E}^{(n,n-1)}\right)^{\mathrm{T}} \mathbb{M}^{(n)} \\ \mathbb{M}^{(n)}\,\mathbb{E}^{(n,n-1)} & 0 \end{bmatrix} \begin{pmatrix} \mathcal{N}^{(n-1)}(u^h) \\ \mathcal{N}^{(n)}(\phi^h) \end{pmatrix} = \cdots$$

$$\cdots = -\lambda \begin{bmatrix} 0 & 0 \\ 0 & \mathbb{M}^{(n)} \end{bmatrix} \begin{pmatrix} \mathcal{N}^{(n-1)}(u^h) \\ \mathcal{N}^{(n)}(\phi^h) \end{pmatrix} \tag{B.11}$$

The variable S remains unchanged compared to the primal-primal formulation and the term B becomes much simpler but includes the degrees of freedom $\mathcal{N}^{(n)}(\phi^h)$:

$$S = -\left(\mathbb{M}^{(n)}\,\mathbb{E}^{(n,n-1)}\right)\left(\mathbb{M}^{n-1}\right)^{-1}\left(\left(\mathbb{E}^{(n,n-1)}\right)^{\mathrm{T}} \mathbb{M}^{(n)}\right) \tag{B.12}$$

$$B = -\lambda\,\mathbb{M}^{(n)}\mathcal{N}^{(n)}(\phi^h) \tag{B.13}$$

Thus, the discrete eigenvalue system is given by:

$$\mathbb{M}^{(n)}\,\mathbb{E}^{\,(n,n-1)}\left(\mathbb{M}^{n-1}\right)^{-1}\left(\mathbb{E}^{\,(n,n-1)}\right)^{\mathrm{T}}\,\mathbb{M}^{(n)}\mathcal{N}^{(n)}(\phi^h)=\lambda\,\mathbb{M}^{(n)}\mathcal{N}^{(n)}(\phi^h) \tag{B.14}$$

The system can be compacted by introducing $\widetilde{\mathcal{N}}^0(\phi^h)=\mathbb{M}^{(n)}\mathcal{N}^{(n)}(\phi^h)$. Furthermore, by using the fact that $\widetilde{\mathbb{M}}^{(n-d)}=\left(\mathbb{M}^{(n-1)}\right)^{-1}$ and $\widetilde{\mathbb{M}}^{(0)}=\left(\mathbb{M}^{(n)}\right)^{-1}$, the dual matrices can be utilized. The parameter d depends on the dimension of the embedding space: $n=1\rightarrow d=0$, $n=2\rightarrow d=1$ and $n=3\rightarrow d=2$. Thus, the formulation becomes:

$$\mathbb{E}^{\,(n,n-1)}\widetilde{\mathbb{M}}^{(n-d)}\left(\mathbb{E}^{\,(n,n-1)}\right)^{\mathrm{T}}\,\widetilde{\mathcal{N}}^0(\phi^h)=\lambda\,\widetilde{\mathbb{M}}^{(0)}\,\widetilde{\mathcal{N}}^0(\phi^h) \tag{B.15}$$

C

Eigenfunctions: L-Shape Domain

Since a direct method is utilized for this problem, the function space onto which the eigenfunction is sought is $\phi \in H^1(\Omega)$. As a result, the gradient of the eigenfunctions, $\nabla\phi(\boldsymbol{x})$, must be considered.

For an L-shape domain, if an eigenvalue exhibits poor convergence, it is likely that either $\phi(\boldsymbol{x})$ or $\nabla\phi(\boldsymbol{x})$ exhibit a poor behavior within the domain which can be linked to singularities or regions where the gradient changes rapidly depending on the direction of approximation. The most problematic area is, by far, the so-called *re-entrant* corner that, in this case, is located at $(x, y) = (0, 0)$.

The plots below show the eigenfunctions and their gradients. It will become clear that, had the term $\nabla\phi$ not been considered, the eigenvalues would have no apparent reason to exhibit sub-optimal convergence rates.

All the approximations shown within this section were computed with a polynomial degree $N = 12$ and 9 elements per subdomain Ω_k, hence, 27 elements cover the domain. The first row of each set of plots corresponds to the surfaces of either $\phi(\boldsymbol{x})$ or its gradient while the second row shows their correspondent contours. All functions were calculated such that $\max(f(\boldsymbol{x})) = 1$.

Five sets of plots are shown. Each set corresponds to one of the first five non-zero eigenvalues from Section 5.3.3. Contours for $\nabla\phi(\boldsymbol{x})$ can be found also in [27] where the data for λ_5 is flipped by -1 when compared to the contours shown here.

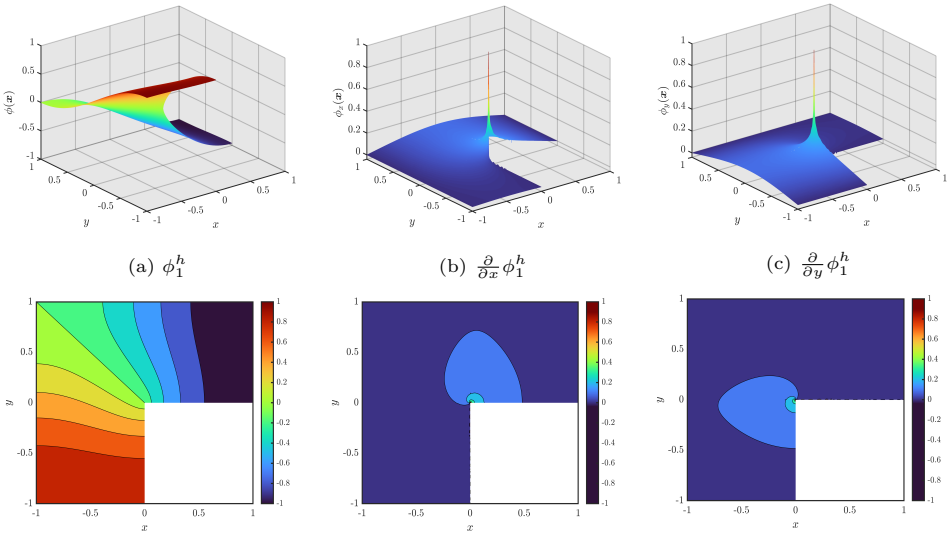

(a) ϕ_1^h (b) $\frac{\partial}{\partial x}\phi_1^h$ (c) $\frac{\partial}{\partial y}\phi_1^h$

(d) ϕ_1^h (e) $\frac{\partial}{\partial x}\phi_1^h$ (f) $\frac{\partial}{\partial y}\phi_1^h$

Figure C.1: Functions $\phi^h(\boldsymbol{x})$ and $\nabla\phi^h(\boldsymbol{x})$ associated to $\lambda_1 = 1.47562182408$.

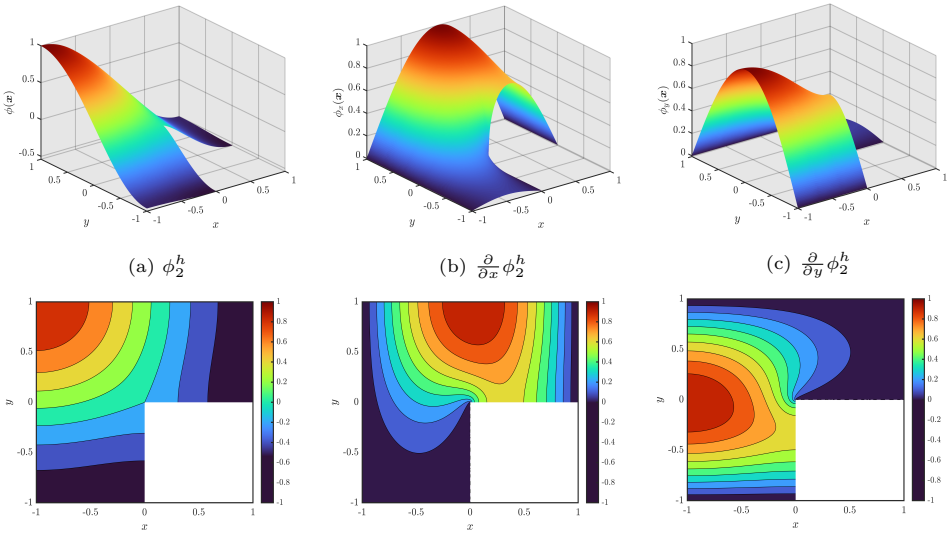

(a) ϕ_2^h (b) $\frac{\partial}{\partial x}\phi_2^h$ (c) $\frac{\partial}{\partial y}\phi_2^h$

(d) ϕ_2^h (e) $\frac{\partial}{\partial x}\phi_2^h$ (f) $\frac{\partial}{\partial y}\phi_2^h$

Figure C.2: Functions $\phi^h(\boldsymbol{x})$ and $\nabla\phi^h(\boldsymbol{x})$ associated to $\lambda_2 = 3.53403136678$.

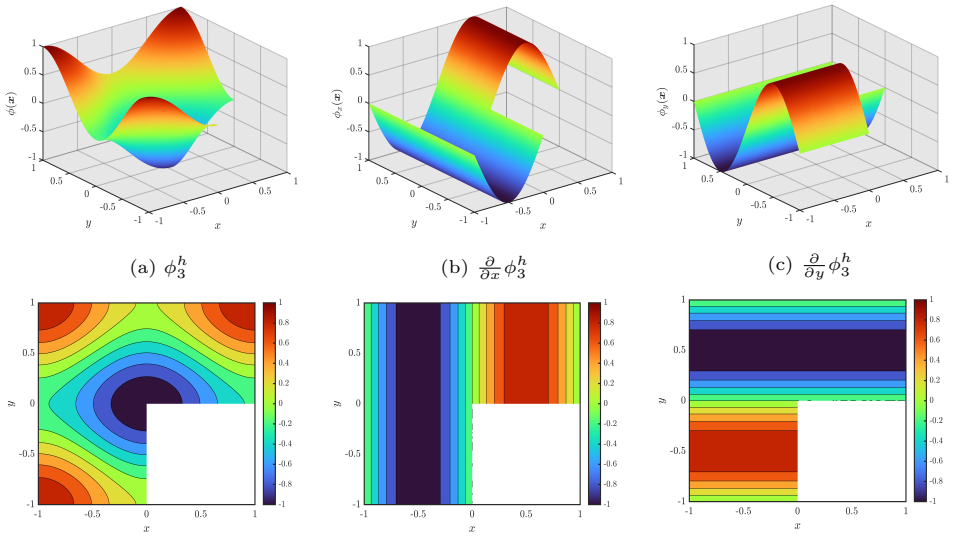

(a) ϕ_3^h (b) $\frac{\partial}{\partial x}\phi_3^h$ (c) $\frac{\partial}{\partial y}\phi_3^h$

(d) ϕ_3^h (e) $\frac{\partial}{\partial x}\phi_3^h$ (f) $\frac{\partial}{\partial y}\phi_3^h$

Figure C.3: Functions $\phi^h(\boldsymbol{x})$ and $\nabla\phi^h(\boldsymbol{x})$ associated to $\lambda_3 = 9.86960440109$.

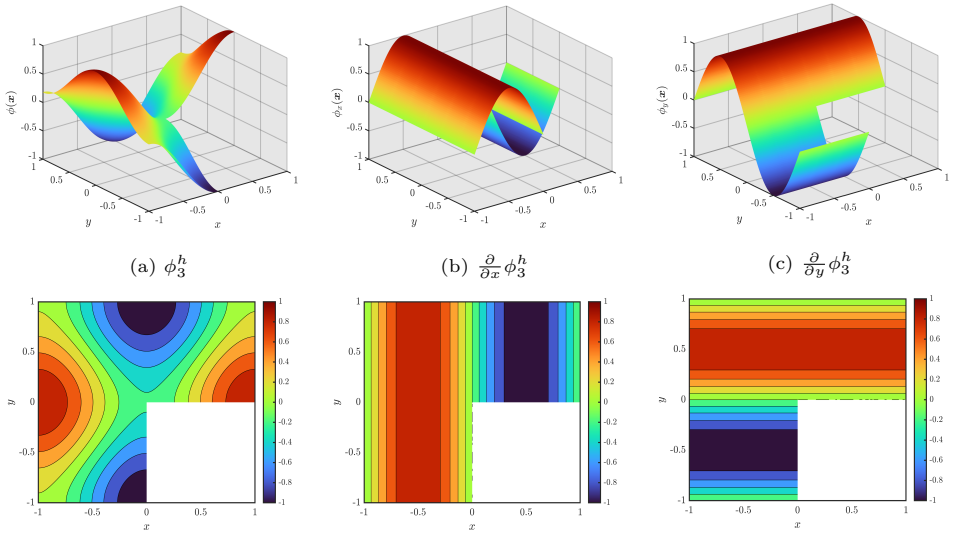

(a) ϕ_3^h (b) $\frac{\partial}{\partial x}\phi_3^h$ (c) $\frac{\partial}{\partial y}\phi_3^h$

(d) ϕ_3^h (e) $\frac{\partial}{\partial x}\phi_3^h$ (f) $\frac{\partial}{\partial y}\phi_3^h$

Figure C.4: Functions $\phi^h(\boldsymbol{x})$ and $\nabla\phi^h(\boldsymbol{x})$ associated to $\lambda_4 = 9.86960440109$.

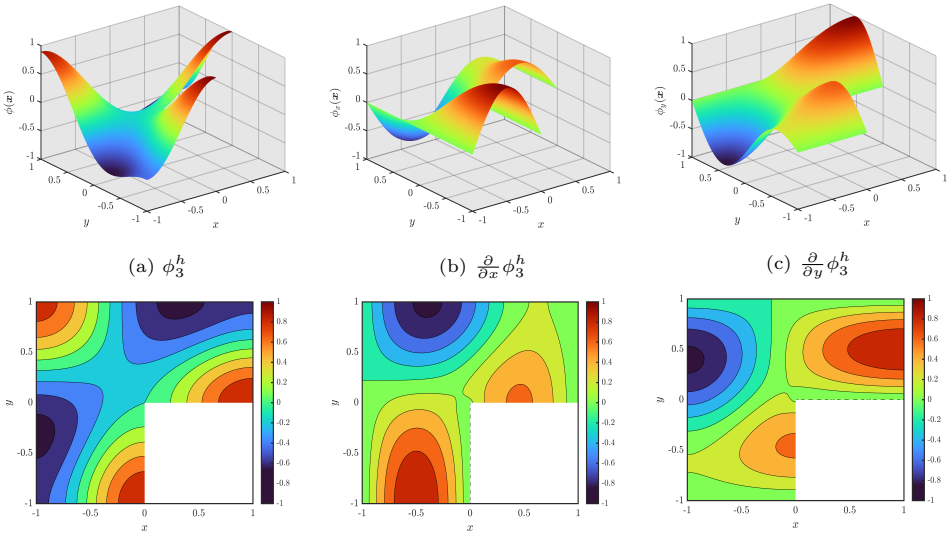

(a) ϕ_3^h (b) $\frac{\partial}{\partial x}\phi_3^h$ (c) $\frac{\partial}{\partial y}\phi_3^h$

(d) ϕ_3^h (e) $\frac{\partial}{\partial x}\phi_3^h$ (f) $\frac{\partial}{\partial y}\phi_3^h$

Figure C.5: Functions $\phi^h(\boldsymbol{x})$ and $\nabla\phi^h(\boldsymbol{x})$ associated to $\lambda_5 = 11.3894793979$.

D

Eigenfunctions: Cracked Domain

Functions $\phi^h(\boldsymbol{x})$ and $\nabla\phi^h(\boldsymbol{x})$ for the eigenvalues of Section 5.3.4.

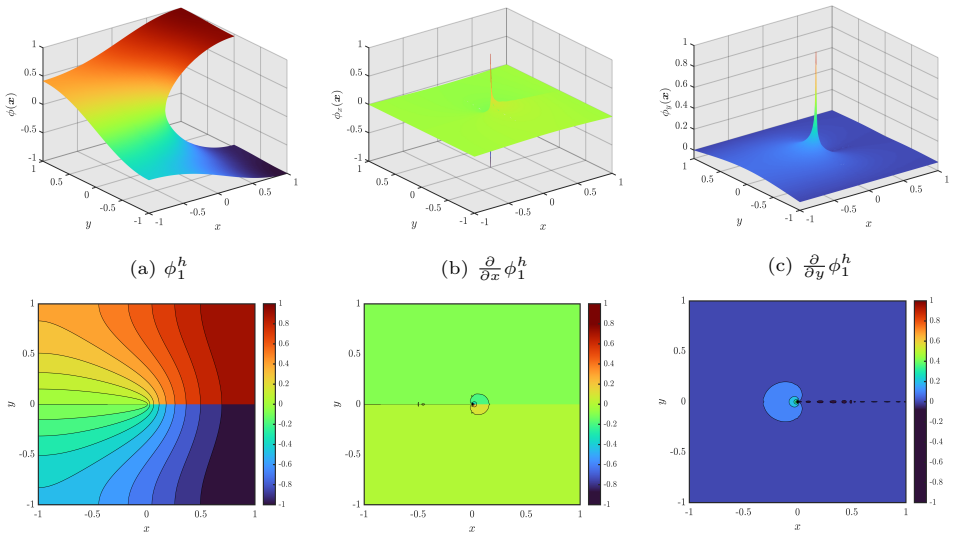

(a) ϕ_1^h (b) $\frac{\partial}{\partial x}\phi_1^h$ (c) $\frac{\partial}{\partial y}\phi_1^h$

(d) ϕ_1^h (e) $\frac{\partial}{\partial x}\phi_1^h$ (f) $\frac{\partial}{\partial y}\phi_1^h$

Figure D.1: Functions $\phi^h(\boldsymbol{x})$ and $\nabla\phi^h(\boldsymbol{x})$ associated to $\lambda_1 = 1.03407400850$.

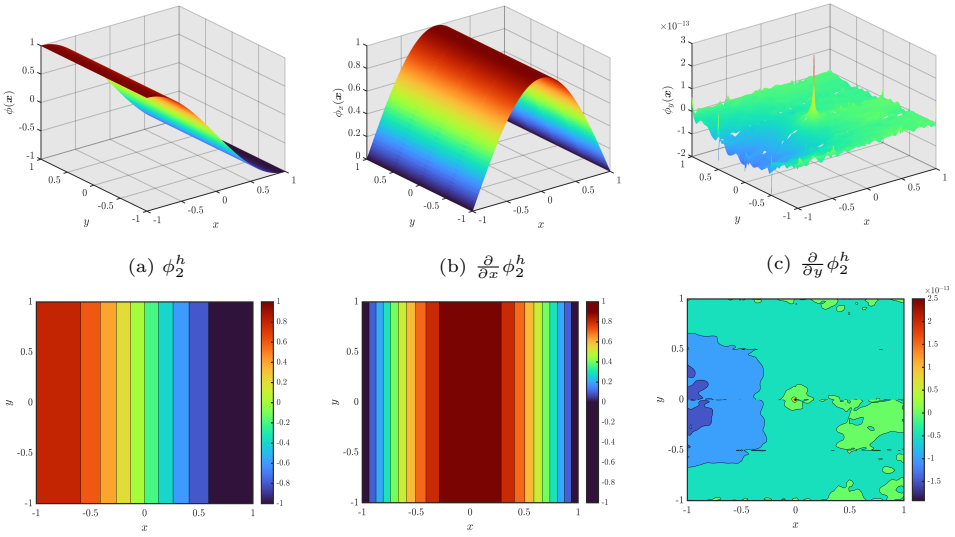

(a) ϕ_2^h (b) $\frac{\partial}{\partial x}\phi_2^h$ (c) $\frac{\partial}{\partial y}\phi_2^h$

(d) ϕ_2^h (e) $\frac{\partial}{\partial x}\phi_2^h$ (f) $\frac{\partial}{\partial y}\phi_2^h$

Figure D.2: Functions $\phi^h(\boldsymbol{x})$ and $\nabla\phi^h(\boldsymbol{x})$ associated to $\lambda_2 = 2.46740110027$.[14]

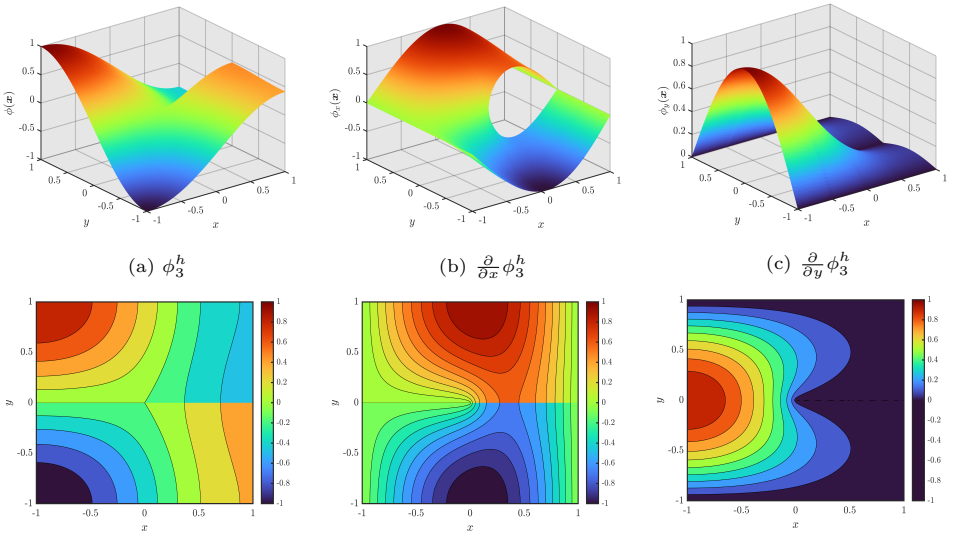

(a) ϕ_3^h (b) $\frac{\partial}{\partial x}\phi_3^h$ (c) $\frac{\partial}{\partial y}\phi_3^h$

(d) ϕ_3^h (e) $\frac{\partial}{\partial x}\phi_3^h$ (f) $\frac{\partial}{\partial y}\phi_3^h$

Figure D.3: Functions $\phi^h(\boldsymbol{x})$ and $\nabla\phi^h(\boldsymbol{x})$ associated to $\lambda_3 = 4.04692529140$.

[14] Both Figure D.2c and Figure D.2f are, essentially, **zero** since its oscillations are of order 10^{-13}.

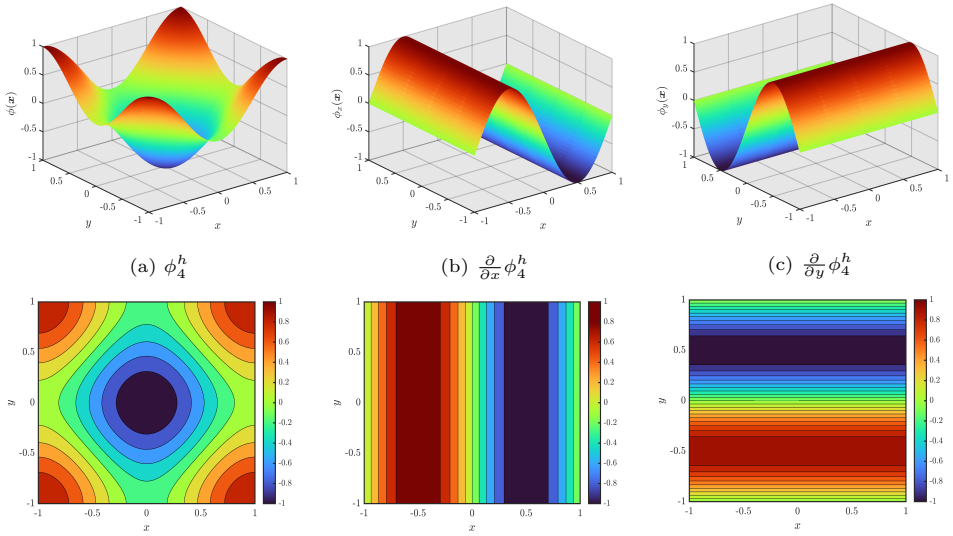

(a) ϕ_4^h (b) $\frac{\partial}{\partial x}\phi_4^h$ (c) $\frac{\partial}{\partial y}\phi_4^h$

(d) ϕ_4^h (e) $\frac{\partial}{\partial x}\phi_4^h$ (f) $\frac{\partial}{\partial y}\phi_4^h$

Figure D.4: Functions $\phi^h(\boldsymbol{x})$ and $\nabla\phi^h(\boldsymbol{x})$ associated to $\lambda_4 = 9.86960440109$.

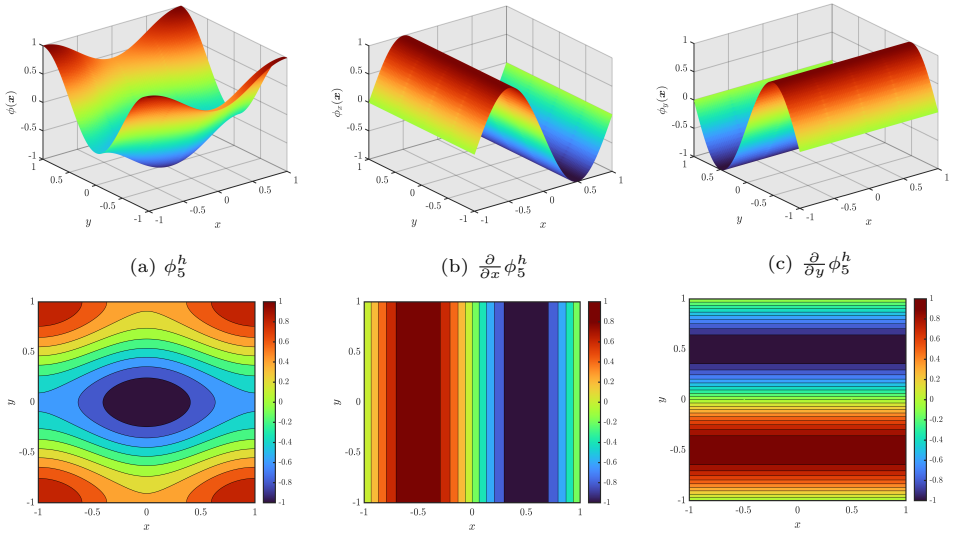

(a) ϕ_5^h (b) $\frac{\partial}{\partial x}\phi_5^h$ (c) $\frac{\partial}{\partial y}\phi_5^h$

(d) ϕ_5^h (e) $\frac{\partial}{\partial x}\phi_5^h$ (f) $\frac{\partial}{\partial y}\phi_5^h$

Figure D.5: Functions $\phi^h(\boldsymbol{x})$ and $\nabla\phi^h(\boldsymbol{x})$ associated to $\lambda_5 = 9.86960440109$.

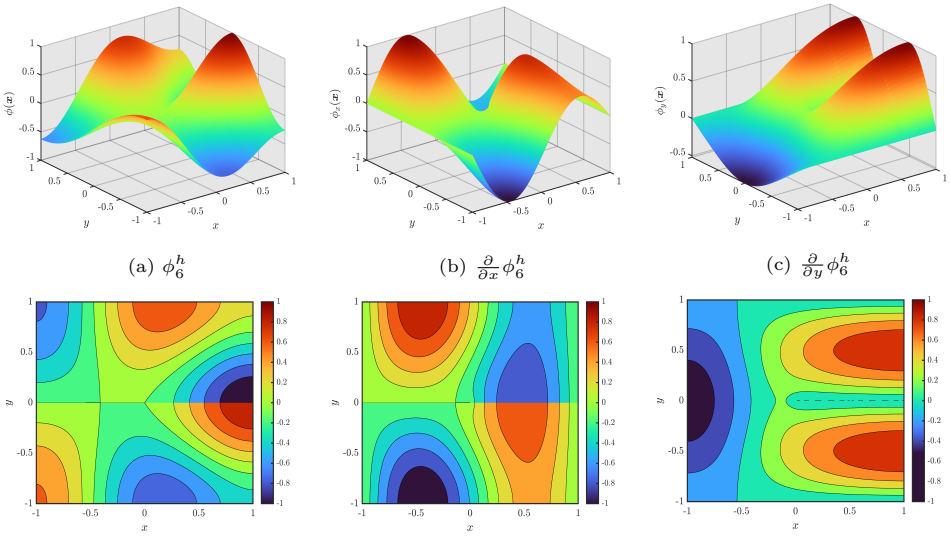

(a) ϕ_6^h (b) $\frac{\partial}{\partial x}\phi_6^h$ (c) $\frac{\partial}{\partial y}\phi_6^h$

(d) ϕ_6^h (e) $\frac{\partial}{\partial x}\phi_6^h$ (f) $\frac{\partial}{\partial y}\phi_6^h$

Figure D.6: Functions $\phi^h(\boldsymbol{x})$ and $\nabla\phi^h(\boldsymbol{x})$ associated to $\lambda_6 = 10.8448542781$.

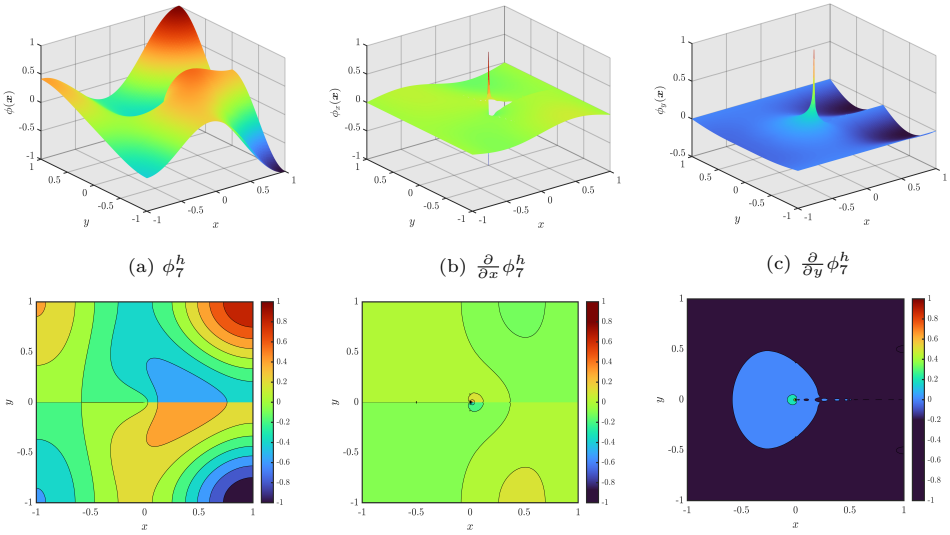

(a) ϕ_7^h (b) $\frac{\partial}{\partial x}\phi_7^h$ (c) $\frac{\partial}{\partial y}\phi_7^h$

(d) ϕ_7^h (e) $\frac{\partial}{\partial x}\phi_7^h$ (f) $\frac{\partial}{\partial y}\phi_7^h$

Figure D.7: Functions $\phi^h(\boldsymbol{x})$ and $\nabla\phi^h(\boldsymbol{x})$ associated to $\lambda_7 = 12.2648958490$.

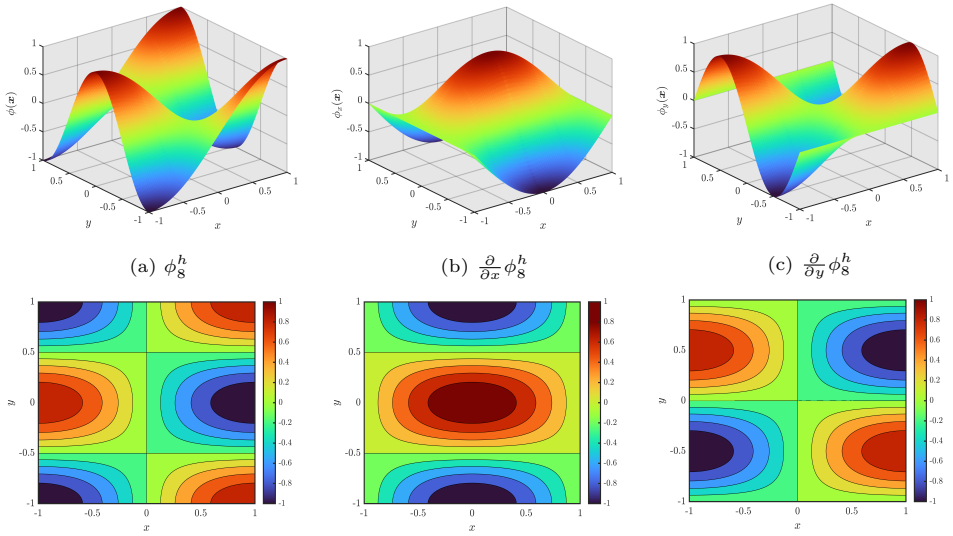

(a) ϕ_8^h (b) $\frac{\partial}{\partial x}\phi_8^h$ (c) $\frac{\partial}{\partial y}\phi_8^h$

(d) ϕ_8^h (e) $\frac{\partial}{\partial x}\phi_8^h$ (f) $\frac{\partial}{\partial y}\phi_8^h$

Figure D.8: Functions $\phi^h(\boldsymbol{x})$ and $\nabla\phi^h(\boldsymbol{x})$ associated to $\lambda_8 = 12.3370055014$.

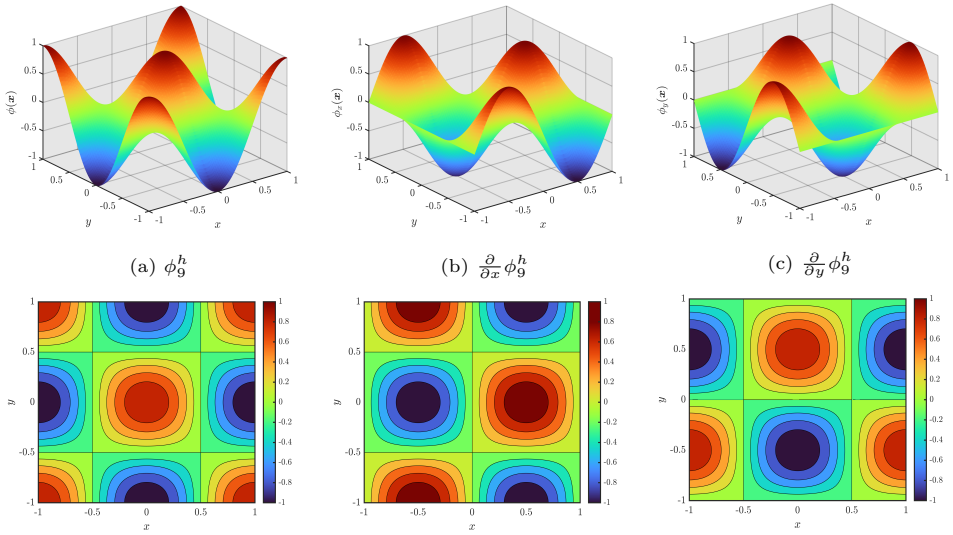

(a) ϕ_9^h (b) $\frac{\partial}{\partial x}\phi_9^h$ (c) $\frac{\partial}{\partial y}\phi_9^h$

(d) ϕ_9^h (e) $\frac{\partial}{\partial x}\phi_9^h$ (f) $\frac{\partial}{\partial y}\phi_9^h$

Figure D.9: Functions $\phi^h(\boldsymbol{x})$ and $\nabla\phi^h(\boldsymbol{x})$ associated to $\lambda_9 = 19.7392088022$.

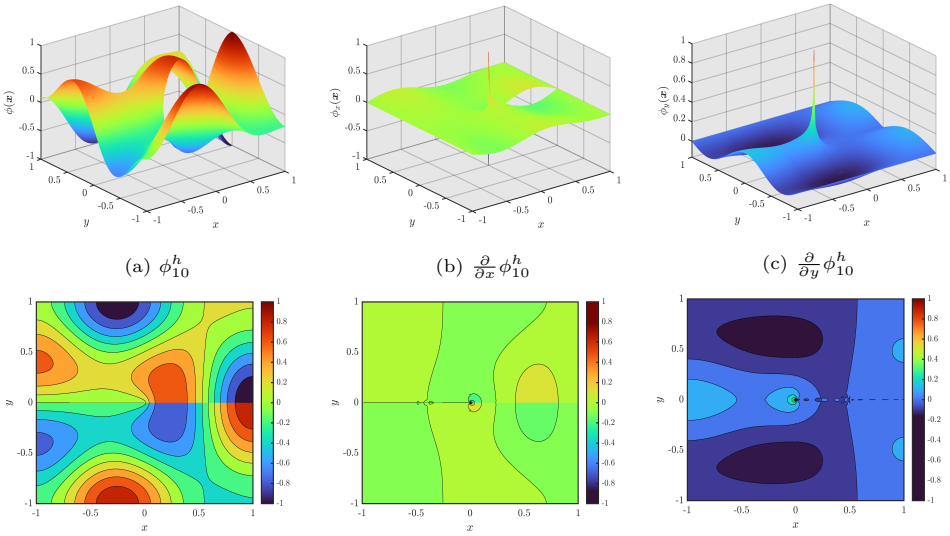

(a) ϕ^h_{10} (b) $\frac{\partial}{\partial x}\phi^h_{10}$ (c) $\frac{\partial}{\partial y}\phi^h_{10}$

(d) ϕ^h_{10} (e) $\frac{\partial}{\partial x}\phi^h_{10}$ (f) $\frac{\partial}{\partial y}\phi^h_{10}$

Figure D.10: Functions $\phi^h(\boldsymbol{x})$ and $\nabla\phi^h(\boldsymbol{x})$ associated to $\lambda_{10} = 21.2441074562$.

E

Eigenfunctions: Doubly Connected Domain

Contours for the eigenfunctions $\mathbf{E}^h(\boldsymbol{x})$ associated to the the eigenvalues computed in Section 6.2.2 are presented here. The eigenfunction associated to λ_3^h is omitted since it resembles the one from λ_2^h but the components E_x and E_y switch their positions while $|\mathbf{E}_3^h|$ is exactly the same as $|\mathbf{E}_2^h|$.

The plots from Figure E.1, Figure E.3 and Figure E.4 where obtained using $N = 10$ and 1 spectral element per subdomain Ω_k as shown in Figure 6.9. Those parameters were good enough as to capture the behavior of the function at the interior corners of the domain.

For the eigenfunction associated to λ_2^h, 10 spectral elements per subdomain were utilized along with $N = 1$. In this case, the components of the eigenfunction present rapid changes at certain locations of the outer boundaries while $|\mathbf{E}|$ ends up having rapid change at the outer corners of the domain. Such behavior, for some reason, was difficult to capture with the settings used for the other plots.

From the plots it can be seen that the one with the *most regular* behavior at the boundaries is the eigenfunction associated to λ_4^h which coincides with the fact that its eigenvalue converges the fastest among the ones presented in Table 6.5.

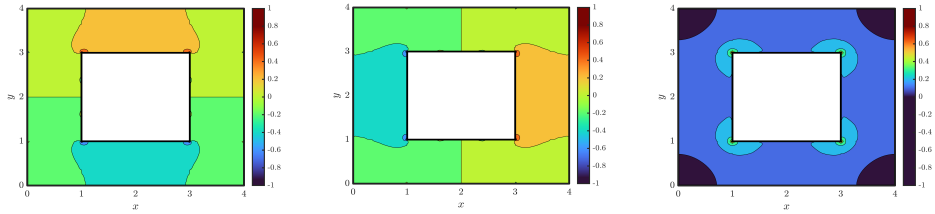

(a) E_x^h (b) E_y^h (c) $|\mathbf{E}^h|$

Figure E.1: Eigenfunction $\mathbf{E}^h(\boldsymbol{x})$ associated to $\lambda_1^h = 0$.

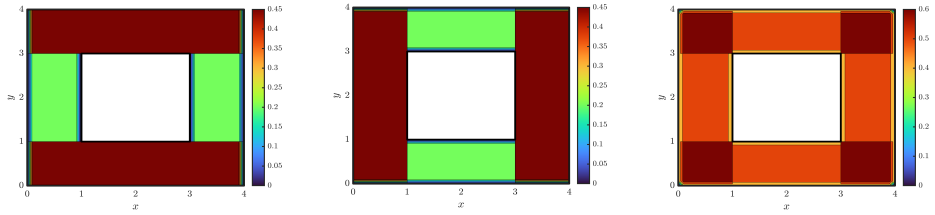

(a) E_x^h (b) E_y^h (c) $|\mathbf{E}^h|$

Figure E.2: Eigenfunction $\mathbf{E}^h(\boldsymbol{x})$ associated to $\lambda_2^h = 0.316216510716555$.

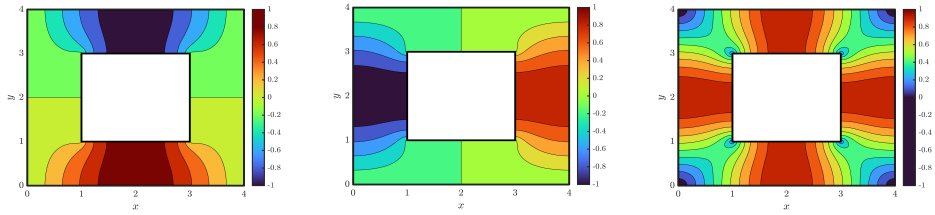

(a) E_x^h (b) E_y^h (c) $|\mathbf{E}^h|$

Figure E.3: Eigenfunction $\mathbf{E}^h(\boldsymbol{x})$ associated to $\lambda_4^h = 1.041521635153060$.

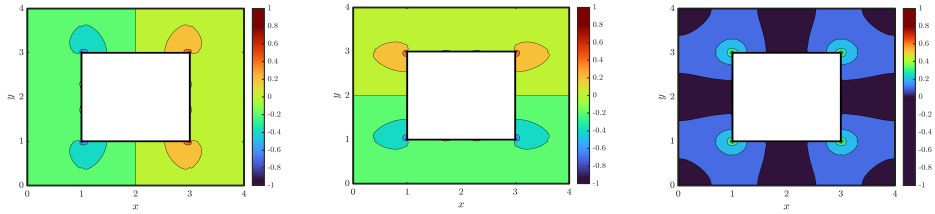

(a) E_x^h (b) E_y^h (c) $|\mathbf{E}^h|$

Figure E.4: Eigenfunction $\mathbf{E}^h(\boldsymbol{x})$ associated to $\lambda_5^h = 1.475228532358697$.

F

Eigenfunctions: Piecewise Constant Permittivity

Eigenfunctions $\mathbf{E}^h(\boldsymbol{x})$ in $\Omega = [\text{-}1, 1]^2$ associated to the eigenvalues of Section 6.2.3 with parameters $\underline{\underline{\epsilon_1}} = \left[\begin{smallmatrix} 1 & 0 \\ 0 & 1 \end{smallmatrix}\right]$, $\underline{\underline{\epsilon_2}} = \left[\begin{smallmatrix} 0.01 & 0 \\ 0 & 0.01 \end{smallmatrix}\right]$ and $\mu = \mathbb{I}$.

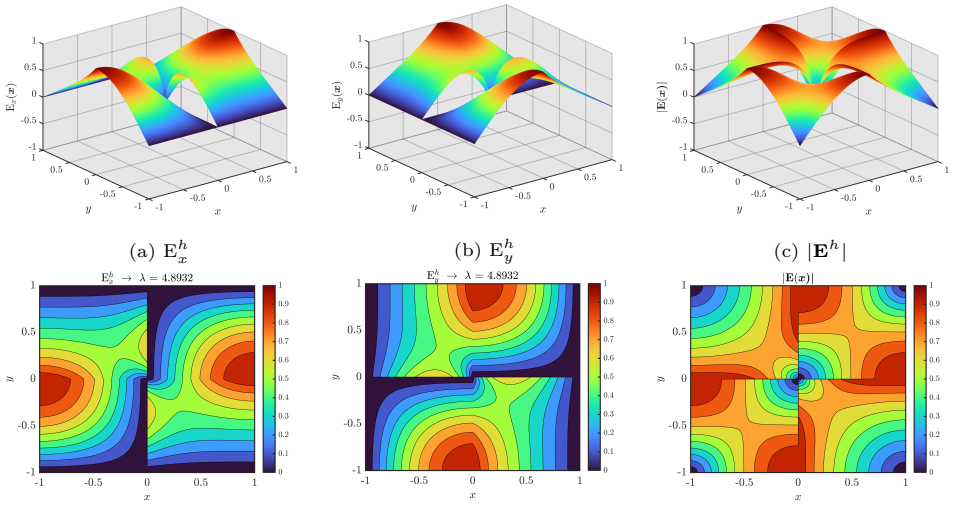

(a) E_x^h (b) E_y^h (c) $|\mathbf{E}^h|$

(d) E_x^h (e) E_y^h (f) $|\mathbf{E}^h|$

Figure F.1: Components of $\mathbf{E}^h(\boldsymbol{x})$ and $|\mathbf{E}^h|$ associated to $\lambda_1^h = 4.8932$.

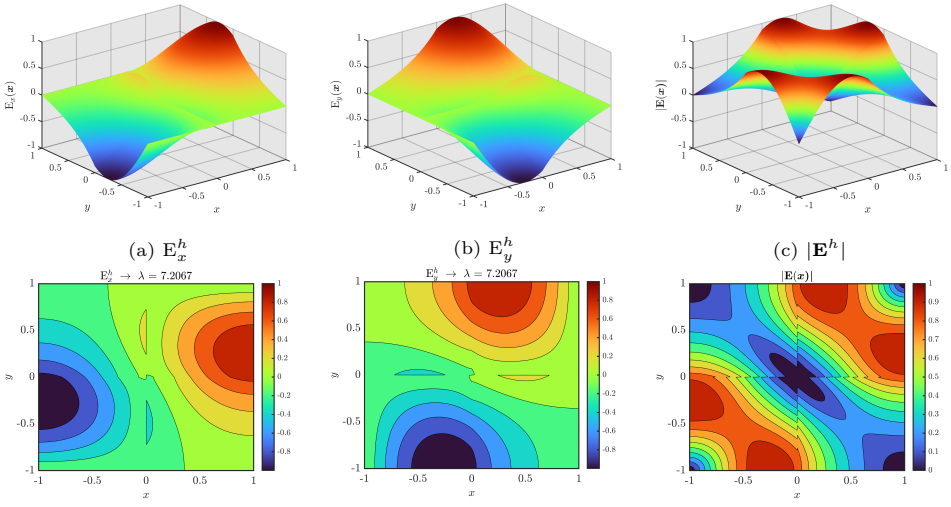

(a) E_x^h (b) E_y^h (c) $|\mathbf{E}^h|$

(d) E_x^h (e) E_y^h (f) $|\mathbf{E}^h|$

Figure F.2: Components of $\mathbf{E}^h(\boldsymbol{x})$ and $|\mathbf{E}^h|$ associated to $\lambda_2^h = 7.2067$.

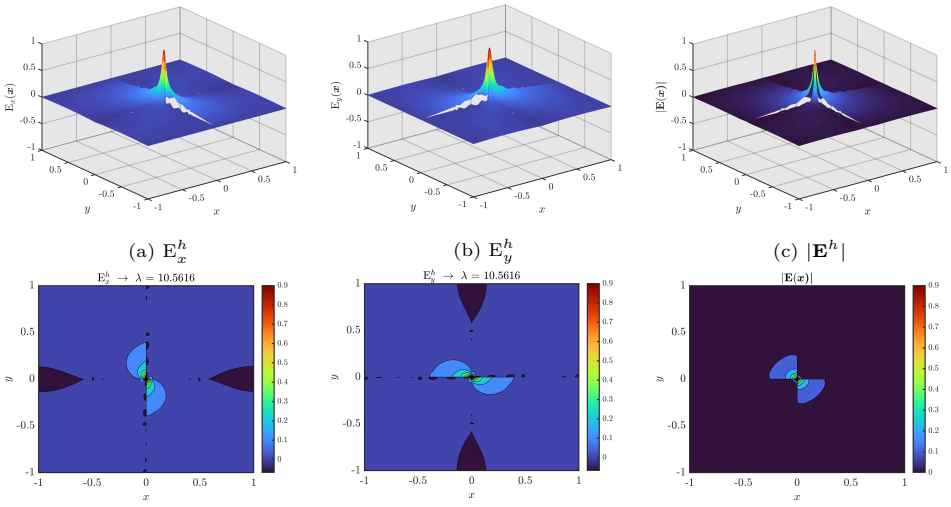

(a) E_x^h (b) E_y^h (c) $|\mathbf{E}^h|$

(d) E_x^h (e) E_y^h (f) $|\mathbf{E}^h|$

Figure F.3: Components of $\mathbf{E}^h(\boldsymbol{x})$ and $|\mathbf{E}^h|$ associated to $\lambda_3^h = 10.5616$.

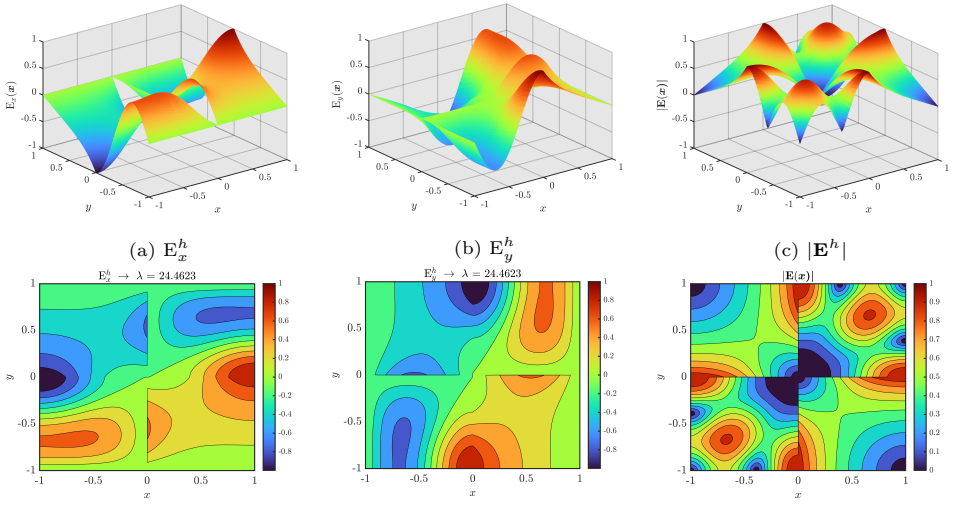

(a) E_x^h (b) E_y^h (c) $|\mathbf{E}^h|$

(d) E_x^h (e) E_y^h (f) $|\mathbf{E}^h|$

Figure F.4: Components of $\mathbf{E}^h(\boldsymbol{x})$ and $|\mathbf{E}^h|$ associated to $\lambda_4^h = 24.4623$.

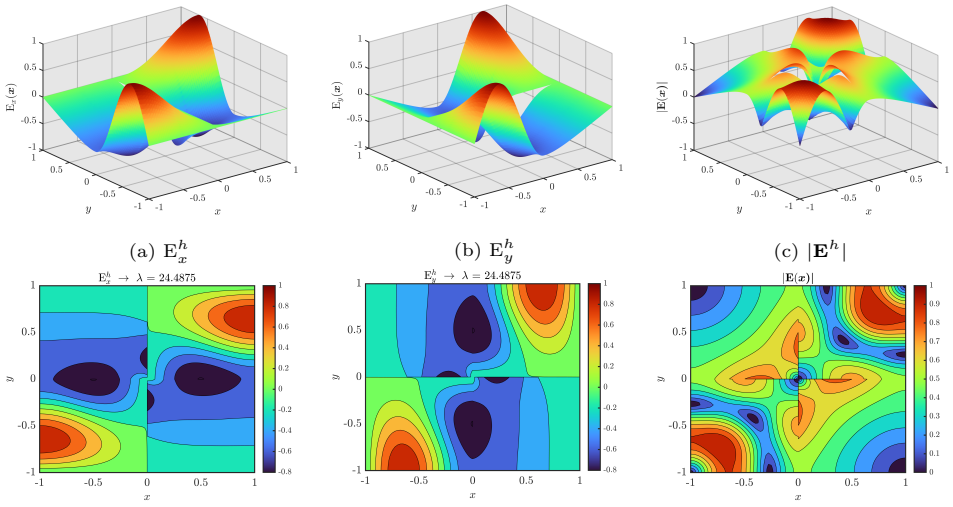

(a) E_x^h (b) E_y^h (c) $|\mathbf{E}^h|$

(d) E_x^h (e) E_y^h (f) $|\mathbf{E}^h|$

Figure F.5: Components of $\mathbf{E}^h(\boldsymbol{x})$ and $|\mathbf{E}^h|$ associated to $\lambda_5^h = 24.4875$.

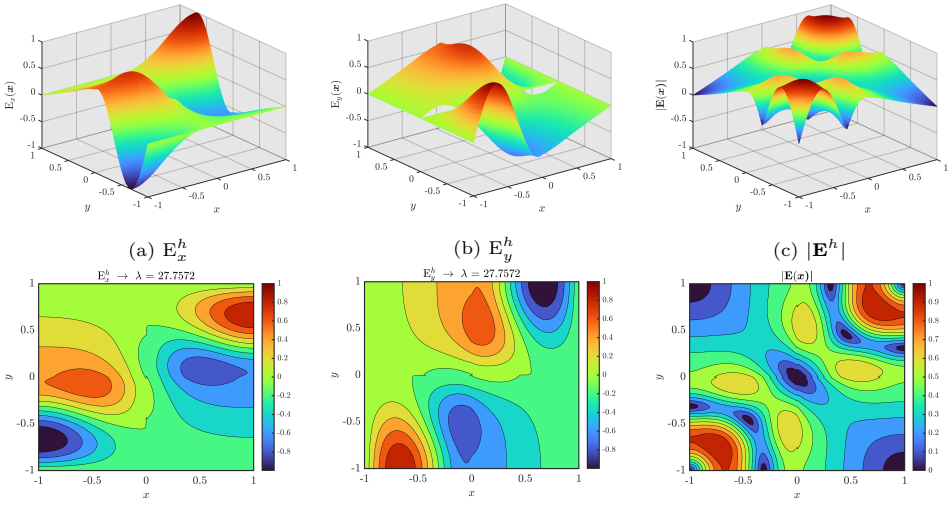

(a) E_x^h (b) E_y^h (c) $|\mathbf{E}^h|$

(d) E_x^h (e) E_y^h (f) $|\mathbf{E}^h|$

Figure F.6: Components of $\mathbf{E}^h(\boldsymbol{x})$ and $|\mathbf{E}^h|$ associated to $\lambda_6^h = 27.7572$.

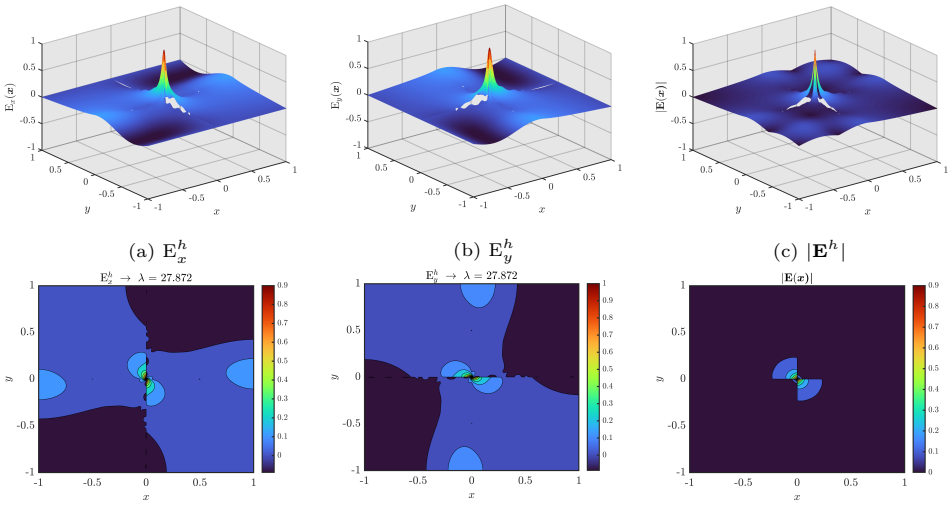

(a) E_x^h (b) E_y^h (c) $|\mathbf{E}^h|$

(d) E_x^h (e) E_y^h (f) $|\mathbf{E}^h|$

Figure F.7: Components of $\mathbf{E}^h(\boldsymbol{x})$ and $|\mathbf{E}^h|$ associated to $\lambda_7^h = 27.8720$.

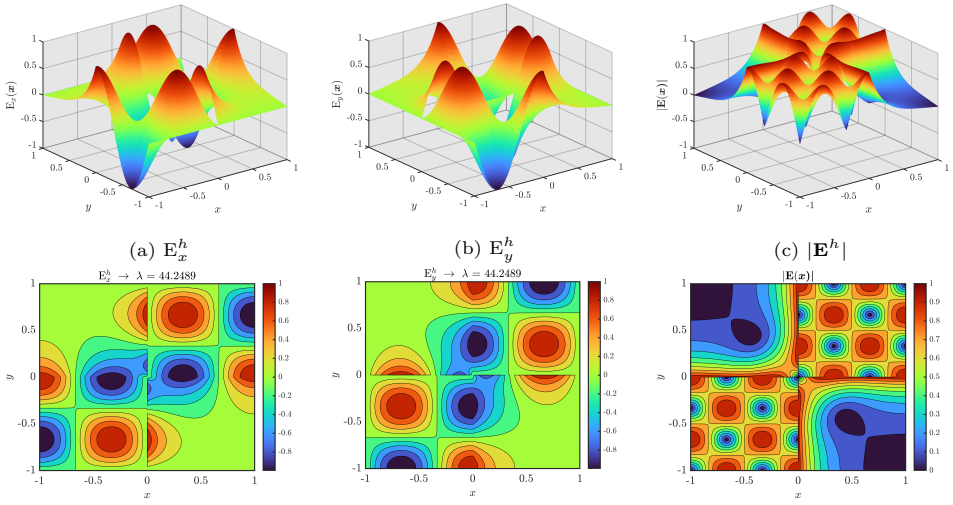

(a) E_x^h (b) E_y^h (c) $|\mathbf{E}^h|$

(d) E_x^h (e) E_y^h (f) $|\mathbf{E}^h|$

Figure F.8: Components of $\mathbf{E}^h(\boldsymbol{x})$ and $|\mathbf{E}^h|$ associated to $\lambda_8^h = 44.2489$.

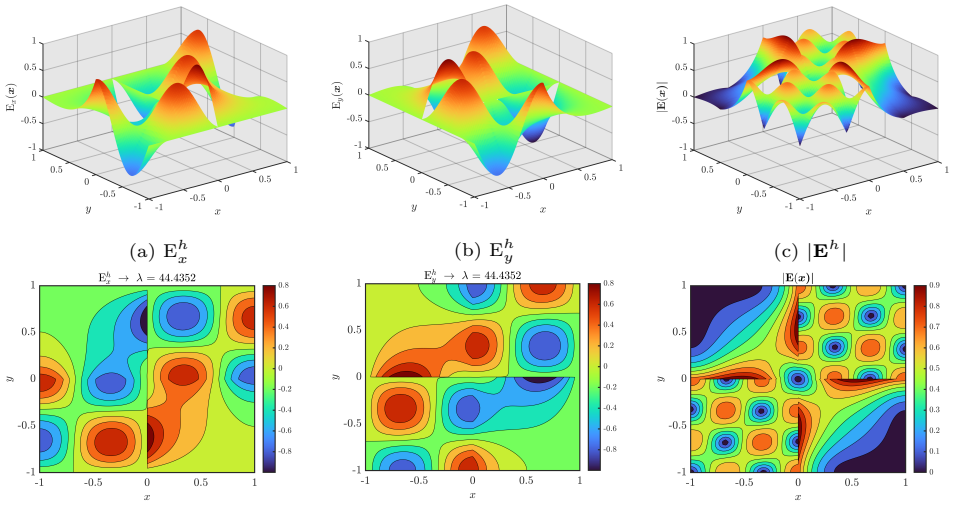

(a) E_x^h (b) E_y^h (c) $|\mathbf{E}^h|$

(d) E_x^h (e) E_y^h (f) $|\mathbf{E}^h|$

Figure F.9: Components of $\mathbf{E}^h(\boldsymbol{x})$ and $|\mathbf{E}^h|$ associated to $\lambda_9^h = 44.4352$.

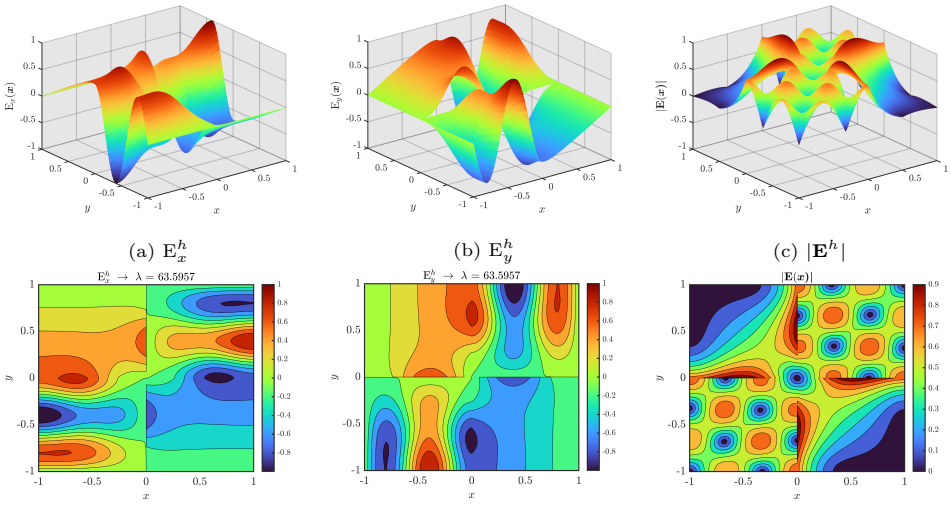

(a) E_x^h (b) E_y^h (c) $|\mathbf{E}^h|$

(d) E_x^h (e) E_y^h (f) $|\mathbf{E}^h|$

Figure F.10: Components of $\mathbf{E}^h(\boldsymbol{x})$ and $|\mathbf{E}^h|$ associated to $\lambda_{10}^h = 63.5957$.

G

Eigenfunctions: Anisotropic Square Domain

Eigenfunctions $\mathbf{E}^h(\boldsymbol{x})$ and $\nabla \times \mathbf{E}^h$ for the eigenvalues of Section 6.3.1 on $\Omega = [0,\, \pi]^2$ and $\underline{\underline{\epsilon_{rt}}} = \left[\begin{smallmatrix} 2 & 1 \\ 1 & 2 \end{smallmatrix}\right]$ and $\mu_{rz} = 1$. Computed using $N = 6$ and 4 spectral elements.

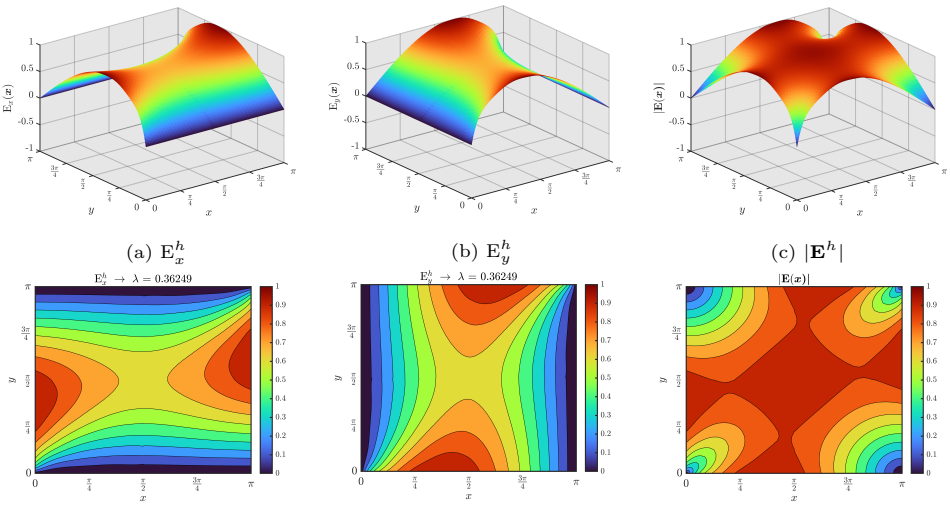

(a) E_x^h (b) E_y^h (c) $|\mathbf{E}^h|$

(d) E_x^h (e) E_y^h (f) $|\mathbf{E}^h|$

Figure G.1: Components of $\mathbf{E}^h(\boldsymbol{x})$ and $|\mathbf{E}^h|$ associated to $\lambda_1^h = 0.362493713534222$.

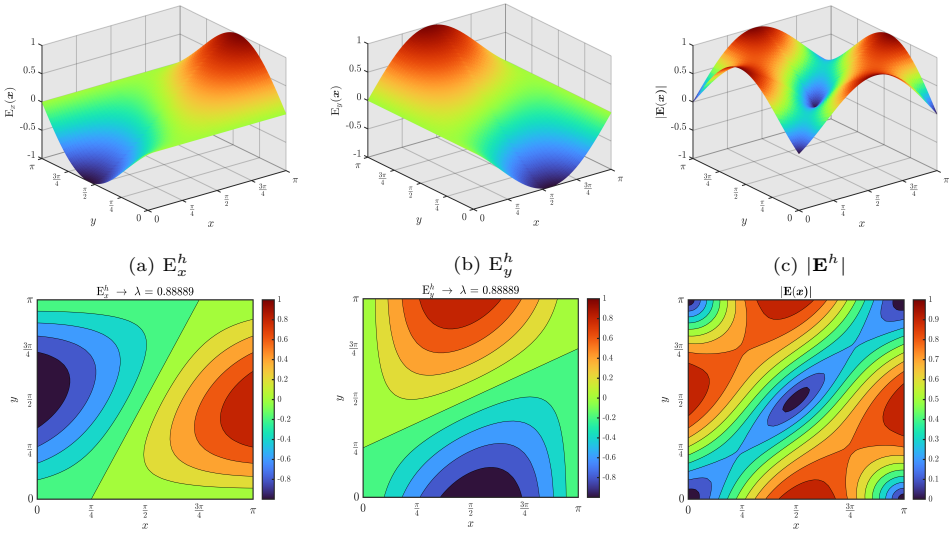

(a) E_x^h (b) E_y^h (c) $|\mathbf{E}^h|$

(d) E_x^h (e) E_y^h (f) $|\mathbf{E}^h|$

Figure G.2: Components of $\mathbf{E}^h(\boldsymbol{x})$ and $|\mathbf{E}^h|$ associated to $\lambda_2^h = 0.888888888888976$.

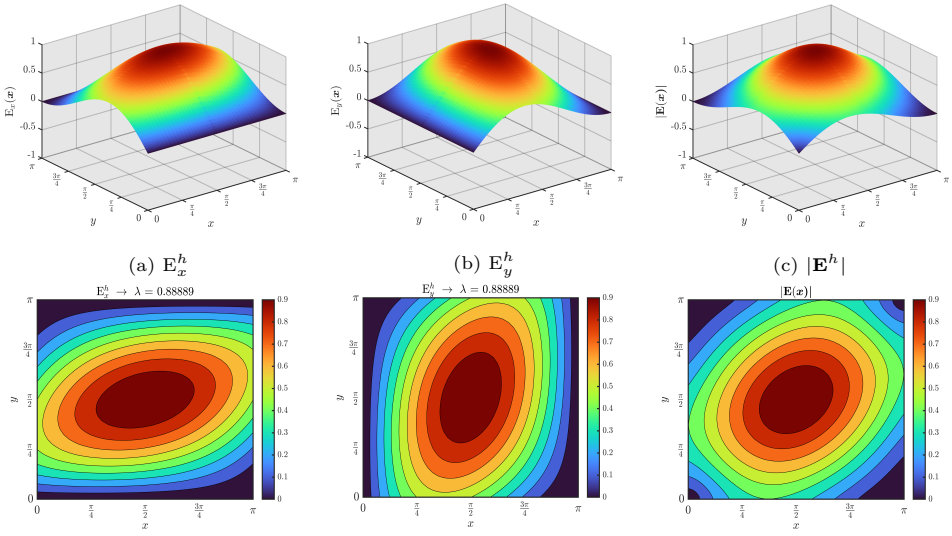

(a) E_x^h (b) E_y^h (c) $|\mathbf{E}^h|$

(d) E_x^h (e) E_y^h (f) $|\mathbf{E}^h|$

Figure G.3: Components of $\mathbf{E}^h(\boldsymbol{x})$ and $|\mathbf{E}^h|$ associated to $\lambda_3^h = 0.888888888890293$.

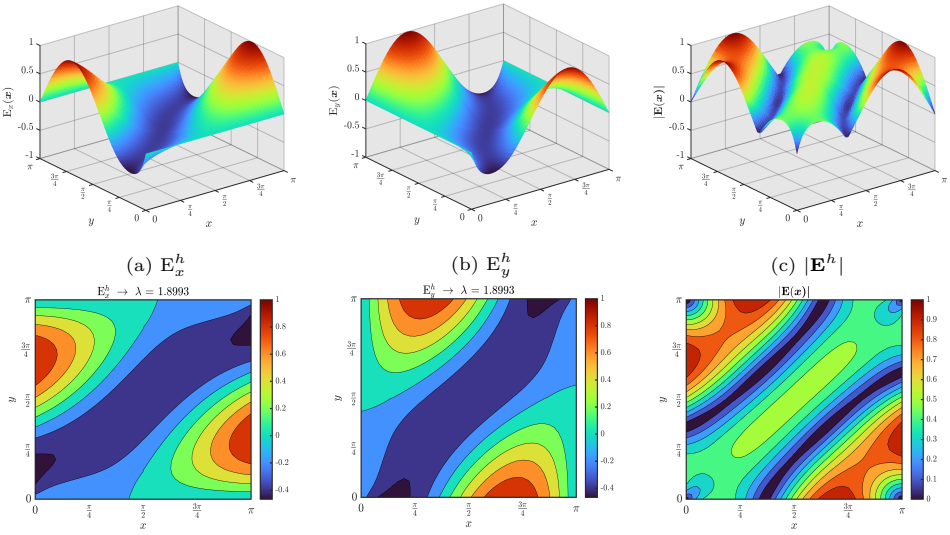

(a) E_x^h (b) E_y^h (c) $|\mathbf{E}^h|$

(d) E_x^h (e) E_y^h (f) $|\mathbf{E}^h|$

Figure G.4: Components of $\mathbf{E}^h(\boldsymbol{x})$ and $|\mathbf{E}^h|$ associated to $\lambda_4^h = 1.899334112725240$.

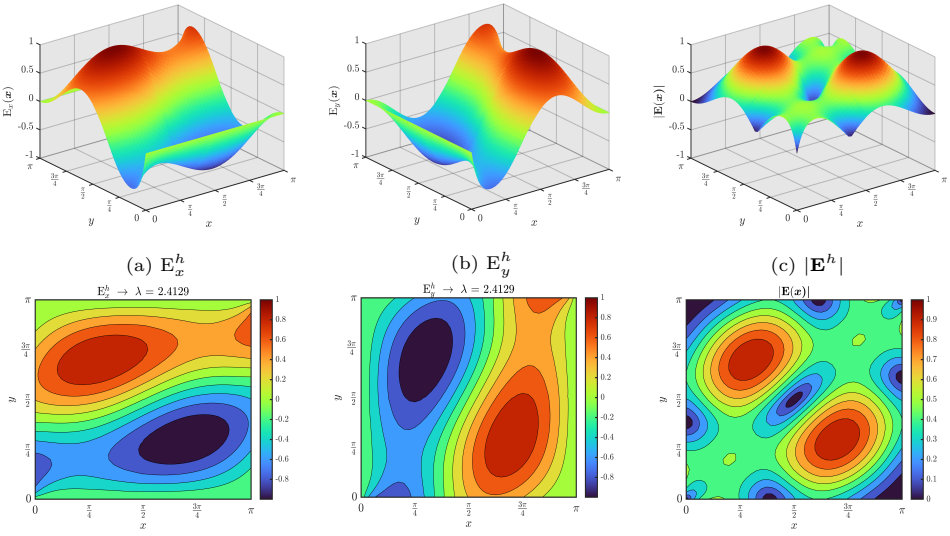

(a) E_x^h (b) E_y^h (c) $|\mathbf{E}^h|$

(d) E_x^h (e) E_y^h (f) $|\mathbf{E}^h|$

Figure G.5: Components of $\mathbf{E}^h(\boldsymbol{x})$ and $|\mathbf{E}^h|$ associated to $\lambda_5^h = 2.412931825959713$.

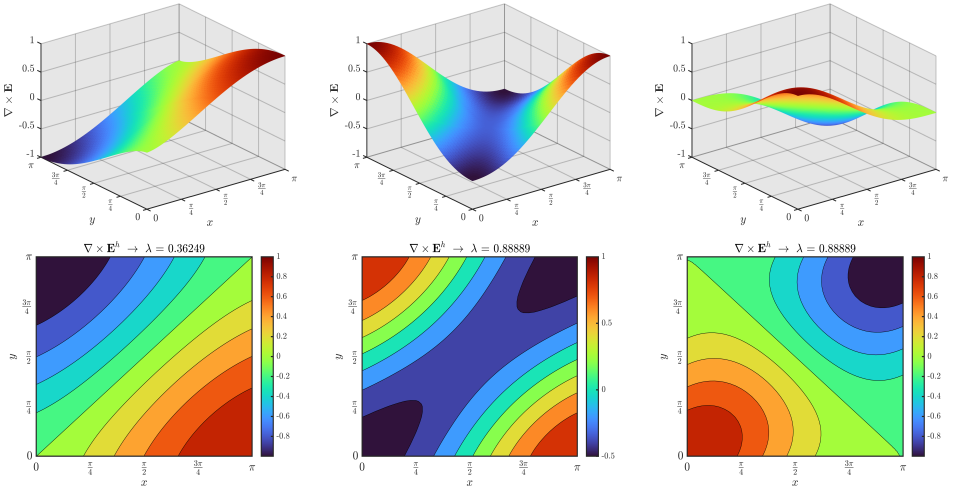

(a) (b) (c)

Figure G.6: Functions $\nabla \times \mathbf{E}^h$ for (a) λ_1^h, (b) λ_2^h and (c) λ_3^h.

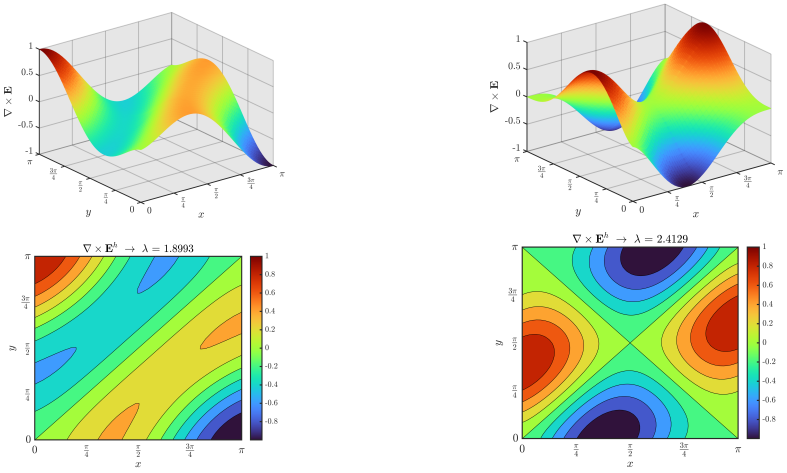

(a) (b)

Figure G.7: Functions $\nabla \times \mathbf{E}^h$ for (a) λ_4^h and (b) λ_5^h.

H

Eigenfunctions: H-Domain

Eigenfunctions $\mathbf{E}^h(\boldsymbol{x})$ associated to the eigenvalues of Section 6.3.2 with parameters $\underline{\underline{\epsilon}} = \left[\begin{smallmatrix} 1 & -j \\ j & 4 \end{smallmatrix}\right]$ & $\mu_{rz} = 1$ are presented. Since there is no indication in [53] about the amplitude used to match the eigenfunctions, the value 0.35 was utilized since it seems to be the maximum value reached by $\mathrm{Re}(|\mathbf{E}^h|)$ for λ_1^h.

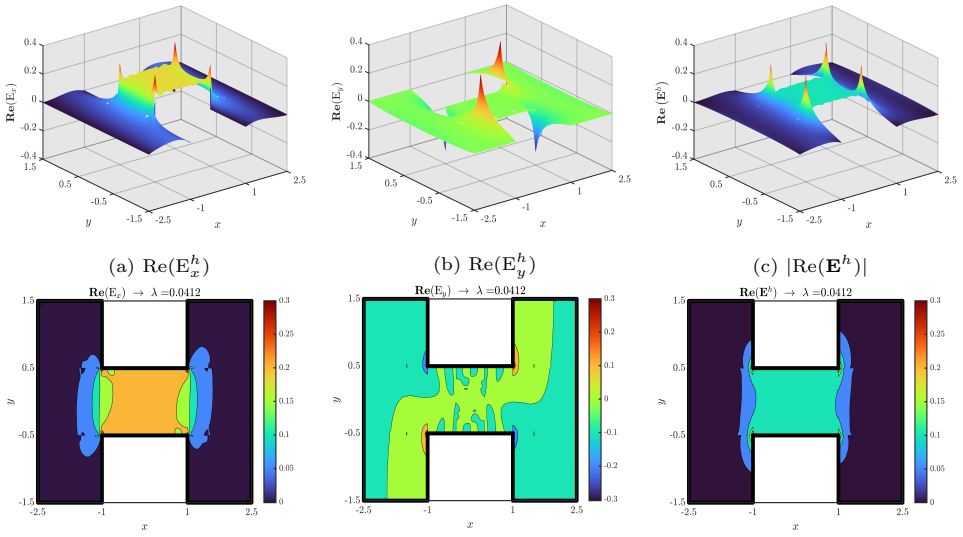

(a) $\mathrm{Re}(\mathrm{E}_x^h)$ (b) $\mathrm{Re}(\mathrm{E}_y^h)$ (c) $|\mathrm{Re}(\mathbf{E}^h)|$

(d) $\mathrm{Re}(\mathrm{E}_x^h)$ (e) $\mathrm{Re}(\mathrm{E}_y^h)$ (f) $|\mathrm{Re}(\mathbf{E}^h)|$

Figure H.1: Components of $\mathrm{Re}(\mathbf{E}^h)$ and norm $|\mathrm{Re}(\mathbf{E}^h)|$ associated to $\lambda_1^h = 0.041170265695516$.

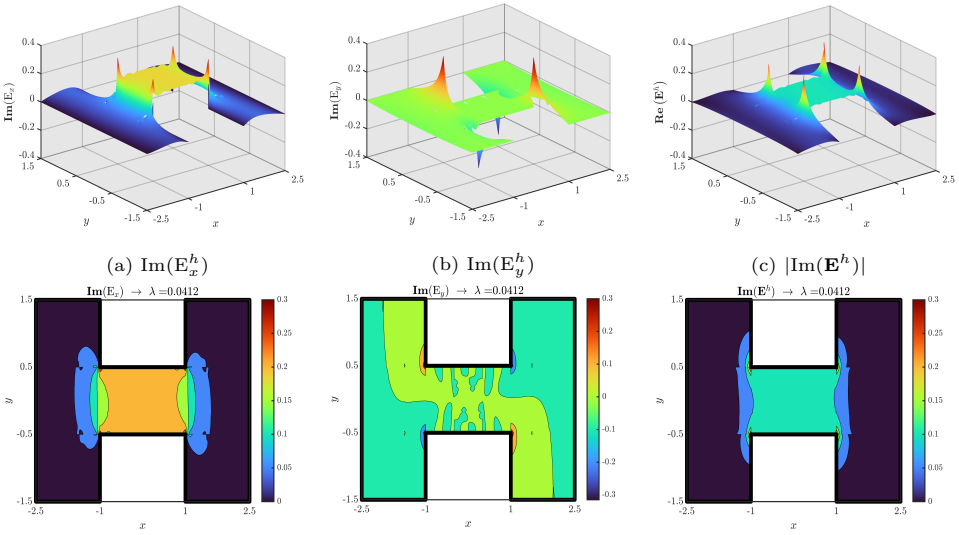

(a) $\mathrm{Im}(\mathrm{E}_x^h)$ (b) $\mathrm{Im}(\mathrm{E}_y^h)$ (c) $|\mathrm{Im}(\mathbf{E}^h)|$

(d) $\mathrm{Im}(\mathrm{E}_x^h)$ (e) $\mathrm{Im}(\mathrm{E}_y^h)$ (f) $|\mathrm{Im}(\mathbf{E}^h)|$

Figure H.2: Components of $\mathrm{Im}(\mathbf{E}^h)$ and norm $|\mathrm{Im}(\mathbf{E}^h)|$ associated to $\lambda_1^h = 0.041170265695516$.

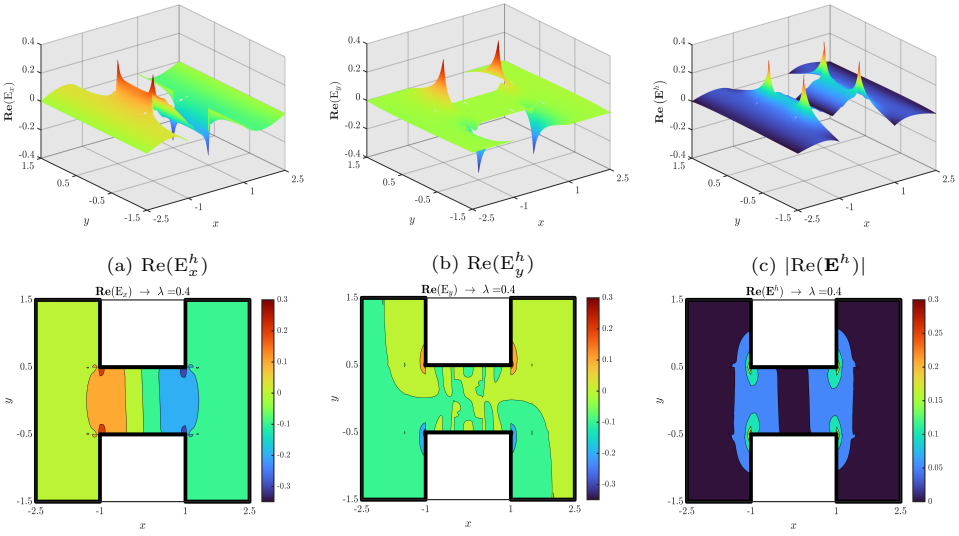

(a) $\mathrm{Re}(\mathrm{E}_x^h)$ (b) $\mathrm{Re}(\mathrm{E}_y^h)$ (c) $|\mathrm{Re}(\mathbf{E}^h)|$

(d) $\mathrm{Re}(\mathrm{E}_x^h)$ (e) $\mathrm{Re}(\mathrm{E}_y^h)$ (f) $|\mathrm{Re}(\mathbf{E}^h)|$

Figure H.3: Components of $\mathrm{Re}(\mathbf{E}^h)$ and norm $|\mathrm{Re}(\mathbf{E}^h)|$ associated to $\lambda_2^h = 0.400029005155471$.

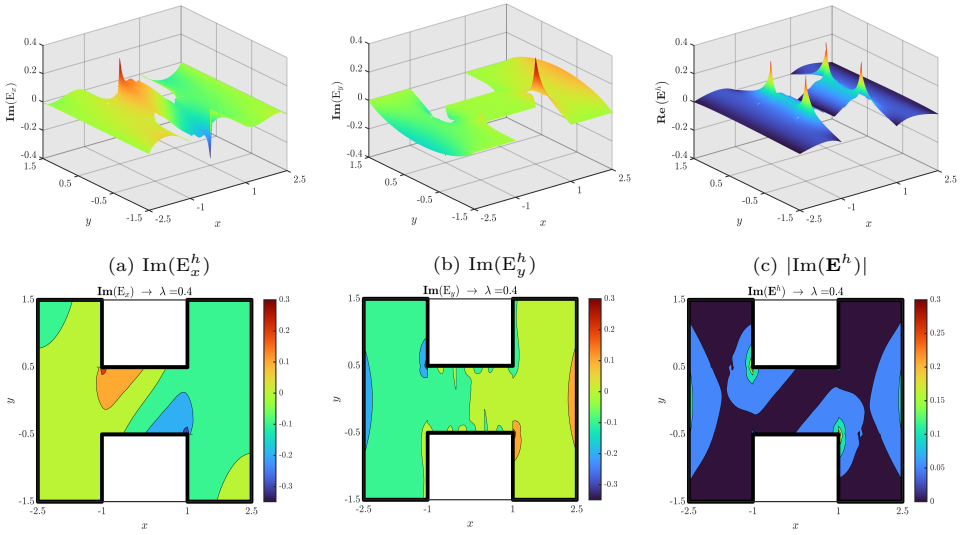

(a) $\mathrm{Im}(\mathrm{E}_x^h)$ (b) $\mathrm{Im}(\mathrm{E}_y^h)$ (c) $|\mathrm{Im}(\mathbf{E}^h)|$

(d) $\mathrm{Im}(\mathrm{E}_x^h)$ (e) $\mathrm{Im}(\mathrm{E}_y^h)$ (f) $|\mathrm{Im}(\mathbf{E}^h)|$

Figure H.4: Components of $\mathrm{Im}(\mathbf{E}^h)$ and norm $|\mathrm{Im}(\mathbf{E}^h)|$ associated to $\lambda_2^h = 0.400029005155471$.

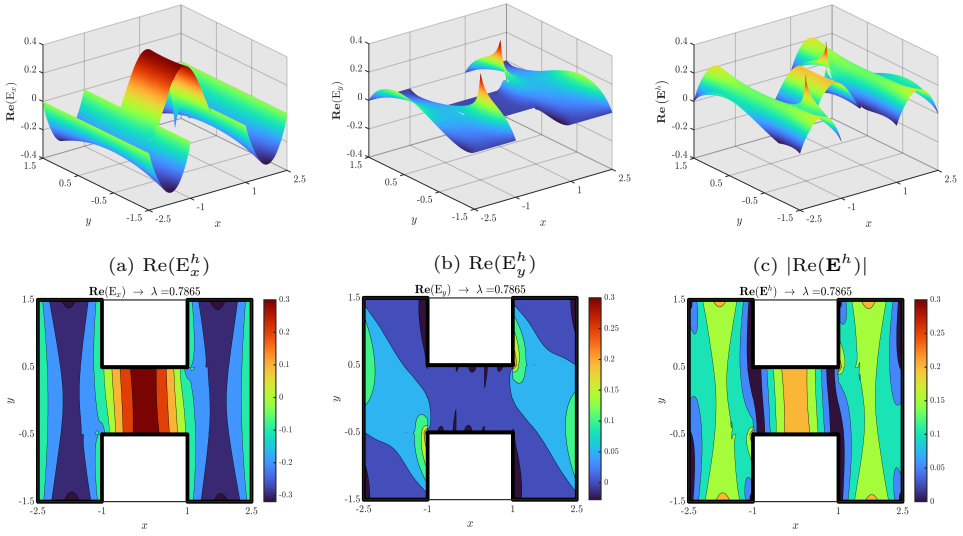

(a) $\mathrm{Re}(\mathrm{E}_x^h)$ (b) $\mathrm{Re}(\mathrm{E}_y^h)$ (c) $|\mathrm{Re}(\mathbf{E}^h)|$

(d) $\mathrm{Re}(\mathrm{E}_x^h)$ (e) $\mathrm{Re}(\mathrm{E}_y^h)$ (f) $|\mathrm{Re}(\mathbf{E}^h)|$

Figure H.5: Components of $\mathrm{Re}(\mathbf{E}^h)$ and norm $|\mathrm{Re}(\mathbf{E}^h)|$ associated to $\lambda_3^h = 0.786486748946923$.

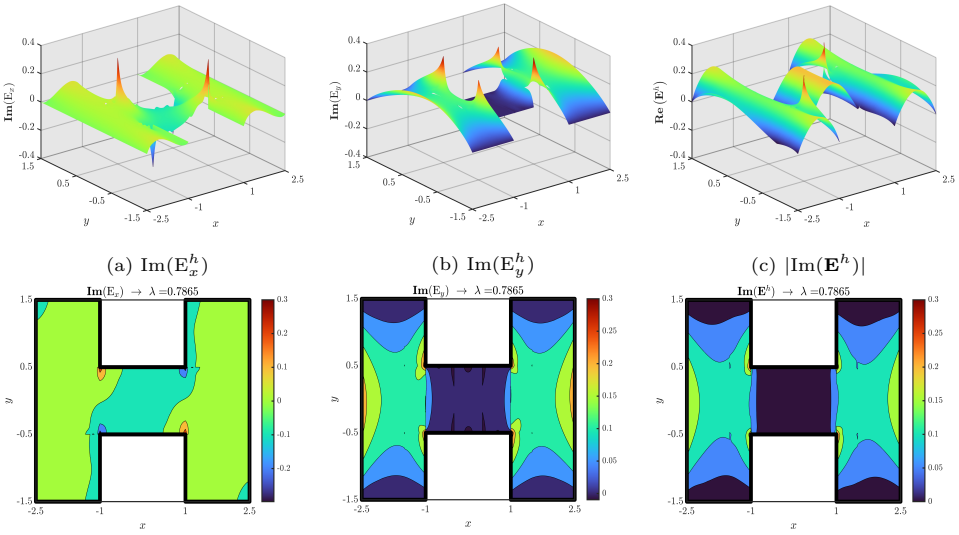

(a) $\mathrm{Im}(\mathrm{E}_x^h)$ (b) $\mathrm{Im}(\mathrm{E}_y^h)$ (c) $|\mathrm{Im}(\mathbf{E}^h)|$

(d) $\mathrm{Im}(\mathrm{E}_x^h)$ (e) $\mathrm{Im}(\mathrm{E}_y^h)$ (f) $|\mathrm{Im}(\mathbf{E}^h)|$

Figure H.6: Components of $\mathrm{Im}(\mathbf{E}^h)$ and norm $|\mathrm{Im}(\mathbf{E}^h)|$ associated to $\lambda_3^h = 0.786486748946923$.

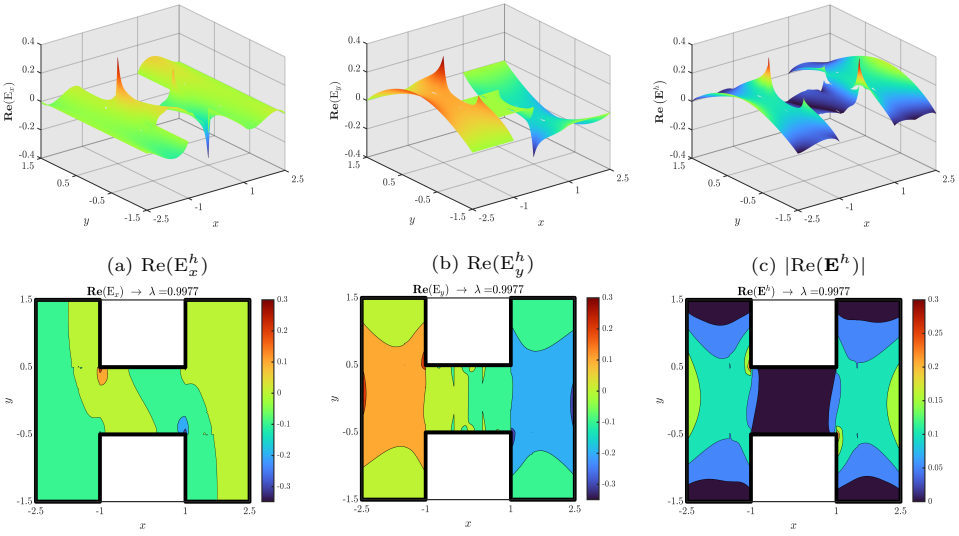

(a) $\mathrm{Re}(\mathrm{E}_x^h)$ (b) $\mathrm{Re}(\mathrm{E}_y^h)$ (c) $|\mathrm{Re}(\mathbf{E}^h)|$

(d) $\mathrm{Re}(\mathrm{E}_x^h)$ (e) $\mathrm{Re}(\mathrm{E}_y^h)$ (f) $|\mathrm{Re}(\mathbf{E}^h)|$

Figure H.7: Components of $\mathrm{Re}(\mathbf{E}^h)$ and norm $|\mathrm{Re}(\mathbf{E}^h)|$ associated to $\lambda_4^h = 0.997709453437649$.

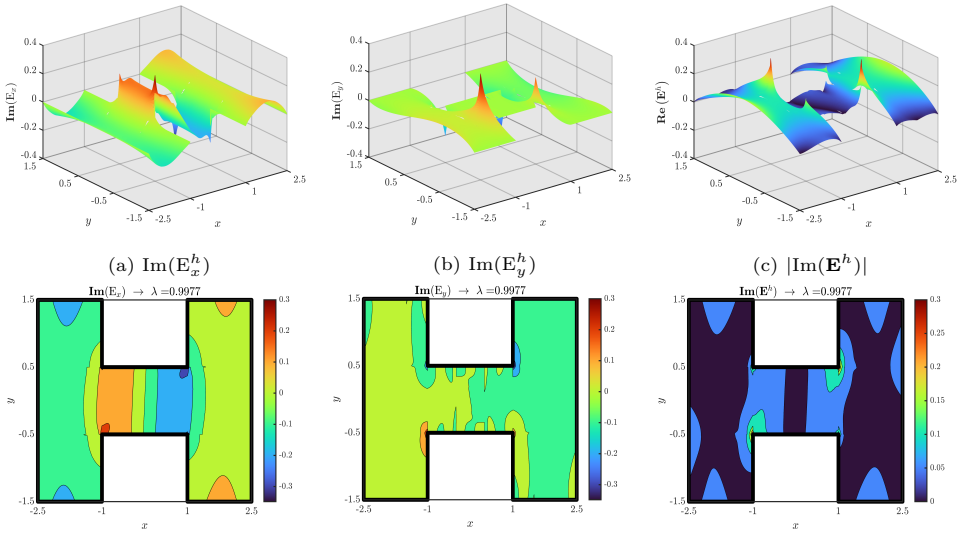

(a) $\mathrm{Im}(\mathrm{E}_x^h)$ (b) $\mathrm{Im}(\mathrm{E}_y^h)$ (c) $|\mathrm{Im}(\mathbf{E}^h)|$

(d) $\mathrm{Im}(\mathrm{E}_x^h)$ (e) $\mathrm{Im}(\mathrm{E}_y^h)$ (f) $|\mathrm{Im}(\mathbf{E}^h)|$

Figure H.8: Components of $\mathrm{Im}(\mathbf{E}^h)$ and norm $|\mathrm{Im}(\mathbf{E}^h)|$ associated to $\lambda_4^h = 0.997709453437649$.

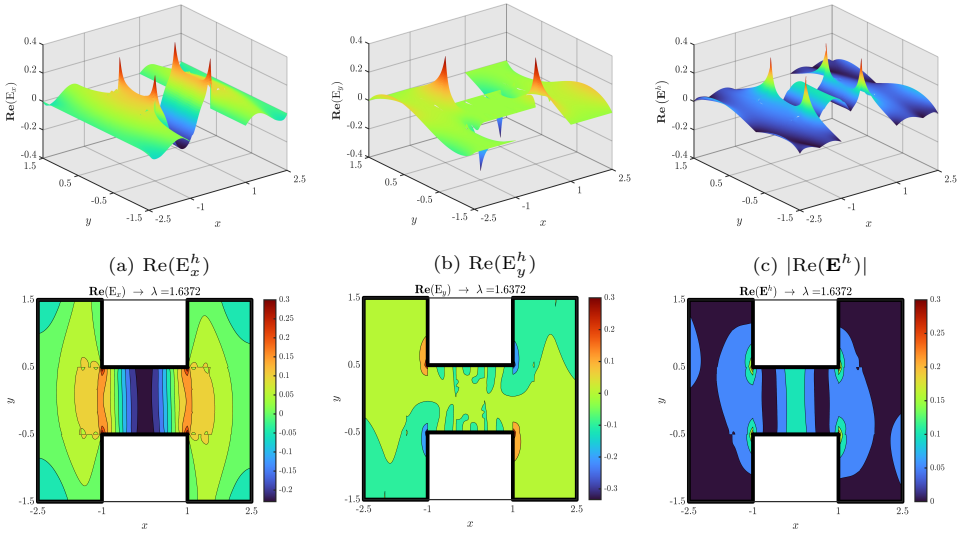

(a) $\mathrm{Re}(\mathrm{E}_x^h)$ (b) $\mathrm{Re}(\mathrm{E}_y^h)$ (c) $|\mathrm{Re}(\mathbf{E}^h)|$

(d) $\mathrm{Re}(\mathrm{E}_x^h)$ (e) $\mathrm{Re}(\mathrm{E}_y^h)$ (f) $|\mathrm{Re}(\mathbf{E}^h)|$

Figure H.9: Components of $\mathrm{Re}(\mathbf{E}^h)$ and norm $|\mathrm{Re}(\mathbf{E}^h)|$ associated to $\lambda_5^h = 1.637215155912761$.

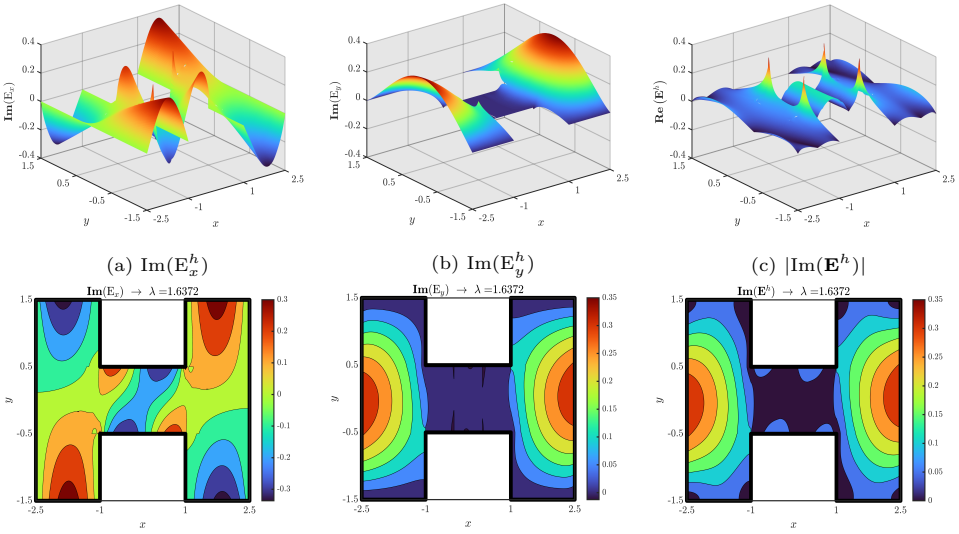

(a) $\mathrm{Im}(\mathrm{E}_x^h)$ (b) $\mathrm{Im}(\mathrm{E}_y^h)$ (c) $|\mathrm{Im}(\mathbf{E}^h)|$

(d) $\mathrm{Im}(\mathrm{E}_x^h)$ (e) $\mathrm{Im}(\mathrm{E}_y^h)$ (f) $|\mathrm{Im}(\mathbf{E}^h)|$

Figure H.10: Components of $\mathrm{Im}(\mathbf{E}^h)$ and norm $|\mathrm{Im}(\mathbf{E}^h)|$ associated to $\lambda_5^h = 1.637215155912761$.